UNIVERSITY COLLEGE LONDON

Faculty of Mathematics and Physical Sciences

Department of Physics & Astronomy

CONSTRAINING THE SOURCES OF ULTRA-HIGH ENERGY COSMIC RAYS WITH MULTI-MESSENGER DATA

Thesis submitted for the Degree of Doctor of Philosophy of the University of London

by

Foteini Oikonomou

Supervisors:

Prof. Ofer Lahav

Prof. David Waters

Examiners:

Prof. Jim Hinton

Dr Ryan Nichol

15th March 2014

To Dimitra and Kostas

I, Foteini Oikonomou, confirm that the work presented in this thesis is my own. Where information has been derived from other sources, I confirm that this has been indicated in the thesis.

All the research has been conducted in collaboration with my supervisors Ofer Lahav and David Waters as well as Filipe Abdalla, Amy Connolly and Kumiko Kotera.

The work presented in chapter 4 has been published in *The Journal of Cosmology and Astroparticle Physics* **JCAP05(2013)015** (Oikonomou et al. 2013).

The work presented in chapter 5 has been submitted for publication to *Astronomy & Astrophysics* (Oikonomou et al. 2014b).

The material in chapter 6 is presently in preparation for submission to *The Journal of Cosmology and Astroparticle Physics* (Oikonomou et al. 2014a).

Abstract

Ultra-high energy cosmic rays (UHECRs) are cosmic rays with energy exceeding 10^{18} electronvolts. The sources of these particles remain unknown despite decades of research. This thesis presents a series of studies aimed at constraining the sources of UHECRs both directly by studying their observed arrival directions and indirectly through their expected secondary gamma-ray signatures.

An analysis of the arrival direction distribution of the highest energy cosmic rays detected at the Pierre Auger Observatory is presented. The aim of the study was to determine whether the arrival directions of observed UHECRs follow the distribution of nearby extragalactic sources, which is expected if UHECRs are light nuclei of extragalactic origin. A departure from isotropy at the 95% level is observed but no clear correlation with the extragalactic matter distribution is found.

The sensitivity of upcoming UHECR experiments, with an order of magnitude higher annual exposure than current experiments, to the expected UHECR anisotropy has been investigated through simulations. It is shown, that with five years of data from such a detector an anisotropy should be detectable at the 99% level as long as the composition is proton dominated. In a scenario where the UHECR source distribution is strongly clustered, similar to the distribution of galaxy clusters, an anisotropy at the 99.9% level is expected even if the fraction of protons at the highest energies is as low as 30%.

Constraints on the sources of UHECRs may also come from the secondary particles that UHECRs produce during their propagation. A study of the expected secondary gamma-ray signatures of UHECR accelerators embedded in magnetised environments is presented. The secondary gamma-ray emission expected in this model is shown to be consistent with the spectra of a number of extreme blazars. It is shown that this model is

more robust to variations of the overall extragalactic magnetic field strength than other proposed scenarios, which is appealing in view of the large uncertainty surrounding the strength and configuration of extragalactic magnetic fields.

Acknowledgements

During the years over which this research was conducted, I have had the fortune of working alongside a number of exceptional people that have generously contributed to this work. First I'd like to express my gratitude to Ofer Lahav and David Waters. 'Are you a happy customer?' Ofer used to ask every once in a while, when our meeting was about to end; for the always encouraging and supportive mentoring, thank you Ofer. Thank you Dave for always providing wisdom and invaluable support, for making time for all of my questions and always providing me with excellent feedback and advice.

I am deeply grateful to Kumiko Kotera, the UHECR expert, who co-supervised me during the final year of this work, for the immense fortune of her arrival in London and for the chance I've had to work with her since. For the tireless support and advice and tireless encouragement, for the incredible opportunities you've given me and for so generously sharing your insight, thank you Kumiko! It has been a real pleasure working with you.

A very big thank you to Filipe Abdalla, who always supported my progress during this PhD. For the support and honest advice, for always helping out with whatever the issue: science, coding, broken cluster queues, nerves, life. You have been a vital source of support, thank you Fil.

I am very grateful to Amy Connolly, who co-supervised me during the first year of this work, before she had to leave for the US. Thank you for your enthusiastic guidance and encouragement Amy. It was wonderful working with you and I am very happy that you'll be right next door in the US for the next few years.

Thank you to my incredible collaborators, Kohta Murase and Eli Waxman; it has been a privilege working with you. Thank you also to Shaun Thomas for the help at the early stage of this thesis, when we overlapped at UCL. I would also like to thank

the other scientists that I've had the fortune to meet and discuss the mysteries of the non-thermal Universe with. In particular, I acknowledge helpful discussions with Markus Ahlers, John Beacom, Pirin Erdogdu, Eichiro Komatsu, Daniel Mortlock, Angela Olinto, Etienne Parizot, Hiranya Peiris, Dmitri Semikoz, Joe Silk and Hajime Takami. Thank you also to Glen Cowan and Matthew Wing for two very useful and interesting sets of lectures at the very beginning of this PhD.

My research in UCL was supported by the UCL Institute of Origins. I also thank the Institut Lagrange de Paris and the Institut d'Astrophysique de Paris for the three months of kind hospitality in Paris and all the staff and students at the IAP for the very warm and welcoming environment.

To the wonderful people in the UCL Astrophysics Group that I've shared these years with: it has been amazing working near you in this uniquely pleasant and friendly atmosphere and I will miss all of you very very much! Thank you for all the great moments, your support and the general craziness.

Finally thank you to Dimitra and Kostas, my parents. Thank you for your unconditional support and tireless encouragement.

The great thing about science is that you can get it wrong over and over again because what you're after - call it truth or understanding - waits patiently for you. Ultimately, you'll find the answer because it doesn't change.

-Dudley Herschbach, shared 1986 Nobel Prize in Chemistry

Contents

Table of Contents **7**

List of Figures **11**

List of Tables **15**

1 Ultra-high energy cosmic rays **17**

1.1 Cosmic ray energy spectrum 17

1.2 Detection 19

1.2.1 Early experiments 20

1.2.2 Current and upcoming experiments 20

1.3 Sources and acceleration of UHECRs 22

1.3.1 Acceleration 24

1.3.2 Candidate sources 26

1.4 Mass composition 28

2 Interactions of UHECRs in the intergalactic medium and secondary products **31**

2.1 Cosmic background radiation fields 32

2.1.1 Cosmic microwave background 32

2.1.2 Extragalactic background light 33

2.1.3 Universal radio background 34

2.2 Proton propagation and interactions 35

2.2.1 Pair production 36

2.2.2 Pion photoproduction 37

2.2.3 Redshift energy losses . . . 38
2.2.4 Neutrons and nuclei . . . 39
2.2.5 Secondary products of UHECRs . . . 40
2.3 Gamma-rays . . . 42
2.3.1 Instruments for the detection of gamma-rays . . . 43
2.3.2 Intergalactic electromagnetic cascades . . . 46

3 Propagation of UHECRs in a magnetised universe and anisotropies 53
3.1 Magnetic fields . . . 53
3.1.1 Measurement techniques and observations . . . 54
3.1.2 galactic magnetic field . . . 56
3.1.3 Extragalactic magnetic fields . . . 57
3.1.4 Numerical simulations . . . 59
3.1.5 UHECR deflections . . . 60
3.2 UHECR anisotropies . . . 63

4 Search for correlation of UHECRs with the local galaxy distribution 67
4.1 Introduction . . . 67
4.2 Galaxy surveys . . . 68
4.3 Auger exposure . . . 70
4.4 Model of UHECR source distribution . . . 70
4.4.1 Source density . . . 71
4.4.2 UHECR energy losses during propagation . . . 73
4.4.3 Galaxy survey completeness . . . 74
4.4.4 Galaxy peculiar velocities . . . 77
4.4.5 Magnetic fields . . . 78
4.5 Statistical approach . . . 79
4.6 Results . . . 81
4.6.1 Cross-correlation of UHECRs and nearby LSS . . . 82
4.6.2 Cross-correlation in equal predicted flux radial shells . . . 89
4.6.3 Magnetic deflections . . . 94
4.6.4 Systematic uncertainties . . . 95
4.7 Discussion . . . 96

5 Gamma-ray spectra of Blazars 101

5.1 Introduction . . . 102

5.1.1 Blazars . . . 102

5.1.2 Leptonic origin . . . 103

5.1.3 Hadronic origin . . . 105

5.1.4 The role of magnetic fields . . . 109

5.2 Methodology . . . 110

5.2.1 Selection of sources . . . 110

5.2.2 Magnetic field model . . . 112

5.2.3 Simulations . . . 114

5.3 Robustness of synchrotron signal with application to specific sources . . . 117

5.3.1 1ES 0229+200 . . . 119

5.3.2 Other sources . . . 120

5.3.3 UHE photons . . . 121

5.4 Discussion . . . 127

6 Simulations for a next-generation UHECR observatory 135

6.1 Introduction . . . 135

6.2 Model building . . . 139

6.2.1 Bias prescription of UHECR source clustering . . . 139

6.2.2 UHECR intensity maps and simulations . . . 141

6.3 Results . . . 148

6.3.1 Isotropic fraction . . . 148

6.3.2 Sensitivity to the UHECR source density . . . 149

6.3.3 Sensitivity to the bias of the source distribution . . . 150

6.4 Discussion . . . 151

7 Conclusions and future work 163

7.1 Future work . . . 165

A Appendix A: Distances in cosmology 169

B Appendix B: Details of the Monte Carlo setup in chapter 5 173

Bibliography 177

This page was intentionally left blank

List of Figures

1.1 All-particle cosmic ray spectrum as a function of energy. 18
1.2 The layout of the Pierre Auger Observatory and one of the Cherenkov tanks on site. 21
1.3 The combined energy spectrum measured at the Pierre Auger Observatory. 22
1.4 Cumulative exposure of UHECR experiments. 23
1.5 Hillas diagram. 23
1.6 Elongation rate measurements and model predictions for different primary UHECR compositions. 29

2.1 The spectrum of cosmic background radiations. 32
2.2 Compilation of recent models of the EBL spectrum at redshift z = 0.0. . . . 34
2.3 Pion photoproduction cross-section as a function of photon energy. 37
2.4 Proton energy loss lengths and interaction lengths for dominant energy loss processes. 39
2.5 The fraction of surviving UHE nuclei for different species as a function of propagation distance. 41
2.6 The sensitivity of a compilation of gamma-ray detectors. 44
2.7 The interaction length of high energy electrons and photons on background radiation fields. 49
2.8 The attenuation of gamma-ray photons on background radiation fields. . . . 50
2.9 Electron attenuation length as a function of energy. 51

3.1 Expected deflections of 6×10^{19} eV protons in the Galactic magnetic field. . 57
3.2 Cumulative filling factor of extragalactic magnetic fields in recent numerical studies. 59

3.3 Numerical estimate of deflections suffered by UHECR protons in extragalactic magnetic fields. 61
3.4 Schematic representation of the trajectory of a UHECR through individual magnetised scattering centres. 62

4.1 The geometrical acceptance of Auger in equatorial coordinates. 71
4.2 The probability that a UHECR emitted by a source at luminosity distance $r_{\rm L}$ with initial energy $E_{\rm i}$, will be observed with final energy above $E_{\rm f}$ as a function of propagation distance. 75
4.3 The radial selection function of the PSCz survey. 76
4.4 Redshift distribution and selection function of the PSCz and 6dF surveys. . 77
4.5 Maps of the predicted, local UHECR source distribution, in Galactic coordinates for UHECRs with final energy 55 EeV. 83
4.6 Map of the predicted, local UHECR source distribution, in Galactic coordinates for UHECRs with final energy 55 EeV, with local superclusters marked on. 84
4.7 The predicted UHECR source distribution as in figure 4.5 and the arrival directions of observed Auger UHECRs. 85
4.8 The distribution of values of the correlation statistic X for simulations of UHECRs from the PSCz catalogue and for the 69 Auger UHECRs. 86
4.9 The same distributions as in figure 4.8 but using the 6dF catalogue. 87
4.10 The significance of the UHECR-galaxy distribution correlation as a function of cell size. 88
4.11 A different measure of the significance of the UHECR-galaxy distribution correlation as a function of cell size. 89
4.12 Comparison of the UHECR-galaxy distribution cross-correlation results with the PSCz and the 6dF in their common field of view. 90
4.13 The distribution of values of X in simulations of UHECRs from different shells of the expected UHECR source distribution obtained with the PSCz and significance of these results. 92
4.14 Same as in figure 4.13 but for the 6dF survey. 93

4.15 The distribution of values of the normalised correlation coefficient R in simulations of UHECRs from different shells of the expected UHECR source distribution. 94
4.16 The distribution of values of the correlation statistic X for simulations of UHECR arrival directions with simulated deflections. 95

5.1 Average spectral energy distribution of blazars demonstrating the "blazar sequence" classification. 103
5.2 Model fits to the spectrum of a blazar at redshift $z = 0.14$ assuming a leptonic or UHECR cascade origin of the emission. 108
5.3 Slice through the magnetic field in the simulation volume 113
5.4 Median deflection angle at different distances from the source as a function of energy of the propagating protons in the simulations. 113
5.5 Profile of the mean and median magnetic field strength in the vicinity of the source in the simulation volume. 114
5.6 The energy flux of secondary leptons produced by $p\gamma$ interactions in a 3 Mpc magnetised region around a UHECR source at redshift $z = 0.14$. . . . 118
5.7 The fit of the UHECR secondary synchrotron model to the spectrum of 1ES 0229+200 for a range of values of the volume averaged magnetic field strength in the magnetised region surrounding the accelerator. 121
5.8 Robustness of the UHECR secondary electron synchrotron model fit to the spectrum of 1ES 0229+200 for a selection of EBL models. 122
5.9 Robustness of the UHECR secondary electron synchrotron model fit to the spectrum of 1ES 0229+200 for different UHECR injection parameters. . . . 123
5.10 The energy flux, resulting from the UHECR secondary electron synchrotron model for RGB J0710+591, 1ES 1218+304 and PG 1553+113. 124
5.11 The injected and arriving energy flux expected in the UHE photon model for 1ES 0229+200. 127
5.12 The arriving energy flux in the UHE photon model for 1ES 0229+200 and 1ES 1218+304. 128

6.1 The fraction of PSCz galaxies that are included in the *threshold* bias model as a function of comoving distance. 142

6.2 Maps of the integrated UHECR source distribution out to 337 Mpc in the various bias models considered for the UHECR source distribution. 144
6.3 The expected UHECR intensity averaged over realisations in the unbiased model. 145
6.4 The expected UHECR intensity averaged over realisations in the linear bias model. 146
6.5 The expected UHECR intensity averaged over realisations in the threshold bias model. 156
6.6 Example of the expected UHECR arrival direction distribution, for the statistics that JEM-EUSO would collect in ~ 5 years of operation. 157
6.7 The distribution of values of $X_{\rm UB}$ in realisations of UHECRs with energy $E \geq 100, 80, 50$ EeV for different values of the UHECR source number density. 158
6.8 The distribution of values of $X_{\rm UB}$ in realisations of UHECRs with energy $E \geq 100, 80, 50$ EeV in the different bias models. 159
6.9 Same as figure 6.8 but assuming 30% of detected UHECRs arrive isotropically. 160
6.10 Same as figure 6.9 but assuming 70% of detected UHECRs arrive isotropically. 161

A.1 Comparison of the different distance measures as a function of redshift. . . 171

B.1 Schematic representation of the source-observer setup in our simulation volume. 175

List of Tables

4.1 The number of galaxies and the distances covered in each of the three radial shells defined in the expected UHECR source distribution model 91
4.2 Sensitivity of cross-correlation results to the uncertainty in the PSCz selection function 97

5.1 Properties of the blazars studied. 111

6.1 Statistical significance with which the various models of UHECR source distribution considered can be ruled out with a next-generation UHECR detector, considering only events with energy $E \geq 100$ EeV. 152
6.2 Statistical significance with which the various models of UHECR sources considered can be ruled out with a next-generation UHECR detector, considering all expected events with energy $E \geq 50$ EeV. 153

This page was intentionally left blank

Chapter 1

Ultra-high energy cosmic rays

"Sir,' I said to the universe, 'I exist.' 'That,' said the universe, 'creates no sense of obligation in me whatsoever."

-Douglas Adams, The Hitchhiker's Guide to the Galaxy

In 1912 Victor Hess discovered that the ionisation of air in the atmosphere increases with altitude in a series of daring balloon flights reaching up to 5 km in altitude (see Hess 1912). His experiments mark the beginning of the scientific field dedicated to the study of cosmic rays. Fifty years later, in the Volcano Ranch experiment led by John Linsley, the first ultra-high energy cosmic ray (UHECR) with energy exceeding 10^{20} eV was discovered, initiating the search for the sources of these extreme particles. Despite 50 years of observations and painstaking efforts of a large number of dedicated groups, the origin of the highest energy cosmic rays remains unknown, but a lot of insight has been gained in the process.

1.1 Cosmic ray energy spectrum

Cosmic rays are extraterrestrial particles incident on the Earth's atmosphere with energies between 10^9 - 10^{20} eV. Of the cosmic rays incident on Earth 98% are nuclei and 2% are electrons (see e.g., Simpson 1983 for a review.) The cosmic ray spectrum is a remarkable

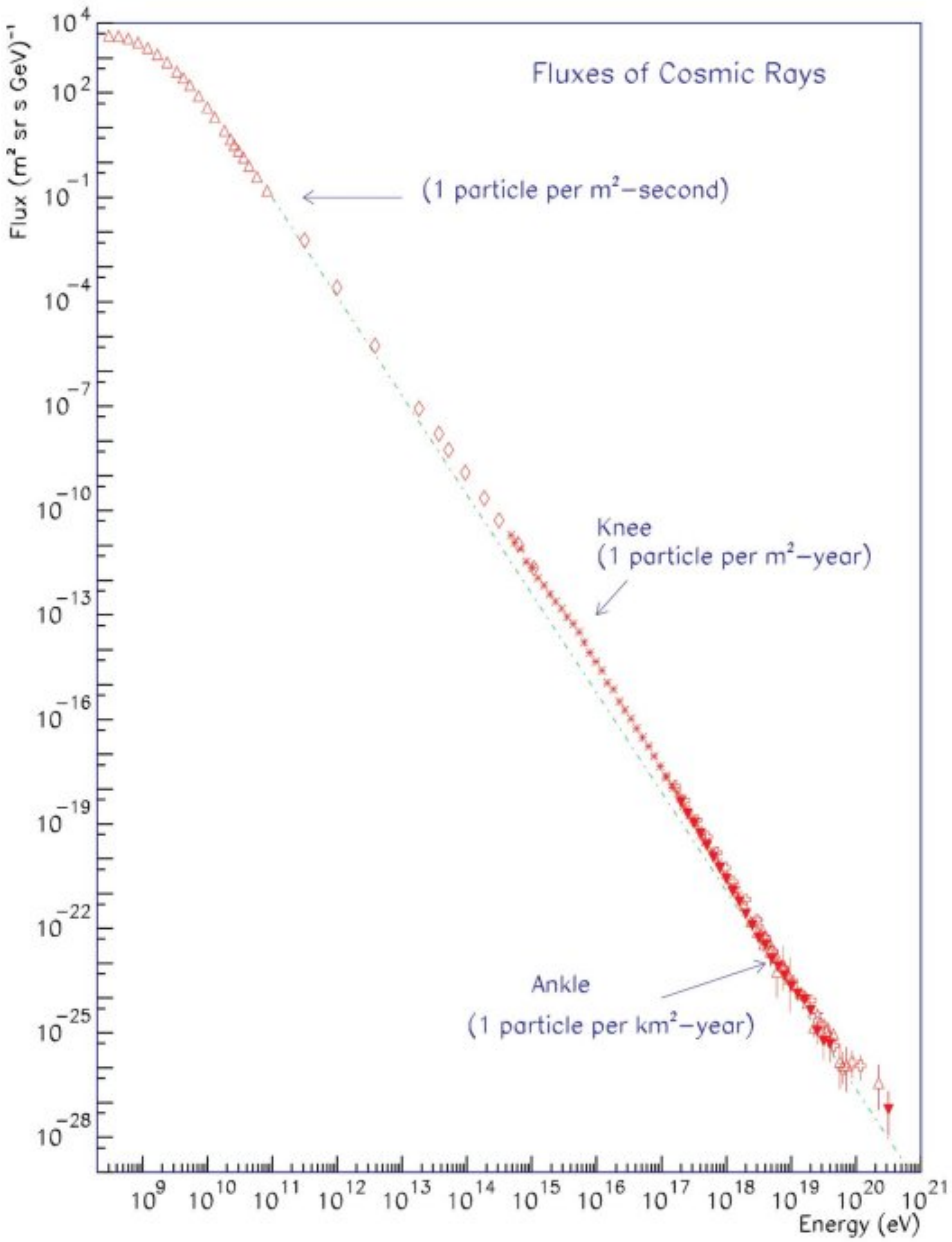

Figure 1.1. All-particle cosmic ray spectrum as a function of energy. Image attributed to S. Swordy, adapted here from Olinto (2005).

power-law fit well by a function of the form

$$\frac{\mathrm{d}N}{\mathrm{d}E} = E^{-\alpha} \tag{1.1}$$

with spectral index, $\alpha = 2.7$, for much of the energy range, as shown in figure 1.1. At the lowest energies the cosmic ray flux is thought to be dominated by the Sun. At the high energy end of the spectrum there are a number of interesting features. At about 10^{15} eV the slope of the spectrum abruptly becomes steeper, with $\alpha \simeq 3.1$. This feature, which is referred to as the "knee", is often attributed to the maximum proton acceleration energy attainable by supernovae. At 5×10^{18} eV the spectrum flattens again (so called "ankle"). There is some evidence that around 10^{17} eV a second steepening of the spectrum occurs, the so called "second knee" (Apel et al. 2011). There is no consensus as to the exact transition energy between Galactic and extragalactic cosmic rays, although most models place it around $\sim 10^{18}$ eV; beyond this energy UHECR protons become too rigid to be confined by the Galactic magnetic field. In the models of Hillas (1984) and Bahcall & Waxman (2003) the ankle marks the Galactic-extragalactic transition, whereas in the so called dip model (Berezinsky et al. 2006) the ankle is attributed to energy losses of extragalactic UHECRs through pair production on the CMB (see section 2.2.1) and the transition is thought to occur below 10^{18} eV. The cosmic ray spectrum cuts off at $\sim 10^{20}$ eV. At present it is unclear whether this energy corresponds to the maximum acceleration energy attainable, or whether the cut-off is due to severe energy losses of the cosmic rays as they propagate through the CMB - the *GZK effect* (see section 2.2.2).

1.2 Detection

The flux of ultra-high energy cosmic rays above 10^{14} eV is too low to be detected directly by balloon and satellite experiments. Instead, cosmic-rays are detected by the *extensive air shower* that they produce when they enter the Earth's atmosphere. A cosmic ray entering the atmosphere with sufficiently high energy will cause a cascade of particles with characteristics that depend on the primary composition and energy. Above 10^{19} eV the flux is below 1 $\mathrm{km}^{-2}\mathrm{sr}^{-1}\mathrm{yr}^{-1}$, meaning that a huge detection area is needed. Some of the experiments and experimental techniques deployed for the study of these elusive particles are reviewed below.

1.2.1 Early experiments

In 1963 the first particle with energy above 10^{20} eV was detected in the first giant shower array, which was located at Volcano Ranch (Linsley 1963). The discovery inspired the beginning of a series of such experiments, constructed with the aim of detecting more of these spectacular ultra-high energy particles. The Volcano Ranch array consisted of 20 plastic scintillators separated by 884 m. The detection principle is that of registering the time, energy and spatial distribution of the muons and electrons that hit the surface. From these observables, the energy and direction of the primary particle are reconstructed. The next giant surface array was constructed in Haverah Park, Yorkshire and operated between 1967-1987 (Lawrence et al. 1991). Water Cherenkov tanks were used to register the air shower particles on the ground.

An altogether different experimental technique for the detection of UHECR showers was developed in Utah with the Fly's Eye detector (Bergeson et al. 1977). A relativistic charged particle travelling through the atmosphere can excite nitrogen molecules that produce fluorescence in the 300-450 nm range. The light produced is detectable when a very large number of particles are incident in the atmosphere at once. The first fluorescence telescopes were tested in Volcano Ranch taking data in coincidence with the surface array and a dedicated fluorescence experiment run in Utah between 1981-1993. The same principle was behind the more recent High Resolution Fly's Eye (HiRes) that operated between 1997-2006 (Abbasi et al. 2002). The final of the last generation of extensive air shower arrays was the Akeno Giant Air Shower Array (AGASA) (Chiba et al. 1991), that consisted of ground scintillators which were distributed over a total area of 100 km^2. The Yakutsk array in Siberia should also be mentioned here. Albeit covering a small detection area $\sim$ 10 km^2, it has been in operation since 1970 and is currently still active (Ivanov et al. 2009).

1.2.2 Current and upcoming experiments

The Pierre Auger Observatory, in Malargue Argentina is the largest giant shower array to be constructed to date (Abraham et al. 2004). It has a detection area of 3000 km^2 and UHECR particle showers are detected by a combination of 1660 ground based Cherenkov detectors, surrounded by 27 fluorescence telescopes at five different sites. The combination of these two techniques provides the most accurate reconstruction of UHECR shower

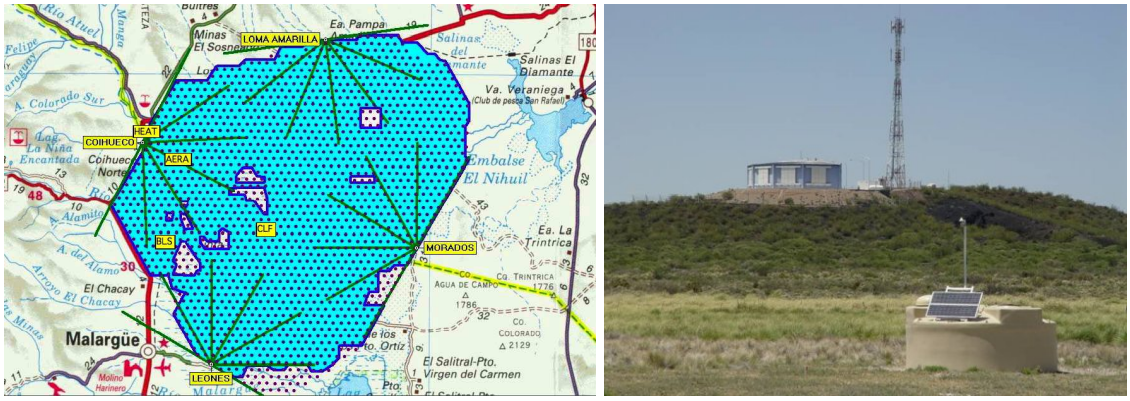

Figure 1.2. Left: The layout of the Pierre Auger Observatory as of July 2009. Each of the dots points to the location of one of the water tanks which are arranged in a grid with 1.5 km spacing. The green lines show the reach of the fluorescence detectors which overlook the ground detectors. The total area over which the detectors are distributed is approximately 3000 km^2. **Right:** One of the Cherenkov tanks at Auger, with one of the fluorescence telescope buildings in the background.

geometry to date. The layout of the array and one of the water tanks and fluorescence telescope buildings are shown in figure 1.2.

Auger is fully efficient for UHECR primaries with energy greater than 10^{18} eV and showers incident with a zenith angle $\theta_z \leq 60°$. An infill array and proposed upgrades to Auger push the energy threshold to lower energies (see e.g., Abreu et al. 2012b). Data taking in Auger started in January 2004. Since its completion in 2008 it has been collecting data at an approximate rate of 2 events per month beyond 6×10^{19} eV (the arrival directions and reconstructed energy of 69 of these have been published in Abreu et al. 2010). The angular resolution is better than 0.9° for events that trigger 6 or more surface detectors ($E \geq 10$ eV). The energy resolution is 15% and there is a 14% systematic uncertainty in the absolute energy scale given by the calibration of the fluorescence technique (Aab et al. 2013). The most recent, combined (surface and fluorescence) energy spectrum measured at Auger is shown in figure 1.3.

The Telescope Array (TA) experiment in Utah, which started operations in 2007, complements the observations of Auger in the Northern hemisphere. A combination of 507 scintillators on the ground array and 3 fluorescence telescopes are active at the TA experiment, which is largely built on the detection techniques established by AGASA and HiRes. The total detection area is 680 km^2. The detection of 52 events with energy exceeding 57 EeV at the TA has been reported to date (Fukushima et al. 2013).

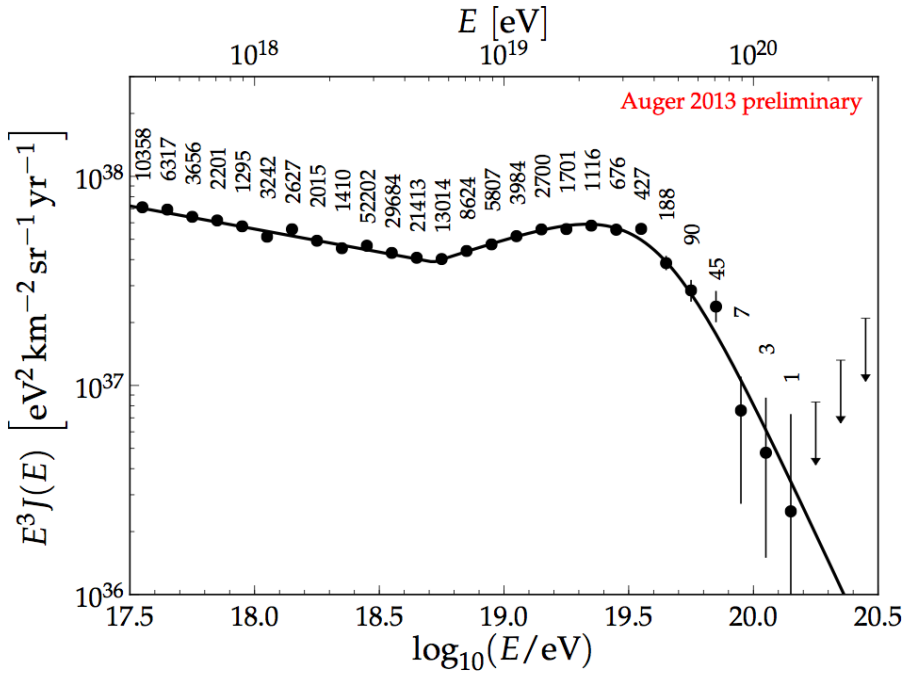

Figure 1.3. The most recent combined energy spectrum measured at Auger. The numbers give the total number of events inside each energy bin. The total exceeds 130,000 events. The downward facing arrows represent upper limits at 84% confidence. Figure adapted from Aab et al. (2013).

The proposed JEM-EUSO experiment (Medina-Tanco et al. 2009) is planned to be the first space based UHECR experiment. If realised, it will be mounted on the International Space Station and survey the Earth's night sky from $\sim$ 400 km altitude for the fluorescence and Cherenkov radiation produced by UHECR showers in the Earth's atmosphere, with a super-wide field-of-view telescope ($\pm 30°$). JEM-EUSO would orbit the Earth every 90 minutes and be the first full sky UHECR experiment. It would increase the exposure to UHECR showers by a factor of $\sim 10 - 20$ compared to Auger (Adams et al. 2013). The accumulated exposures of past, current and planned major UHECR experiments at energy $E = 3 \times 10^{20}$ eV are shown in figure 1.4.

1.3 Sources and acceleration of UHECRs

In the ultra relativistic limit, the Larmor radius of a charged particle with energy E and atomic number Z is given by

$$r_{\mathrm{Lar}} = \frac{E}{ZeB} \simeq 1.08 \text{ Mpc } \frac{1}{Z} \left(\frac{E}{10^{18} \text{ eV}}\right) \left(\frac{B}{1 \text{ nG}}\right)^{-1}, \tag{1.2}$$

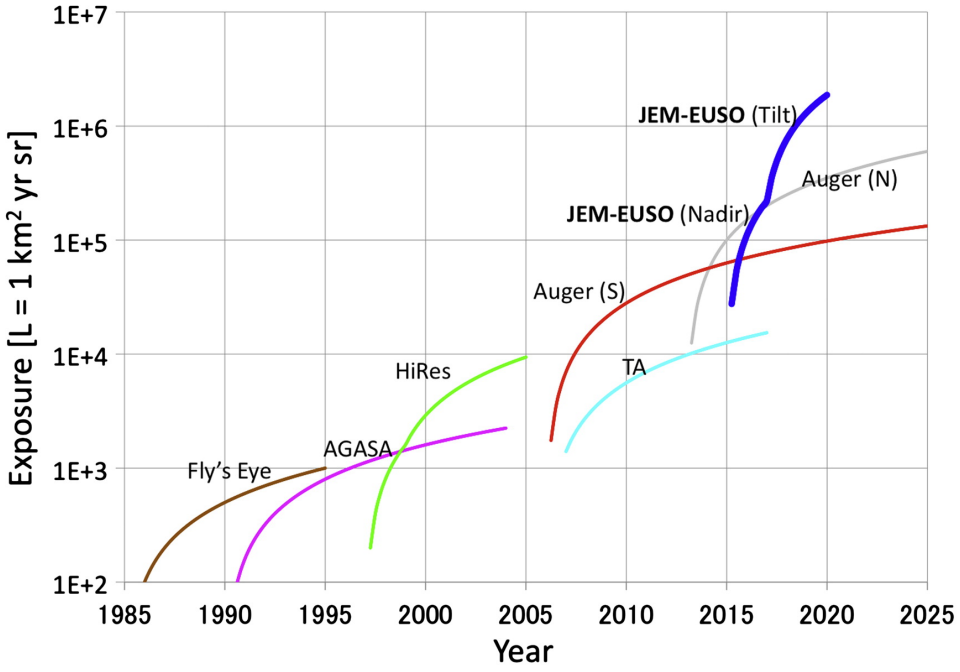

Figure 1.4. Cumulative exposure of past, current and proposed UHECR experiments at $E_{\mathrm{UHECR}} = 3 \times 10^{20}$ eV reproduced from Kajino (2010).

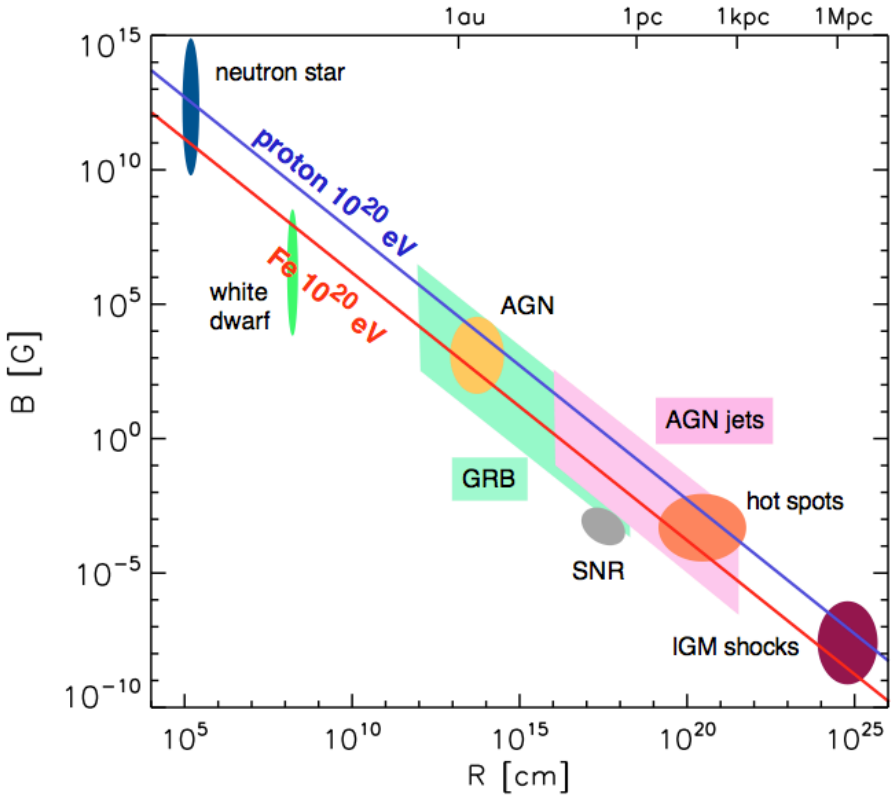

Figure 1.5. Updated Hillas diagram (see text) from Kotera & Olinto (2011)

where B is the magnetic field strength in the direction perpendicular to the momentum of the particle. A necessary condition for the acceleration of UHECRs in an astrophysical source is the so called *Hillas criterion* proposed in Hillas (1984). It states that an accelerator must have a radius $R \geq r_{\mathrm{Lar}}$ in order to be able to magnetically confine a particle with gyroradius r_{Lar}. The Hillas criterion, expressed in terms of the magnetic field strength B and R of the source gives the maximum confinement energy, which reads

$$E_{\mathrm{max}} \sim 1 \text{ EeV} \cdot Z \cdot \left(\frac{B}{1\ \mu\mathrm{G}}\right)\left(\frac{R}{1 \text{ kpc}}\right). \tag{1.3}$$

Powerful astrophysical sources in $B-R$ phase space are shown in figure 1.5, where typical values for B and R and associated uncertainties are plotted. Only sources above the red line can confine nuclei with energy 10^{20} eV and only sources above the blue line can confine 10^{20} eV protons. Therefore, the only viable candidate sites for UHECR acceleration are active galactic nuclei (AGN), gamma ray bursts (GRBs), neutron stars and shocks in the intergalactic medium. In relativistic outflows, particles are only accelerated over a fraction of R, comparable to R/Γ with Γ the Lorentz factor of the outflow, therefore the Hillas criterion needs to be updated in this case (see e.g., discussion in Waxman 2011, or Waxman 1995a for a detailed derivation).

The Hillas criterion is a necessary but not sufficient condition for the acceleration of UHECRs. For a more sophisticated estimate of the maximum acceleration energy we can compare the acceleration timescale, t_{acc}, to the time it takes UHECRs to escape the acceleration region, t_{esc}, the age of the source and the energy loss time of the particles that are being accelerated in the ambient medium, t_{loss}. As long as $t_{\mathrm{acc}} \leq \min\left(t_{\mathrm{esc}}, t_{\mathrm{loss}}, \mathrm{Age}_{\mathrm{source}}\right)$ acceleration is feasible (see e.g., Lemoine & Waxman 2009).

1.3.1 Acceleration

Acceleration mechanisms in which particles can attain ultra-high energies in reasonable timescales are a challenge for theory. Proposed mechanisms for cosmic-ray acceleration can be broadly divided into *inductive* (or *one-shot acceleration*) and *stochastic* (or *diffusive*). The latter are generally preferred for acceleration to the highest energies, because they naturally produce a power-law spectrum spread over many orders of magnitude in energy.

In inductive acceleration models, the particle gains energy in a continuous way in a strong ordered electric field across the accelerating region (see e.g., Ptitsyna & Troitsky

2010; Hillas 1984 for details). Electric fields are hard to establish in astrophysics as they are readily dissipated by the highly conductive plasma. However, the conditions for inductive acceleration might arise through the motion of a rapidly rotating magnetised conductor, such as a black hole or pulsar, which establishes a potential difference between the surface of the object and infinity, in which the particle can be accelerated.

Diffusive acceleration mechanisms and in particular Fermi shock acceleration, are the preferred acceleration mechanism of cosmic-rays in most astrophysical acceleration models, not least because they are very successful in their description of cosmic-ray acceleration in galactic sources, where significantly more detailed observations are available. In Fermi acceleration, the charged particle is accelerated through multiple scatterings, on regions of a varying magnetic field, gaining some energy at each collision. In the first order Fermi mechanism (Axford et al. 1977; Bell 1978; Blandford & Ostriker 1978) particles are accelerated through multiple crossings of strong (but non-relativistic) astrophysical shocks, gaining some energy with every crossing[1]. It can be shown that with every crossing the particle gains

$$\left\langle \frac{\Delta E}{E} \right\rangle = \frac{4}{3}\beta, \tag{1.4}$$

where β is approximately the shock velocity in units of c. The spectrum expected in the first order Fermi mechanism, in the test particle limit, for non-relativistic shock acceleration, is a power law with a fixed index α,

$$N(E)\mathrm{d}E = \text{const.} \times E^{-\alpha}\ \mathrm{d}E, \tag{1.5}$$

where $\alpha \approx 2.0$. Observations of supernova remnants and theoretical developments over the last years, suggest that this, standard spectrum, may not be exactly what is released in reality. For particular magnetic field configurations, it is thought that α can become smaller (harder spectrum) at high energies, whereas for older, slower shocks, α may become a lot softer (see for example the detailed discussion in Hillas 2005).

[1]The *second order Fermi mechanism* that was originally proposed by Fermi (Fermi 1949) is now less popular, as the energy gain goes as $\langle \Delta E/E \rangle = (4\beta^2)/3$.

1.3.2 Candidate sources

Active galactic nuclei

Active galactic nuclei are the most powerful steady sources known and as such they strong candidates as UHECR sources (e.g., Ginzburg & Syrovatskii 1964; Hillas 1984). They are the most commonly observed extragalactic gamma-ray emitters, which necessarily implies particle acceleration to at least moderately high energies. AGN are commonly classified into radio-loud and radio-quiet, the former presenting no prominent radio emission while the latter possess prominent jets, that emit in the radio and often other wavelengths, and terminate in lobes or hot-spots. Within the unified AGN scheme (Urry & Padovani 1995), the differences between different types of AGN are a result of the viewing angle (orientation) of the AGN and possibly evolutionary effects.

Although the size and magnetic field strength of AGN central engines (i.e. black holes) is such that from the Hillas criterion one expects $E_{\rm max} \sim 10^{20}$ eV, it is believed that in this zone energy losses are significant, due to the presence of dense radiation fields and that in practice such high energies are not achieved (e.g., Norman et al. 1995). In radio-loud AGN, UHECR acceleration may also occur in the jet (Mannheim 1993; Berezinsky et al. 2006) and lobes or hot-spots (Rachen & Biermann 1993), which seem more promising candidates. Although AGN seem an obvious candidate as UHECR sources, the absence of very powerful AGN within 100 Mpc or so ($L_\gamma \gtrsim 10^{46}$erg s^{-1}) makes it unclear whether they can supply the locally observed UHECR flux (see e.g., Lemoine & Waxman 2009; Waxman 2011).

Transient events in AGN, such as flares, have also often been discussed as UHECR source candidates (e.g., Farrar & Gruzinov 2009) and may meet the energetic requirements for UHECR acceleration more easily. The observed gamma-ray flux of AGN can be used as a powerful probe of UHECR acceleration in AGN, if one can distinguish between the possible hadronic and leptonic origin of this emission. This will be discussed in detail in chapter 4 (see also e.g., Hinton & Hofmann 2009).

Gamma-ray bursts

Gamma-ray bursts were first proposed as UHECR sources by Waxman (1995b); Vietri (1995). The peak luminosity of these violent stellar explosions is of order $L_\gamma = 10^{52}$erg s^{-1}. If an equal amount of power goes into cosmic-ray production as in gamma-ray production,

the observed rate of GRBs can explain the diffuse UHECR flux levels. In the GRB *fireball* model, gamma-rays are created by electrons that are accelerated through the Fermi mechanism, in shocks, during the GRB and its afterglow. In this model, UHECRs are accelerated in the same regions as the high energy electrons. One of the appealing features of GRBs as UHECR sources is that because of their transient nature, neutrinos, which will inevitably be produced by interactions of UHECRs near the source (see sections 2.2, 2.2.5), should be detectable in approximate coincidence with the gamma-ray signal ($\pm$ few days). As will be discussed in section 3.1, charged UHECRs are significantly delayed in magnetic fields and are not expected in coincidence. The IceCube experiment is sensitive to the expected neutrino signal and starting to cut in on the allowed parameter space (see e.g., Abbasi et al. 2012, but also Dar 2012; He et al. 2012).

Pulsars

Soon after their discovery, pulsars were proposed as possible sources of high energy cosmic rays (Gunn & Ostriker 1969). These highly magnetised, rapidly rotating neutron stars fulfil the Hillas criterion as shown in figure 1.5. Pulsars produce relativistic outflows to which they induce a large potential drop, Φ, through their rapid rotation. This can in principle be as high as $\Phi = 10^{21}$ eV. It was shown in Blasi et al. (2000), that young neutron stars with millisecond rotation periods can accelerate particles up to $E_{\rm max} \sim Z\ \Phi\eta \sim Z \times 10^{20}$ eV in such potential drops, where η is the fraction of the potential experienced by the accelerating particle. More recently it has been shown that an extragalactic pulsar population can reproduce the Auger spectrum and composition measurements very well (Fang et al. 2012, 2013b). A particularly appealing feature of pulsars compared to other candidate accelerators of UHECRs, is that the model can be confirmed or ruled out with 5-10 years of IceCube data, as a consequence of the expected diffuse neutrino counterpart associated with pulsar UHECR sources, as shown in Fang et al. (2013a).

Shocks in the intergalactic medium

In the large scale structures of the universe, filaments and galaxy clusters, the accretion of gas produces shocks. In particular in galaxy clusters, magnetic fields of order $B \sim 1 - 10\ \mu$G have been measured (see detailed discussion in section 3.1) and it is believed that $\gtrsim \mu$G strength fields could be present in $\lesssim 1$ Mpc scales (Kim et al. 1990; Feretti et al. 1995; Ferrari et al. 2008). Hence they should be able to confine UHECRs up to

$E_{\rm max} \gtrsim 10^{21}$eV (e.g., Norman et al. 1995; Murase et al. 2008a). Galaxy clusters have not yet been observed in gamma-rays, although it is believed that the expected signal is not far below the experimental sensitivity of current instruments (see e.g., discussion in Rieger et al. 2013 as well as the work of Aharonian et al. 2009; Aleksic et al. 2012a; Arlen et al. 2012). Gamma-ray observations will help constrain the properties of these structures and as a result the cosmic-ray content.

Non-acceleration origin of UHECRs

Other models of particle physics beyond the Standard Model have also been proposed for the origin of UHECRs (so called $top-down$ models, see Bhattacharjee & Sigl 2000 for a review). In these models, UHECRs are the products of the decay of heavy relic particles, left from the very early universe. The UHECR spectrum measured by the earlier, AGASA experiment did not exhibit the cutoff expected due to the interaction of extragalactic hadrons with the CMB (Takeda et al. 2003), causing top-down models to be invoked for the origin of UHECRs.

The most recent published cosmic ray spectra measured by the HiRes, Auger and TA experiments measure a cutoff in the CR spectrum with statistical significance $\geq 5\sigma$ (Abbasi et al. 2008; Abraham et al. 2010b; Abu-Zayyad et al. 2013a), strengthening the view that the origin of UHECRs is in astrophysical accelerators. The non-observation of ultra-high energy photons and neutrinos in current UHECR experiments (see section 3.2 or e.g., Aab et al. 2013) and of a significant excess of events from the direction of the galactic centre at the highest energies (e.g. Dubovsky & Tinyakov 1998), which are firm predictions of top-down models, strongly constrain these models.

1.4 Mass composition

The characteristics of the shower that develops when a UHECR enters the atmosphere depend on the primary composition. Measurements of shower properties related to the composition are challenging to interpret, as the characteristics of the shower are governed by hadronic interactions at centre of mass energies beyond the reach of accelerator experiments. A powerful observable of the primary composition is the depth where the maximum number of electromagnetic particles in a shower, $X_{\rm max}$, is reached. For heavier nuclei, $X_{\rm max}$ is expected to occur higher in the atmosphere than for protons, as to a crude

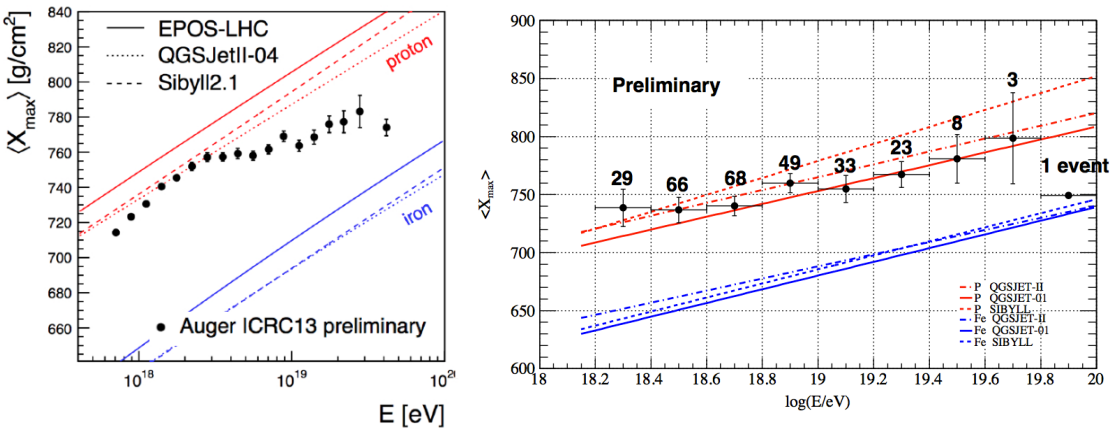

Figure 1.6. The elongation rate (see text) predicted by hadronic interaction models for protons (red) and iron nuclei (blue) and the data obtained at Auger (Aab et al. 2013) - left and with the TA (Jui 2012) - right. Note that the hadronic interaction models plotted in the two figures are not exactly the same.

approximation, a shower initiated by a primary nucleus with mass A and energy E can be described as a superposition of A showers with energy E/A. $X_{\rm max}$ can be measured directly by fluorescence detectors. In ground arrays a number of $X_{\rm max}$ related observables can be studied, but principally the primary composition is inferred from the muon content of the shower (see e.g., Abreu et al. 2011b).

For a UHECR with energy E, the dependence of the average depth of shower maximum, $\langle X_{\rm max}\rangle$, on the mass number A is given by (Heitler 1954; Matthews 2005)

$$\langle X_{\rm max}\rangle = \alpha(\ln E - \langle \ln A\rangle) + \beta, \tag{1.6}$$

where the coefficients α and β depend on the details of the hadronic interactions governing the evolution of the shower (due to the large statistical fluctuations in $X_{\rm max}$, it is common practice to study $\langle X_{\rm max}\rangle$ for a large number of showers at a given energy).

The slope of $X_{\rm max}$ as a function of energy is called the elongation rate and also depends on the primary mass following

$$D = \frac{{\rm d}\,\langle X_{\rm max}\rangle}{{\rm d}\log E} \approx \alpha\,\left(1 - \frac{{\rm d}\langle \ln A\rangle}{{\rm d}\ln E}\right)\ln 10. \tag{1.7}$$

The elongation rate for a selection of the most advanced hadronic interaction models for protons and iron nuclei, and the data recorded with the fluorescence detectors of Auger and the TA, are shown in figure 1.6. Above $10^{18.4}$ eV, the elongation rate appears to

change for the UHECRs detected at Auger, suggesting a change in composition from light to heavier nuclei (see e.g., Abraham et al. 2010a for details or Aab et al. 2013 for the most recent results). The TA dataset is consistent with a proton composition all the way to the highest energies (Jui 2012), although it should be noted that the data from the two experiments are compatible within the quoted systematic uncertainty. Efforts are currently ongoing for a joint analysis between the two experiments (see Barcikowski et al. 2013; Abu-Zayyad et al. 2013b).

In general, one does not expect the UHECR source composition to be dominated by intermediate or heavy mass nuclei, given that they are so rare in the local universe. In this sense, the observation of Auger of composition diagnostics inconsistent with protons at the highest energies is surprising. A UHECR composition enriched in heavier nuclei at the source, is consistent with some astrophysical models, for example those in which UHECRs originate in pulsars, which are believed to be natural sources of iron and possibly also helium and CNO nuclei (see e.g., Fang et al. 2013b and references therein).

On the other hand, in a given source, if the timescale that limits the maximum attainable UHECR energy is related to the size of the accelerating region (i.e. the Hillas condition, equation 1.3) and the source is enriched in nuclei, the higher Z elements can be accelerated to higher energies than protons $\sim Z \times E_{\mathrm{proton,max}}$. Such a setup can naturally explain the existence of heavier nuclei at the highest energies.

Studies that attempt to fit the observed Auger composition observables require either an unusual UHECR composition at the source (e.g., a nitrogen or silicon dominated as shown in Hooper & Taylor 2010) or a low maximum proton energy (e.g., Allard et al. 2008; Aloisio et al. 2011). One of the features of the propagation of nuclei with mass number A < 20, is that they cannot travel farther than ~ 20 Mpc without disintegrating. As a result, for a heavy composition to be observed at the detector beyond GZK threshold energies, the injected spectrum must be essentially dominated by iron group nuclei beyond 10^{20} eV for sources beyond ~ 20 Mpc. Such a composition can arise if the maximum acceleration energy of protons at the source is below 6×10^{19} eV (see Allard et al. 2008; Aloisio et al. 2011; Allard 2012).

Chapter 2

Interactions of UHECRs in the intergalactic medium and secondary products

"I am always doing that which I can not do, in order that I may learn how to do it."

-Pablo Picasso

From the moment they are produced, the propagation of UHECRs is significantly influenced by their surrounding medium. Inside the source or in the source environment, UHECRs interact with ambient photon and hadron fields. Outside the immediate vicinity of the source, the diffuse extragalactic radiation backgrounds, that permeate the universe from the radio to gamma-rays, are the main medium impeding the propagation of UHECRs inducing mass and energy losses. In what follows, the extragalactic propagation of UHECRs is considered. Next, the secondary particles produced during UHECR propagation are considered, focusing on gamma-rays. We consider their extragalactic propagation and discuss experimental efforts for their detection. Magnetic fields also affect the propagation and energy losses of charged particles as they accelerate them causing them to radiate; their effect is discussed in chapter 3.

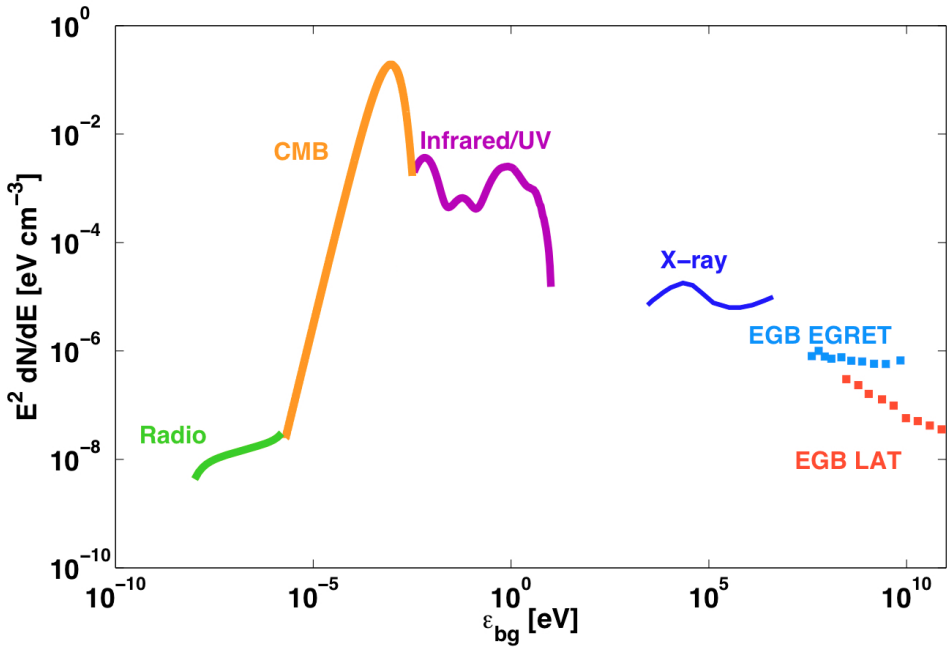

Figure 2.1. The spectrum of cosmic background radiations. The CMB is modelled as a blackbody spectrum at 2.725 K. The IR and UV backgrounds are from the work of Kneiske & Dole (2010). The extragalactic gamma-ray background datapoints (EGB) are from EGRET measurements (Sreekumar et al. 1998) and *Fermi*-LAT measurements (Abdo et al. 2010). For the X-ray and radio backgrounds the models presented in the works of Fabian & Barcons (1992), Clark et al. (1970) are shown respectively.

2.1 Cosmic background radiation fields

Diffuse extragalactic background radiation fields span 20 orders of magnitude in energy as can be seen for example in figure 2.1. Apart from the CMB all the other backgrounds are presumably made up of the fluxes of all the discrete sources of radiation. Light from the solar system and the Milky Way are strong foregrounds, nevertheless measurements exist and robust bounds have been inferred. The background photon fields most relevant to the propagation of high energy protons, leptons and high energy photons are reviewed below.

2.1.1 Cosmic microwave background

The CMB, which is the left over radiation from the Big Bang, is energetically the dominant extragalactic photon background (Penzias & Wilson 1965). It is remarkably uniform and has an ideal black body spectrum given by the Planck function. The comoving CMB

photon number density per unit energy interval $n_{\rm CMB}(\varepsilon) = {\rm d}N_{\rm CMB}/{\rm d}\varepsilon$ is thus given by

$$n_{\rm CMB}(\varepsilon) = \frac{\varepsilon^2}{\pi^2\hbar^3c^3\left[\exp\left(\frac{\varepsilon}{kT}\right)-1\right]}, \tag{2.1}$$

where T is the temperature of the CMB and today $T = 2.725 \pm 0.001$ K. The mean energy of CMB photons today is given by $\varepsilon_{\rm CMB} \simeq 2.7kT \simeq 6.34 \times 10^{-4}$ eV. It turns out that $n_{\rm CMB} \sim 410$ cm^{-3} today. The peak temperature of the CMB emission changes with redshift as $T(1+z)$, as a result of the Hubble expansion and the physical number density at redshift z is given by $(1+z)^3 n_{\rm CMB}$. The CMB impedes the propagation of protons with energy $E_p \gtrsim 5 \times 10^{18}$ eV (at $z = 0$) and photons with $E_\gamma \gtrsim 10^{14}$ eV (see sections 2.2, 2.3.2).

2.1.2 Extragalactic background light

The light emitted by galaxies during their formation and evolution, forms the second most energetic diffuse photon background after the CMB (see e.g., Dwek & Krennrich 2013 for a recent review). It consists of most of the light emitted by star-formation processes and AGNs which is still travelling through the universe at wavelengths longer than it was emitted at, due to redshift energy losses, absorption and re-radiation by dust. The extragalactic background light (EBL) spans energies between $\varepsilon \sim 10^{-3} - 10$ eV, thus including the ultraviolet (UV), optical and infra-red (IR) parts of the electromagnetic spectrum. Protons with $E_p \gtrsim 5 \times 10^{15}$ eV and photons with $E_\gamma \gtrsim 10^{11}$ eV are above the threshold for interaction with EBL photons.

The EBL, being intrinsically faint, is hard to measure directly due to strong contamination from the zodiacal light (solar light absorbed and reradiated by dust) at these wavelengths. Lower limits on the EBL are derived by integrating the light of observed galaxies (such as in the works of Madau & Pozzetti 2000; Fazio et al. 2004; Dole et al. 2006). Upper limits are derived from the non-attenuation of gamma-ray spectra (see section 5.1.2 as well as e.g., Aharonian et al. 2006; Mazin & Raue 2007; Aliu et al. 2008; Meyer et al. 2012). The most recent, notable models of the EBL spectrum and redshift evolution include the works of Kneiske & Dole (2008, 2010); Franceschini et al. (2008); Dominguez et al. (2011); Gilmore et al. (2009); Inoue et al. (2013). A collection of recent EBL model spectra at $z = 0$ are shown in figure 2.2.

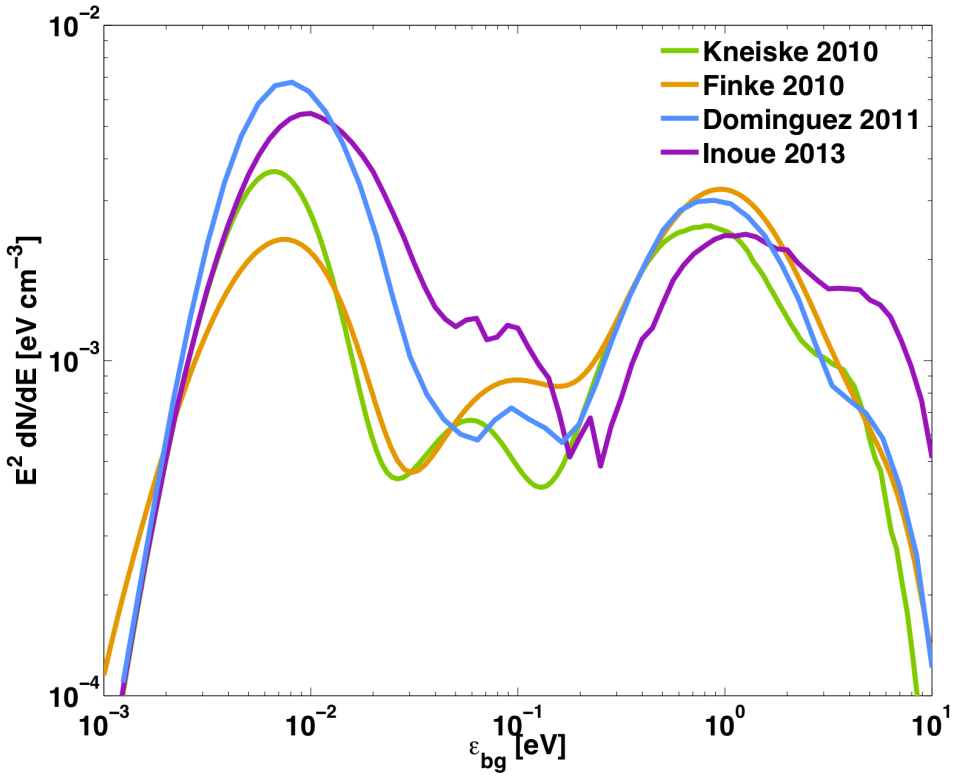

Figure 2.2. Recent models of the EBL spectrum at redshift $z = 0.0$ from the work of Kneiske & Dole (2010); Dominguez et al. (2011); Inoue et al. (2013); Finke et al. (2010). The peak at optical wavelengths is thought to be due to direct emission, whereas the infrared peak is believed to be due to the reradiated emission of light absorbed by dust.

2.1.3 Universal radio background

At wavelengths longer than those of CMB photons, the universal radio background photons interact with super-GZK protons with energy, $E_p \geq 10^{22}$ eV and UHE photons with $E_\gamma \geq 10^{18}$ eV. The energy density of the radio background is lower than that of the CMB and the EBL and it's exact spectrum and level are uncertain due to contamination from our own galaxy, which emits and absorbs at these wavelengths. The radio background is thought to originate in the emissions of radio galaxies, with possible contribution from other normal galaxies. Notable estimates and models of the radio background have been presented in the works of Clark et al. (1970); Protheroe & Biermann (1996a) and most recently Seiffert et al. (2009); Singal et al. (2010).

2.2 Proton propagation and interactions

In this section, the interactions of ultra-high energy protons with diffuse extragalactic background photon fields are considered in some detail. As throughout most of this thesis, the case in which UHECRs are protons is considered primarily. A brief account of the interactions of ultra-high energy nuclei is given at the end of this section. In what follows, quantities in the rest frame of the nucleon are given by primed variables, whereas unprimed quantities denote quantities in the laboratory frame.

To calculate the interaction length, or mean free path of protons, $\lambda_{p\gamma}$, through the photon backgrounds, one must consider the continuous energy distribution of the photons. The phase space density of photons with momentum $\mathbf{p}_\gamma{}'$ can be written $f_\gamma(\mathbf{p}'_\gamma)\mathrm{d}^3p'_\gamma$. In the laboratory frame, for a proton with energy $E_p = \gamma_p m_p c^2$, where, γ_p, is the Lorentz factor of the particle's motion and m_p, the mass of the proton, the mean free path to photohadronic interactions is given by

$$\lambda(\gamma_p) = \gamma_p \left[\int \mathrm{d}^3p'_\gamma f_\gamma(\mathbf{p}'_\gamma)\sigma_{p\gamma}(\varepsilon') \right]^{-1}, \tag{2.2}$$

where ε' is the energy of the background photon in the nucleon rest frame and $\sigma_{p\gamma}(\varepsilon')$ is the cross-section of the process, i.e. the expression of the likelihood of interaction between the incoming particles in units of area. The proton Lorentz factor appears in equation 2.2 as the interactions per unit time have been expressed in the rest frame of the nucleon ($\mathrm{d}t = \gamma_p\ \mathrm{d}t'$). In the laboratory frame the energy of the photon is given by $\varepsilon = (1 + \beta_p\mu')\varepsilon'\gamma_p$, where μ' is the angle between the photon and the nucleon direction, in the nucleon rest frame. Further we can write $\mathrm{d}^3p'_\gamma = 2\pi c^{-3}\varepsilon'^2\ \mathrm{d}\varepsilon'\mathrm{d}\mu'$. Changing the integration variable from μ' to ε so as to transform to the laboratory frame, in which the background photons are isotropic, and substituting into equation 2.2 gives the standard formula (Stecker 1968)

$$\lambda = 2\gamma_p^2 \left[\int_0^\infty \mathrm{d}\varepsilon \frac{1}{\varepsilon^2} n_\mathrm{b}(\varepsilon) \int_{\varepsilon'_\mathrm{th}}^{2\gamma_p\varepsilon} \mathrm{d}\varepsilon'\ \varepsilon'\ \sigma_{p\gamma}(\varepsilon') \right]^{-1}, \tag{2.3}$$

where the bounds on the second integral are $\varepsilon'_\mathrm{th} = \varepsilon/\left[\gamma_p(1+\beta_p)\right] \sim \varepsilon/2\gamma$, with ε'_th the threshold energy for the interaction to occur, and $\varepsilon'_\mathrm{max} = \varepsilon/\left[\gamma_p(1-\beta_p)\right] \sim 2\gamma_p\varepsilon$ in the limit where $\gamma_p \gg 1$. Here, $\varepsilon'_\mathrm{max}$ is the maximum background photon energy, as seen in the nucleus rest frame. The quantity $n_\mathrm{b}(\varepsilon)$ is the photon number density per unit energy

interval

$$n_{\rm b}(\varepsilon) = \frac{4\pi}{c^3}\varepsilon^2 f_\gamma(\varepsilon). \tag{2.4}$$

The interactions of UHECRs with the ambient photon fields result in an energy loss per unit time, given by

$$-\frac{1}{E}\frac{{\rm d}E}{{\rm d}t} = \langle k_{\rm inel}\sigma_{p\gamma} n_{\rm b} c\rangle, \tag{2.5}$$

where $k_{\rm inel} = \Delta E/E$, is the inelasticity, i.e. the fractional energy loss per interaction. The energy loss length to a given process is defined as

$$L_{\rm loss} = \left|\frac{1}{E}\frac{{\rm d}E}{c\ {\rm d}t}\right|^{-1}. \tag{2.6}$$

2.2.1 Pair production

Above a certain proton energy, electron-positron pair production can occur, upon collision with a low energy, background photon. This is known as the Bethe-Heitler process,

$$p + \gamma_{\rm b} \longrightarrow p + e^+ + e^-. \tag{2.7}$$

The threshold for the process in terms of the proton energy, assuming a head-on collision, is given by

$$E_p = \frac{m_e m_p c^4}{\varepsilon} \sim 5\times 10^{18}\ {\rm eV}\left(\frac{\varepsilon}{10^{-3}\ {\rm eV}}\right)^{-1}, \tag{2.8}$$

where ε is the energy of the background photon. Therefore, Bethe-Heitler pair production on the EBL starts at proton energy $E_p \sim 5\times 10^{15}$ eV (taking $\varepsilon_{IR} \sim 0.1$ eV). The energy loss from this process is small per interaction, due to the light nature of the pairs, $k_{\rm inel} \simeq 2m_e/m_p \sim 10^{-3}$. The cross-section for the process can be approximated near the threshold by $\sigma^{ee}_{p\gamma} \sim 1.2\times 10^{-27}\ {\rm cm}^2(\varepsilon/\varepsilon'_{\rm th} - 1)^3$ (in the nucleon rest frame $\varepsilon'_{\rm th} \sim 2m_e c^2 \sim 1$ MeV). It then increases monotonically with energy to $\sigma^{ee}_{p\gamma} \sim 1.8\times 10^{-27}\ {\rm cm}^2(\ln 2\varepsilon' - 2.6)$. The typical interaction distance is $\lambda^{ee}_{p\gamma} \sim 1/(n_{\rm CMB}\cdot\sigma^{ee}_{p\gamma}) \sim 1$ Mpc. As $n_{\rm CMB} \simeq 411\ {\rm cm}^{-3}$, the proton energy loss length to this process at high energies, way above the threshold is $L^{ee}_{p\gamma} \sim (\lambda^{ee}_{p\gamma}/k_{\rm inel}) \sim (1/n_{\rm CMB}\cdot\sigma^{ee}_{p\gamma}\cdot k_{\rm inel}) \simeq 1000$ Mpc.

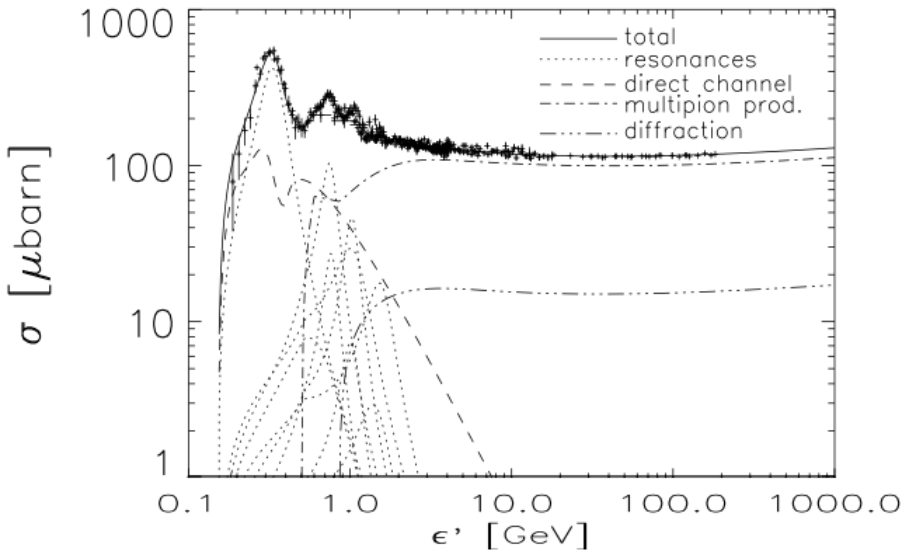

Figure 2.3. Pion photoproduction cross-section as a function of photon energy in the nucleon rest frame. The contribution from the different channels as well as the total cross-section are shown. Image adapted from Mücke et al. (1999).

2.2.2 Pion photoproduction

At the ultra-high energy end of the cosmic ray spectrum, protons are above the threshold for the production of pions, the lightest mesons, upon collision with CMB photons

$$p + \gamma_{\mathrm{CMB}} \longrightarrow \Delta^{+} \longrightarrow n\pi^{+}/p\pi^{0}, \tag{2.9}$$

where Δ^{+} is the unstable delta baryon (see e.g., Beringer et al. 2012 for details). This process, known as the GZK process, was proposed soon after the discovery of the CMB independently by Greisen (1966) and Zatsepin & Kuz'min (1966). It was predicted that it would impose an upper limit to the energy range covered by the cosmic ray spectrum, if UHECR sources are at cosmological distances, because the energy losses suffered by the protons from this process are severe.

Considering a proton-photon head-on collision with a proton and a pion in the final state, an estimate of the proton threshold energy for the process, E_{th}, in the CMB rest frame, is obtained

$$E_{\mathrm{th}} = \frac{m_{\pi}\left(2m_{p} + m_{\pi}\right)c^{4}}{4\varepsilon} \sim 10^{20}\ \mathrm{eV}\left(\frac{\varepsilon}{6\times10^{-4}\ \mathrm{eV}}\right)^{-1}. \tag{2.10}$$

The full calculation, which includes the contribution of the high energy tail of the CMB spectrum, gives $E_{\rm th} \sim 6 \times 10^{19}$ eV. The threshold proton energy for the GZK process on the more energetic IR photons (taking $\varepsilon_{IR} \sim 0.1$ eV) is $E_{\rm th} \sim 7 \times 10^{17}$ eV, but as the latter have a much lower number density than CMB photons, the interaction length for pion photoproduction on IR photons is significantly longer.

As the pion mass is a significant fraction of that of the proton, the energy loss per interaction here is significant, $k_{\rm inel} \simeq m_\pi/m_p \simeq 0.14$ at threshold. In figure 2.3, the cross-section for the process as a function of photon energy is shown, with the contribution from different production channels indicated. Very close to the threshold, which coincides with the production of the Δ resonance, the cross-section peaks at $\sigma^{\pi}_{\rm p\gamma} \simeq 5 \times 10^{-28}$ cm^2. Here, the mean free path of UHECR protons on CMB photons for the process is $\lambda^{\pi}_{p\gamma} \sim 6$ Mpc and the loss length $L^{\pi}_{p\gamma} \sim 50$ Mpc. At higher energy, the cross-section levels off at 1.4×10^{-28} cm^2, multipion production takes over and the inelasticity rises to $k_{\rm inel} \simeq 0.5$.

The GZK process creates an effective horizon, beyond which, the highest energy cosmic rays cannot reach us. As a result, more than ∼half of the UHECRs with energy $\geq 6 \times 10^{19}$ eV must come from sources at distances smaller than 100 Mpc, assuming the sources are extragalactic and cosmologically distributed. This important property is used in chapter 4, where a search for a possible correlation between extragalactic sources within the GZK horizon of $\gtrsim 6 \times 10^{19}$ eV protons and UHECRs observed by Auger is performed.

2.2.3 Redshift energy losses

At energies below the threshold for Bethe-Heitler pair production, protons lose energy predominantly due to the adiabatic expansion of the universe, at a rate given by

$$-\frac{1}{E}\frac{{\rm d}E}{{\rm d}t} = H(z) = H_0 \left[\Omega_{\rm M}(1+z)^3 + \Omega_\Lambda\right]^{1/2}, \tag{2.11}$$

if a flat universe is assumed. Here, $\Omega_{\rm M}$ and Ω_Λ are the dimensionless density parameters, denoting the "matter density" and "dark energy density" of the universe respectively (see appendix A for details). At $z = 0$, the loss length to this process for protons is given by $L^{\rm ad}_{\rm loss}(z = 0) = c/H_0 \simeq 4000$ Mpc. The energy loss lengths of UHECR protons are summarised in figure 2.4.

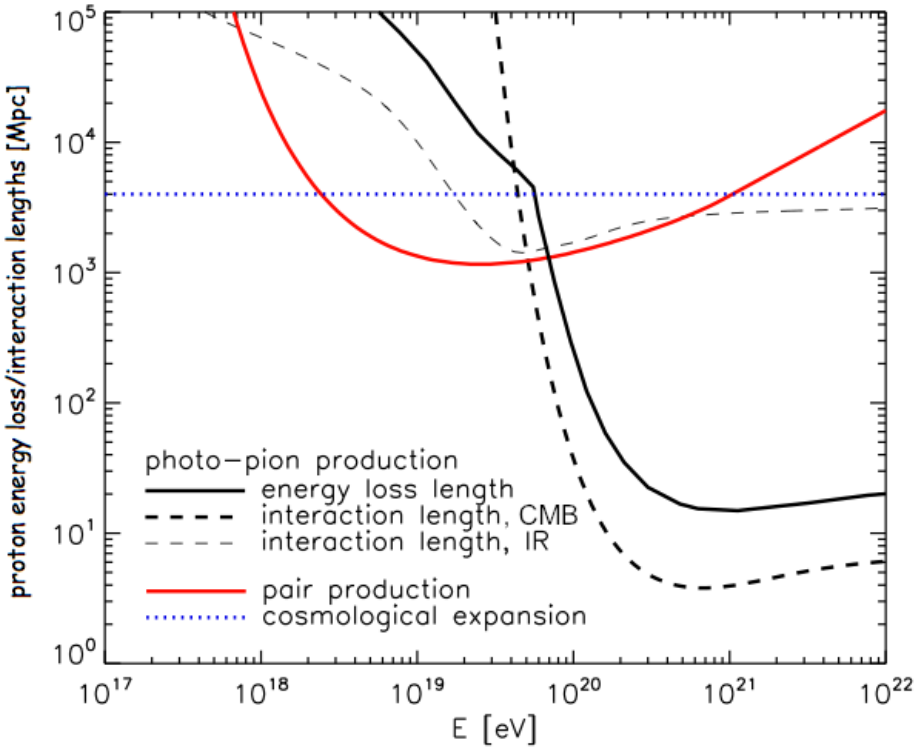

Figure 2.4. Proton interaction length for pion-photoproduction on the CMB (thick dashed line) and IR (thin dashed line) background of Stecker et al. (2006), and energy loss length for pion-photoproduction (black solid line), Bethe-Heitler pair production (red solid line) and cosmological expansion (blue dotted line). Image from Kotera & Olinto (2011).

2.2.4 Neutrons and nuclei

For neutrons, that have a half-life $\tau_n = 880.0 \pm 0.9$ s (Beringer et al. 2012), the dominant energy loss process is β-decay. Being electrically neutral, neutrons are not expected to be accelerated in astrophysical sources, nevertheless they are produced in pp collisions in high density regions, near or inside the source and in proton GZK interactions. Neutrons are very interesting because their trajectories are not affected by magnetic fields. The propagation length of neutrons is

$$L_n = c\tau_n\gamma_n \sim 0.9 \left(\frac{E_n}{10^{20}}\right) \text{ Mpc}, \tag{2.12}$$

where γ_n is the Lorentz factor of the neutron; therefore, neutrons with energy 100 EeV can travel ~ 1 Mpc before they decay.

Nuclei suffer energy losses from pair production, photomeson production and photo-

disintegration. In the rest frame of a nucleus with mass number A, the threshold for photo-pair production is $\varepsilon'_\gamma \sim 1$ MeV. Photodisintegration is particularly important at $\varepsilon'_\gamma \sim 10 - 25$ MeV ($E_A \geq A \times 10^{19}$ eV on the CMB) and photomeson production above $\varepsilon'_\gamma \sim 150$ MeV ($E_{\rm th} \sim 5 \times 10^{21}$ eV for iron nuclei on the CMB).

During photodisintegration, nuclei lose a fragment of the nucleus, most often a nucleon. The highest cross-section, lowest threshold ($\varepsilon'_\gamma \gtrsim 10$) photodisintegration process is the *giant dipole resonance*. At higher energies, the *quasi deuteron* process becomes important before finally photomeson production losses (*baryonic resonances*) take over (see e.g., Rachen 1996; Allard 2012 for a detailed discussion). The first detailed study on the energy losses of cosmic ray nuclei was presented in Puget et al. (1976) and more recently in the works of e.g., Stecker & Salamon (1999); Khan et al. (2005).

Figure 2.5 shows a comparison of the fraction of surviving nuclei for different species as a function of propagation distance at energy $E \geq 60$ EeV. As shown, only iron nuclei and protons can survive more than ∼few tens of Mpc of propagation above GZK energies. As a consequence, for sources beyond 20 Mpc, one expects to detect essentially only secondary nucleons at the detector, even if the source is enriched in intermediate (CNO type) nuclei (see e.g., the work of Bertone et al. 2002; Allard et al. 2008). For a heavy dominated composition to be observed at the detector, the injected spectrum must be dominated by iron group nuclei beyond 10^{20} eV as discussed in section 1.4.

2.2.5 Secondary products of UHECRs

As we saw with equations 2.7 and 2.9, UHECRs give rise to secondary electrons and pions. Pions are unstable ($\tau_{\pi^\pm} \simeq 2.6 \times 10^{-8}$ s, $\tau_{\pi^0} \simeq 8.5 \times 10^{-17}$ s) and most frequently decay via the following channels

$$\begin{aligned} \pi^0 &\longrightarrow \gamma\gamma \\ \pi^+ &\longrightarrow \mu^+\nu_\mu : \mu^+ \longrightarrow e^+\nu_e\bar{\nu}_\mu \\ \pi^- &\longrightarrow \mu^-\bar{\nu}_\mu : \mu^- \longrightarrow e^-\bar{\nu}_e\nu_\mu. \end{aligned} \tag{2.13}$$

UHECRs are therefore also sources of high energy neutrinos and photons. Neutrinos are discussed next, and gamma-rays in section 2.3 in some more detail.

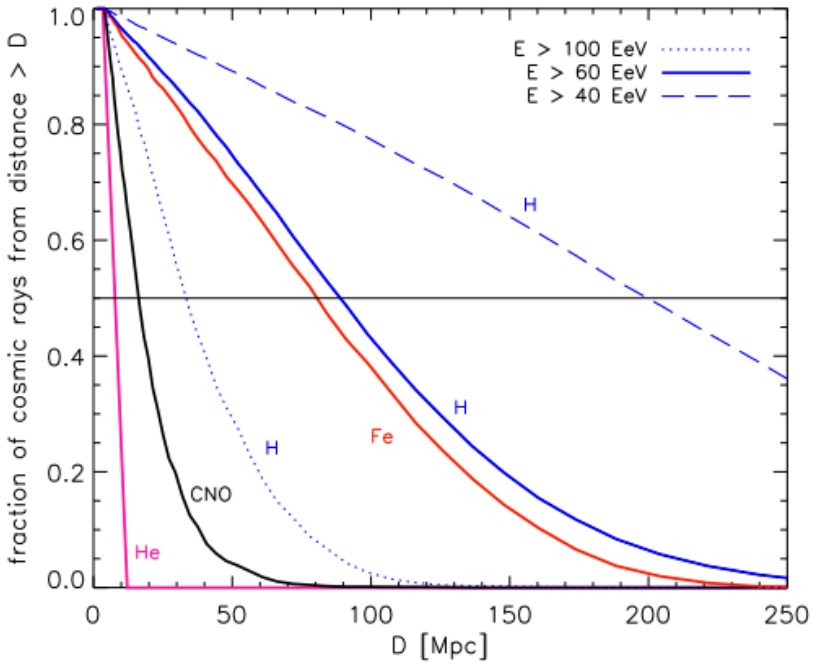

Figure 2.5. The fraction of surviving nuclei for different species as a function of propagation distance at energy $E \geq 60$ EeV (and $E \geq 40, 100$ EeV for protons). Image credit: Denis Allard (adapted from Kotera & Olinto 2011).

Neutrinos

Each of the neutrinos produced in equation 2.13 typically carries 20% of the energy of the pion. These neutrinos, produced in the interactions of UHECRs with cosmological backgrounds (Berezinsky & Zatsepin 1969), are referred to as *cosmogenic* or *GZK* neutrinos. High energy astrophysical neutrinos may also originate in hadronic interactions at the source (these are often referred to as *prompt* or *direct*).

As neutrinos interact only via the weak nuclear force, they are difficult to detect and giga-ton detectors are required. However, neutrinos travel attenuated only by redshift losses and are unaffected by magnetic fields, hence they are very interesting cosmic messengers because they point back to their sources. High energy neutrinos are the object of the searches of several high energy physics experiments, including AMANDA, IceCube, ANITA (Gorham et al. 2010), the currently in prototype phase ARA experiment (Allison et al. 2012) as well as searches at Auger (Abreu et al. 2012b).

We have recently witnessed what has been termed the "birth of neutrino astronomy" with the detection of 28 neutrinos with energies between $\sim$ 50 TeV$-$ $\sim$ 2 PeV at the IceCube detector (Aartsen et al. 2013). This is a $\sim 4\sigma$ excess above the expected atmo-

spheric neutrino background (that is, neutrinos produced by cosmic ray interactions with the Earth's atmosphere) and is considered the first evidence for very high energy neutrinos of astrophysical origin. If associations of neutrinos with astrophysical sites are established in future, it will be direct evidence that hadronic acceleration is taking place at these sites. With present statistics, individual sources cannot be distinguished but the total neutrino spectrum may allow to distinguish between different scenarios for their origin. The spectrum of the recently discovered IceCube neutrinos does not seem consistent with a cosmogenic origin of these events.

2.3 Gamma-rays

The secondary gamma-rays produced in the reactions of equation 2.13 above, are also of special interest. Like the neutrinos, they do not suffer magnetic deflections, however as we will see in the rest of this chapter, they suffer severe energy losses, greater than those suffered by protons of the same energy. Unlike neutrinos, astrophysical gamma-rays are not necessarily produced in hadronic interactions. They are thought to originate primarily in *leptonic* (electromagnetic) processes. To distinguish between the two populations the secondary gamma-rays produced in the interactions of protons, will be referred to as *hadronic*.

The first compelling evidence of hadronic gamma-rays was recently reported in Tavani et al. (2010); Giuliani et al. (2011); Ackermann et al. (2013). This gamma-ray emission, which originates in the Galactic supernova remnants W44 and IC443, has been distinguished from leptonic gamma-ray emission due to the characteristics of the observed gamma-ray spectrum, which bears the characteristic signature of pion decay. If the hadronic origin of this emission is confirmed, these sources will be the first known hadronic accelerators. Irrespective of their leptonic or hadronic origin, gamma-rays once produced, propagate in a way that depends only on their energy and characteristics of the propagation medium. The field of gamma-ray astronomy started 40 years ago, with satellite detectors, and has now matured into an important new window into the non-thermal universe. In section 2.3.1 the experimental status of gamma-ray astronomy and future prospects are discussed. In section 2.3.2 we discuss the processes that characterise gamma-ray propagation.

2.3.1 Instruments for the detection of gamma-rays

The Earth's atmosphere is opaque to photons above 10 eV. To study astrophysical photons above this energy, either satellite experiments need to be deployed, or if the photons are sufficiently energetic, they may be detected indirectly, through the shower and Cherenkov light they produce in the atmosphere. The first steps in gamma-ray astronomy were made with the launch of the American OSO-III balloon experiment in 1967. It was followed by the SAS-II and COS-B satellite experiments in the 1970s, which detected a few tens of gamma-ray sources. Major progress was made in the field with EGRET, which was the main instrument on board NASA's Compton Gamma Ray Observatory. EGRET took data from 1991 to 2000 and it's major scientific results included putting an upper limit on the diffuse gamma-ray emission of the Milky Way, establishing pulsars as a source of gamma-rays and blazars as the largest class of extragalactic gamma-ray emitters (Hartman et al. 1999). Today gamma-ray astronomy is pursued with satellite experiments in the GeV regime and with ground based detectors above 100 GeV.

Satellite experiments

Since its launch, in August 2008, the *Fermi* gamma ray space telescope has initiated a new era in gamma ray astronomy. Together, the Large Area Telescope (LAT) and Gamma ray Burst Monitor (GBM) on board *Fermi*, cover a very broad energy range, from 8 keV to ~ 300 GeV. *Fermi* observations, have increased the number of observed gamma-ray point sources by an order of magnitude and new gamma-ray source classes have been discovered[1]. The *Fermi*-LAT surveys the entire sky in 3 hours and achieves full time operation. It is equipped with an anti-coincidence detector for rejecting charged cosmic rays and uses tracking to achieve good pointing resolution. It also achieves energy resolution better than 10% (Atwood et al. 2009).

The operation of the *Fermi*-LAT so far has lead to the detection of more than 1800 point sources (Nolan et al. 2012) and to the compilation of separate class catalogues of Pulsars, Gamma-ray bursts and AGN. At the same energy range as the *Fermi*-LAT, the Italian AGILE satellite currently in operation is providing complementary data (see e.g., Tavani et al. 2009 for details). The complementarity of these satellite experiments with ground based gamma-ray instruments in terms of wavelength, allows for up to six orders of magnitude of coverage in gamma-ray energy.

[1] see e.g., http://fermi.gsfc.nasa.gov/science/mtgs/symposia/2012/ for details

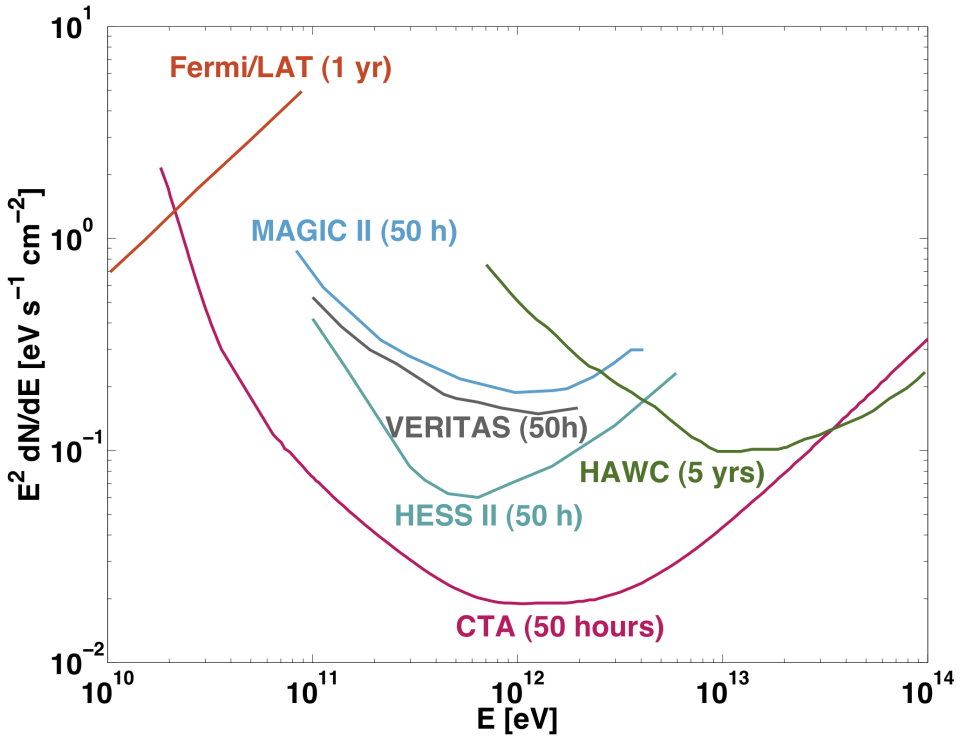

Figure 2.6. The sensitivity of a compilation of gamma-ray detectors. The quantity E dN/dE is the minimum gamma-ray flux in $\mathrm{cm}^{-2}\,\mathrm{s}^{-1}$ that can be detected above a specified threshold energy with 5σ significance after 50 hours of observation, or in 1 or 5 years in the case of the unsteered detectors.

Ground-based detectors

Satellite experiments are limited by the small collection areas that can be accommodated. The intensity of gamma-ray emission above 100 GeV, referred to as the very high energy (VHE) gamma-ray band, is too low to be detected with this technique[2].

Energetic gamma-ray photons produce a cascade of photons, electrons and positrons when they enter the Earth's atmosphere. The shower propagates longitudinally but also spreads laterally. The relativistic electrons and positrons in the shower emit blue Cherenkov light, which can be recorded on the ground with Cherenkov telescopes even though the the electromagnetic shower does not reach sea level. Above 100 GeV, gamma-ray photons produce a powerful enough electro-magnetic shower to be detectable on the ground via the Cherenkov light produced. The technique was pioneered at the Whipple

[2] At 100 GeV the differential *Fermi*-LAT sensitivity to point sources is $\sim 10^{-11}$ TeV cm^{-2} s^{-1} in 10 years (see e.g., Funk et al. 2013 for details of the calculation). The quoted LAT sensitivity roughly corresponds to 10 *milliCrab* (where the flux of the Crab nebula has been used as a unit of intensity, as a reference, approximating the Crab spectrum by a power law $\mathrm{d}N/\mathrm{d}E = 3.45(E/\mathrm{TeV})$ TeV^{-1} cm^{-2} s^{-1} F. Aharonian et al. 2006). Beyond 100 GeV, the LAT sensitivity worsens with increasing energy proportional to E^1.

Observatory with the detection of the Crab Nebula in 1989 (Weekes et al. 1989).

Today, imaging atmospheric Cherenkov telescopes (IACTs) are often arranged in arrays, hence increasing the effective collection area up to 10^5 that of the *Fermi*-LAT, and the field of view to 5°. Currently in operation are the two MAGIC-II telescopes in La Palma, the VERITAS array in Arizona with four telescopes, and HESS in Namibia. HESS recently entered Phase 2, following the deployment of a fifth 28 m diameter telescope in the middle of the HESS-I array. The angular resolution of the reconstructed primary gamma-ray arrival direction is approximately $5'$. A challenge for ground based Cherenkov telescopes is discriminating gamma-ray showers from the overwhelming background of charged cosmic ray showers. However, today's IACTs can reject $\sim 99.98\%$ of cosmic rays (e.g. Krawczynski et al. 2006). The energy resolution of IACTs is approximately 15%. At low energies, the detection threshold can be as low as $\sim$ few $\times$ 10 GeV(MAGIC-II, HESS-II). A disadvantage of IACTs is that they can only observe incoming gamma-rays on clear, moonless nights, thus achieving about 1000 hours of observations per year.

A major step is planned as the next step in TeV astronomy, which is the deployment of the Cherenkov Telescope Array (CTA) (see e.g., Actis et al. 2011). The CTA, which is envisaged to have $\mathcal{O}(100)$ telescopes covering an area of several square kilometres, will bring a dramatic increase to the number of detected gamma-rays: it is expected to bring the total number of detected TeV sources to $\mathcal{O}(1000)$, and to increase the number of known types of TeV sources. The CTA is planned to consist of two arrays, one in the Southern hemisphere and one in the North, hence achieving full sky coverage. It is expected to be fully deployed by 2020 and will have an order of magnitude higher sensitivity in the 100 GeV to 10 TeV range, as well as extending to energies well below 100 GeV and above 100 TeV. It is expected to achieve an angular resolution better than $1'$.

The detection of gamma-rays with IACTs is complemented by the use of ground based particle detectors. The latter technique relies on recording the cascade particles that reach the ground. Large water or scintillator detectors are deployed, often at high altitudes. The technique was pioneered with HEGRA and continued with the Milagro, AS-gamma and ARGO experiments. The current state-of-the art water Cherenkov observatory is HAWC at the Sierra Negra, Mexico. More than two-thirds of the array are now deployed and taking data (Mostafa 2013; Abeysekara et al. 2013). The advantage of ground based particle detectors is that they allow for full time operation and have a large field of view (~ 2 sr), surveying a large fraction of the sky in a 24 hour period. Difficulties in the arrival

direction reconstruction and discrimination of CR and gamma-ray induced air-showers with this technique, mean that the sensitivity to gamma-ray detection is lower than can be obtained with IACTs. A summary of the sensitivities of a selection of gamma-ray experiments is shown in figure 2.6.

2.3.2 Intergalactic electromagnetic cascades

High energy photons, electrons and positrons promptly interact with the cosmological background photon fields and develop electromagnetic cascades. In this section we consider the relevant electromagnetic processes in some detail.

Pair production

When sufficiently energetic photons of energy E_γ collide with background photons, γ_b of energy ε they undergo pair production,

$$\gamma + \gamma_b \longrightarrow e^+ + e^-. \tag{2.14}$$

This process poses strict limitations for the mean free path of gamma-rays. The threshold gamma-ray energy for the process is given by

$$E_\gamma \geq \frac{m_e^2 c^4}{\varepsilon} \simeq 2.6 \times 10^{11}\ \text{eV} \left(\frac{\varepsilon}{1\ \text{eV}}\right)^{-1}, \tag{2.15}$$

therefore the universe is essentially opaque to gamma-rays with energy above $\sim 10^{11}$ eV.

These, high-energy photons, are absorbed by pair production on the EBL. Gamma-rays interact with CMB photons above $E_\gamma \sim 10^{14}$ eV and with radio background photons above $\sim 10^{19}$ eV. Below $\sim 10^{11}$ eV gamma-rays propagate without interacting as the EBL density drops significantly above ~ 1 eV. As a result, the photon flux at energies $\gtrsim 10^{11}$ eV from distant sources, such as blazars, is significantly attenuated. Such photons are however not really absorbed, but initiate electromagnetic cascades in the intergalactic medium, via subsequent pair production and inverse-Compton scattering (see section 2.3.2).

The cross-section for pair production is given by

$$\sigma_{\gamma\gamma} = \frac{3}{16}\sigma_{\text{T}} \frac{m_e^2}{s} \left[(3-\beta^4)\ln\frac{1+\beta}{1-\beta} - 2\beta(1-\beta^2)\right], \tag{2.16}$$

where $\sigma_{\text{T}} = (8\pi/3)(\alpha\hbar c/3m_e c^2)^2$ is the electron Thompson cross-section, with $\alpha \simeq 1/137$,

the electromagnetic fine-structure constant and $\beta = (1 - \varepsilon_{\rm th}/\varepsilon)^{1/2}$. Here $\varepsilon_{\rm th}$ is the pair production threshold energy in terms of the energy of the background photon, $\varepsilon_{\rm th} = 2(m_e c^2)^2/E_\gamma(1-\mu)(1+z)$, where the $(1+z)$ factor takes into account the adiabatic energy loss of the high energy photon and $\mu = \cos(\theta)$ where θ is the angle between the two incoming photons. The pair production cross-section peaks near the threshold; as a result the mean free path to pair production on CMB photons in the PeV range is extremely small, $\lambda_{\gamma\gamma} = 1/(n_{\rm CMB}\sigma_{\gamma\gamma}) \sim 8$ kpc, as shown in figure 2.7.

One can define the optical depth to pair production at energy E_γ and redshift z as (Hauser & Dwek 2001)

$$\tau(E,z) = \int_0^z {\rm d}z' c \left|\frac{{\rm d}t}{{\rm d}z'}\right| \int_{-1}^{1} {\rm d}\mu \, \frac{(1-\mu)}{2} \int_{\varepsilon'_{\rm th}}^{\infty} {\rm d}\epsilon \, n_\varepsilon(\varepsilon, z') \left(1+z'\right)^3 \sigma_{\gamma\gamma}(\beta', z'), \qquad (2.17)$$

where $n_\varepsilon(\varepsilon, z) = {\rm d}n\left(\varepsilon, z\right)/{\rm d}\varepsilon$ is the comoving number density of background photons of redshift z with energy ε and the $(1+z')^3$ term converts n_ε to a proper number density. As a result of the attenuation due to pair production, the observed gamma-ray spectrum of a source is related to the intrinsic spectrum through:

$$\frac{{\rm d}N}{{\rm d}E}_{\rm observed} = \frac{{\rm d}N}{{\rm d}E}_{\rm intrinsic} \cdot e^{-\tau(E,z)}. \qquad (2.18)$$

The quantities $\tau(E,z)$, $e^{-\tau(E,z)}$ are plotted as a function of the incoming gamma-ray energy in figure 2.8 for a range of redshifts, using the EBL model of Kneiske & Dole (2008).

inverse-Compton Scattering

High energy electrons also promptly interact with the cosmic photon backgrounds through inverse-Compton scattering

$$e + \gamma_b \longrightarrow e + \gamma. \qquad (2.19)$$

producing energetic photons. Inverse-Compton scattering proceeds in the Thompson regime for $\varepsilon' \ll m_e c^2$, where ε' is the background photon energy in the electron rest frame, and in the Klein-Nishina regime in the opposite case, when $\varepsilon' \gg m_e c^2$; here we are primarily interested in the latter regime.

The cross-section for the process is well approximated by the following expression

(Coppi & Blandford 1990)

$$\sigma_{\rm IC} = \frac{3\sigma_{\rm T}}{8\kappa}\left[\left(1-\frac{2}{\kappa}-\frac{2}{\kappa^2}\right)\ln\left(1+2\kappa\right)+\frac{1}{2}+\frac{4}{\kappa}-\frac{1}{2(1+2\kappa)^2}\right], \tag{2.20}$$

over a wide range of energies, where we've introduced $\kappa = \varepsilon E_e/m_e c^2$, with ε the initial photon energy. In the ultra-relativistic limit the expression reduces to $\sigma_{\rm IC} \simeq (3/8)\sigma_{\rm T}\kappa^{-1}\ln 4\kappa$ i.e. the cross-section decreases with increasing photon energy for a given value of E_e.

Intergalactic electromagnetic cascades generally proceed in the Thompson regime where the inverse-Compton cooling length is given by (Blumenthal & Gould 1970)

$$D_{\rm IC} = \frac{3m_e^2c^3}{4\sigma_{\rm T}U_{\rm CMB}E_e} \simeq 300\ {\rm kpc}\ \left(\frac{E_e}{1\ {\rm TeV}}\right)^{-1}, \tag{2.21}$$

where $U_{\rm CMB} \sim 0.25$ eV cm^{-3} is the CMB energy density. In the Klein-Nishina regime inverse-Compton cooling is significantly less efficient and the cooling length of electrons on the CMB is of order $D_{\rm IC} \sim 5\,{\rm Mpc}(E_e/10^{18}\ {\rm eV})$ between $10^{15}\ {\rm eV} \lesssim E_e \lesssim 10^{18}$ eV (note that the cooling length now increases with increasing electron energy as shown on the left panel of figure 2.7). Beyond 10^{18} eV interactions with the highly uncertain radio background become important and the scaling of $D_{\rm IC}$ with electron energy possibly changes.

The development of the electromagnetic cascade stops when the energy of the secondary photons falls below the threshold for pair production on the EBL. Below this energy electrons continue to Thompson scatter off background photons contributing to the observed photon spectrum of the source down to the MeV region.

In the absence of magnetic fields in the intergalactic medium, through which the cascade propagates, all the energy of the cascade is deposited at the $\lesssim 100$ GeV part of the spectrum (see detailed discussion on this in chapter 5).

Synchrotron Radiation

The motion of a relativistic charged particle of mass m and velocity $\mathbf{v}$ in a magnetic field satisfies

$$\frac{\rm d}{{\rm d}t}\gamma m\mathbf{v} = \frac{Ze}{c}(\mathbf{v}\times\mathbf{B}) \tag{2.22}$$

as a result of the Lorentz force acting on it. Relativistic charged particles in a uniform magnetic field $\mathbf{B}$ move in a helix at a constant pitch angle (the angle between the magnetic

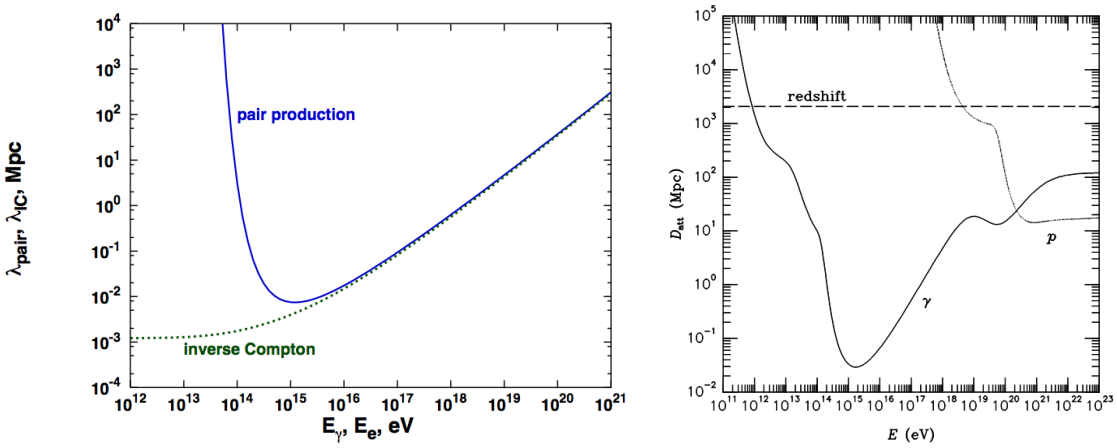

Figure 2.7. Left: The interaction length for pair production and inverse-Compton scattering on the CMB. Image from Stanev (2005). **Right:** The interaction length of photons on background radiation fields. The estimate of Lee (1998) has been used for the EBL and of Clark et al. (1970) for the universal radio background. The mean free path of protons of the same energy is also given for comparison. Image adapted from Lee (1998).

field vector and the particle's velocity) emitting "synchrotron" photons. The synchrotron cooling length of electrons is given by

$$D_{\rm syn} = \frac{6\pi m_e^2 c^4}{\sigma_{\rm T}} E^{-1} B^{-2} \simeq 3.8\,{\rm kpc} \left(\frac{B}{10^{-8}\ {\rm G}}\right)^{-2} \left(\frac{E_e}{10^{19}\ {\rm eV}}\right)^{-1}. \tag{2.23}$$

The typical energy of synchrotron photons radiated by electrons of energy E_e is

$$E_\gamma = \frac{3}{2}\frac{heBE_e^2}{2\pi m_e^3 c^5} \simeq 6.8\times 10^9 \left(\frac{E_e}{10^{18}\ {\rm eV}}\right)^2 \left(\frac{B}{10^{-7}\ {\rm G}}\right)\ {\rm eV}. \tag{2.24}$$

Synchrotron photons produced with energy below the threshold for pair production (equation 2.15) propagate unimpeded by energy losses except for redshifting.

The synchrotron cooling length may be compared to the inverse-Compton cooling length, to determine through which of the two processes the electrons will cool first at a given energy and magnetic field strength. Comparing the inverse-Compton and synchrotron cooling lengths, we observe that synchrotron losses of electrons dominate over inverse-Compton attenuation on the EBL above $E_{\rm cr} \simeq 10^{18}\,(B/10\ {\rm nG})^{-1}$ eV. Figure 2.9, which shows the cooling length of electrons as a function of energy for different average values of the magnetic field strength, also demonstrates this cross-over energy as well as the opposite scaling of inverse-Compton and synchrotron energy losses with energy at

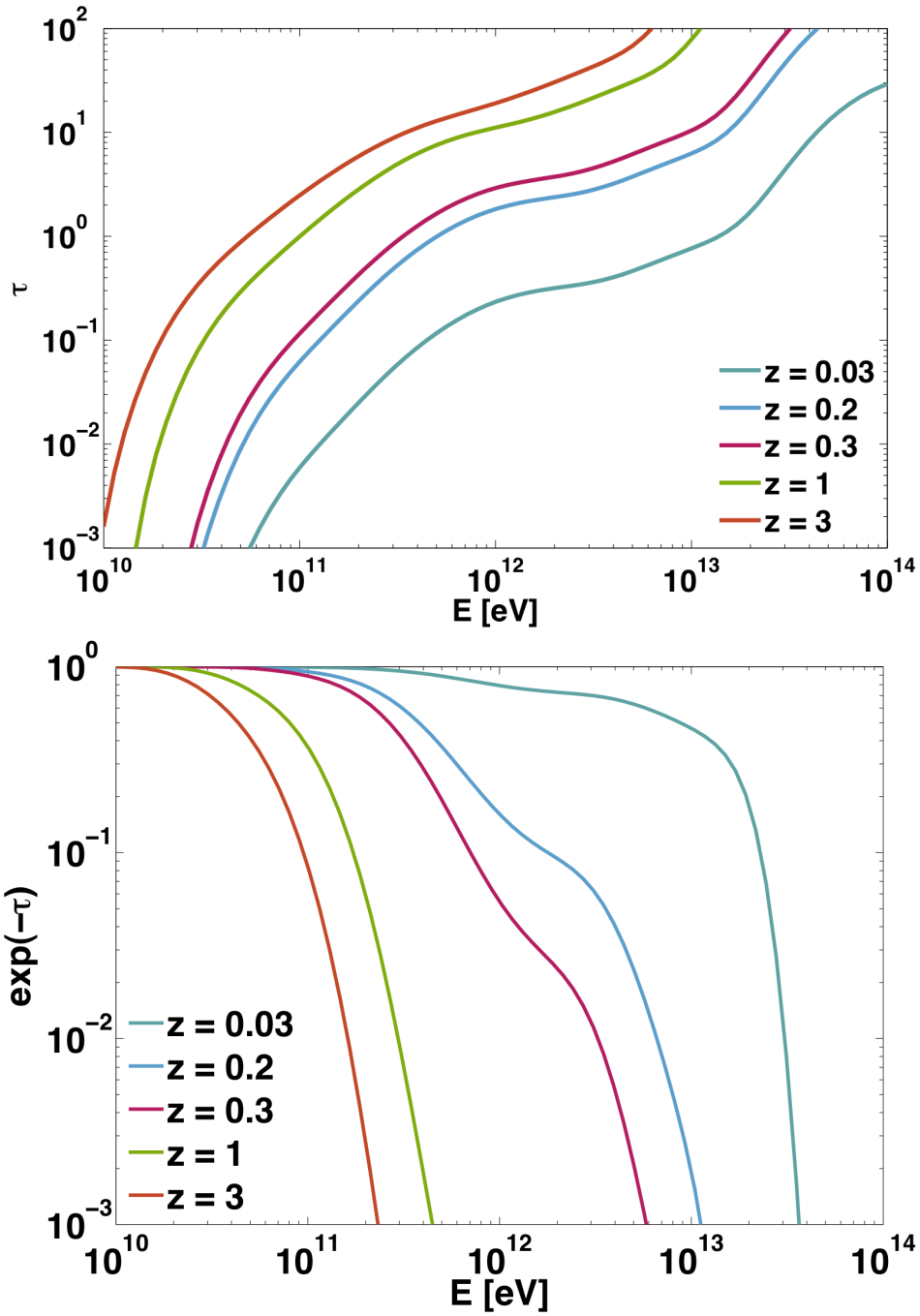

Figure 2.8. Top: The optical depth, τ, of the EBL to gamma-rays for a range of redshifts based on the model of Kneiske & Dole (2008). **Bottom:** The attenuation factor $\exp(-\tau)$ for gamma-ray photons on the EBL for the optical depth shown on the top panel.

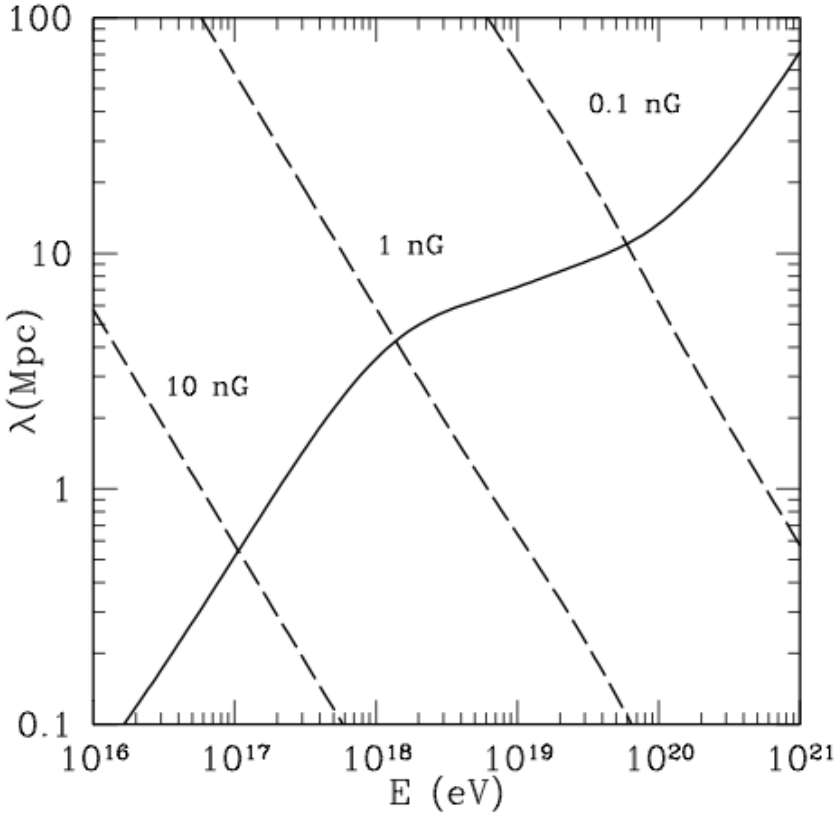

Figure 2.9. Electron cooling length as a function of energy. The dotted lines give the synchrotron losses in an extragalactic magnetic field of r.m.s. strength 0.1, 1, 10 nG. The solid line gives the attenuation length due to inverse-Compton scattering/pair production on the CMB and the radio background of Clark et al. (1970). Image from Gabici & Aharonian (2005).

UHE energies. Electrons with energy of order 10^{18} eV cannot be accelerated in leptonic processes (due to the synchrotron cooling proceeding faster than acceleration) and must therefore be the secondary products of UHECRs.

The result of the above discussion is that in a magnetised region such as for example a filament of large scale structure with typical magnetic field strength of order ~ 10 nG, the first generation of secondary electrons created by UHECRs through interactions with background photons cool rapidly, through synchrotron radiation, and the cascade that would otherwise develop is strongly inhibited. The consequences for the detectable signature of this process were first discussed in Gabici & Aharonian (2005, 2007) and studied numerically in Kotera et al. (2010) and will be studied numerically in the context of recently detected extra-Galactic gamma-ray sources in chapter 5.

This page was intentionally left blank

Chapter 3

Propagation of UHECRs in a magnetised universe and anisotropies

To complete the picture of the propagation of UHECRs we must discuss the effect of magnetic fields on their trajectories. Unlike photons, hadrons suffer deflections and time delays as a result of the effect of magnetic fields. The sources that produce UHECRs are not known, but one expects their distribution to be associated with the distribution of matter in the universe. The propagation distance of UHECRs is limited to a few hundred Mpc at the highest energies due to the GZK process. The matter distribution is not homogeneous over such distances, hence if UHECRs are extragalactic one expects an anisotropy in their arrival direction distribution reflecting the inhomogeneity of the galaxy distribution, if magnetic deflections do not completely smear their trajectories. From the above discussion it is clear that one cannot discuss UHECR anisotropies without magnetic fields and vice versa. In what follows, the two closely linked topics, are discussed together.

3.1 Magnetic fields

It is known from observations that magnetic fields permeate the universe. Everywhere we look we see the effects of magnetisation, on the Earth, in the solar system, in our own

Galaxy and other nearby and distant galaxies, in the intergalactic medium in filaments, sheets and clusters of large scale structure, whereas there are observational hints and strong theoretical arguments that even the voids of large scale structure are mildly magnetised.

Despite a growing number of measurements the configuration, coherence length (i.e. the distance over which the field direction can be considered constant), strength and origin of extragalactic magnetic fields remains largely unknown. Current and upcoming large astronomy instruments, among them the Low-Frequency Array (LOFAR) and the Square Kilometre Array (SKA), define the study of cosmic magnetic fields as a key science goal.

Cosmic magnetic fields seem to play an important role in the universe, possibly dynamically affecting the evolution of structures. Magnetic fields play a dominant role in determining the fate of UHECRs, from confining them in the vicinity of astrophysical shocks where they can be accelerated, to reigning over their propagation throughout their journey.

In what follows, observational techniques for the measurement of magnetic fields, the magnetic field of the Milky Way and extragalactic magnetic fields are discussed. Next, the state of the art in numerical simulations of magnetic fields in the universe are discussed and analytical tools for estimating UHECR magnetic deflections are outlined.

3.1.1 Measurement techniques and observations

Synchrotron radiation is a tracer of magnetic fields in areas where relativistic particles (mainly electrons) exist. The typical frequency of the emitted synchrotron radiation, $\nu_{\max}$, depends on the magnetic field strength as

$$\nu_{\max} \simeq 11 \text{ MHz } \left(\frac{E_e^2}{1 \text{ GeV}}\right)\left(\frac{B}{1\ \mu\text{G}}\right), \tag{3.1}$$

where E_e is the electron energy and B the magnetic field component perpendicular to the line of sight. For the typical magnetic field strengths in galaxies and clusters of galaxies of order 1 μG the peak of synchrotron radiation is in the radio band. In practice, a distribution of electron energies will exist in the source, typically modelled as a power law, $\mathrm{d}N/\mathrm{d}E \propto E^{-\gamma}$, which results in a synchrotron spectrum with index $\alpha = (\gamma + 1)/2$. For a

source with extension, L, along the line of sight the intensity of synchrotron radiation is

$$I_\nu = n_e \; B^{(1-\gamma)/2} \; L, \tag{3.2}$$

where n_e is the density of electrons per energy interval. Given a description of the electron energy distribution and assumption about the relative energy density of the magnetic field, cosmic rays and gas, one can obtain an estimate of the magnetic field strength in the source (see e.g. Beck & Krause 2005).

For more distant, Galactic and extra-galactic sources, a measurement of (or an upper bound on) the integrated magnetic field strength along the line of sight to a specific radio source can be obtained through the effect of *Faraday Rotation* which is the rotation of the polarisation plane of linearly polarised radio emission (Kronberg 1994; Vallee 1997). The rotation angle is given by the wavelength squared times the rotation measure, RM,

$$\mathrm{RM} = \mathcal{C} \int_0^L \left(\frac{n_e}{1 \text{ cm}^{-3}}\right) \left(\frac{B_{\text{l.o.s.}}}{1 \; \mu\text{G}}\right) (1+z)^{-2} \frac{\mathrm{d}s}{1 \text{ Mpc}}, \tag{3.3}$$

where the numerical constant $\mathcal{C} = 8.1 \times 10^5$ rad m^{-2}, n_e is the free electron number density, $B_{\text{l.o.s.}}$ is the magnetic field component in the line of sight, and L, the distance to the source. The factor $(1+z)^{-2}$ accounts for the redshift of the photons as they travel from the source. Given the distribution of free electrons, n_e, we can infer the integrated magnetic field strength of the regular magnetic field along the line of sight, as long as observations in two or more wavelengths exist. The effect of Faraday rotation on Galactic sources (primarily pulsars), allows a measurement of the Galactic magnetic field, in general towards the Galactic plane. A large number of rotation measures of extragalactic radio sources also constrain the Galactic magnetic field in all directions (see e.g. early work by Simard-Normandin & Kronberg 1980). Rotation measures of distant extragalactic sources can give an estimate of the integrated magnetic field strength out to distant extragalactic sources such as quasars. This is an important measurement because, as will be shown below, the strength of magnetic fields in the interstellar medium is very poorly constrained. The SKA, which is expected to start operations in 2018, will significantly enlarge the available number of extragalactic rotation measures, giving a clearer view of local extragalactic magnetic fields.

Inside the Galaxy we can measure the magnetic field strength of a source through the *Zeeman splitting* of atomic or molecular lines. Magnetic fields interfere with the magnetic

moment of the valence electrons causing a subdivision of electronic energy levels. This is observed as a split of the spectral line, the magnitude of which is proportional to the magnetic field strength. The amplitude of the effect is small and thermal broadening makes the observation of Zeeman splitting challenging, unless a high magnetic field and low ambient temperature exist in the source. The technique has been used with success in studies of the magnetic field of the Sun and a number of Galactic sources.

3.1.2 galactic magnetic field

Apart from extragalactic magnetic fields, the magnetic field of the Milky Way deflects observed UHECRs. Despite numerous measurements, we do not have a clear global picture of the magnetic field of the Milky Way due to our position. From observations we find that the Galaxy supports a ∼few μG strength regular magnetic field in the disk, aligned along the Galactic plane. Apart from the regular field, a random component of similar intensity exists, whose origin is not known (see e.g. the reviews of Beck & Wielebinski 2013; Kulsrud & Zweibel 2008).

The situation in the halo of the Galaxy is less clear. In the Galactic centre, vertical magnetic fields apparently extend into the halo. From RMs of extragalactic radio sources towards the Galactic poles some studies infer a local large-scale field perpendicular to the plane of $\mathcal{O}(\mu\text{G})$ towards the South Galactic Pole but no significant field towards the North Galactic Pole. In contrast, Jansson & Farrar (2012) find an X-shaped halo field similar to those observed in other spiral galaxies.

Detailed modelling of the deflections of UHECRs in the Galactic magnetic field has been performed in a large number of works Harari et al. (1999, 2002b,a); Tinyakov & Tkachev (2005); Alvarez-Muñiz et al. (2002); Roberts & Farrar (2013). Commonly in numerical methods, given a model of the Galactic magnetic field, particles are backtraced through the field to obtain an estimate of the deflection and the arrival direction of the UHECR before it enters the Galaxy. The highest energy protons are expected to travel mostly in straight lines while traversing the Galaxy. When crossing the Galactic disk however, their Larmor radii are of order $r_{\text{L}} \simeq 100\,\text{kpc}(E/10^{20}\,\text{eV})(B/1\,\mu\text{G})$ in the typically expected $\sim \mu$G field and deflections might be significant, especially when crossing the Galactic centre. Most works referenced in this section, find that 10^{20} eV protons, crossing the Galaxy at low latitudes, experience $\gtrsim 4^\circ$ deflections (see however the recent model of Jansson & Farrar 2012, who find larger deflections on average and significant deflections

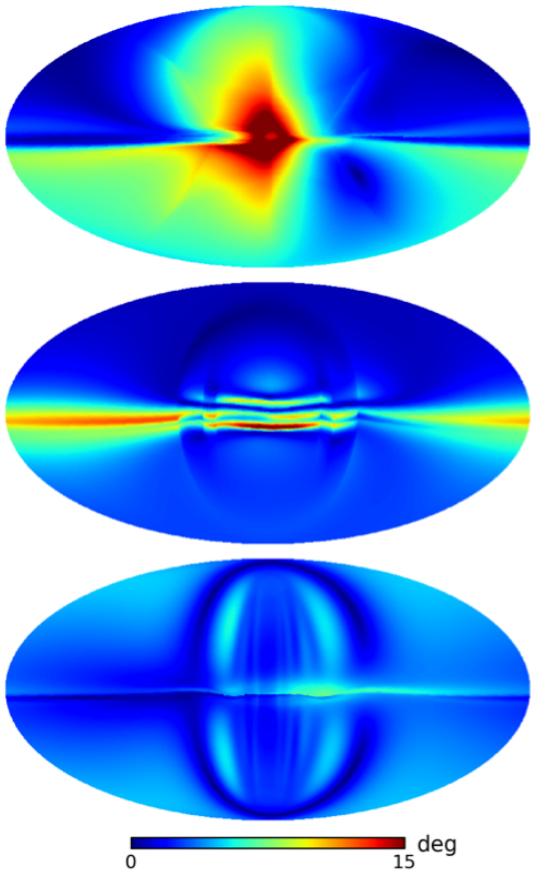

Figure 3.1. Simulated maps showing the expected deflections of 6×10^{19} eV protons in the Galactic magnetic field in the model of Jansson & Farrar (2012)-top, Sun et al. (2008)-middle, Stanev (1997)-bottom in Galactic coordinates, with the Galactic centre $l = 0°$ in the centre and Galactic longitude increasing to the left. Image from Jansson & Farrar (2012).

even at high Galactic latitudes). Figure 3.1 summarises the expected deflections of 6×10^{19} eV protons in three different Galactic magnetic field models.

3.1.3 Extragalactic magnetic fields

Outside the Milky Way the uncertainties surrounding magnetic fields are significantly larger. Theories of the origin of extragalactic magnetic fields can be divided into two main categories: those that propose that magnetic fields were created in the primordial universe, during inflation or phase transitions (see e.g. Widrow 2002 for a review) and those in which the universe is magnetically enriched much later, through the magnetised pollution ejected by the first stars or galaxies (e.g. Kulsrud & Zweibel 2008).

From theory, analytical mapping relations between the baryonic density, ρ, and the

magnetic intensity, B, can be derived. It can be shown that $B \simeq \rho^{2/3}$ for isotropic gravitational collapse, or $B \simeq \rho$ for anisotropic collapse during structure formation (King & Coles 2006; Kotera & Lemoine 2008a). Therefore one expects the magnetised universe to be highly structured, with enhanced magnetic fields in the filaments and walls of large scale structure, and even more enhanced in galaxies and clusters of galaxies.

Observations support this picture. Measurements of Faraday rotation provide detailed measurements of the magnetic field strength in the core of galaxy clusters, which have typical strengths of order 1 - 10 μG. Magnetic fields are otherwise detected in galaxies through synchrotron emission and have similar strengths to those of galaxy clusters. Magnetic fields have also been detected in the Coma supercluster (Kim et al. 1989).

Little is known about the strength and correlation length of magnetic fields on larger scales and in the intergalactic medium, where there is no significant concentration of relativistic particles to trace the fields. If magnetic fields were created at the early moments of the universe, then some magnetisation is expected even in voids. No observations of fields in the intergalactic medium exist to date. Upper limits have been derived from the absence of Faraday rotation of the polarisation of the radio emission of distant quasars. The most constraining limits from these searches are of order $B_{\rm mean}\lambda^{1/2} \lesssim 10^{-8}$ G Mpc$^{1/2}$, with λ the coherence length of the fields, (Kronberg & Simard-Normandin 1976; Kronberg & Perry 1982; Blasi et al. 1999). Upper bounds are also derived from the non-observation of the effects of cosmic magnetic fields on the anisotropy and polarisation of the Cosmic Microwave Background (see e.g. discussion in Durrer & Neronov 2013 and references therein).

Lower limits are derived from *Fermi*-LAT gamma-ray observations of extragalactic sources for intergalactic magnetic fields. The techniques, model dependence of the results and implications for particle propagation, will be discussed in detail in chapter 4, after the propagation of gamma-rays in the intergalactic medium has been discussed in some detail. The derived lower limits are model dependent, but as tight as $B_{\rm mean}\lambda^{1/2} \gtrsim 10^{-14}$ G Mpc$^{1/2}$ (see references in section 5.1.2).

In this section, a general picture of intergalactic magnetic fields was sketched. In the absence of a precise description of the structures crossed by a specific trajectory, it is hard to estimate exact deflections, which is why we generally rely on numerical simulations of large scale magnetic fields, which are discussed next. Given some knowledge of the magnetisation of the medium traversed, the deflections can be estimated analytically (see

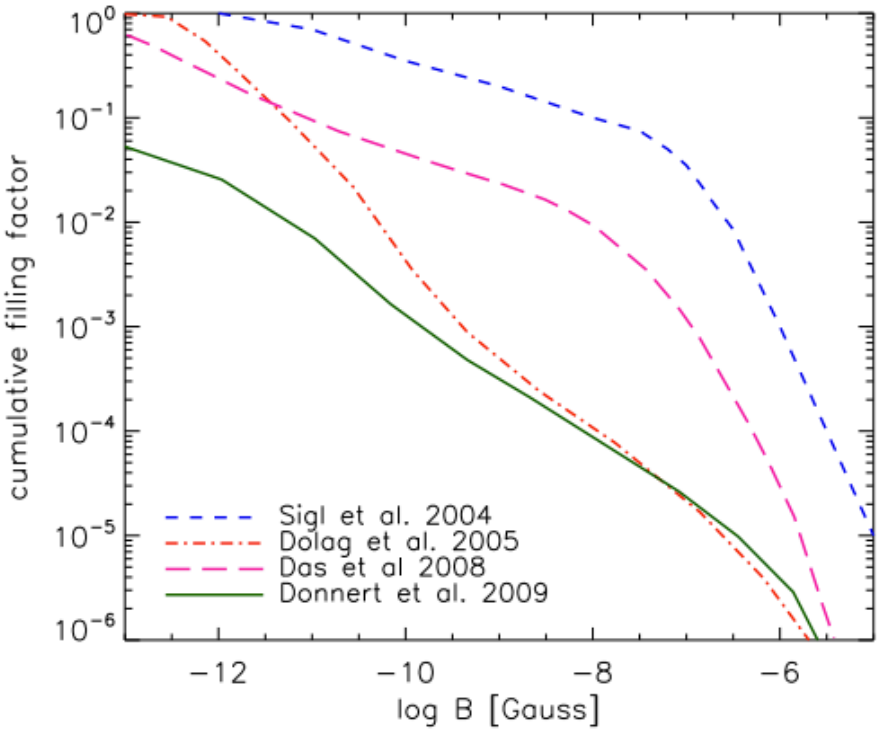

Figure 3.2. Cumulative filling factor of extragalactic magnetic fields from a selection of recent numerical studies adapted from ref. Kotera & Olinto (2011). Blue dashed: Sigl et al. (2004b), red dash-dotted: Dolag et al. (2005), pink long dashed: Das et al. (2008), green solid: Donnert et al. (2009).

section 3.1.5).

3.1.4 Numerical simulations

Several groups have modelled the magnetic fields in the universe using numerical simulations (e.g. Sigl et al. 2004b; Dolag et al. 2005; Das et al. 2008; Donnert et al. 2009). In these studies, it is assumed that magnetic fields follow baryonic matter and the numerical simulations follow the evolution of magnetic fields during structure formation. UHECRs are then propagated inside a simulation volume and their deflections are calculated. In these simulations, the magnetic field strength is in general normalised to the values derived from observations in galaxies and clusters of galaxies.

The most sophisticated such studies have led to significantly discrepant results. The volume filling factor of magnetic fields as a function of B is shown in figure 3.2, for a collection of works. Discrepancies are largest for low magnetic field strengths, which likely occupy the voids of large scale structure and are least constrained by observations.

The different works also predict radically different deflections for UHECRs. In Sigl et al. (2004b) it was found that 10^{20} eV protons experience of order 20° deflections, whereas in Dolag et al. (2005) a simulation which approximately reproduces the large scale structure 115 Mpc from the Milky Way was performed and it was found that 10^{20} eV protons experience deflections of no more than a few degrees (see figure 3.3). A detailed discussion of reasons for these discrepancies was published in Sigl et al. (2004a). The different magnetic field amplification mechanisms assumed can account for some of the discrepancy, but numerical issues seem to play an important role. In the more recent work of Das et al. (2008), intermediate UHECR deflections were found; in their simulations 60% of 10^{20} eV protons suffer deflection $\theta < 5°$.

A different, phenomenological approach was followed by Takami et al. (2006) who mapped the magnetic field strength to the galaxy luminosity density, using the PSCz galaxy catalogue, and found few degree deflections for 10^{20} eV protons. In Kotera & Lemoine (2008a) similar (but more generalised) mapping relations were adopted and the magnetic field intensity was mapped on a dark matter simulation. Again, deflections of up to a few degrees were found for 10^{20} eV protons. In chapter 5, the latter method is adopted to model extragalactic magnetic fields.

3.1.5 UHECR deflections

A charged relativistic particle of energy E, traversing a magnetic field $\mathbf{B}$, experiences a Lorentz force

$$F = \frac{\mathrm{d}\mathbf{p}}{\mathrm{d}t} = Ze\frac{\mathbf{p}}{\gamma m} \times \mathbf{B} = \frac{\mathrm{Zec}^2}{\mathrm{E}}\mathbf{p} \times \mathbf{B}, \tag{3.4}$$

where e is the electron charge and $\mathbf{p}$ the momentum of the particle. The force, which is perpendicular to the momentum vector of the particle, curves the particle's trajectory in such a way that the trajectory can be described by the Larmor radius r_{Lar} (equation 1.2). Another important quantity for characterising the transport of cosmic rays in a magnetic field is the scattering time, t_{scatt}, which is defined as the timescale below which the motion can be considered quasilinear.

Comparing r_{Lar} to the coherence length of the magnetic field λ and t_{scatt} to the travel time of the particle t_{trav}, we can define distinct regimes in which the propagation might proceed:

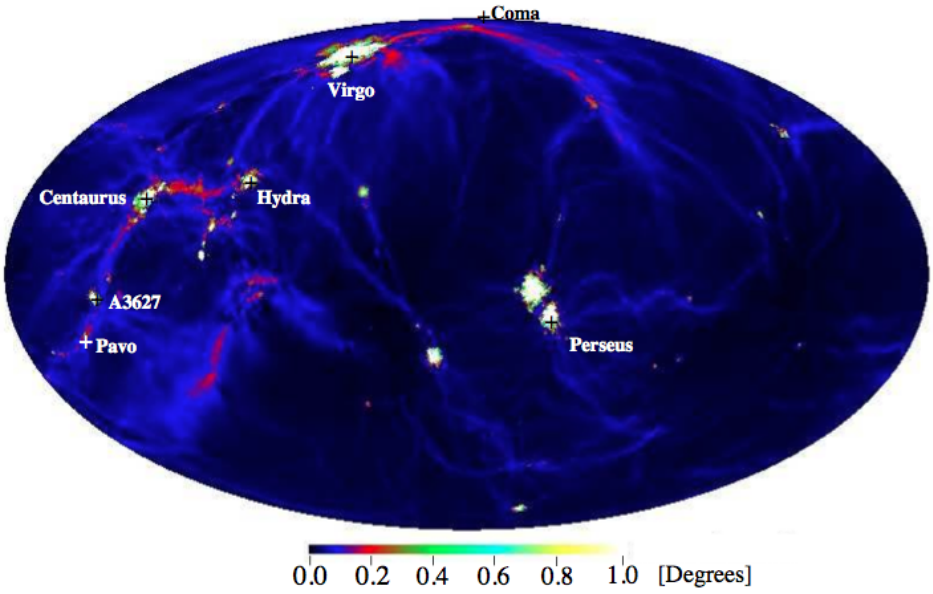

Figure 3.3. Numerical estimate of deflections suffered by 10^{20} eV protons in extragalactic magnetic fields within a 110 Mpc radius from the Galaxy taking into account energy losses from the work of Dolag et al. (2005).

- $r_{\rm Lar} > \lambda$, $t_{\rm scatt} > t_{\rm trav}$: Weak deflection regime.
- $r_{\rm Lar} > \lambda$, $t_{\rm scatt} < t_{\rm trav}$: After $t = t_{\rm scatt}$ the particle enters a diffusive regime.
- $r_{\rm Lar} \ll \lambda$: Diffusive regime.

These regimes are discussed in turn, below.

Weak deflection regime

If the coherence length of individual intervening magnetic fields, λ, is much smaller than $r_{\rm Lar}$, the particle experiences a series of small random deflections, $\delta\theta = \lambda/r_{\rm Lar}$ as it traverses individual magnetised regions, as illustrated in figure 3.4. The accumulated deflection of a particle travelling a distance L through $\sim L/\lambda$ scattering centres in this regime is given by (Waxman & Miralda-Escude 1996):

$$\theta(E,L) \simeq \left(\frac{L}{\lambda}\right)^{1/2} \delta\theta \simeq 0.22^\circ Z \left(\frac{L}{10\ {\rm Mpc}}\right)^{1/2} \left(\frac{E}{10^{20}\ {\rm eV}}\right)^{-1} \left(\frac{\lambda}{0.1\ {\rm Mpc}}\right)^{1/2} \left(\frac{B}{10^{-9}\ {\rm G}}\right). \tag{3.5}$$

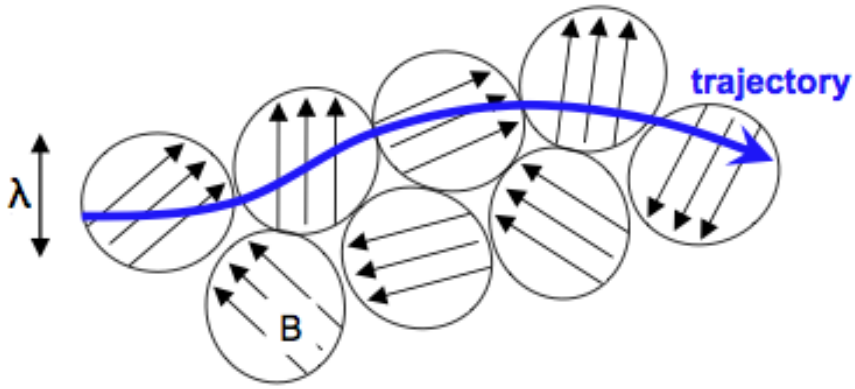

Figure 3.4. Schematic representation of the trajectory of a UHECR through individual magnetised scattering centres in the regime where $\lambda \ll r_{\rm L}$ (see text). The arrows give the direction of the magnetic field vector. Source: Martin Lemoine.

Clearly, the highest energy cosmic rays are in this regime from the upper limits of the strength of extragalactic magnetic fields. As a result of their deflected trajectories, UHECRs are also expected to suffer a time delay with respect to photons, given by (Alcock & Hatchett 1978)

$$\tau \simeq \frac{L}{c}\,\frac{\theta^2}{2} \simeq 230 \text{ years } Z^2 \left(\frac{L}{10 \text{ Mpc}}\right)^2 \left(\frac{\lambda}{0.1 \text{ Mpc}}\right) \left(\frac{E}{10^{20} \text{ eV}}\right)^{-2} \left(\frac{B}{10^{-9} \text{ G}}\right)^2 . \quad (3.6)$$

Therefore, UHECRs are not expected in coincidence with other emission from their sources, making identification of the sources even more difficult, especially if they originate in transient sources or periods of enhanced activity in steady sources.

Diffusive regime

In a situation where $t_{\rm scatt} < t_{\rm trav}$, cosmic-rays enter a diffusive regime. Diffusion is the description of the motion of particles propagating a random walk, whose distance from their source increases as $t^{1/2}$. We can define the critical energy below which particles enter a diffusive regime as

$$E_{\rm crit} = 10^{19} \text{ eV} \left(\frac{L}{1 \text{ Gpc}}\right)^{1/2} \left(\frac{B\sqrt{\lambda}}{1 \text{ nG} \cdot \text{Mpc}^{1/2}}\right), \quad (3.7)$$

which is obtained considering $t_{\rm trav} = t_{\rm scatt} \sim r_{\rm Lar}^2/(\lambda c)$.

The characteristics of diffusion depend on the characteristics of the magnetised medium, and are frequently parametrised by the diffusion coefficient, $D(E)$. During a short time Δt

the particle moves by an amount $\Delta x = u\Delta t + \delta x$, where the first term is due to the bulk motion of the medium with velocity u and δx is due to diffusion. The diffusion coefficient for the medium is proportional to the variance of δx and is given by

$$D(E) = \frac{\langle \delta x^2 \rangle}{2\Delta t}. \tag{3.8}$$

Considering the different regimes in which diffusion may proceed one gets:

- In the case where $r_{\rm Lar} \gg \lambda$, at small distances the particle experiences weak deflections and a diffusive regime is entered after $t_{\rm scatt}$. The diffusion coefficient is given by

$$D = \frac{1}{3}\, t_{\rm scatt} c^2 \simeq \frac{c}{3}\, \frac{r_{\rm Lar}^2}{\lambda}. \tag{3.9}$$

- In the case where $r_{\rm Lar} \ll \lambda$, the diffusion is in the *Kolmogorov* regime and D is given by

$$D = \frac{1}{3}\, c\lambda \left(\frac{r_{\rm Lar}}{\lambda}\right)^{1/3}. \tag{3.10}$$

- In the intermediate regime, where $r_{\rm Lar} \sim \lambda$, the diffusion is in the *Bohm* regime, with D given by

$$D = \frac{1}{3} r_{\rm Lar} c. \tag{3.11}$$

Detailed studies of the evolution of $D(E)$, with energy depending on the properties of the magnetic turbulence of the medium, have been presented in e.g. Casse et al. (2002); Deligny et al. (2004). For a detailed discussion of the transport of UHECRs through inhomogeneous magnetic fields see Kotera & Lemoine (2008b).

3.2 UHECR anisotropies

As a result of the expectation that at the highest energies, cosmic-rays could point back to their sources within a few degrees, if they are lightly charged, the arrival directions of UHECRs have attracted great attention. Since the mid 1990s, when the previous generation of extensive air shower arrays had collected a significant number of events with

$E \geq 10^{19}$ eV, a large number of searches for a correlation of UHECRs with extragalactic sources have been performed. In the work of Stanev et al. (1995), a correlation with the Supergalactic plane was reported, whereas Waxman et al. (1997) studied the correlation of UHECR arrival directions with IRAS 1.2 Jy galaxies. Since then, a large number of authors have searched for a correlation between UHECR arrival directions and galaxy surveys, namely the PSCz (Kashti & Waxman 2008; Berlind et al. 2010; Takami et al. 2009b; Cuoco et al. 2006; Koers & Tinyakov 2009), the 2MRS (Abbasi et al. 2010; Abreu et al. 2010; Abraham et al. 2009) and the SDSS (Takami et al. 2009a). Others have looked for a correlation between observed UHECRs and the positions of specific classes of objects, namely AGN (Abraham et al. 2007, 2008; George et al. 2008; Pe'Er et al. 2009; Watson et al. 2011), BL Lacertae objects (BL Lacs) (Tinyakov & Tkachev 2001; Gorbunov et al. 2004), luminous infrared galaxies (LIRGs) (Berlind et al. 2010) and *Fermi* detected AGN (Jiang et al. 2010; Mirabal & Oya 2010), reporting different degrees of correlation depending on the UHECR sample, statistical approach and source population used.

In Abraham et al. (2007), the cross-correlation of the first 27 UHECRs detected at Auger with energy greater than 5.5×10^{19} eV and the local matter distribution was studied. In particular, a test was set up to establish the fraction of UHECRs that correlate with one of the sources in the 12th VCV AGN catalogue (Véron-Cetty & Véron 2006). An angular scan for the parameters that maximise the correlating fraction of UHECRs with VCV sources was performed with the first 14 detected UHECRs (period 1) and subsequent events were tested against this prescription. Of the 13 UHECRs with energy greater than 5.5×10^{19} eV found subsequently (period 2), 9 correlated with a VCV AGN. The probability of finding such a correlation assuming isotropy is 2×10^{-4}. In Abreu et al. (2010), the arrival directions of two more years of data (bringing the total to 69) were analysed. It was reported that 21 of the 55 UHECRs detected after period 1 correlated with a VCV AGN, bringing the correlating fraction down to $\sim$ 39%, but still above isotropic expectations (21%). Further, in the same work, they cross-correlated the arrival directions of the UHECRs with the positions of 2MRS galaxies and *S*wift-BAT X-ray sources (Tueller et al. 2010). For the values of the free parameters in their models that maximise the likelihood they found that the fraction of isotropic realisations that yield a higher likelihood than the observed UHECRs is 0.004 and 2×10^{-4} for the 2MRS and *S*wift-BAT respectively. The results obtained thus are *a posteriori* and do not constitute a confidence level on anisotropy. The TA collaboration have also searched for anisotropy in

their data and have most recently reported hints of a departure from isotropy (Fukushima et al. 2013), by cross-correlating the arrival directions of UHECRs observed at TA with galaxies in the yet unpublished 2MASS-XSCz catalogue.

The nearby radio galaxy Cen A ($z \sim 0.001$) has long been proposed as a possible UHECR source (Cavallo 1978; Romero et al. 1996; Anchordoqui et al. 2001). In Abreu et al. (2010) hints of an excess in the direction of Cen A, were reported. The evolution of the significance of this excess is being monitored by the Auger Collaboration. As noted however in e.g. Waxman (2011); Kotera & Olinto (2011) Cen A lies in front of the largest overdensity of matter in the local universe (the Hydra-Centaurus supercluster at $z \sim 0.0128$), hence if an excess of events in that direction is confirmed, it does not mean that Cen A is the source.

At energies below the GZK threshold, it is thought that the deflections of UHECRs become too large for a correlation with the parent population to be established. The only exception to this expectation is the case of neutral particles. As seen in section 2.2.4, neutrons with energy $E \sim 10^{18}$, can travel approximately ~ 10 kpc before they decay. Hence, if neutrons can be accelerated to such high energies in Galactic sources, they could reach the Earth while pointing back to their sources. The shower produced in the Earth's atmosphere by neutrons is indistinguishable from that of protons, however, neutrons from Galactic sources with $E \sim 10^{18}$ should appear as a localised excess in the UHECR arrival direction map, in the direction of their source. No statistically significant excess of events in any small solid angle, that would be indicative of a flux of neutral particles from a discrete source, has been found. This result constrains scenarios for the production of ultra-high energy cosmic rays in the Galaxy (Rouille d'Orfeuil 2011; Abreu et al. 2012a; Salesa Greus 2013). UHE photons are also expected to correlate with their sources, that are expected to lie at very short distances ($d \sim$ few Mpc). Due to the high opacity of the universe to photons, that was discussed in section 2.3.2, they would be a powerful tracer of nearby extragalactic sources (see e.g. the work of Taylor et al. 2009). Directional searches for point sources of UHE photons at Auger as well as composition observables have yielded null results so far (Settimo 2011; Kuempel 2013) and place strong constraints on the fraction of primary UHE photons, f, at the highest energies ($f \lesssim 1\%$, 10% above 10^{18} eV, 10^{19} eV respectively).

At energies around $\sim 10^{18}$ eV, charged cosmic rays are not expected to correlate with their sources due to severe deflections and/or diffusive motion inside the galaxy. The

distribution of the arrival directions at this energy is expected to exhibit a large scale anisotropy related to the motion of the local cosmic ray rest frame around the Galactic centre relative to the solar system. This large scale motion is expected to induce a dipole anisotropy in the cosmic ray spectrum, with characteristics that might help constrain the Galactic-extragalactic transition energy and models of the Galactic magnetic field (see e.g. Giacinti et al. 2012). Searches conducted so far have resulted in interesting hints about such an anisotropy (see e.g. Abreu et al. 2012a for recent results), whereas the first full sky harmonic analysis of cosmic ray arrival directions with data from the Auger and TA experiments is underway (Abu-Zayyad et al. 2013b).

Chapter 4

Search for correlation of UHECRs with the local galaxy distribution

In this chapter, the arrival directions of the 69 UHECRs that were observed by the Auger Observatory with energies exceeding 55 EeV until the end of 2009 are studied. I investigate whether the Auger UHECRs exhibit the anisotropy signal expected if the primary particles are protons that originate in galaxies in the local universe, or in sources correlated with these galaxies, by cross-correlating the UHECR arrival directions with the positions of IRAS-PSCz and 2MASS-6dF galaxies taking into account UHECR energy losses and deflections during propagation.

4.1 Introduction

As a result of the GZK process UHECRs that arrive on Earth with energy exceeding 50 EeV must originate in sources within a few hundred Mpc. If UHECRs are protons and intervening magnetic fields are not too strong, observed UHECRs must point back to their sources within a few degrees. Further, if UHECRs originate in some astrophysical population, their arrival direction distribution should be correlated with that population as well as with the distribution of large scale structure (LSS) in the local universe, since matter in the universe is clustered. Heavier UHECR nuclei with energy around 50 EeV would have their arrival directions smeared by intervening magnetic fields.

In section 1.4 we saw that the primary composition of UHECRs is at present uncertain. Beyond the GZK threshold the composition is very poorly understood due to the small number of observed events. Auger composition measurements are consistent with a transition from a proton-like to a heavier mixed composition between $1 - 20$ EeV. The smaller HiRes and TA datasets agree with a proton-like composition up to the highest energies (Sokolsky et al. 2010; Jui 2012). Given the considerable experimental difficulties intrinsic to the measurement of composition observables the issue is far from settled (see also discussion in section 1.4).

In this work, the question of the origin of the highest energy cosmic rays is revisited, following the release of the arrival directions of the 69 UHECRs with energy above 55 EeV detected until December 2009 at Auger (Abreu et al. 2010). The local UHECR source distribution is modelled using galaxy catalogues of the nearby universe, namely the six degree Field Galaxy Survey (6dF), which is being used in this work for the first time to derive the expected UHECR source distribution and is an order of magnitude larger than other spectroscopic wide field galaxy surveys and the IRAS Point Source Catalogue of redshifts (PSCz), which is being used here for the first time to analyse the updated dataset of 69 UHECRs. A flat universe with $\Omega_M = 0.25$, $\Omega_\Lambda = 0.75$ and $H_o = 70$ km s^{-1} Mpc^{-1} is assumed throughout.

4.2 Galaxy surveys

Galaxy redshift surveys map large volumes of the universe, identifying the locations of galaxies which are point tracers of the overall matter distribution. One can divide galaxy surveys into two basic categories: photometric, that obtain a two-dimensional map of the galaxy distribution over a large area of the sky and spectroscopic, which obtain an accurate redshift of the objects studied at the cost of being more time consuming. Recently, a hybrid approach has become popular, that of obtaining galaxy redshifts through photometric information from multiple wavelength bands of a photometric survey. This provides a rough but quick measure of galaxy redshifts.

Galaxy surveys can be further classified into wide-field or deep-field. Surveys of the former category observe a large area of the sky but only extend to modest redshifts, whereas in the latter category surveys observe only a small patch of the sky for an extended period of time with the aim to observe out to very large redshifts. Galaxy surveys of

the former type are appropriate for the study here, in which two of the largest existing spectroscopic wide area surveys have been used.

6 degree Field Galaxy Survey

The 6dF is a spectroscopic, redshift and peculiar velocity survey of 2MASS, near-infrared selected galaxies. The survey was carried out using the Six-Degree Field instrument on the Schmidt Telescope of the Anglo-Australian Observatory (Jones et al. 2009). It covers the entire Southern Sky (excluding the Galactic plane) and has resulted in a catalogue of 125,071 galaxies and 110,256 associated redshifts. The 6dF has median redshift $\overline{z} = 0.053$ which corresponds to a comoving distance of 225 Mpc in the cosmological model assumed. The 6dF field of view covers 80% of the Auger field of view by area. Taking into account the total declination dependent Auger acceptance (equation 4.1), which is smaller for positive declinations, it covers 86% of the instantaneous Auger exposure. The 6dF is near-infrared selected, which means it is dominated by elliptical galaxies. Here, the K-selected sample of the 6dF survey is used. That is, the magnitude limited portion of the 6dF survey that is complete down to a near-infrared K-magnitude $K \leq 12.65$. This, K-selected sample, constitutes the dominant portion of the 6dF survey (83,995 redshifts).

IRAS Point Source Catalogue of redshifts

The PSCz is a spectroscopic redshift catalogue of far-infrared selected galaxies detected by the Infrared Astronomical Satellite (IRAS). The PSCz covers approximately 84% of the sky (Saunders et al. 2000). It contains 14,677 galaxies with associated redshifts, and median redshift ($\overline{z} = 0.028$) which corresponds to a comoving distance of $\sim$ 119 Mpc. Since the galaxies in the PSCz are far-infrared selected there is a preference for young, star-forming galaxies in the catalogue.

Two complementary galaxy surveys have been chosen, to derive the expected UHECR source distribution. The PSCz is a shallow nearly full-sky galaxy survey and its use facilitates comparison with results of previous studies. The 6dF on the other hand is a much larger survey ($\sim$ 20 times more galaxies than the PSCz in the southern hemisphere). The different median depths of the 2 surveys mean that they highlight different structures of the nearby universe, for example the Shapley Concentration, centred at ($l \sim -50°, b \sim 30°$) at a distance $\sim$ 200 Mpc is prominent in the 6dF. There is nonetheless a significant overlap between the two surveys. As galaxy populations dominating the two surveys differ,

their clustering properties also differ.

4.3 Auger exposure

The geometrical acceptance of Auger is uniform in right ascension as a result of full time operation. Auger is fully efficient for zenith distance up to $\theta_m = 60°$. The Auger acceptance as a function of declination is given by (Sommers 2001)

$$\omega(\delta) \propto \cos(a_0)\cos(\delta)\sin(\alpha_m) + \alpha_m \sin(a_0)\sin(\delta), \tag{4.1}$$

where δ is the declination and a_0 is the latitude of Auger which is $-35.2°$. Here, α_m is given by

$$\alpha_m = \begin{cases} 0 & \text{if } \xi > 1 \\ \pi & \text{if } \xi < -1 \\ \cos^{-1}(\xi) & \text{otherwise} \end{cases}$$

and

$$\xi \equiv \frac{\cos(\theta_m) - \sin(a_0)\sin(\delta)}{\cos(a_0)\cos(\delta)}.$$

The acceptance of Auger is illustrated in figure 4.1. The actual instantaneous exposure of the observatory varies according to the number of detectors active and atmospheric conditions which are closely monitored (see e.g., Abreu et al. 2011 for details). For the present study, detector downtime has a negligible effect when averaged over the years of observation over which the data were collected and is not considered.

4.4 Model of UHECR source distribution

The 6dF and PSCz are used to model a UHECR source population which is steady and follows the distribution of local galaxies. For simplicity, it is assumed that all UHECR sources are intrinsically identical. Although this is probably an unrealistic assumption, relaxing it would introduce more free parameters in the model, on which there are no constraints at the moment, neither observationally nor theoretically. One could for example use a luminosity function, in which case the expected anisotropy predicted by the matter-tracing model would increase, but there is no firm reason to assume that the infrared luminosity of galaxies in the PSCz and 6dF is a tracer of UHECR production.

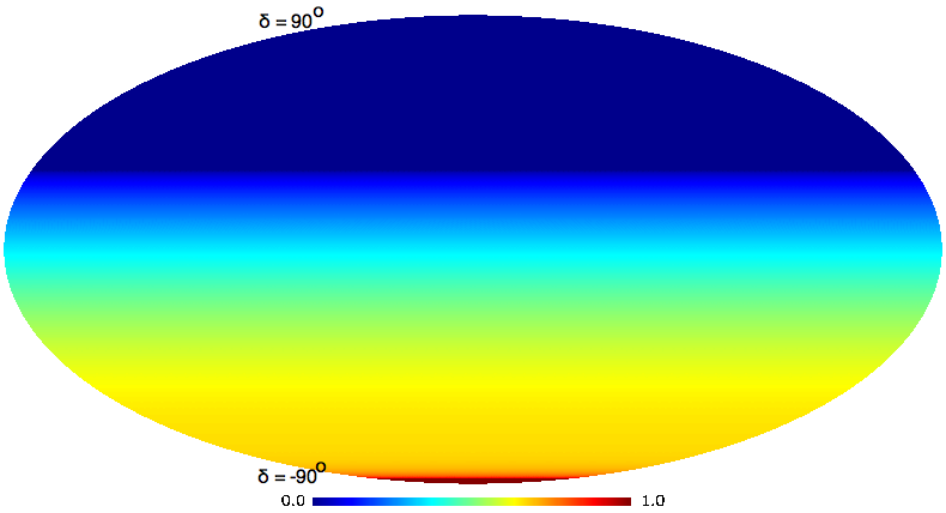

Figure 4.1. The geometrical acceptance of Auger in equatorial coordinates, given by equation4.1.

4.4.1 Source density

The number density of UHECR sources is not known a priori. Given the very high luminosity requirements it is possible that the observed UHECR flux is dominated by a few "bright" sources (such as in models in which the nearby radiogalaxy Cen A is responsible for much of the observed UHECR flux). The number of "repeaters", i.e. groups of UHECRs with arrival directions separated by less than a few degrees that may be associated with a single source, can constrain the number density of sources of UHECRs if a scale is assumed for the deflections of observed UHECRs, as shown analytically in the work of Waxman et al. (1997); Dubovsky et al. (2000); Fodor & Katz (2001) and numerically in e.g., Cuoco et al. (2009); Decerprit et al. (2012).

For an estimate of the UHECR source density, a search for repeaters, separated by less than 3° in the Auger data has been performed. The chosen, $\leq 3°$ separation radius, is intended to reflect the uncertainty associated with instrumental resolution ($\sim 1°$) and possible magnetic deflections of a few degrees, among the 69 Auger events. Four pairs of events were found in the dataset. Following Dubovsky et al. (2000), the number of clusters of multiplicity m, expected to be observed if there are S UHECR sources, within

a horizon of radius r, producing UHECRs at an apparent average rate $\bar{n}$, is expressed as

$$\bar{N}_m = S\frac{\bar{n}^m}{m!}e^{-\bar{n}}. \tag{4.2}$$

This implies that the total number of expected events is $\sum_m m\bar{N}_m$. One can use the observed number of clusters in the data to get an estimate of S, using equation 4.2. From equation 4.2, the number of singlets in the data is $\bar{N}_1 \sim S\bar{n}$, the number of doublets is $\bar{N}_2 \sim S\bar{n}^2/2$ and so on. Rearranging the expressions for $\bar{N}_1$, $\bar{N}_2$, one gets $S \sim \bar{N}_1^2/(2\bar{N}_2)$. The four doublets present in the set of 69 Auger events, give $S \sim 61^2/(2\cdot 8) \sim 200$ UHECR sources in the whole sky for the presently observed clustering. Using $r = 100$ Mpc for 60 EeV UHECRs, the minimum source density consistent with the observed clustering in the present dataset is

$$\frac{200 \text{ sources}}{\frac{4\pi}{3}\cdot(100 \text{ Mpc})^3} \gtrsim 10^{-5} \text{ Mpc}^{-3}. \tag{4.3}$$

If the observed number of pairs arises by chance, which is found to be the case 22% of the time in Monte Carlo simulations of 69 UHECRs from an isotropic source distribution, the source density could be much larger than this. Further, as shown in Dubovsky et al. (2000) the case of equal flux sources, which is assumed here, corresponds to the absolute minimum source density. If however, deflections are larger than assumed here, the UHECR source density could be lower than the derived bound. Further, it has been assumed for this estimate that the UHECR sources are steady. If the sources are transient instead, the true number density, $\bar{\rho}_0$, should be related to $\bar{n}_0$ by $\bar{\rho}_0 = \bar{n}_0/\delta t$, where δt is the UHECR arrival time spread due to magnetic fields (Murase & Takami 2009).

After the work presented in this chapter was completed and published the Auger Collaboration performed a numerical analysis in the same spirit with their most recent, larger dataset, scanning the whole parameter space (Abreu et al. 2013). The lower bound on the source density that they find agrees well with the estimate presented here. For comparison the number density of bright galaxies in the local universe is $\sim \overline{n}_0 = 10^{-2}$ Mpc^{-3}, that of AGN is $\sim \overline{n}_{\rm AGN} = 5\times 10^{-4}$ Mpc^{-3} and that of GRBs is $\sim \overline{n}_{\rm GRB} = 10^{-5}$ Mpc^{-3}. Rarer objects, such as BL Lacs with $\sim \overline{n}_{\rm BLLac} = 10^{-6}$ Mpc^{-3} and galaxy clusters with $\sim \overline{n}_{cluster} = 10^{-7}$ Mpc^{-3} are disfavoured by the derived bounds on the source density.

In the present model of the local UHECR source distribution, individual sources are faint i.e. each source produces one or no events and the probability of a single source

producing multiple events is low, which is well motivated in the light of the discussion above. The number density of UHECR sources is assumed to be comparable to that of bright galaxies, compatible with constraints from observed clustering. In section 4.7 the sensitivity of the results presented in this chapter to this choice for the UHECR number density is discussed.

4.4.2 UHECR energy losses during propagation

Each galaxy in the model source distribution is assigned a weight, proportional to the expected UHECR flux from that source, which depends on the energy with which protons are emitted and the flux suppression with distance. The flux weight for a galaxy at luminosity distance, $r_{\rm L}$, that emits a cosmic ray proton with initial energy $E_{\rm i}$ which reaches the Earth with energy equal to or greater than $E_{\rm f}$, is given by

$$\omega(r_{\rm L})_{\rm flux} = \frac{1}{{r_{\rm L}}^2} \int_{E'_{\rm f}}^{E_{\rm i,max}} {\rm d}E_{\rm i} \int_{E'_{\rm f}}^{E_{\rm i}} {\rm d}E_{\rm f}\ \rho_p(r_{\rm L}, E_{\rm i}; E_{\rm f})\ I(E_{\rm i}), \tag{4.4}$$

where

$$\rho_p(r_{\rm L}, E_{\rm i}; E_{\rm f}) = \left| \frac{\partial P_p(r_{\rm L}, E_{\rm i}; E_{\rm f})}{\partial E_{\rm f}} \right|, \tag{4.5}$$

is the derivative of the function $P_p(r_{\rm L}, E_{\rm i}; E_{\rm f})$ which gives the probability of a proton arriving with energy above $E_{\rm f}$ if it was emitted with energy $E_{\rm i}$ by a source at distance r_L, introduced in Bahcall & Waxman (2000). For $E'_{\rm f}$, the final energy of the 69 Auger UHECRs, the lowest measured energy (55 EeV) present in the Auger dataset is conservatively adopted. The value of $E_{\rm i,max}$, which is the maximum energy **injected** through astrophysical processes, is set to 10^{21} eV. The value of $E_{\rm i,max}$ is not fully constrained by observations, but cannot be much lower than $\sim 10^{21}$ eV, given the recent observations of UHECRs with **observed** energy $\sim 10^{20.5}$ eV and the lack of (identified) local UHECR sources. It was checked that the results of this chapter are insensitive to varying $E_{\rm i,max}$ within its anticipated range of values, as expected, since UHECRs in this energy range promptly interact with background photons. The intrinsic spectrum of UHECRs produced by UHECR sources is not yet known. The observed cosmic ray spectrum is well fit by a number of models (see for example Kotera et al. 2010). Here, a power law spectrum

$$I(E_{\rm i}) = I_0\ E_{\rm i}^{\alpha}\ e^{-E_{\rm i}/E_{\rm i,max}} \tag{4.6}$$

with index $\alpha = -2.0$ is considered. An intrinsic power-law spectrum with $\alpha \approx -2.0$ is consistent with that expected in most models of shock acceleration, which is the most frequently expected acceleration mechanism in leading extragalactic cosmic ray candidates, such as AGN jets, hotspots and GRBs (see e.g., 1.3). Further, an intrinsic power law spectrum with $\alpha \approx -2.0$ is in agreement with the observed UHECR spectrum after accounting for propagation effects (e.g., Bahcall & Waxman 2003; Katz et al. 2009). The sensitivity of the results to the choice of α is discussed in section 4.6.4. The normalisation factor, I_0, is chosen so that

$$I_0 \int_{E_\mathrm{f}}^{E_\mathrm{i,max}} \mathrm{d}E_\mathrm{i}\ E_\mathrm{i}^{\alpha}\ e^{-E_\mathrm{i}/E_\mathrm{i,max}} = 1. \tag{4.7}$$

For the simulation of the proton propagation and energy losses the $P_p(r_\mathrm{L}, E_\mathrm{i}; E_\mathrm{f})$ function which was numerically calculated by Fodor & Katz (2001); Fodor et al. (2003) is used[1]. In figure 4.2, $P_p(r_\mathrm{L}, E_\mathrm{i}; E_\mathrm{f})$ for UHECRs with $E_\mathrm{i} = 200$ EeV and $E_\mathrm{f} \geq 40, 60, 80, 100$ EeV is shown.

4.4.3 Galaxy survey completeness

To correct for the absence of the fainter galaxies in the galaxy catalogues due to the flux limit of the survey the survey's selection function, defined as the expected number density of galaxies in the survey as a function of distance, in the absence of clustering is needed. One can model the selection function using a fit to the survey's redshift distribution, often parametrised as:

$$\mathrm{d}N(z) = Az^{\beta} \exp\left[-\left(\frac{z}{z_\mathrm{p}}\right)^{\gamma}\right] \mathrm{d}z, \tag{4.8}$$

with $N(z)$ the observed number of galaxies at redshift z. The parameter A gives the normalisation, z_p the peak of the distribution and β, γ are constants that control the slope. The overall selection function $\psi(r_c)$ is the redshift distribution divided by the volume element

$$\psi(r_c) = \frac{1}{\Omega_s r_c^2} \left(\frac{\mathrm{d}N}{\mathrm{d}z}\right)_{r_c} \left(\frac{\mathrm{d}z}{\mathrm{d}r_c}\right)_{r_c}, \tag{4.9}$$

[1] available online at `http://www.desy.de/~uhecr/P_proton`

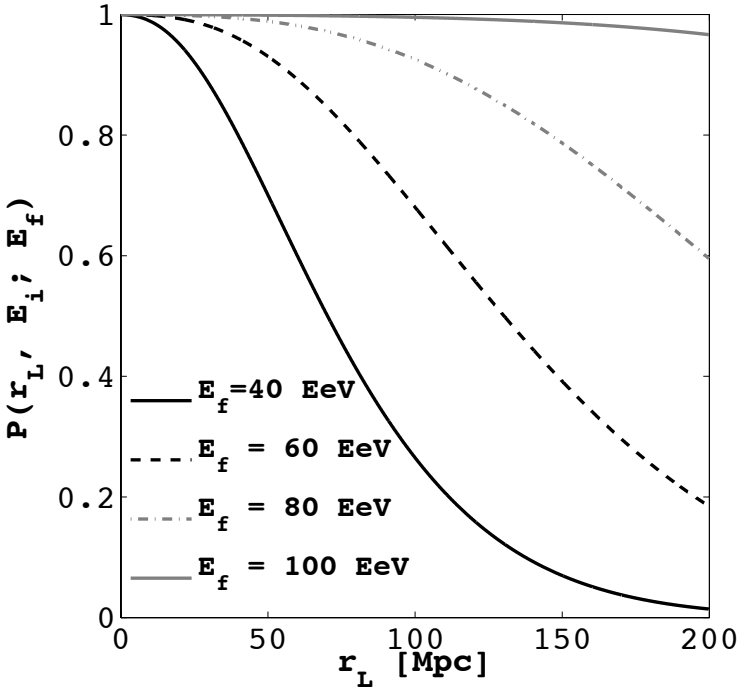

Figure 4.2. The function $P_p(r_{\rm L}, E_{\rm i}; E_{\rm f})$, which represents the probability that a UHECR emitted by a source at luminosity distance $r_{\rm L}$, with initial energy $E_{\rm i}$, will be observed with final energy above $E_{\rm f}$, here shown as a function of propagation distance for $E_{\rm i} = 200$ EeV and $E_{\rm f} \geq 40, 60, 80, 100$ EeV.

where Ω_s is the solid angle of the survey and r_c the comoving distance, as discussed in e.g., Erdoğdu et al. (2006). The PSCz selection function is given by (Saunders et al. 2000)

$$\psi(r_c) = \psi_* \left(\frac{r}{r_*}\right)^{(1-\alpha)} \left[1 + \left(\frac{r}{r_*}\right)^{\gamma}\right]^{-\left(\frac{\beta}{\gamma}\right)}, \tag{4.10}$$

where $\psi_* = 0.0077$ is the normalisation, $\alpha = 1.82$ is the nearby slope, $r_* = 86.4\ h^{-1}$ Mpc is the break distance, $\gamma = 1.56$ its sharpness and $\beta = 4.43$ the additional slope beyond it. The quoted uncertainty in the PSCz selection function is $\lesssim 10\%$ for distances $30-200\ h^{-1}$ Mpc and $\simeq 10\%$ for $10 - 300\ h^{-1}$ Mpc. Figure 4.3 shows the PSCz selection function as a function of comoving distance. ocal group galaxies, such as M31, are included in the catalogue.

The redshift distribution of the $K-$selected 6dF sample is well fit by the expression

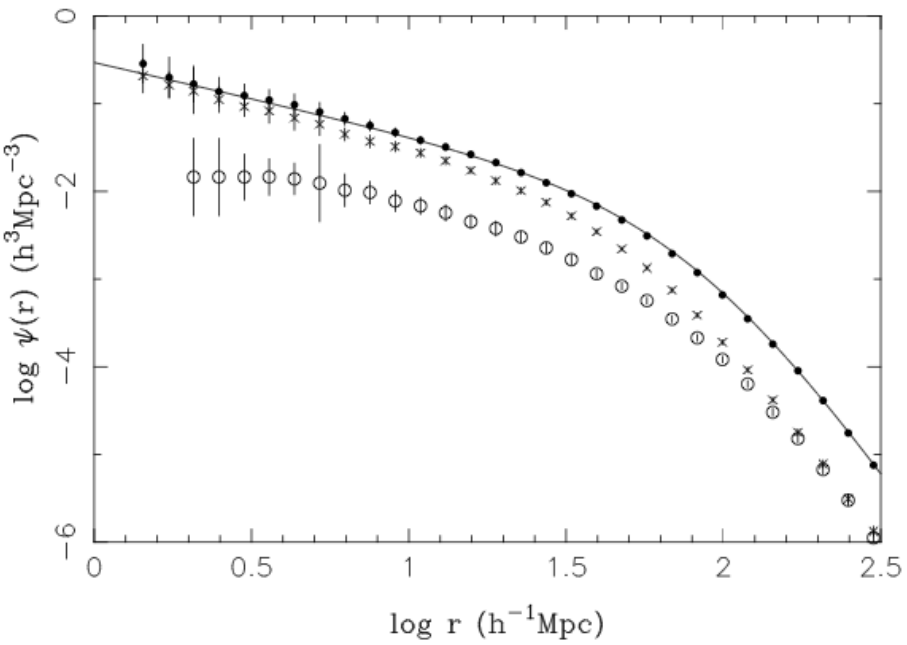

Figure 4.3. Parametric (solid line) and non-parametric selection function with associated error-bars (filled circles) for the PSCz survey. The non-parametric selection functions for the QDOT (open circles) and 1.2Jy (crosses) galaxy surveys are also shown. Figure from Saunders et al. (2000).

(Jones et al. 2009)

$$N_{\rm fit}(z) = Az^{\gamma} \exp\left[-(z/z_{\rm p})^{\gamma}\right], \tag{4.11}$$

where $\gamma = 1.6154 \pm 0.0001$, $z_{\rm p} = 0.0446 \pm 0.0001$, and $A = 622978 \pm 10$. The redshift distributions and corresponding fits for the parametric selection function of the two surveys are shown in figure 4.4. The selection function is normalised to the value it takes at some small distance $r_{\rm min}$ below which we believe the survey includes all existing galaxies. The value of $r_{\rm min}$ is not very well constrained by observations. The minimum redshift found in each survey ≈ 1 Mpc, is chosen as the default $r_{\rm min}$, but in section 4.6.4 the sensitivity of the results to the choice of $r_{\rm min}$ is studied.

Each galaxy, is weighted by the inverse of $\psi(r_c)$, so that the effective contribution of each survey galaxy to the model source distribution is

$$\omega_{\rm gal} = \frac{\omega(r_{\rm L})_{flux}}{\psi(r_c)}. \tag{4.12}$$

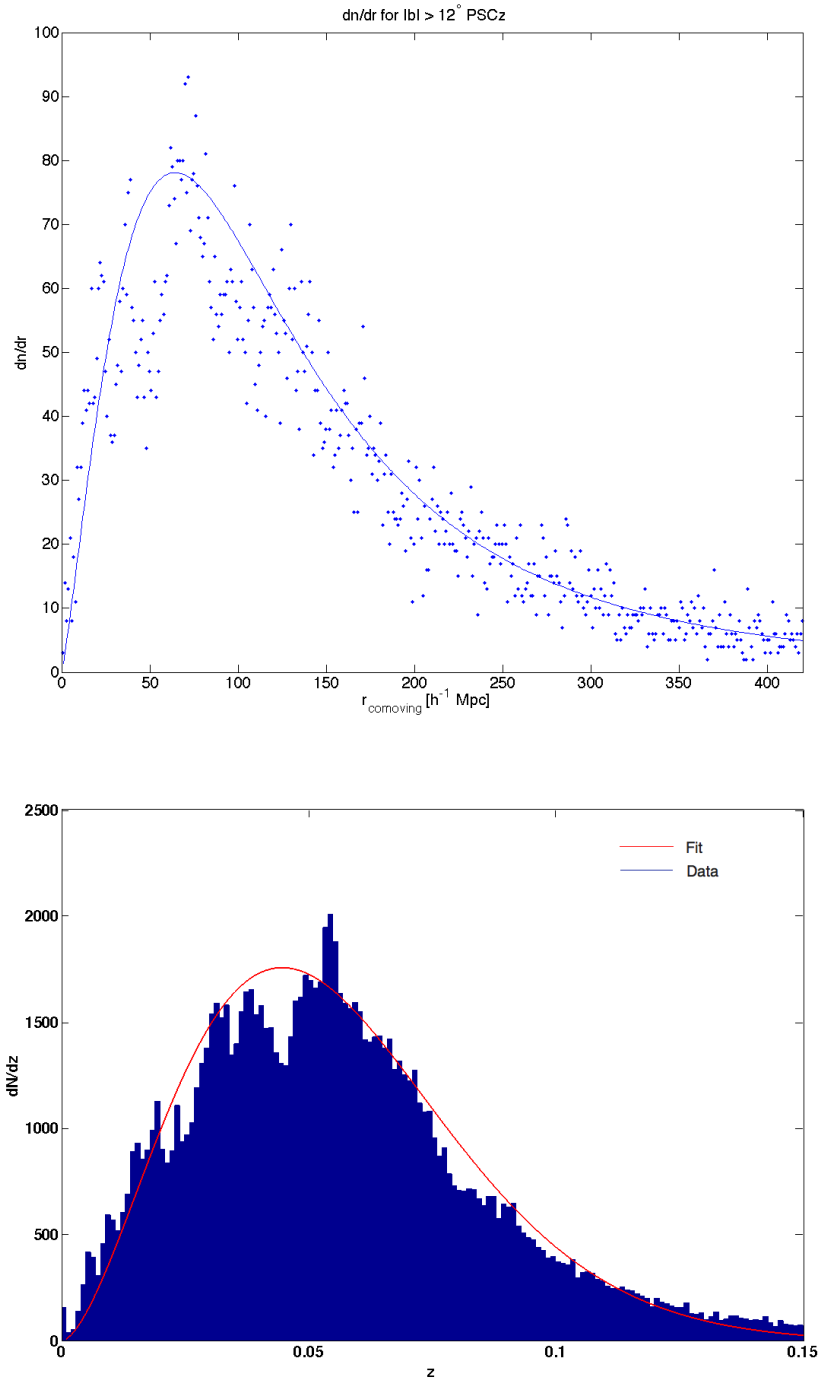

Figure 4.4. Redshift distribution of galaxies in the PSCz (top) and the 6dF survey (bottom). The fits give the prediction from the selection function.

4.4.4 Galaxy peculiar velocities

The observed recession velocity cz is not only due to the Hubble flow. Other motions, such as bulk flows of large structures or velocities within such structures, may not be negligible.

Galaxy redshift surveys measure recession velocities, not distances, and peculiar velocities along the line-of-sight affect our estimates of actual distances, in particular nearby, where the peculiar velocity might be a large fraction of the observed recession velocity. The observed recession velocity is given by

$$cz = H_0 r + (\mathbf{v}(\mathbf{r}) - \mathbf{v}(\mathbf{0})) \cdot \hat{\mathbf{r}}, \tag{4.13}$$

where $\mathbf{v}(\mathbf{r})$ is the object's peculiar velocity and $\mathbf{v}(\mathbf{0})$ is the observer's peculiar velocity. Working in a reference frame where $\boldsymbol{\Delta}\mathbf{v} = \mathbf{v}(\mathbf{r}) - \mathbf{v}(\mathbf{0})$ is small allow a more accurate estimate of the object's distance. In the local universe, out to $cz \sim 3000$ kms^{-1}, where galaxies share the motions of the Local Group it is best to convert to the Local Group rest frame. Further away galaxy peculiar velocities are independent of the Local Group velocity and $\boldsymbol{\Delta}\mathbf{v}$ is smaller in the CMB rest frame. In this work, the focus is on the distribution of matter nearby, hence it is most useful to work with Local Group frame redshifts, therefore all recession velocities are converted to the Local Group frame in this analysis.

The Sun moves with a velocity of 306 ± 18 km s^{-1}, relative to the Galactic centroid towards ($l = 99^\circ \pm 5^\circ$, $b = -4^\circ \pm 4^\circ$) as derived by Courteau & van den Bergh (1999). To convert between $cz_{\rm Hel}$, that is the recession velocity of a given object measured in the heliocentric frame (often given by the galaxy catalogues), and $cz_{\rm LG}$, the recession velocity in the Local Group frame, the relation (Courteau & van den Bergh 1999)

$$cz_{\rm LG} = cz_{\rm Hel} - 79\cos(l)\cos(b) + 296\sin(l)\cos(b) - 36\sin(b) \tag{4.14}$$

is used. Here l and b are the Galactic longitude and latitude of the object respectively.

4.4.5 Magnetic fields

In section 3.1 we saw that the strength and distribution of extragalactic magnetic fields are poorly known. Dense large scale structures, such as galaxy clusters and galaxy filaments, have been observed to support relatively strong magnetic fields, whereas in between structures magnetic fields are probably negligible. Although numerical analyses do not agree as to the filling factor of magnetic fields as we saw in figure 3.2, most of these studies agree that deflections of proton UHECRs of energy E $\geq$ 40 EeV do not exceed 3° over

99% of the sky for propagation distance $\sim$ 100 Mpc. Magnetic deflections suffered by heavier UHECR nuclei are expected to be much larger and can completely wash out the directional correlation of UHECRs with their sources (see e.g., the model of Aloisio et al. 2009).

The composition of the UHECR sample we are considering here is at present uncertain. If an anisotropy signal, produced by heavy nuclei of charge Z above an energy $E_{\rm thr}$, is observed as reported in Abraham et al. (2007), one should observe an even stronger anisotropy at energies $> E_{\rm thr}/Z$ due to the proton component that is expected to be associated with the sources of the heavy nuclei (Lemoine & Waxman 2009). Such an anisotropy at $E_{\rm thr}/Z$ is not observed for $6 < Z < 26$, for $E_{\rm thr} = 55$ EeV, in the Auger data (Abreu et al. 2011a). This is one of the arguments against the composition becoming heavy at the highest energies according to Lemoine & Waxman (2009). On the other hand, this absence of significant anisotropy at E_{thr}/Z has been interpreted by the Auger collaboration as an absence of light nuclei at $E_{\rm thr}/Z$ (Abreu et al. 2011a).

In this analysis, it is assumed that UHECRs are protons. In order to bracket possible proton UHECR magnetic deflections, the analysis is performed by averaging over angular bins in the range $3.9^\circ - 7.3^\circ$ (see details of the binning method in section 4.5). The Galactic plane is excluded from the analysis, $|b| \geq 12^\circ$, following the prescription in Jones et al. (2009), since observations in this region are strongly contaminated by Galactic emission.

4.5 Statistical approach

To detect any existing anisotropy signal the sky is divided into equal area bins. For the statistical analysis, the counts-in-cells statistic X, proposed in Kashti & Waxman (2008), which characterises the correlation between the predicted and observed UHECR arrival direction distribution, is considered. In Kashti & Waxman (2008) X was shown to be more sensitive to the expected anisotropy signal than the angular power spectrum (e.g., Sommers 2001; Tegmark et al. 1996) and the two point correlation function (Kachelrieß & Semikoz 2006), which are other statistical measures commonly used in clustering analyses.

Let $\omega_{\rm Auger,i}$ be the exposure of Auger in bin i (equation 4.1) and $\omega_{\rm survey,i}$ the weight

imposed by the survey mask (given by Jones et al. 2009; Saunders et al. 2000)

$$\omega_{\mathrm{6dF,i}} = \begin{cases} 1 & \text{for } |b| > 12^\circ \text{ and } \delta \leq 0^\circ \\ 0 & \text{otherwise} \end{cases}$$

$$\omega_{\mathrm{PSCz,i}} = \begin{cases} 1 & \text{for } |b| > 12^\circ \\ 0 & \text{otherwise.} \end{cases}$$

Here $\{i\}$ is the set of angular bins in the mask defined region. Each angular bin, is assigned the value of $\omega_{\mathrm{Auger}}(\delta)$ at the centre of that bin and ω_{Auger} is treated as a constant within each bin. For the survey mask ω_{survey}, every bin that overlaps with the region excluded by the survey mask (even if it partly overlaps) is excluded.

To account for the combined effects of the survey mask and Auger exposure in bin i, $\omega_{\mathrm{exposure,i}}$ is defined

$$\omega_{\mathrm{exposure,i}} = \omega_{\mathrm{Auger,i}} \cdot \omega_{\mathrm{survey,i}}. \tag{4.15}$$

It is required that each of the quantities in the analysis are (a) weighted exactly once by the combined weight and (b) normalised so that each has a sum equal to the weighted sum of observed UHECRs in the mask defined region.

The number of survey galaxies visible by Auger is limited by the observatory's declination dependent exposure (equation 4.1). To account for this effect, as well as to exclude those survey galaxies that lie near the Galactic plane where observations are not reliable, each survey galaxy in bin i is subjected to the combined weight,

$$N_{\mathrm{gal,i}} = \omega_{\mathrm{exposure,i}} \cdot \sum_j \omega_{\mathrm{gal,j}}, \tag{4.16}$$

where the sum is over the weighted contribution to the flux of each survey galaxy j (equation 4.12) in bin i. Note that the Auger exposure $\omega_{\mathrm{exposure,i}}$ is treated as a constant within a given angular bin and hence remains outside the sum. In the model where UHECR sources are correlated with galaxies in the nearby LSS, the expected number of cosmic rays $N_{\mathrm{M,i}}$ is simply $N_{\mathrm{gal,i}}$ normalised to the number of observed UHECRs according

to condition (b)

$$N_{\mathrm{M,i}} = \frac{\sum_i N_{\mathrm{CR,i}}}{\sum_i N_{\mathrm{gal,i}}} \cdot N_{\mathrm{gal,i}}. \tag{4.17}$$

The number of UHECRs in bin i is written $N_{\mathrm{CR,i}}$ and the number of UHECRs expected to be detected in bin i in an isotropic model $N_{\mathrm{iso,i}}$.

Mock realisations of UHECRs drawn from an isotropic distribution are generated and cross-correlated with the predicted source distribution based on the PSCz/6dF to model the distribution of values that the statistic X takes in the case of an isotropic source distribution. Similarly mock realisations of UHECRs correlated with PSCz/6dF galaxies are generated by sampling from a Poisson distribution with a mean equal to the number of UHECRs expected to be detected per unit area at Auger above energy E_{f} using the model of the UHECR source distribution presented in section 4.4. Finally the value of X for the observed Auger UHECRs is calculated, and compared to the distribution of X obtained in two models of source distribution considered. The statistic X is defined as

$$X = \sum_i \frac{(N_{\mathrm{CR,i}} - N_{\mathrm{iso,i}}) \cdot (N_{\mathrm{M,i}} - N_{\mathrm{iso,i}})}{N_{\mathrm{iso,i}}}. \tag{4.18}$$

4.6 Results

The analysis is performed, by dividing the sky in equal area bins (counts-in-cells), using the HEALPix package (Górski et al. 2005). The disadvantages of the counts-in-cells scheme are the effect of boundaries and the ability to arbitrarily choose the bin size. Both these limitations are dealt with by treating the size of the equal area bins as a free parameter, in a range that covers expected random proton UHECR magnetic deflections (section 4.6.1). In section 4.6.2 the Auger UHECRs are cross-correlated with shells of the expected source distribution, which is achieved by dividing the galaxy distribution into redshift shells of equal predicted UHECR flux. In section 4.6.3 the sensitivity of the results to the magnitude of magnetic deflections is investigated. Since the Galactic plane and regions of the sky not covered by the galaxy survey are always excluded from the analysis, the number of observed UHECRs that remain in the mask defined region is never 69 and depends on the survey used and the bin size considered. In section 4.6.4 the dependence of the results on systematic uncertainties is investigated.

4.6.1 Cross-correlation of UHECRs and nearby LSS

In figure 4.5, the predicted distribution of sources of 55 EeV UHECRs based on the PSCz/6dF catalogues is shown. To aid with illustration, the model source distribution is smeared with a 2 dimensional Gaussian filter with standard deviation $\sigma = 7.2°$, whereas throughout the rest of this work galaxies are treated as discrete point sources. In the map of the PSCz shown in figure 4.6 one can see a very large contribution from the Virgo cluster ($l \sim -80°, b \sim 75°$), Hydra-Centaurus ($-60° \leq l \leq 0°, 0° \leq b \leq 45°$) and the Perseus-Pisces supercluster ($l \sim 140°, b \sim -25°$). In the map of the 6dF of figure 4.5 there is a large excess as a result of flux from Hydra-Centaurus and the Shapley Concentration (centred at $l \sim -50°, b \sim 30°$, at a distance ~ 200 Mpc). The predicted source distribution, with those of the 69 observed Auger UHECRs in the mask defined region superimposed, are plotted in figure 4.7. Note that the Auger exposure has not been taken into account in these plots. After doing so, the relative weights of structures change so that for example Virgo no longer dominates in the PSCz derived model.

Because the observed galaxy distribution is in the form of flux limited as opposed to volume limited samples, observed galaxies in the PSCz and 6dF have been weighted by the inverse of the selection function $\psi(r_c)$ (section 4.4). There is some uncertainty associated with this process, however this procedure is well motivated given that matter in the universe is clustered, hence unobserved galaxies that are below the galaxy survey's magnitude limit are more likely to reside near the observed galaxies than in regions where no sources were observed.

In figures 4.8 and 4.9 the distribution of values that the statistic X takes in 10,000 mock realisations of isotropically distributed UHECRs, as observed by Auger (dashed histograms) and the distribution of values of X in 10,000 mock realisations of 55 EeV UHECR protons with sources drawn from the predicted UHECR source distribution that follows the distribution of matter in the PSCz and 6dF catalogues are shown respectively (solid histograms). The black vertical line in each subplot shows the value of X for the observed Auger UHECRs assuming $E_{\rm f} = 55$ EeV. Each subplot corresponds to a different bin-size in the range $7.3° - 3.9°$. The picture that emerges from 4.8 and 4.9 is that the observed Auger UHECRs are not consistent with the mean of either one of the two models, although there is weak evidence for a source distribution correlated with nearby galaxies in bin sizes $6.5° \times 6.5°$ and $7.3° \times 7.3°$.

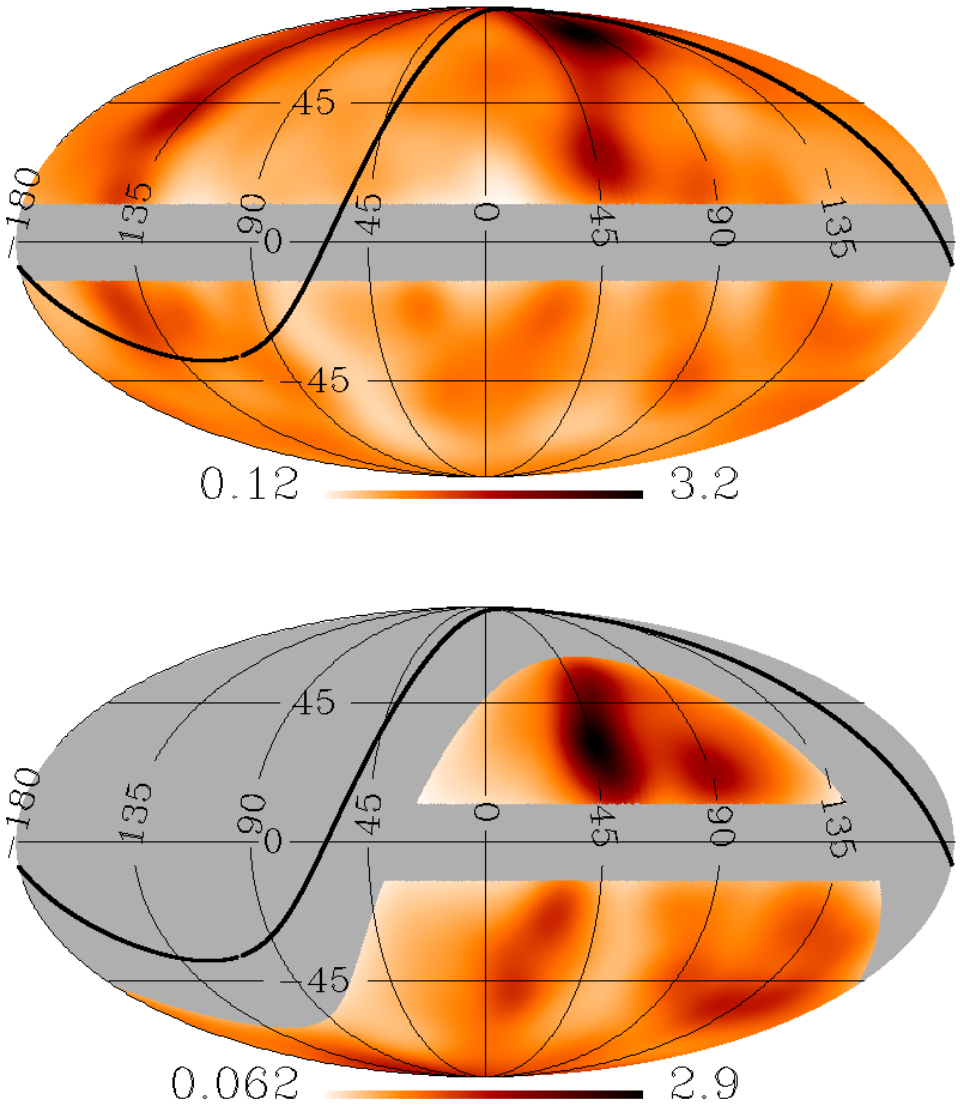

Figure 4.5. Maps of the predicted, local UHECR source distribution, in Galactic coordinates centred at the Galactic centre with the longitude l increasing anti-clockwise, derived from the PSCz (top) and 6dF (bottom) for UHECRs with final energy 55 EeV. The predicted source distribution has been smoothed with a Gaussian filter, with $\sigma = 7.2°$ for presentation purposes. The intensity at each point is normalised to the average intensity in the map. Auger is sensitive to the part of the sky below the thick black line. The regions in grey are excluded from the statistical analysis.

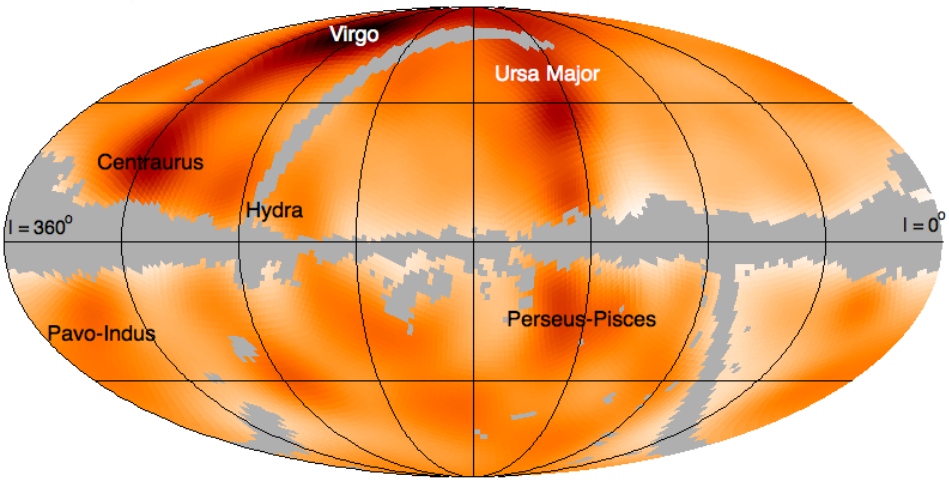

Figure 4.6. Map of the predicted, local UHECR source distribution, in Galactic coordinates, derived from the PSCz catalogue, as in figure 4.5 above, for UHECRs with final energy 55 EeV. The longitude l increases anti-clockwise here, with $l = 0°$ on the right of the plot. Contributions to the predicted flux from local superclusters are marked on. The PSCz has been masked with the mask described in Saunders et al. (2000).

The significance of this result is quantified in figure 4.10, where the percentage of realisations in which the value of X was more extreme than $X_{\rm Auger}$, the value of X obtained with the observed Auger UHECRs, in each of the models of UHECR source distribution considered ($P_{\rm iso}$ in the isotropic model and $P_{\rm PSCz}/P_{\rm 6dF}$ in the model where the UHECR sources are PSCz/6dF galaxies) as a function of cell size are plotted. One first notices that $P_{\rm iso}$ and $P_{\rm survey}$ are very sensitive to bin size and that this behaviour is not monotonic as a function of bin-size. This is a result of very low UHECR counts making the results susceptible to boundary effects. Overall there is very good agreement between the results obtained with the two galaxy surveys. Although the 6dF and PSCz samples are selected differently (near-infrared and far-infrared respectively) and the 6dF is deeper than the PSCz, they probe approximately the same large scale structure. For most of the parameter space considered the observed Auger UHECRs are inconsistent with isotropy at a level $\geq 95\%$, as can be seen by the dashed line that gives the 95% confidence level ($\simeq 2\sigma$ from the mean expectation). At the same time they have a lower value of X than $\geq 85\%$ of mock realisations from a source distribution following LSS, which is lower than

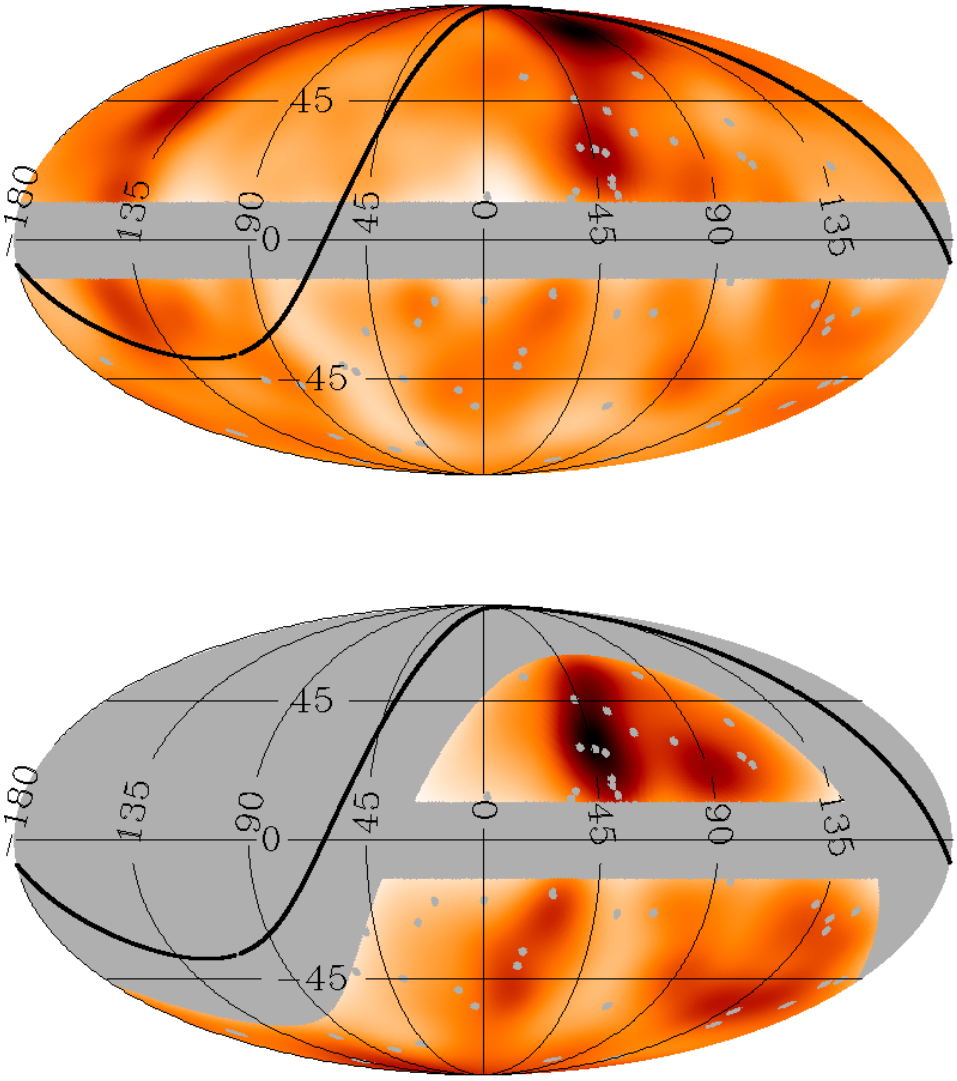

Figure 4.7. The predicted UHECR source distribution as in figure 4.5 above, with those of the 69 Auger observed events whose arrival directions fall in the galaxy survey's field of view superimposed (in grey). The non-uniform Auger exposure has not been taken into account in these intensity maps, hence visual inspection of correlations can be misleading. A statistical analysis as in section 4.5 is required.

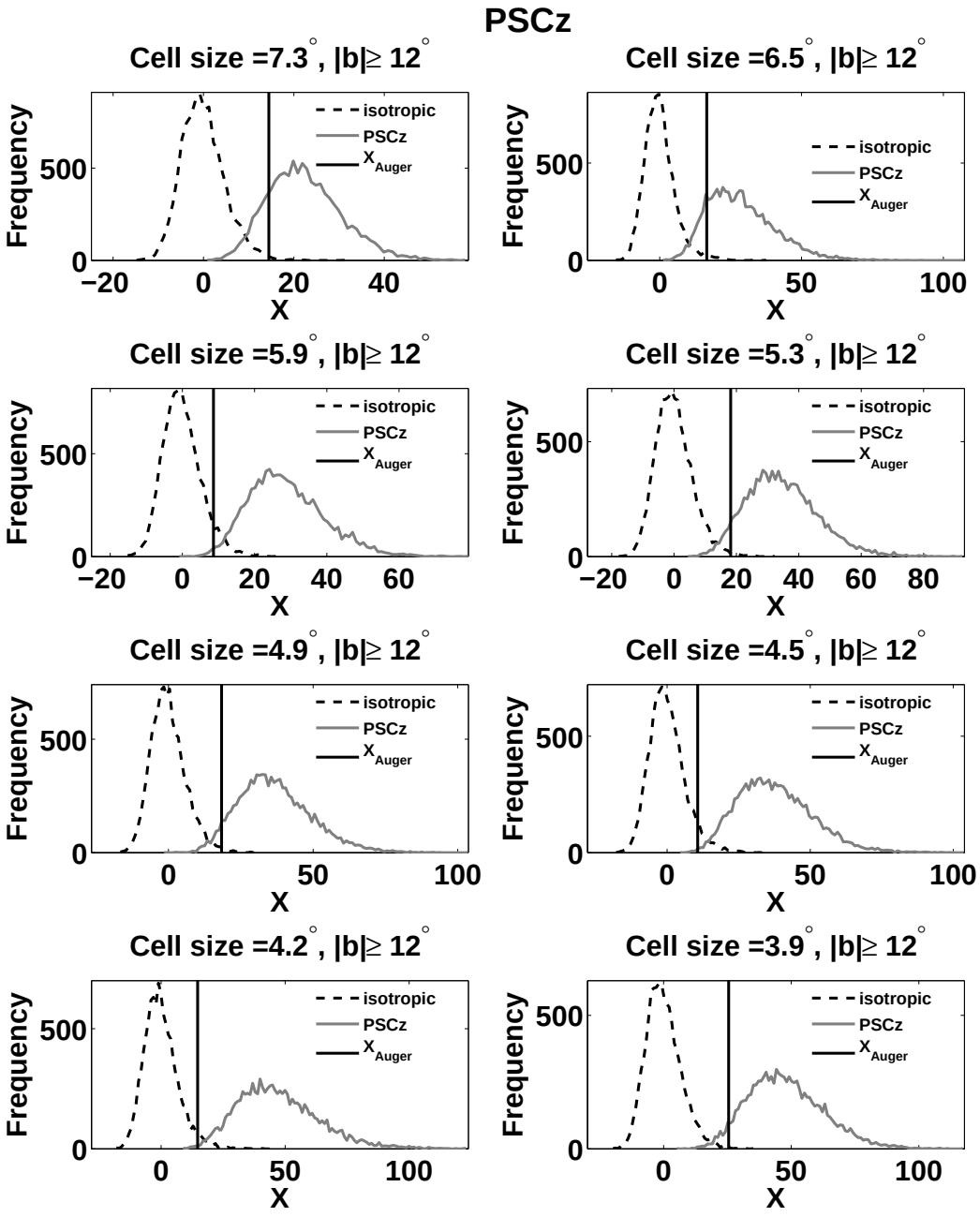

Figure 4.8. The distribution of values of the correlation statistic X (equation 4.18) in 10,000 mock realisations of a set of UHECRs drawn from an isotropic distribution (dashed histograms) and from the model UHECR source distribution that follows the PSCz (solid histograms). The value of X obtained for the observed Auger events, $X_{\rm Auger}$, is given by the black solid line. Each subplot corresponds to a different cell size used for the counts-in-cells analysis in the range 7.3° (top left) to 3.9° (bottom right).

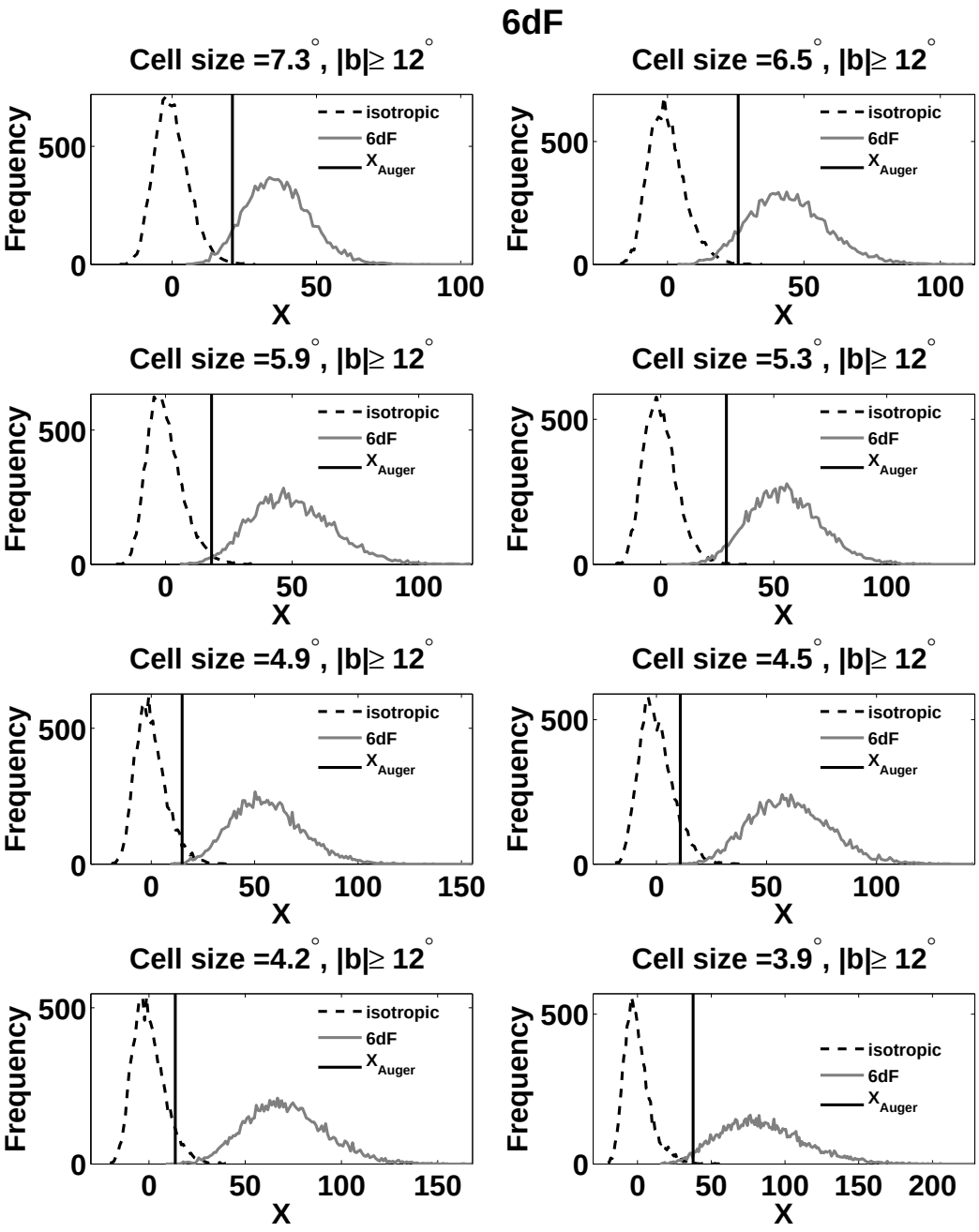

Figure 4.9. The same distributions as in figure 4.8 but using the 6dF catalogue.

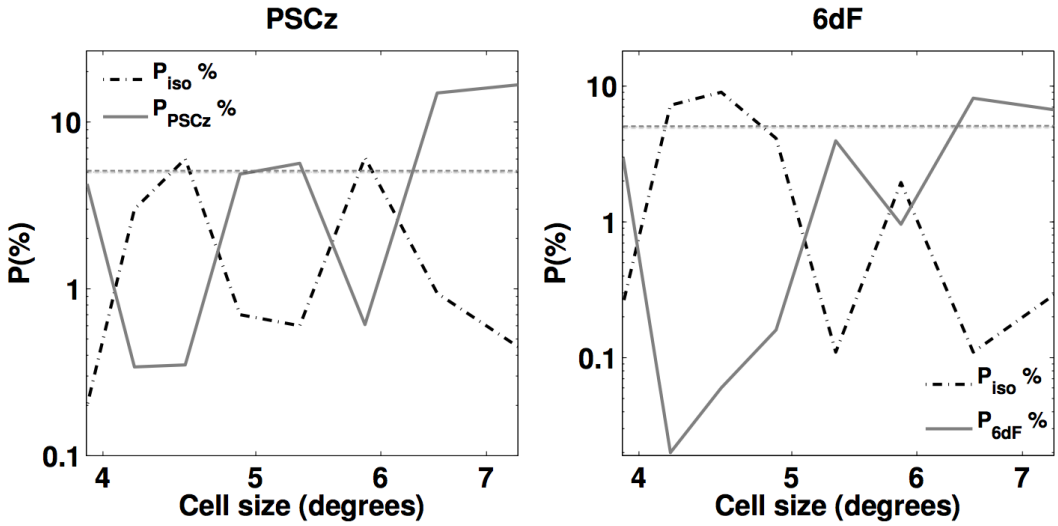

Figure 4.10. Left: $P_{\rm iso}$ - dashed line ($P_{\rm PSCz}$ - grey solid line), the percentage of realisations of UHECR samples drawn from an isotropic (following the PSCz) source distribution in which the value of X (equation 4.18) obtained was more extreme than $X_{\rm Auger}$, the value of X obtained for the observed Auger UHECRs, as a function of cell size. The dashed horizontal line shows the 95% confidence level. **Right:** Same as on the left plot but using the 6dF survey.

is expected on average if the observed UHECRs originate in galaxies in either survey.

Another way to quantify the significance of the results of 4.8 and 4.9 is to consider the frequency with which X equal to $X_{\rm Auger}$ occurs in mock realisations of the two different models of UHECR source distribution considered, which is proportional to the likelihood ratio of the two models. If this ratio is greater than 1 then the model in the numerator is preferred by the observed data, whereas if it is smaller than one the model in the denominator is preferred. This ratio

$$\frac{P(\text{LSS source model is true}|X_{\rm Auger})}{P(\text{isotropic source model is true}|X_{\rm Auger})}, \tag{4.19}$$

hereafter

$$\frac{P(\text{LSS}|\text{Auger})}{P(\text{ISO}|\text{Auger})} \tag{4.20}$$

is shown separately for the two galaxy catalogues as a function of cell size in figure 4.11. Here again, we see that the results are extremely sensitive to the choice of bin size and much less sensitive to the choice of galaxy survey. A future, larger UHECR dataset will

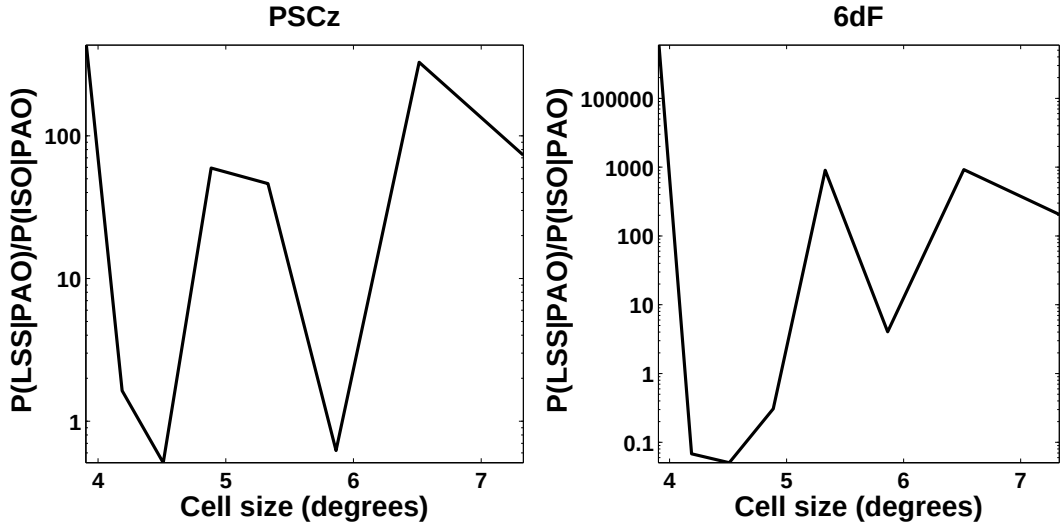

Figure 4.11. Left: The quantity $P(\text{LSS}|\text{Auger})/P(\text{ISO}|\text{Auger})$ (equation 4.20), the ratio of the frequencies with which a value of X equal to X_{Auger} (the value of X obtained with the observed Auger UHECRs) is obtained in realisations of UHECR sets from the 2 model source distributions (following the PSCz - *LSS*, isotropic -*ISO*) as a function of cell size. **Right:** Same as on the left plot but using the 6dF survey.

suffer significantly less from such fluctuations and allow to draw firmer conclusions within the framework that is presented here.

In figure 4.12 the results of the correlation analysis performed using the 6dF survey are shown next to the same results for the PSCz, as well as the results of the analysis performed with the PSCz survey but restricted to the Southern hemisphere for cell size $5.9^\circ \times 5.9^\circ$. This allows for a direct comparison between the results of the two surveys which have been confine to the same field of view. Again, we see very good agreement between the two surveys, but no concrete conclusion emerges as to the distribution of the sources of UHECRs.

4.6.2 Cross-correlation in equal predicted flux radial shells

In this section, a new method of studying any correlation between observed UHECR arrival directions and predicted UHECR source distribution, by dividing the predicted source distribution into radial shells with distance, is presented. If a correlation exists, this method will help localise the source population and constrain some of its properties, such as for example the redshift evolution.

The expected UHECR source distribution is divided into three shells, each contributing

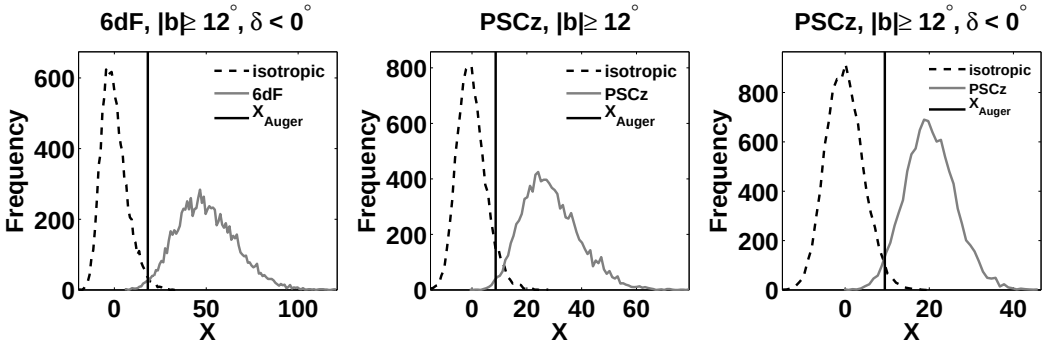

Figure 4.12. The distribution of values of the statistic X obtained in 10000 realisations of UHECRs from an isotropic source distribution (dashed histograms), from a distribution of sources that follows LSS (solid grey histograms) and $X_{\rm Auger}$, the value of X for the observed Auger events (black solid line). The distribution of sources that follows LSS was modelled with the 6dF (left), the PSCz (centre), and the PSCz sources that lie in the southern hemisphere, i.e. the the PSCz sources in the 6dF field of view (right). The plots shown are for cell size $5.9^\circ \times 5.9^\circ$.

a third of the expected UHECR flux based on the predicted source distribution presented above, and cross-correlate the observed Auger UHECRs with the predicted source distribution in each of the shells. In order to define shells contributing equal predicted UHECR flux, $r_{\rm start}$ and $r_{\rm end}$ are determined, such that for each shell:

$$\int_{r_{\rm near}}^{r_1} \frac{\mathrm{d}}{\mathrm{d}r_{\rm L}} \left(n(r_{\rm L}) \cdot \omega_{\rm gal}(r_{\rm L})\right) \cdot \mathrm{d}r_L = \int_{r_1}^{r_2} \frac{\mathrm{d}}{\mathrm{d}r_{\rm L}} \left(n(r_{\rm L}) \cdot \omega_{\rm gal}(r_{\rm L})\right) \cdot \mathrm{d}r_L = \int_{r_2}^{r_{\rm far}} \frac{\mathrm{d}}{\mathrm{d}r_{\rm L}} \left(n(r_{\rm L}) \cdot \omega_{\rm gal}(r_{\rm L})\right) \cdot \mathrm{d}r_L = \frac{1}{3} \int_{r_{\rm near}}^{r_{\rm far}} \frac{\mathrm{d}}{\mathrm{d}r_{\rm L}} \left(n(r_{\rm L}) \cdot \omega_{\rm gal}(r_{\rm L})\right) \cdot \mathrm{d}r_L, \tag{4.21}$$

where $n(r_{\rm L})$ is the number of sources at distance $r_{\rm L}$, $\omega_{\rm gal}$ is the weighted contribution of a source at distance $r_{\rm L}$ to the expected UHECR flux defined in equation 4.12 and $r_{\rm near}$ and $r_{\rm far}$ are the distances of the nearest and most distant sources in the galaxy survey (in practice $r_{\rm max}$ is a cut applied, well beyond the GZK-horizon, in order to avoid diverging weights of the few, very distant sources, present in the galaxy surveys). Any contribution to the observed UHECR flux from sources beyond this distance should be isotropic but at this energy, such a contribution will amount to less than 1%. Since each nearby galaxy contributes more of the expected UHECR flux than any other more distant galaxy, due to flux suppression with distance and particle energy losses during propagation, the three shells that have been defined are not equal in width nor in the number of galaxies they contain. In table 4.1, the number of sources in each of the shells as well as the distances

	PSCz			6dF		
	shell 1	shell 2	shell 3	shell 1	shell 2	shell 3
$r_{\rm start} - r_{\rm end}$ [Mpc]	0 - 47	47 - 132	132 - 365	0 - 29	29 - 100	100 - 365
Number of sources	2189	5577	5300	1103	10711	65785

Table 4.1. The number of galaxies and the distances covered in each of the three radial shells (section 4.6.2) expected to contribute equal UHECR flux, for a model UHECR source distribution based on the PSCz (left) and on the 6dF (right). Beyond $\sim$ 100 Mpc the PSCz selection function, $\psi(r_c)$ (equation 4.9), drops off quicker than $\omega(r_{\rm L})_{\rm flux}$ of equation 4.4, the flux weight for a source at distance $r_{\rm L}$. As a result the effective weight of each galaxy, $\omega_{\rm gal}$ (equation 4.12), does not monotonically decrease with distance for the PSCz, which is why shell 3 contains fewer galaxies than shell 2 (see also section 4.6.4 for a more detailed discussion of the PSCz selection function).

covered by each shell for the PSCz and the 6dF are given.

In the top row of 4.13 and 4.14, the distribution of the values that X takes in 10000 realisations of UHECR samples from an isotropic distribution of sources and from a distribution of sources based on the local galaxy distribution as well as for the observed Auger UHECRs, in each of the three shells, for $5.9^\circ \times 5.9^\circ$ bins, for the PSCz and 6dF respectively is shown. In the middle and bottom row $P_{\rm iso}$, $P_{\rm PSCz}$ and $P({\rm LSS|Auger})/P({\rm ISO|Auger})$ (defined in section 4.6.1) are shown, for shells 1, 2 and 3 from left to right, as a function of cell size. We see a strong sensitivity to the choice of cell-size as in section 4.6.1 in these results. Overall, when cross-correlated with shell 1 of the PSCz and shells 1, 2 of the 6dF the observed Auger UHECRs are consistent with isotropy, whereas there is weak evidence for correlation of the observed UHECRs with the predicted source distribution is shells 2 and 3 of the PSCz and with shell 3 of the 6dF.

The normalised correlation coefficient R is used, to determine the relative strength of any detected anisotropy signal with respect to source clustering in the shell

$$R = \frac{\sum_i \left(N_{\rm CR,i} - N_{\rm iso,i}\right) \cdot \left(N_{\rm M,i} - N_{\rm iso,i}\right)}{\sqrt{\sum_i \left(N_{\rm CR,i} - N_{\rm iso,i}\right)^2} \cdot \sqrt{\sum_i \left(N_{\rm M,i} - N_{\rm iso,i}\right)^2}}. \tag{4.22}$$

In figure 4.15, the distribution of R obtained in 10000 realisations of UHECR samples from an isotropic distribution of sources and from a distribution of sources based on the local galaxy distribution, as well as for the observed Auger UHECRs, $R_{\rm Auger}$ are shown, for shells 1, 2 and 3 from left to right, for the PSCz (top row) and the 6dF (bottom row).

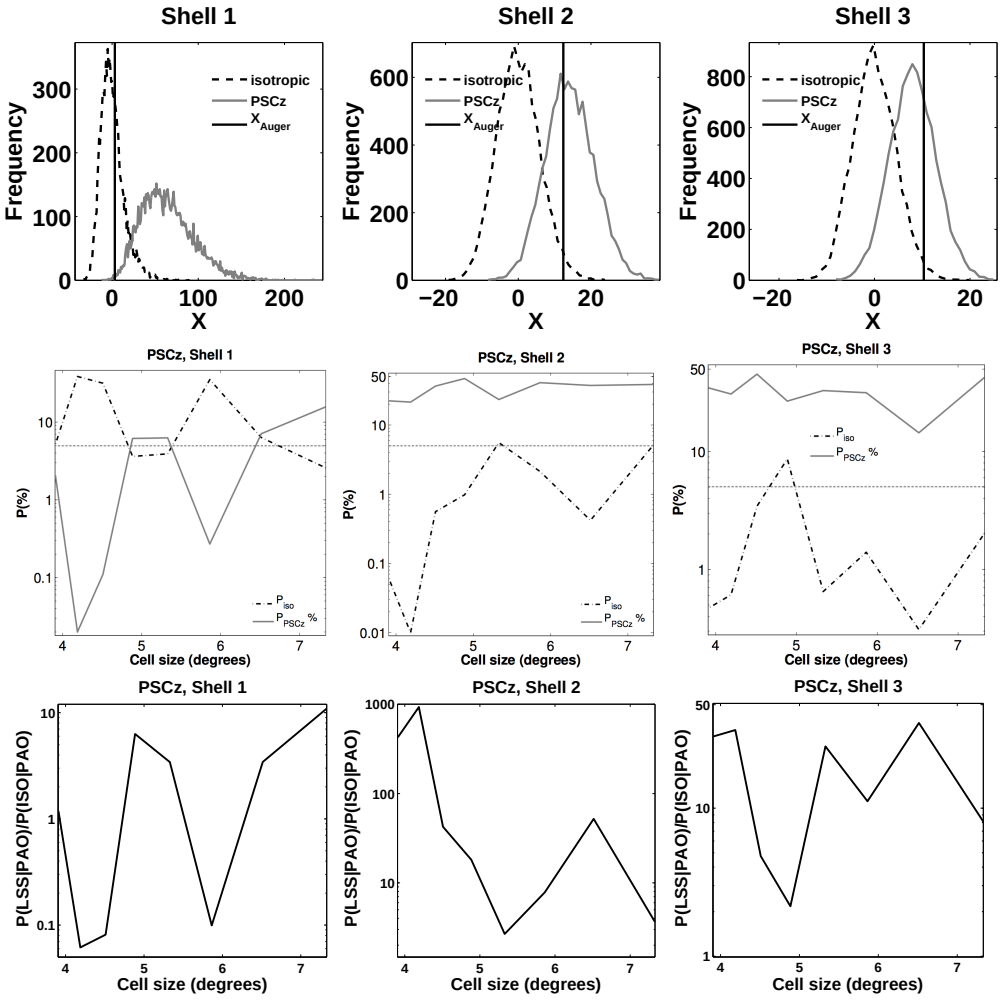

Figure 4.13. Top Row: Distribution of values of the statistic X (equation 4.18) for 10,000 realisations of UHECR sets drawn from an isotropic source distribution (dashed histograms), a distribution of sources based on the PSCz (solid histograms) and $X_{\rm Auger}$, the value of X obtained for the observed Auger UHECRs (black solid line) for shells 1, 2 and 3 (see section 4.6.2). The cell size used for these plots is $5.9^\circ \times 5.9^\circ$.
Middle Row: $P_{\rm iso}$ - dashed line ($P_{\rm PSCz}$ - solid line), the percentage of realisations of sets of UHECRs from an isotropic (correlated with LSS) source distribution in which the value of X was more extreme than $X_{\rm Auger}$ as a function of cell size.
Bottom Row: $P({\rm PSCz}|{\rm Auger})/P({\rm ISO}|{\rm Auger})$ (equation 4.20), the ratio of realisations of the two models that had a value of X equal to $X_{\rm Auger}$ as a function of cell size.

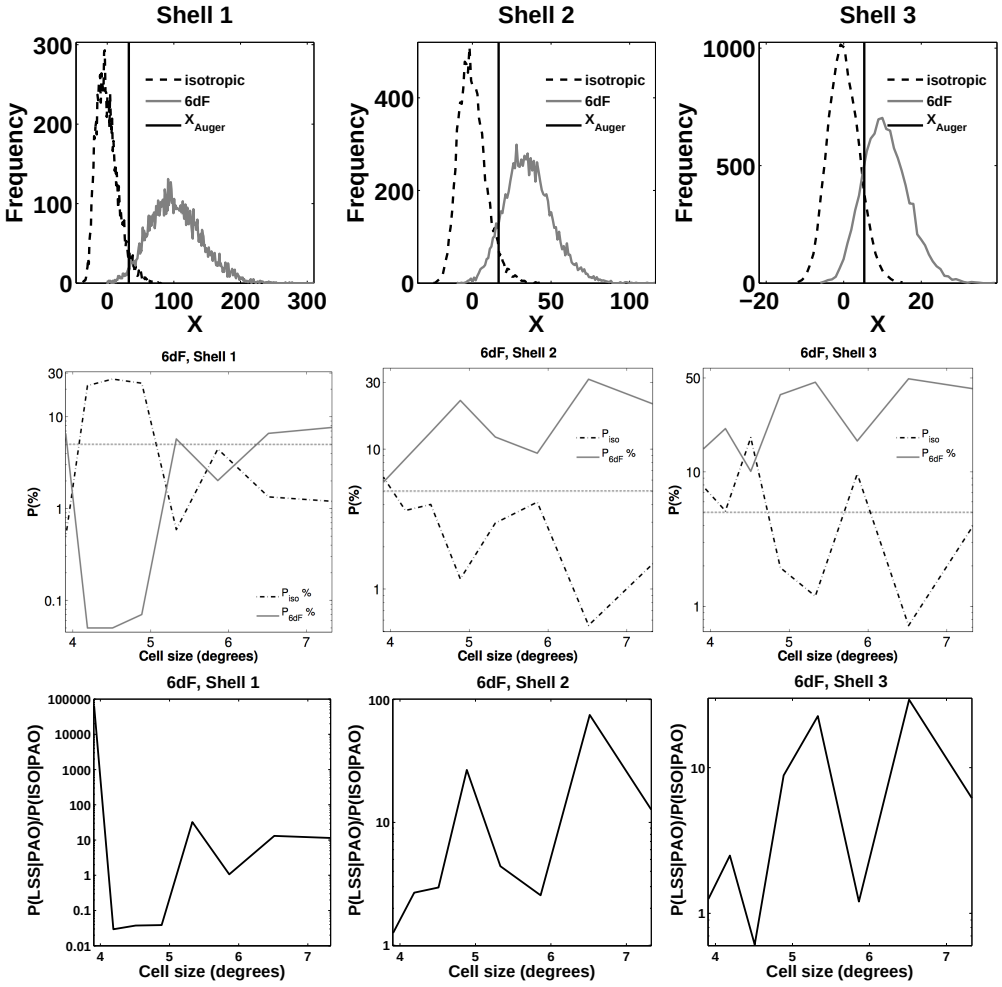

Figure 4.14. Same as in figure 4.13 but for the 6dF survey.

The plots shown are for $5.9^\circ \times 5.9^\circ$ angular bins. In shell 1 of the PSCz, which includes all sources nearer than 47 Mpc, R has greater discriminatory power than shells 2 and 3 and the mean value of R_{PSCz} in shell 1 is twice that of shells 2 and 3. The picture is similar for the 6dF. The mean value of R_{6dF} drops from ~ 0.3 in shell 1, to ~ 0.2 in shell 2 and ~ 0.1 in shell 3. The reason for this behaviour is that going from shell 1 to 3 there are progressively more galaxies in each shell, occupying a larger volume and hence we move to larger scales, where the galaxy distribution is less anisotropic and there is significantly less contrast. In shell 1 where R has the greatest statistical power the Auger UHECRs are consistent with an isotropic hypothesis, whereas in shells 2 and 3 of the PSCz and shell 3 of the 6dF which have lower contrast and less discriminatory power there is weak evidence of correlation with the predicted source distribution. If the magnetic deflections of the UHECRs studied are not larger than has been assumed, this result would suggest

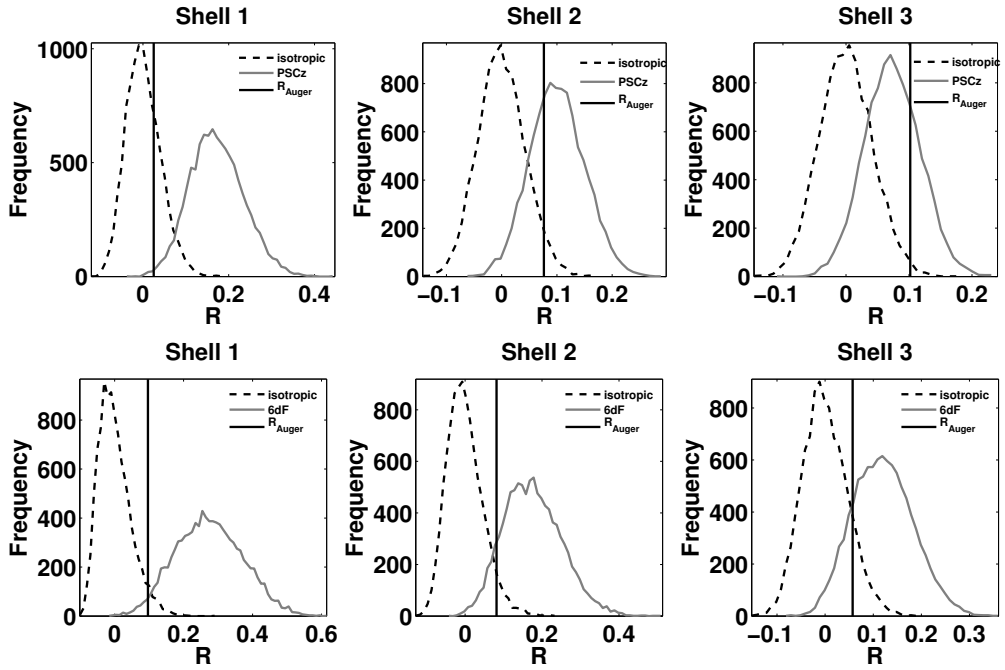

Figure 4.15. Top Row: Distribution of values of the normalised correlation coefficient R (equation 4.22) for 10,000 realisations of UHECR sets drawn from an isotropic source distribution (dashed histograms), from a distribution of sources based on the PSCz (solid histograms) and $R_{\rm Auger}$, the value of R obtained for the observed Auger UHECRs (black solid line), for Shells 1, 2 and 3 (see section 4.6.2). The cell size used for these plots is $5.9° \times 5.9°$. **Bottom Row:** Same as in the row above, but with the 6dF survey.

that the true UHECR source population has similar clustering properties to those of the galaxy distribution in shells 2 and 3 and is less clustered than the source distribution in shell 1, which is consistent with the results in the other sections of this work.

4.6.3 Magnetic deflections

In this section, the dependence of the results on the amplitude of the magnetic deflections, that are suffered by UHECRs during their propagation, is investigated. If the mass composition of UHECRs is mixed as recent experimental data suggest, or magnetic fields in the local universe are stronger than typically found in relevant studies, average magnetic deflections will likely be larger than has been assumed so far in this work.

Mock realisations, in which UHECRs suffer simulated magnetic deflections, are generated, and the expected level of correlation with the galaxy distribution in this model is compared to that of the Auger UHECRs. Random magnetic deflections are simulated using a 2 dimensional Gaussian function, centred at the position of the source. A gaussian

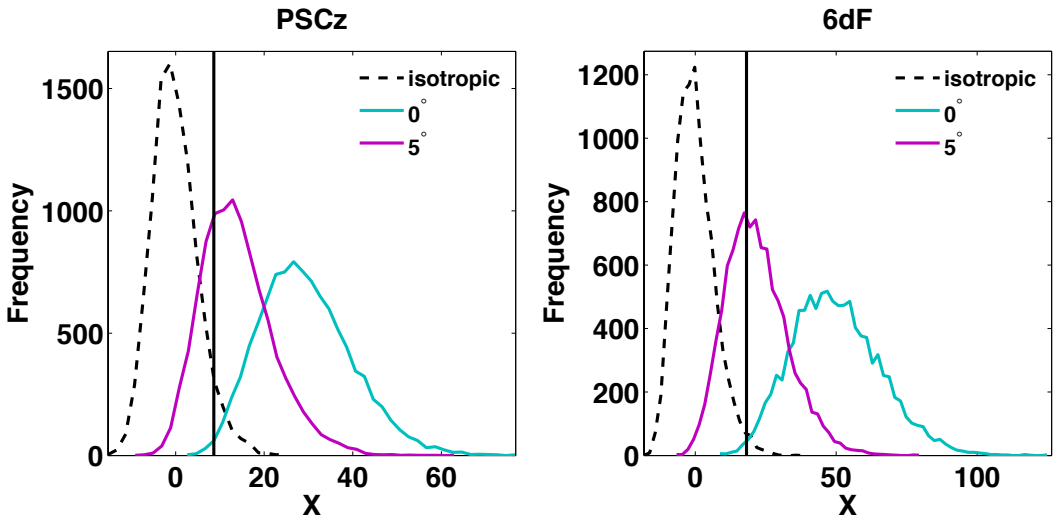

Figure 4.16. Left: The distribution of values of X in 10,000 realisations of UHECRs from an isotropic distribution of sources (dashed histogram) and from a distribution of sources based on the PSCz (solid histograms) with and without simulated magnetic deflections with amplitude 5°. The cell size shown in this plot is 5.9° × 5.9°. **Right:** Same as on the plot on the left panel but using the 6dF.

with a standard deviation $\sigma_{\rm d} = 5^\circ$ is considered. With this function, randomly oriented angular displacements for each UHECR with respect to its source are generated.

In figure 4.16 the distribution of values of X obtained for mock UHECRs, whose sources are nearby galaxies with and without simulated deflections, is shown. We see that even if the sources of the UHECRs are correlated with nearby galaxies (as the ones in the LSS model), increasing the deflection angle dilutes the anisotropy signal as expected intuitively. The distribution of the arrival directions of Auger UHECRs is consistent with that expected, if the sources are correlated with the galaxy distribution, if deflections are of order 5°.

4.6.4 Systematic uncertainties

In the previous section the uncertainties introduced by the unknown composition of UHECRs and the magnitude of magnetic deflections were discussed. In this section, the sensitivity of the results to the uncertainty on the selection function of the galaxy surveys is studied.

When modelling the selection function of a galaxy survey the uncertainty is largest nearby where the luminosity function is calculated from a very small number of galaxies. This

uncertainly nearby has a non-negligible effect on the UHECR source distribution models where nearby galaxies have a greater weight than more distant ones due to flux suppression with distance and particle energy losses during propagation. The PSCz survey is studied in what follows, but qualitatively similar findings are expected for the 6dF. The PSCz selection function is well fit by equation 4.10. In table 4.2, the sensitivity of P_{iso}, P_{PSCz} and P(PSCz|Auger)/P(ISO|Auger) on the error in $\psi(r)$, which is estimated by varying the parameter α of equation 4.10 so as to reproduce the published errors, is shown. Further, in the same table, the sensitivity of these quantities on the choice of $r_{\rm min}$, the distance at which the selection function is normalised, the choice of which affects the predicted galaxy number density as a function of distance nearby, is quantified.
We see that the values of $P_{\rm iso}$, $P_{\rm PSCz}$ and P(PSCz|Auger)/P(ISO|Auger) obtained for shells 1 and 2 are particularly sensitive to the systematics, whereas those obtained for shell 3 are significantly more robust. This is as expected, as the nearby slope of the selection function, where systematic uncertainties have a large impact to the results, since nearby sources are expected to contribute significantly to the observed UHECR flux, has been varied. The sensitivity of $P_{\rm iso}$, $P_{\rm PSCz}$ and P(PSCz|Auger)/P(ISO|Auger) to the systematics discussed here is comparable to the sensitivity to the choice of bin size everywhere but in shell 3 where the systematic uncertainty is small. With a larger UHECR dataset the sensitivity of this method to bin size will significantly decrease but the systematic uncertainty discussed here will not, at least not for the galaxy surveys discussed.

The systematic uncertainty in the energy determination of the primary particles detected at Auger introduces an error to the results. At the time of this analysis the systematic uncertainty was 23%. The effect of this uncertainty on the results is studied, by changing $E_{\rm f}$ in the models by 23% i.e. assuming that the energy of the observed Auger UHECR events has been under(over)-estimated by 23%. This produces changes in $P_{\rm iso}(P_{\rm PSCz})$ of order few(10)%, but doesn't strongly change the conclusions drawn here. The sensitivity to the injection spectrum index (equation 4.6) is smaller, at most few % relative to the value of $P_{\rm iso}(P_{\rm PSCz})$ in the range $-2.5 \leq \alpha \leq -1.5$.

4.7 Discussion

The set of 69 observed Auger UHECRs with energy greater than 55 EeV have been used, to assess whether their arrival directions are correlated with the positions of nearby galax-

$(\alpha, r_{\rm min}$ [Mpc])	Entire PSCz			Shell 1			Shell 2			Shell 3		
	$P_{\rm iso}(\%)$	$P_{\rm PSCz}(\%)$	$\frac{P({\rm LSS}\vert{\rm Auger})}{P({\rm ISO}\vert{\rm Auger})}$	$P_{\rm iso}(\%)$	$P_{\rm PSCz}(\%)$	$\frac{P({\rm LSS}\vert{\rm Auger})}{P({\rm ISO}\vert{\rm Auger})}$	$P_{\rm iso}(\%)$	$P_{\rm PSCz}(\%)$	$\frac{P({\rm LSS}\vert{\rm Auger})}{P({\rm ISO}\vert{\rm Auger})}$	$P_{\rm iso}(\%)$	$P_{\rm PSCz}(\%)$	$\frac{P({\rm LSS}\vert{\rm Auger})}{P({\rm ISO}\vert{\rm Auger})}$
$1.82, 0.84$	6.12	0.61	0.5	35.1	0.27	0.1	2.13	40.9	7	1.40	31.5	10
$1.68, 0.84$	12.2	0.04	0.1	38.2	0.05	0.05	3.46	22.9	5	2.12	28.7	7
$1.94, 0.84$	4.09	2.86	1	13.1	4.31	0.5	20.7	12.7	0.7	2.26	43.9	8
$1.82, 5$	20.2	0.03	0.06	48	0.01	0.03	2.46	40.4	8	2.54	29.6	6
$1.82, 10$	23.9	< 0.01	0.01	44.7	< 0.01	0.01	2.76	20.5	5	2.72	25.8	5

Table 4.2. Sensitivity of $P_{\rm iso}$ ($P_{\rm PSCz}$), the percentage of realisations of an isotropic (correlated with LSS) UHECR source distribution in which the value of X was more extreme than $X_{\rm Auger}$, the value of X obtained with the observed Auger UHECRs, and $P({\rm PSCz}|{\rm Auger})/P({\rm ISO}|{\rm Auger})$, the ratio of the likelihoods of the two models of source distribution, to errors in the PSCz selection function and to the choice of the selection function normalisation distance $r_{\rm min}$. From left to right, the sensitivity for the source model based on the entire PSCZ catalogue (introduced in section 4.6.1) and for shells 1, 2 and 3 as defined in section 4.6.2 are shown. All values quoted in this table are for an analysis performed with equal area angular bins with size $5.9^\circ \times 5.9^\circ$. The top row gives the canonical choice of parameters for this analysis, the second and third row give sensitivity to the parameter α of equation 4.10 and the two bottom rows give the sensitivity to $r_{\rm min}$ (introduced in section 4.4).

ies or sources correlated with those galaxies. A steady UHECR source distribution, in which individual UHECR sources are faint, has been modelled using the PSCz and 6dF. The latter has being used here for the first time to model the predicted UHECR source distribution. Throughout this work, the UHECR flux suppression due to energy losses during particle propagation, expected random magnetic deflections of a few degrees, and the non-uniform Auger exposure, have been taken into account.

In figures 4.8-4.12, it is shown that the observed Auger UHECRs have a higher degree of correlation with the predicted UHECR source distribution than 94% (98%) of mock realisations from an isotropic source distribution, when cross-correlated with the PSCz (6dF), sensitive to the choice of cell-size for the analysis and other systematics discussed in section 4.6.4. At the same time the observed cross-correlation signal is lower than in $\gtrsim 85\%$ of realisations of UHECRs that originate in galaxies in either survey. As shown in figure 4.16, the observed Auger UHECRs favour a model in which the sources are galaxies in the PSCz/6dF, but random magnetic deflections of UHECRs are slightly greater than

in the default model parameters, of order 5°. The results are very sensitive to the choice of cell-size due to low statistics, but this sensitivity will certainly decrease when the number of observed UHECRs increases.

Compared to studies of the 2007 Auger dataset of 27 events the significance of the correlation has decreased (as shown in e.g., Abreu et al. 2010). This is something that was tested with the setup presented here, and which I can confirm. As was pointed out in e.g., Kashti & Waxman (2008) the fact that half of the original 27 events had been selected to maximise the UHECR-AGN correlation, may have lead to an overestimate of the significance with which isotropy was ruled out.

In this work it was assumed that individual UHECR sources are faint, i.e. the probability of a given source producing more than one observed event is low. This is favoured by the clustering of the UHECR dataset that was analysed, as well as the more recent study of Abreu et al. (2013). Further, it was assumed that the number density of UHECRs is comparable to the local density of galaxies. The mean value of X in a given model does not depend on the source number density n_0. The width of the distribution of X does depend on n_0, since for lower source number density the number of sources contributing to the flux is lower, fluctuations are larger, and the distribution of values of X is wider, as shown in the work of Waxman et al. (1997); Kashti & Waxman (2008). For a dataset of the present size this effect is subdominant to the sensitivity of X to other model parameters, primarily the choice of cell size.

A new way of analysing any observed correlation between observed UHECRs and model source distribution was presented. The method proposed is to divide the predicted source distribution into radial shells of equal predicted UHECR flux contribution. It was shown that the 69 observed Auger UHECRs are consistent with an isotropic distribution, when cross-correlated with the source distribution in the nearest shell (shell 1) of the PSCz and shells 1 and 2 of the 6dF, whereas there is weak evidence of correlation with the source distribution of shells 2 and 3 of the PSCz and shell 3 of the 6dF (4.13 - 4.15). The principle of the method proposed here can be further developed in future and with larger datasets, to help localise the true sources of UHECRs and constrain some of their properties. In chapter 6 the expected sensitivity of future, larger UHECR detectors to the predicted UHECR anisotropy signal will be studied in detail.

The analysis was performed with two galaxy surveys, which have been carried out using different selection criteria, and have different median depths, hence probing different

LSS. Observing a correlation with a specific astrophysical population does not constitute proof that the sources of UHECRs are members of that population, as matter in the universe is clustered and different astrophysical populations are correlated with each other. There is very good agreement between the results obtained with the two surveys despite them having different fields of view and median depths, highlighting the robustness of the method.

In this work a Frequentist approach to the long standing question of the origin of UHECRs was taken, as it the most straightforward approach for this type of study, with the smallest number of assumptions, regarding the source population. Other authors have taken a Bayesian approach to the question (e.g., Watson et al. 2011; Soiaporn et al. 2012). The authors of Watson et al. (2011) have obtained results that are qualitatively similar to these obtained here, namely they conclude that the Auger UHECRs observed to date are neither consistent with an isotropic distribution of sources nor with a model in which all UHECRs are protons that originate in nearby galaxies.

Observed UHECRs may have suffered magnetic deflections larger than a few degrees, if at least a fraction of them are heavily charged nuclei as opposed to nucleons which were assumed in this work, or if intervening magnetic fields are stronger than most recent studies conclude (as e.g., in the work of Sigl et al. 2004b), in which case even proton UHECRs may have suffered deflections much larger than 3°. Identifying the mass composition of the primaries and progress in understanding extragalactic magnetic fields, will help break the degeneracy between the above scenarios.

This page was intentionally left blank

Chapter 5

Gamma-ray spectra of Blazars

"There are more things in heaven and earth, Horatio, than are dreamt of in your philosophy."

-Shakespeare, Hamlet

Blazars are AGN with jets that point towards the observer. As we saw in section 1.3 AGN are some of the very few types of astrophysical sources where UHECR acceleration is thought to be viable. At the same time blazars are now the most frequently observed extragalactic gamma-ray sources. If proton acceleration up to ultra-high energies takes place in these sources, it may be possible to identify the signature of this process in blazar gamma-ray spectra, depending on the total energy output in hadrons. Clearly, unambiguous detection of secondary gamma-rays of hadronic origin would have a lasting impact on the long standing question of the origin of UHECRs (see e.g., review by Kotera & Olinto 2011 and references therein). One of the signatures of UHECR production is the synchrotron emission expected from secondary electrons and positrons that are produced when the source resides in a magnetised region, such as a filament of large scale structure, in which many blazars should be embedded. In this chapter, numerical modelling of the expected blazar gamma-ray emission from this channel are performed. It is shown, that this channel successfully reproduces the gamma-ray spectra of some recently discovered, extreme blazars.

5.1 Introduction

5.1.1 Blazars

BL Lacertae objects (BL Lacs) and flat spectrum radio quasars (FSRQs), commonly referred to as blazars, are a radio loud subclass of AGN that have jets, i.e. collimated highly relativistic outflows, that point almost directly towards the observer (Urry & Padovani 1995). Blazars appear point-like and exhibit rapidly varying non-thermal emission across all energy bands. Blazar broadband spectral energy distributions have a characteristic double-bump shape. The low frequency peak is found in the optical to X-ray band and is generally thought to originate in the synchrotron emission of relativistic electrons and positrons in the jet. The high energy peak occurs in the gamma-ray band and its origin is less well understood. Commonly it is assumed to be due to leptonic inverse-Compton scattering, but in some cases, in which conventional leptonic models fail to explain the observations, a hadronic origin is a viable alternative interpretation. Physical mechanisms that could be responsible for the observed high-energy emission, will be discussed in detail in sections 5.1.2, 5.1.3 below.

FSRQs have broad prominent emission lines and are believed to be hosted by high-luminosity radio galaxies (Fanaroff- Riley type II [FR II]; Fanaroff & Riley 1974), whereas BL Lacs are believed to be hosted by the lower luminosity Fanaroff-Riley type I [FR I] and have weak or absent emission lines. In the commonly used "blazar sequence" classification (Fossati 1998; Donato et al. 2001), blazars are described as a continuous distribution, characterised by a decreasing source luminosity and increasing synchrotron peak energy as shown in figure 5.1. FSRQs are the highest luminosity and peak at lower energies. BL Lacs are further classified into into low- (LBL), intermediate- (IBL) and high-frequency peaked (HBL), the latter having high energy peaks as high as in the TeV gamma-ray band. The "blazar sequence", although popular, often fails to properly account for the very diverse and intensely variable characteristics of blazars. It is often challenged on the grounds of systematic biases; for example, the recent, detailed study of multiwavelengh blazar data of Giommi et al. (2012) suggests that the apparent correlation between decreasing source luminosity and increasing synchrotron peak energy, advocated by the blazar sequence model, is a selection effect. More than 90% of the extragalactic gamma-ray sources that have been detected to date are blazars. In its five years of operation the *Fermi*-LAT (Abdo et al. 2011) has detected and compiled a catalogue of more than 1000 blazars

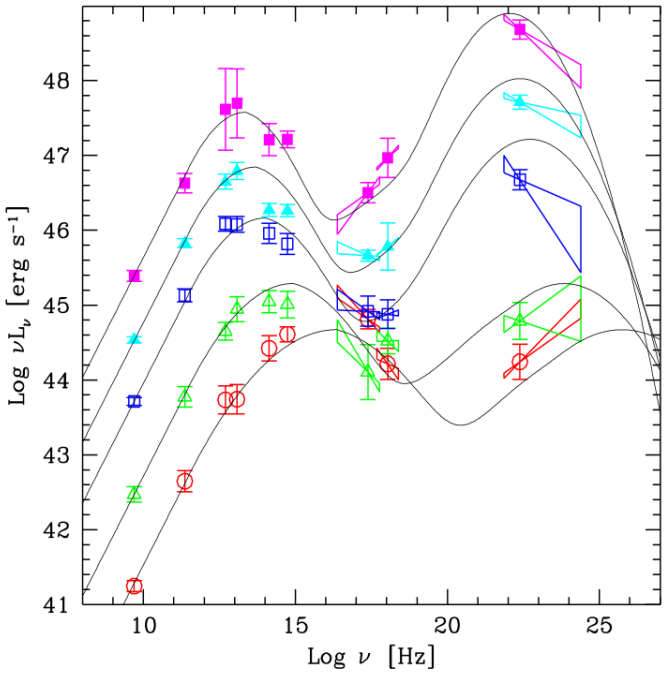

Figure 5.1. Average spectral energy distributions of blazars demonstrating the "blazar sequence" classification with FSRQs being the most luminous (upper curve) and HBLs the lowest luminosity, highest frequency peaked (bottom curve). Figure from Donato et al. (2001).

divided approximately equally into BL Lacs and FSRQs. Since 2004, when the current generation of ground based imaging atmospheric Cherenkov telescopes (IACTs) began operations, more than 50 blazars have been detected in the TeV region[1]. The majority of the TeV blazars detected so far are HBLs. Below, possible models for the origin of the observed blazar gamma-ray spectra, which can be broadly separated into leptonic and hadronic, are discussed.

5.1.2 Leptonic origin

The most popular interpretation for the gamma-ray bump in HBLs, which are the most numerous TeV blazars known, is synchrotron self-Compton emission (SSC) (Mastichiadis & Kirk 1997; Tavecchio et al. 1998). In this model, it is assumed that relativistic electrons in the jet radiate in synchrotron, producing photons up to X-ray energies, which are subsequently inverse-Compton scattered by the same electron population to gamma-ray energies. Alternatively, electrons in the source inverse-Compton scatter on external photon fields (see e.g., Dermer & Schlickeiser 1993), or ambient photon fields in different parts

[1] http://tevcat.uchicago.edu

of the jet (e.g., Ghisellini et al. 2005). In general, leptonic models are the preferred explanation for blazar gamma-ray spectra. They require acceleration of electrons to only TeV energies (unlike hadronic models, which typically require acceleration of protons and nuclei to ultra-high energies). Further, the production of gamma-rays proceeds through the very efficient inverse-Compton process. Theoretical challenges of leptonic models include accelerating electrons to high enough energies without suffering severe synchrotron losses, and having a target for the inverse-Compton to occur that isn't opaque enough to attenuate the outgoing gamma-rays.

The attenuation of VHE gamma-rays from blazars by pair-production on the EBL, is expected to leave a unique, redshift dependent cutoff in the blazar spectra, assuming that there are no breaks in the intrinsic spectrum below the characteristic cutoff energy. Under some assumptions about the maximum achievable hardness of the intrinsic spectrum, it is possible to constrain the EBL at earlier epochs, from observations of the exact position and shape of this cutoff in the TeV spectra of hard-spectrum blazars (e.g., Aharonian et al. 2006; Kneiske & Dole 2008). Such studies typically assume a purely leptonic origin of the blazar emission.

Within leptonic models, blazar gamma-ray spectra are also used to constrain the strength of intergalactic magnetic fields (IGMFs). In the absence of intervening IGMFs, one expects a given level of flux in the GeV region, associated with the blazars that have been detected at VHE with IACTs. The expected GeV flux, should be the intrinsic flux of the source in that energy range plus any contribution from the electromagnetic cascade, that typically deposits energy from cascaded higher energy gamma-rays to the GeV region below the pair-production threshold. There are a number of VHE blazars that seem to have an unusually low level of flux in the GeV (inferred from *Fermi*-LAT observations or upper limits). The absence of the expected GeV flux has been interpreted as the result of intervening IGMFs deflecting the low energy electrons in the cascade, thus diluting the cascade signal in the GeV band. This line of reasoning has been used in a number of recent studies, that, analysing the spectra of such hard-spectrum blazars place a lower limit on the strength of intervening IGMFs. Assuming that blazar emission is steady, *Fermi* data lead to lower limits of $B_{\rm IGMF}\lambda^{1/2} \lesssim 10^{-15}$ G Mpc$^{1/2}$ (e.g.,, Neronov & Vovk 2010; Taylor et al. 2011; Ahlers & Salvado 2011; Vovk et al. 2012). Taking into account the possibility that blazar emission is transient rather than steady, conservative constraints can be obtained, which are of order $10^{-18} - 10^{-20}$ G Mpc$^{1/2}$ (e.g.,, Murase et al. 2008b;

Dolag et al. 2011; Dermer et al. 2011). Recent results from HESS however, exclude some of the previously allowed parameter space from this type of search (see Abramowski et al. 2014). The top panel of figure 5.2 shows the model fit to the spectrum of 1ES 0229+200 obtained in the work of Taylor et al. (2011).

It was recently pointed out, that the electrons and positrons in the electromagnetic cascade of TeV emitting blazars, might collectively interact with the electrons in the integalactic medium, and lose energy by generating plasma waves, at a rate much larger than the energy loss rate through inverse-Compton scattering (Broderick et al. 2012). If such a mechanism does dominate the cooling of the pairs in intergalactic cascades, the otherwise expected GeV cascade emission from TeV emitting blazars will be suppressed. If this scenario is true, constraints on the strength of IGMFs, derived from the absence of GeV cascaded emission of TeV emitting blazars, do not hold. The fraction of the total energy of the beam dissipated in heating the intergalactic medium due to such instabilities, depends on the properties of the pair beam and those of the plasma which it traverses, and is currently a topic of debate (see Miniati & Elyiv 2013; Sironi & Giannios 2014 and references therein).

5.1.3 Hadronic origin

Along with electrons, protons may also be accelerated in blazars. As discussed in section 1.3, AGN with their black-holes, jets and hot-spots are some of the few astrophysical sites where UHECR confinement is expected to be possible. Theoretically, the magnetic luminosity of the relativistic outflow of the source, that is, the energy density of the magnetic field, must satisfy $L_B \gtrsim 10^{47.2}\, Z^{-2} E_{20}^2 \Gamma_1^2$ erg s^{-1}, where $E = 10^{20}\,\mathrm{eV}/E_{20}$ is the cosmic ray energy and $\Gamma = 10\,\Gamma_1$ is the Lorentz factor of the outflow (see Lemoine & Waxman 2009 for a detailed derivation). This limit places a stringent constraint on the candidate sources, as these are luminosities typically reached only by FRII-type galaxies.

Apart from the very high energy output required in the form of hadrons, hadronic models strain to account for the observed rapid variability of blazar gamma-ray spectra. Leptonic models in general provide a simpler model for the blazar emission, where only one primary population of particles is responsible for the observed non-thermal blazar emission. Further, in SSC models, observations of correlated, multi wavelength, blazar variability arise naturally and can easily explain such observations. However, for a fraction of TeV emitting blazars, the parameters required in order for classical SSC models to fit

the data are extreme and suggest the need for alternative models. In particular, a fraction of VHE detected blazars, exhibit spectra that, after correcting for the expected absorption of the intrinsic emission by the intervening EBL, are exceptionally hard, peaking at energy ~ 1 TeV or higher. For classical SSC models to explain these observations, an extremely low magnetic field (orders of magnitude below equipartition) and/or a very large doppler factor are required ($D \sim 100$) in order to fit the observations. These observations, which challenge pure SSC interpretation have given rise to more complicated leptonic models, which provide alternative possible explanations for these objects (e.g., Aharonian et al. 2006; Tavecchio et al. 2011; Zacharopoulou et al. 2011; Lefa et al. 2011). In these cases, a hadronic origin is a natural alternative, which can provide an attractive interpretation of the data, if it proceeds via an efficient gamma-ray production mechanism.

High energy protons can produce secondary gamma-rays either via photo-hadronic pion production or Bethe-Heitler pair production, $p + \gamma \longrightarrow p + e^+ + e^-$ (see section 2.2 as well as e.g., Mannheim 1993). In the case of heavier nuclei, photo-disintegration should also lead to gamma-ray production. It was recently shown by Murase et al. (2012); Tavecchio (2014) that a number of extreme VHE BL Lacs are capable of accelerating protons to $E_p^{\rm max} \lesssim 10$ EeV and nuclei up to $Z \cdot E_p^{\rm max}$, assuming the validity of the SSC model (i.e. deriving blazar parameters using the SSC model and applying these parameters to hadrons). Higher proton energies ($\sim 10^{20}$ eV) are achievable in blazars in hadronic models, where the SSC model is abandoned and instead a highly magnetised blazar jet with $B \sim 10 - 100$ G is considered (Aharonian 2000; Mücke et al. 2003) and in some other non-standard acceleration models (see discussion in section 5.4).

An alternative model for the gamma-ray emission of blazars is proton-induced intergalactic cascade emission. UHE gamma-rays and pairs seeded by UHECRs via photo-meson production on the EBL could cascade in the intergalactic medium (e.g., Ferrigno et al. 2005; Essey & Kusenko 2010, 2013; Essey et al. 2010, 2011; Murase et al. 2012; Prosekin et al. 2012). If the magnetic field in the vicinity of the source is not strong, then UHECRs will propagate away with little deflection and decay in the intergalactic medium, where their products will initiate inverse-Compton cascades much as they do in the case where the primary particles are leptons. However, there will be differences in the observed gamma-ray spectra, since, in the case of UHECR primaries, the injection energies are much higher to start with and there is continuous injection of high energy electrons from Bethe-Heitler pair production. The Bethe-Heitler pair production, leads to

a tail of emission, that extends deeper into the TeV than is expected in leptonic models. Recently, Takami et al. (2013) showed how this tail could be measured in the integrated flux above $\sim 500\,\mathrm{GeV}$ (depending on source redshift) for several luminous sources with $z \lesssim 1$ with the future CTA, to distinguish between leptonic and the UHECR induced inverse-Compton cascade origin (see also Zech & Cerruti 2013 for the capabilities of the approach for a statistical discrimination). Taking the same argument to extreme redshifts, Aharonian et al. (2013) showed that the discovery of TeV radiation from a source with $z \gtrsim 1$ could only be explained as this type of UHECR cascade emission with conventional physics (to date sources up to $z \lesssim 0.5$ have been observed at VHE). In the bottom panel of figure 5.2 the model fit to the spectrum of 1ES 0229+200 in the UHECR cascade scenario from the work of Essey & Kusenko (2010) is shown.

On the other hand, if the UHECRs are accelerated in blazars that are embedded in regions where the magnetic field strength is at the level of 10 nG or higher, such as a filament or cluster of large scale structure, they will inevitably give rise to secondary electrons, carrying a few percent of the proton energy, which will radiate synchrotron photons inhibiting the development of the inverse-Compton cascade. In figure 2.9 we saw that electrons with energy $E_e \gtrsim 10^{18}$ eV undergo synchrotron cooling before undergoing inverse-Compton scattering when the magnetic field strength is $\gtrsim$ few nG. The characteristic energy of the synchrotron emission (which is given by equation 2.24) is in the GeV band for the magnetic fields expected in filaments ($10^{-9} - 10^{-7}$ G) and in the TeV band for the higher magnetic field strengths expected in galaxy clusters ($\sim 10^{-7} - 10^{-5}$ G). The detectability of such signatures in a general framework has been studied analytically and by Monte-Carlo (concentrating on the synchrotron emission and without including the electromagnetic cascade component) by Gabici & Aharonian (2005), Gabici & Aharonian (2007) and Kotera et al. (2010). Prosekin et al. (2011) studied the expected signature from this model for hypothetical UHECR sources located at high redshifts, when the energy conversion from protons to secondary particles was significantly more effective, because of the denser and more energetic CMB in the past. In sources that accelerate UHECRs, whether this secondary synchrotron signal will dominate over the UHECR induced inverse-Compton cascade signal, depends on the magnetic field strength and configuration, not only in the vicinity of the source but also in the intergalactic medium, as is discussed in section 5.1.4.

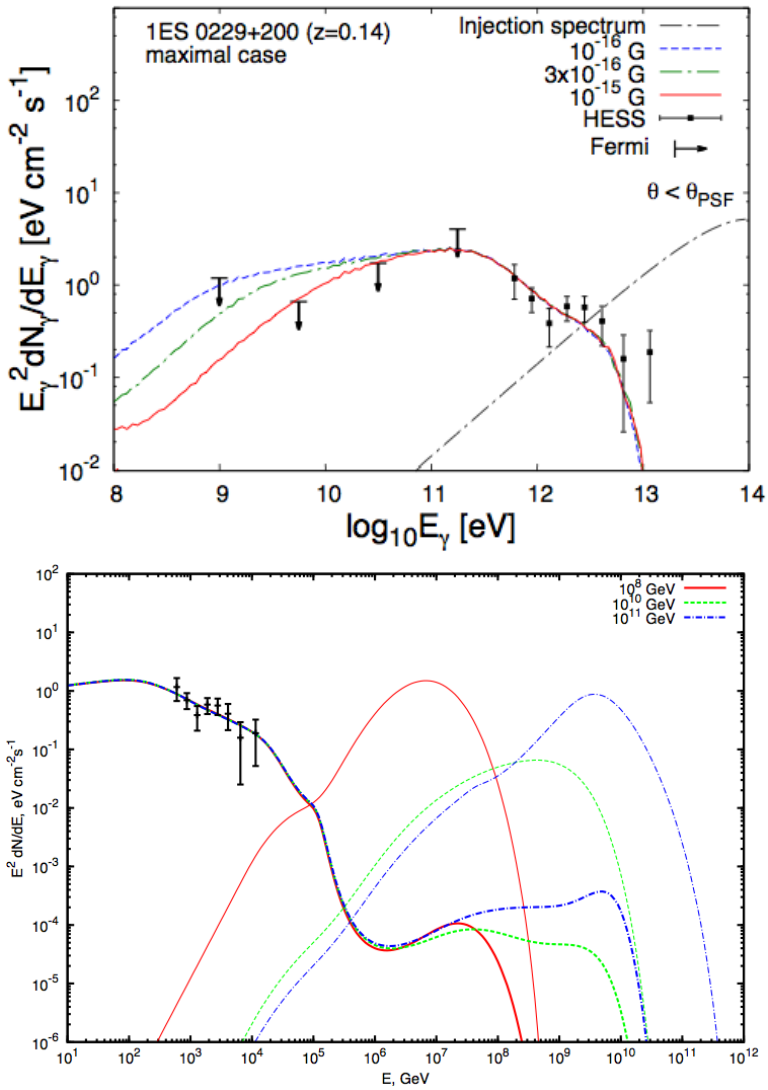

Figure 5.2. Model fits to the spectrum of a blazar at redshift $z = 0.14$. Data points correspond to the gamma-ray spectrum of the blazar 1ES 0229+200.
Top: A leptonic origin of the emission is assumed. Different model fits show the expected flux for different average strengths of homogeneous extragalactic magnetic fields with correlation length, $\lambda_{\rm coh} = 1$ Mpc. Image from Taylor et al. (2011).
Bottom: A UHECR cascade origin of the emission is assumed and the signal expected for a range of maximum UHECR proton injection energies, $E_{\rm max}$ is shown. Neutrino flux predictions are also shown. Extragalactic magnetic fields of negligible strength have been assumed. The injected isotropic equivalent UHECR luminosity in the simulations depends on the maximum injection energy as $L_{\rm cr,iso} = 6 \times 10^{48}$ erg s^{-1} for $E_{\rm max} = 10^{17}$ eV (red), $L_{\rm cr,iso} = 2 \times 10^{46}$ erg s^{-1} for $E_{\rm max} = 10^{19}$ eV (green), $L_{\rm cr,iso} = 9 \times 10^{45}$ erg s^{-1} for $E_{\rm max} = 10^{21}$ eV (blue). Image from Essey & Kusenko (2010).

5.1.4 The role of magnetic fields

We saw in section 3.1 that our knowledge of IGMFs on scales larger than galaxy clusters remains very loosely constrained by observations. Constraints from *Fermi*-LAT blazar observations place lower bounds on the IGMF in voids of $\sim 10^{-17}\,\mathrm{G\,Mpc}^{1/2}$ as discussed in section 5.1.2, whereas upper limits from Faraday Rotation and the CMB constrain the mean IGMF strength to be below $B_{\mathrm{mean}}\,\lambda^{1/2} \lesssim 10^{-8}\,\mathrm{G\,Mpc}^{1/2}$. Nonetheless, one expects the IGMF to be highly structured, with filament and cluster regions supporting significant magnetic fields ($B \gtrsim 10^{-8}$ G).

UHECR induced inverse-Compton cascades are expected to produce almost non-variable, or very slowly variable emission, that has been shown to be a good fit to the TeV spectra of a number of extreme blazars, assuming very low intergalactic magnetic fields. In the presence of IGMFs, the deflection that the cascade electrons will suffer in one cooling time can be estimated by considering the ratio of their Larmor radius, r_{Lar} at a given energy to the inverse-Compton cooling distance (equation 2.21)

$$\theta_e \sim \frac{D_{\mathrm{IC}}}{r_{\mathrm{Lar}}} = 1^{\circ} \left(\frac{B}{10^{-16}\,\mathrm{G}}\right) \left(\frac{E_e}{1\ \mathrm{TeV}}.\right)^{-2}, \tag{5.1}$$

Therefore, for the UHECR-induced inverse-Compton cascade to be observable, very weak IGMFs are required, with strengths in voids of order $B_{\mathrm{voids}}\,\lambda^{1/2} \lesssim 10^{-15} - 10^{-14}\,\mathrm{G\,Mpc}^{1/2}$. For stronger fields, the cascade radiation at TeV energies is diluted by deflections of pairs in the IGMF, as shown in Aharonian et al. (1994). Even if intervening IGMFs are weak enough that the cascade can propagate unsuppressed, it is also necessary that the magnetic field strength in the vicinity of the source is low enough ($\ll 1$ nG) to avoid a suppression of the cascade due to synchrotron losses by the first generation of electrons as discussed in Gabici & Aharonian (2007). This point was demonstrated in Murase et al. (2012) who showed that structured IGMFs in the vicinity of the accelerator suppress the resulting gamma-ray flux by more than one order of magnitude compared to the case without them. This inverse-Compton cascade component is not included in the calculations presented here, as it has been studied extensively by the various authors cited above, and is not within the scope of this work. Contamination from this channel is expected to contribute mostly below $\sim 100\,\mathrm{GeV}$, and the primary aim here is to study the peak and tail of the observed VHE emission of a number of sources that challenge leptonic models. Besides, the level at which this component contributes is very uncertain due to possible dilution in

the IGMF (see discussion in section 5.4).

In what follows it is shown that the synchrotron signal of secondary UHE electrons produced in blazars located in magnetised environments can also successfully reproduce the spectra observed in certain extreme hard-spectrum blazars. Further, it is shown that, this signal is unavoidable if blazars are sources of UHECRs, and that the energy flux at the peak energy is insensitive to the overall strength of the IGMF. Finally, it is demonstrated that the variability of blazar gamma-ray emission can be accommodated by the synchrotron emission of secondary products of UHE photons, if these are produced inside the source in accelerators of UHECRs.

5.2 Methodology

5.2.1 Selection of sources

A number of TeV HBLs, observed with ground based IACTs since the launch of the *Fermi*-LAT in August 2008, are considered. For all TeV blazars observed after that date there exist simultaneous GeV observations (or upper limits) due to full time operation of the *Fermi*-LAT. The present study focuses on high redshift HBLs, as the most extreme accelerators are likely to reside at higher redshifts. Blazars for which there exist long-term observations are of particular interest, so as to constrain their variability properties.

The HBL 1ES 0229+200 is a relatively distant hard spectrum source, that has been studied extensively. The observed spectral index $\Gamma_{\rm VHE} \simeq 2.5$ suggests a very hard intrinsic emission. Its high energy peak is at energy, $E \geq 10$ TeV. Under the assumption that the intrinsic spectrum cannot be harder than $\Gamma \simeq 1.5$ in leptonic models, it has been inferred that the EBL must be very low, close to the minimum inferred by resolved galaxy counts in order to be consistent with the observed spectrum of 1ES 0229+200 (Aharonian et al. 2007). The source has also been used to place lower limits on the strength of IGMFs in the voids of large scale structure, under the assumption of a purely leptonic origin of the gamma-ray emission (see section 5.1.2 and references therein). The gamma-ray spectrum of the source is also possible to explain if the emission is due to inverse-Compton cascades seeded by UHECRs (e.g., Essey & Kusenko 2010; Murase et al. 2012). If the UHECR cascade mechanism is responsible for the observed spectrum, the lower limits of the IGMF inferred are no longer valid, nor are the EBL limits inferred from the study of this source. In addition, a number of non-conventional physics models have been considered in relation to

its unusually hard spectrum (e.g., Horns & Meyer 2012). There is an ongoing VERITAS campaign for deep observations of this object (Dumm 2013), where the first hints for variability on year-long timescales have been reported (Aliu et al. 2014). If this variability is confirmed, it will challenge the UHECR cascade origin of the observed VHE emission as the secondary emission from this channel is not expected to exhibit variability at such timescales. The HBLs RGB J0710+591 and 1ES 1218+304, which have $\Gamma_{\rm VHE} \simeq 2.7$ (Acciari et al. 2010a) and $\Gamma_{\rm VHE} \simeq 3.0$ (Albert et al. 2006; Fortin 2008) respectively, are also studied. There is no reported variability in the gamma-ray emission of RGB J0710+591, whereas 1ES 1218+304 exhibits a $\sim$ 90 hour variability in the VHE band (Acciari et al. 2010b). RGB J0710+591 and 1ES 1218+304 have also been used to set constraints on the IGMF strength assuming a leptonic origin of the emission (Taylor et al. 2011; Huan et al. 2011; Arlen et al. 2012).

PG 1553+113 is a very distant HBL, first observed with HESS in 2006 (Aharonian et al. 2006). Its redshift is uncertain, due to inability to resolve any of the features of the spectrum of the host galaxy, which is not uncommon in blazars as the beamed non-thermal emission often obscures the host galaxy. The latest studies of this object estimate $z = 0.43 - 0.58$ by studying the Lyman forest absorption of the spectrum of this source, by the intervening intergalactic medium (Danforth et al. 2010), making it one of the most distant TeV blazars known. From the requirement that there is no upturn to the spectrum after correction for EBL absorption an upper bound on the redshift of $z < 0.62$ has been obtained (Dumm 2013). PG 1553+113 has a hard GeV spectrum $\Gamma_{\rm LAT} \simeq 1.7$ but a very soft TeV spectrum, $\Gamma_{\rm VHE} \simeq 4.3$ and exhibits no short term variability in the GeV band. In the TeV band hints for a low amplitude variability in the total flux on year-long timescales have been reported Aleksic et al. (2012b). In 2012, the observation of a flare from this source was reported (Steele et al. 2012). The main parameters of the blazars studied are summarised in table 5.2.1.

	z	$\Gamma_{\rm VHE}$	$t_{\rm V}$
1ES 0229+200	0.14	2.5	$\sim$ yr?
RGB J0710+591	0.13	2.7	none
1ES 1218+304	0.18	3.0	$\sim$ 90 hours
PG 1553+113	0.43-0.58	4.3	$\sim$ yr?

Table 5.1. Redshift, z, observed spectral spectral index $\Gamma_{\rm VHE}$, and inferred variability $t_{\rm V}$ of the blazars studied (see text for references). For PG 1553+113, whose redshift is not confirmed, $z = 0.43$ is assumed.

5.2.2 Magnetic field model

As discussed in section 3.1, the most sophisticated numerical simulations of the large scale distribution of magnetic fields in the universe (e.g., Ryu et al. 1998; Dolag et al. 2005; Das et al. 2008) do not converge as to the filling factor of magnetic fields, especially in the weak magnetic field regime that one expects for IGMFs in voids.

Here, the more practical phenomenological method of Kotera & Lemoine (2008a) for modelling the structured magnetic fields in the universe is adopted. The method relies on mapping the strength of magnetic fields, B, to the underlying matter density distribution ρ, following analytic relations of the form $B = B_0 f(\rho)$, where B_0 is a normalisation factor. A model of the form

$$f_{\rm contrast}(\rho) = \rho \left[1 + \left(\frac{\rho}{\langle \rho \rangle} \right)^{-2} \right]^{-1}, \tag{5.2}$$

is considered, which is motivated by physical arguments related to the mechanism of amplification of magnetic fields during structure formation (see e.g. discussion in 3.1.3). This relation ("contrast model" of Kotera & Lemoine 2008a), is an adhoc model, which aims to capture a situation in which the magnetic field in the voids of large scale structure is suppressed with respect to the magnetisation in denser regions, where magnetic pollution is expected to have taken place through e.g., starburst, radio galaxies. The synchrotron emission calculated in this work depends very weakly on the chosen magnetic field model, as the differences between different models are only major in the voids of large scale structure.

To model the density field, a dark matter simulation volume, which is obtained with the hydrodynamical code RAMSES (Teyssier 2002), has been used. The distribution of dark matter is a good description of the underlying density field. The simulation volume is given by a 512^3 cube, which describes a volume of size $200\,h^{-1}$ Mpc comoving. A standard ΛCDM model is assumed in the dark matter simulation and throughout this work, with $\Omega_\Lambda = 0.7$, $\Omega_{\rm M} = 0.3$ and Hubble constant $H_0 = 70$ km s^{-1} Mpc^{-1}. Each cell of the simulation is considered as an independent scattering centre with coherence length $\lambda_{\rm coh} = 0.39\,h^{-1}$ Mpc comoving, with a randomly oriented magnetic field direction. A slice through the magnetic field volume can be seen in figure 5.3.

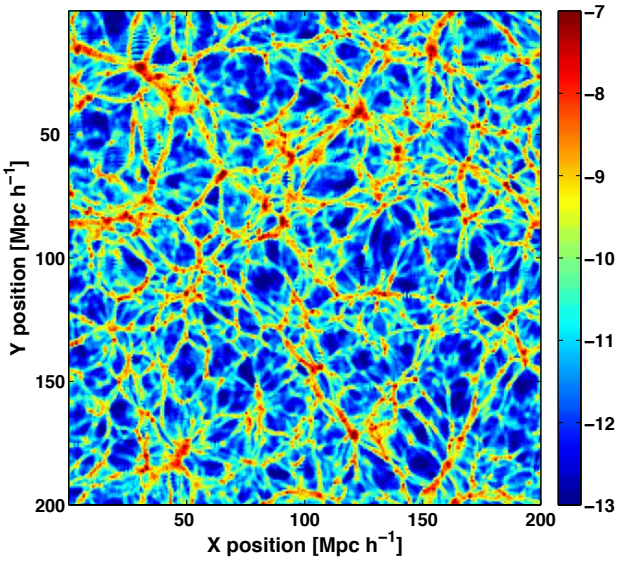

Figure 5.3. Slice through the magnetic field in the simulation volume. The colour-bar gives $\log B$ in Gauss. The slice shown has been obtained considering a normalisation factor $B_0 = 1$ nG (see text). The coherence length of individual scattering centres is $0.39\,h^{-1}$ Mpc comoving.

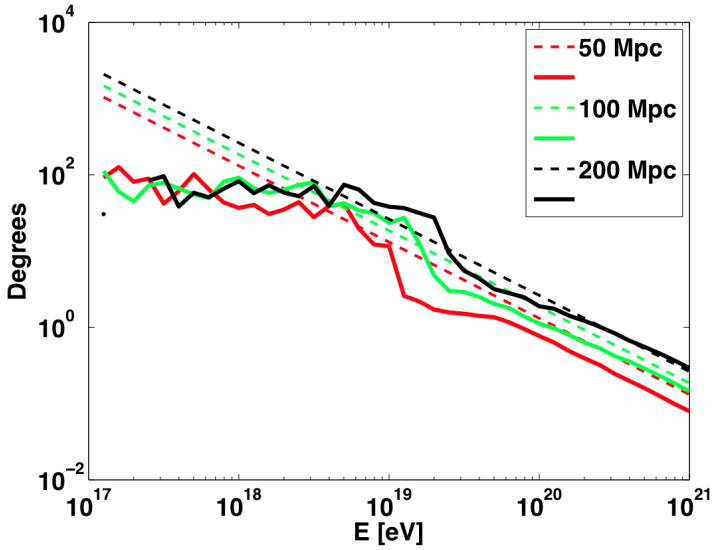

Figure 5.4. Median deflection angle at different distances from the source as a function of energy of the propagating protons in the simulations (solid lines). The dashed lines give the deflection angle expected based on the analytical prediction of Waxman & Miralda-Escude (1996) (equation 3.5). The noise in the numerical results is statistical.

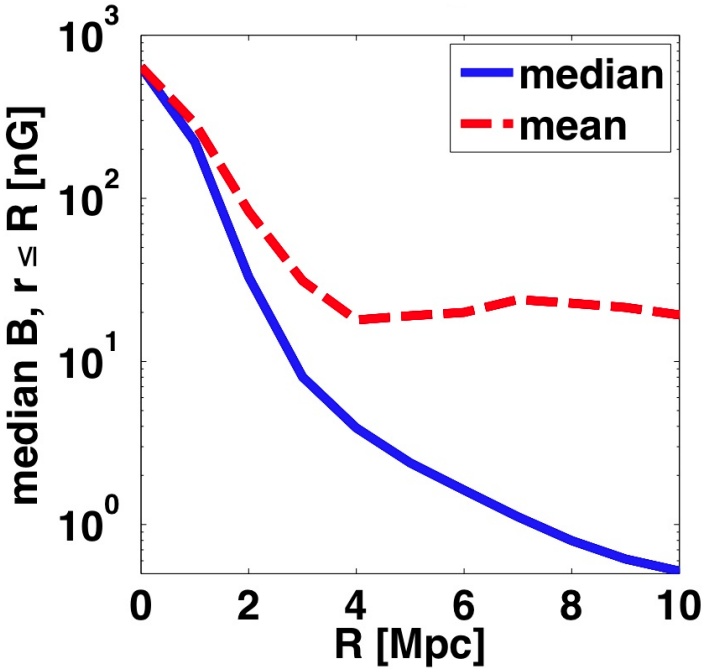

Figure 5.5. Profile of the mean and median magnetic field strength as a function of distance from the source, in the vicinity of the source in the simulation volume. The profile shown corresponds to a normalisation factor $B_0 = 50$ nG (see text).

To verify the robustness of the simulations of the UHECR propagation in a magnetised medium, the deflection angles of protons in the simulations are compared to the analytical prediction of Waxman & Miralda-Escude (1996) (equation 3.5). As shown in figure 5.4, at ultra-high energies the median deflection angle suffered by protons in the simulations is in acceptable agreement with the analytical prediction. At lower energies, the curves obtained numerically deviate from the analytical prediction as protons enter a diffusive regime, the curves saturate at 90° and equation 3.5 no longer holds.

5.2.3 Simulations

The expected gamma-ray signal is modelled through a combination of numerical Monte Carlo simulations and solving the kinetic equations of the particles in the simulations. For the propagation of hadrons emitted by the blazars in the simulation volume, CRPropa 2.0 (Kampert et al. 2013) in 3D mode is used. CRPropa models the interactions of hadrons with the radio, CMB and IR backgrounds and subsequent production of electron/positron pairs, mesons and neutrinos. The deflections and time delays of hadrons in

cosmic magnetic fields are also handled. There are some limitations in the treatment of electromagnetic cascades with CRPropa and for this reason the code presented in Murase (2012), which solves the kinetic equations of the leptons in the simulations at every time step, taking full account of energy losses and interactions with background photons, is used here instead.

In CRPropa, pion production of protons on the CMB is simulated with the SOPHIA package (Mücke et al. 1999) and Bethe-Heitler pair production is treated following the parametrisation of Kelner & Aharonian (2008). The equations of motion of each hadron are solved at every time step, deflections are calculated analytically and a new position and momentum for each particle are determined.

Particles are injected from a filament in the simulation volume. The profile of the magnetic field strength in the vicinity of the source is shown in figure 5.5. The value of B_0 is varied so as to reproduce the typical magnetic field strength in filaments and in the outskirts of galaxy clusters. Quantitatively, with the structured field model presented in section 5.2.2, a normalization factor $B_0 = 1, 2.5, 16, 50$ nG corresponds to a volume averaged magnetic field over 3 Mpc, $\bar{B} = 6, 16, 100, 316$ nG respectively. The size of the magnetised region has been chosen to reflect the typical radius of an overdense region in a cluster of galaxies or a filament. In what follows, the term "magnetised region" refers to the 3 Mpc radius sphere around the source, with mean field $\bar{B}$.

For the UHECR primaries, a pure proton composition is injected. A power-law spectrum of the form $\mathrm{d}N/\mathrm{d}E \propto E^{-\alpha}$ is considered, with isotropic cosmic ray luminosity above 10^{18} eV, $L_{\mathrm{cr,iso}}$ chosen so as to reproduce the observed gamma-ray fluxes of the sources studied. An abrupt cutoff of the spectrum at E_{max}, the maximum injected UHECR energy, is assumed. As a test, a spectrum with an exponential cutoff, $\exp^{-E/E_{\mathrm{max}}}$, was also considered. The results shown here were found to be insensitive to this choice. As a default, a spectral index is $\alpha = 2.0$, is used. A value of 2.0 is approximately what is expected from diffusive shock acceleration and has been shown to agree with the observed diffuse UHECR spectrum, after propagation as discussed in section 4.4. To speed up computation while having sufficient statistics at the highest energies, protons are typically injected in the simulations with a harder index and the propagated spectra are subsequently reweighed to the softer index of choice (see equation B.6). The positions and momenta of the secondary leptons produced in photohadronic interactions in CRPropa in the magnetised region are recorded. The electrons and photons with a momentum vector that points towards a pre-

defined observer at a specified distance from the source are collected, allowing a solid angle error margin of $2\pi(1-\cos\theta)$, with $\theta = 11^\circ$ to increase statistics (see geometry in figure B.1). Rather than using the inbuilt observer modes in CRPropa, the procedure defined above was used, as the former do not accurately mimic the detection of gamma-rays. The collected leptons were subsequently propagated with the kinetic code of Murase (2012).

In the lepton propagation code, as with any kinetic code time averaged fluxes are calculated (see for example the discussion in Lee 1998; Bhattacharjee & Sigl 2000 for more details). Pair production, inverse-Compton and synchrotron losses, interactions, adiabatic energy losses and higher order processes are handled. The scheme relies on solving the coupled transport equations of the ensemble of the flux of each species at every time-step. A sample transport equation for electrons, with explicit pair-production and inverse-Compton terms can be written as (Lee 1998)

$$\begin{aligned}\frac{\mathrm{d}}{\mathrm{d}t}n_e(E_e,t) = &-n_e(E_e,t)\int \mathrm{d}\varepsilon\; n_\varepsilon \int_{-1}^{+1}\mathrm{d}\mu\frac{1-\mu\beta_e}{2}\sigma_{\mathrm{IC}}(E_e,\varepsilon,\mu)\\ &+\int \mathrm{d}E'_e\; n_e(E'_e,t)\int \mathrm{d}\varepsilon\; n_\varepsilon \int_{-1}^{+1}\mathrm{d}\mu\frac{1-\mu\beta'_e}{2}\frac{\mathrm{d}\sigma_{\mathrm{IC}}}{\mathrm{d}E_{E_e}}(E_e;E'_e,\varepsilon,\mu)\\ &+\int \mathrm{d}E'_\gamma\; n_\gamma(E_\gamma,t)\int \mathrm{d}\varepsilon\; n_\varepsilon \int_{-1}^{+1}\mathrm{d}\mu\frac{1-\mu\beta_e}{2}\frac{\mathrm{d}\sigma_{\gamma\gamma}}{\mathrm{d}E_{E_\gamma}}(E_e;E_\gamma,\varepsilon,\mu)+Q(E_e,t).\end{aligned} \tag{5.3}$$

Here, n_e is the local number density of electrons, n_ε is the local number density of background photons of energy ε, β_e is the velocity of the electrons and n_γ is the number density of gamma-rays. The terms on the right hand side of the equation give the loss of electrons of energy E_e due to inverse-Compton scattering, the influx of electrons in this energy bin due to inverse-Compton scattering, the influx of electrons due to pair production and $Q(E_e,t)$ is an external source term, which accounts for external injection of electrons. The method is significantly more efficient computationally than a Monte Carlo and is sufficiently accurate when deflections are negligible, as a one dimensional propagation approximation is used. In the channel studied here, the deflections of leptons are subdominant as any deflections will be these of the UHE electrons in the magnetised region, which promptly interact via synchrotron (and they are typically in a regime where $D_{\mathrm{syn}} \ll r_{\mathrm{Lar}}$).

In the lepton propagation code, the secondary leptons produced in the CRPropa runs, are uniformly injected over the magnetised region. This is a good approximation, given

that the loss length of protons to the relevant processes (Bethe-Heitler pair production and photo-pion production) is significantly larger than the size of the magnetised region. For the magnetic field strength, the volume averaged strength over the magnetised region, out to 3 Mpc, is taken at this stage of the calculation.

The synchrotron signal that escapes from the magnetised region is calculated with this setup. A semianalytic cutoff is applied for the attenuation of the signal, that escapes the magnetised region, by the intervening EBL. The synchrotron photons are below the pair production threshold for the typical magnetic field strength in filaments, hence the gamma-ray photons observed in this case are prompt with no further deflections in the intergalactic medium. For the magnetic field strength typical in galaxy clusters some cascading of the TeV synchrotron photons might occur, but as already discussed this component will likely be isotropised by IGMFs. For the opening angle of the blazar jet, $\theta_{\rm jet} = 0.192 \simeq 11^\circ$ is considered, but the results presented here are not sensitive to this choice.

For the EBL energy density and redshift evolution, a range of models that are consistent with current observations are considered (Kneiske et al. 2004; Kneiske & Dole 2008; Franceschini et al. 2008; Inoue et al. 2013) and for the CMB a black body spectrum of temperature 2.7 K is assumed. For the URB the model of Protheroe & Biermann (1996b) and measurements of Clark et al. (1970) as implemented by CRPropa are used. Uncertainties on the spectrum and redshift evolution of the EBL and to a lesser extent of the radio background, introduce an uncertainty to the results of this work. In particular, the exact position of the cutoff energy in the TeV may vary substantially between different EBL models as it depends exponentially on τ, the optical depth to pair production on the EBL (see equations 2.17, 2.18). However, as we will see in the following section, the results are robust to the choice of EBL model for the representative range of models that have been considered in this work.

5.3 Robustness of synchrotron signal with application to specific sources

The blazars studied have gamma-ray peaks between ∼10 GeV - 10 TeV, however irrespective of their intrinsic spectra, a cut-off is observed in the TeV that strongly depends on the redshift of the source and details of the EBL spectrum and redshift evolution. The

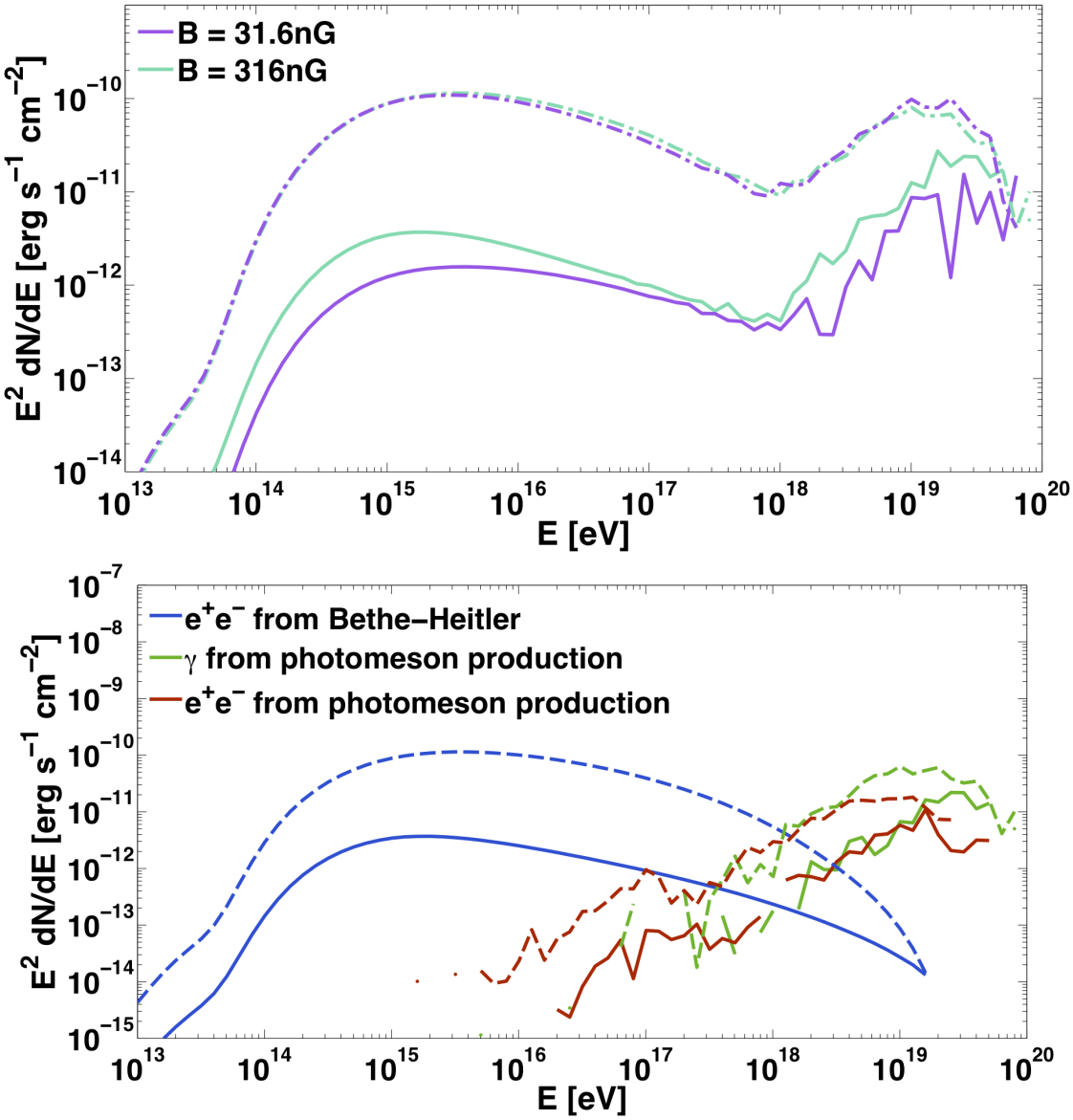

Figure 5.6. Top: Solid lines: The energy flux of secondary leptons produced by $p\gamma$ interactions in a 3 Mpc magnetised region around a source at redshift $z = 0.14$ that emits UHECRs with $L_{\rm cr,iso} = 10^{47}$erg s^{-1}. The magnetic field profile is shown in figure 5.5. The volume averaged magnetic field strength in the magnetised region is $\bar{B} = 31.6$ nG (purple), 316 nG (green). The peak at $\sim 10^{15}$ eV is due to Bethe-Heitler pair production and the high energy peak is due to photo-pion production and subsequent pion decay. The noise in the pion bump statistical. Dot-dashed lines: The energy flux of secondary leptons produced by $p\gamma$ interactions beyond the first 3 Mpc of propagation.
Bottom: Same as in top panel for $\bar{B} = 316$ nG only. The contribution of Bethe-Heitler pair production (blue) and photomeson production to the secondary lepton flux are shown separately and in the later case photons (green) are shown separately from the e^+e^- pairs (red).

optical depth of the EBL to 1 TeV gamma-rays is thought to be $\mathcal{O}(1)$ at $z \sim 0.1$ (see for example figure 2.8), hence for all the sources studied, a strong suppression of the intrinsic source flux above this energy is expected.

In the secondary synchrotron model, the main contribution to the secondary energy flux within the magnetised region will be from photomeson production due to the significantly shorter cooling length compared to that of Bethe-Heitler pair production. This can be seen in figure 5.6 where the solid lines show the secondary leptons (photons and electron-positron pairs) produced inside the magnetised region. We can also see that for the chosen injection spectrum, the peak of the energy spectrum of the first generation of electrons from photomeson production is at $E_e \sim 10^{19}$ eV, as a result of the competition between the abundance of primary protons with increasing energy and the energy loss rate of the primary protons. Thus, the characteristic energy of the synchrotron emission will be at $E_{\rm syn} \sim 6.8 \times 10^{11} (B/100 \text{ nG})$ eV (c.f. equation 2.24), which for the typical magnetic fields expected in the large scale structures we study, is near the peak of the blazar spectra. The synchrotron emission which is emitted with energy beyond few TeV, will be absorbed by the EBL. As already discussed this low energy absorbed component is expected to be diluted by IGMFs and not contribute to the GeV flux of the source. In this sense the results shown here correspond to the limit where IGMFs are strong enough to isotropise this low energy cascade component.

5.3.1 1ES 0229+200

Figure 5.7 shows the model prediction of the secondary synchrotron signal to the observed spectrum of 1ES 0229+200 for $\bar{B}$ in the range $6-316$ nG. The assumed isotropic equivalent luminosity is $L_{\rm cr,iso} = 10^{47}$erg s^{-1}. For this source, whose spectrum peaks at $\gtrsim 10$ TeV, $\bar{B} = 316$ nG is consistent with the combined GeV-TeV data, whereas considering a lower value of $\bar{B}$ results in a poorer fit.

In figure 5.8, the robustness of the model fit to the uncertainty in the intensity and redshift evolution of the EBL is demonstrated, by considering a range of EBL models that are consistent with existing limits and measurements. The goodness of the model fit to the spectrum of 1ES 0229+200 depends on the EBL assumed and the best fit is obtained with the lower limit model of Kneiske & Dole (2008). All models considered, slightly under-predict the energy flux at the highest TeV datapoint, but for the fit with the EBL model of Kneiske & Dole (2008) this disagreement is very small. Considering a

slightly higher value of $\bar{B}$ would improve the consistency of the model with the last TeV data-point.

In figure 5.9 the robustness of the model predictions to the choice of UHECR injection parameters, namely the maximum UHECR injected energy, $E_{\rm max}$ and spectral index, α is shown. The top panel shows the model fit to the spectrum of 1ES 0229+200, for $E_{\rm max} = 10^{20.5}$ eV, 10^{21} eV; higher values of $E_{\rm max}$ are hard to accommodate theoretically. Here, $\bar{B} = 316$ nG has been assumed, and the assumed $L_{\rm cr,iso}$ is given in the figure legend. Lower values of $E_{\rm max}$ result in a poorer fit, implying that if the synchrotron channel presented here is at the origin of the measured blazar spectrum, then these accelerators can reach the highest observed energies of cosmic rays.

Considering a higher value of $E_{\rm max}$ results in a harder model spectrum, increasing the consistency to the highest energy TeV data-point while easing the luminosity requirements on the accelerator. This is as expected intuitively as higher energy UHECRs undergo $p\gamma$ interactions quicker thus creating more flux in the first few megaparsecs of propagation. In the bottom panel, the model prediction for the spectrum of 1ES 0229+200 for $\alpha = 2.0, 2.3$ is shown. A softer spectrum increases the required $L_{\rm cr,iso}$, but the model prediction remains otherwise unaltered.

5.3.2 Other sources

The fits to the combined GeV-TeV band spectra found in the UHECR secondary synchrotron model under the assumption of $\bar{B} = 100$ nG, in a 3 Mpc magnetised region around the source, are shown in figure 5.10 for RGB J0710+591, 1ES 1218+304 and PG 1553+113. The isotropic equivalent luminosity required, $L_{\rm cr,iso}$, for the model shown, is given in the legend. For RGB J0710+591 the secondary synchrotron model is consistent with the data across the GeV and TeV bands and $L_{\rm cr,iso} = 10^{47}$erg s^{-1}.

The fit to the TeV data for 1ES 1218+304 is poorer, although the model is consistent with the GeV observations for this source. Considering a slightly lower value of $\bar{B}$ and/or a softer injection spectrum would fit the TeV data, at the cost of a slight increase in the required $L_{\rm cr,iso}$ as demonstrated in figure 5.7 for 1ES 0229+200. However, as already noted, the gamma-ray emission from this source exhibits a variability in $\sim$ day timescales. The observed variability does not favour a secondary UHECR synchrotron origin of the spectrum of this source (see discussion in section 5.3.3).

The fit to the spectrum of PG 1553+113 is poor. The main source of discrepancy

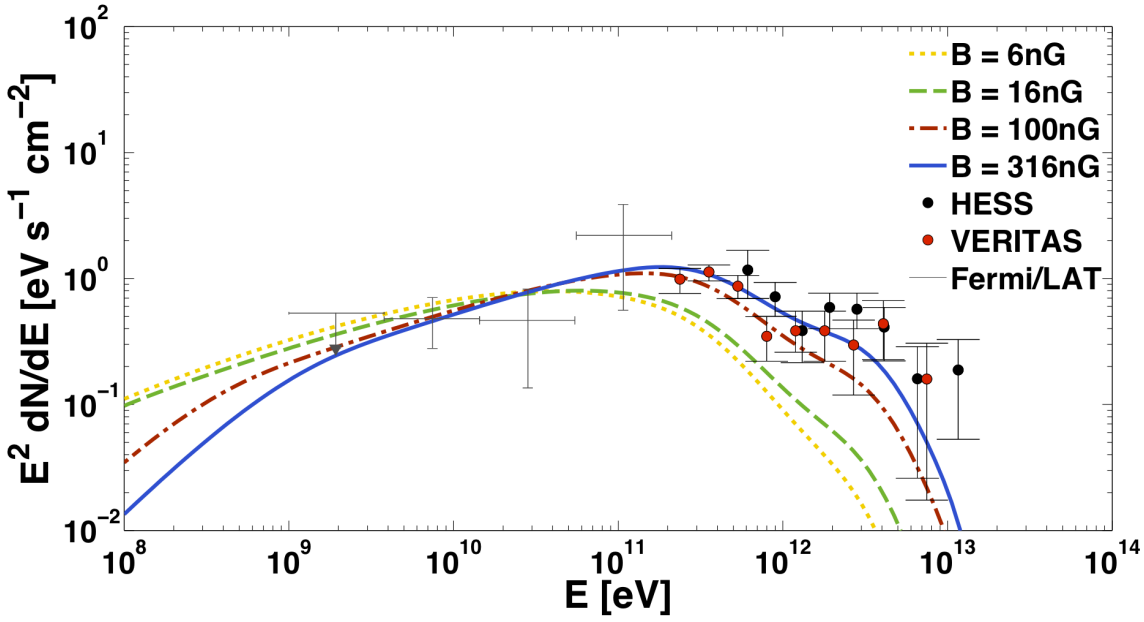

Figure 5.7. The fit of the UHECR secondary synchrotron model to the spectrum of 1ES 0229+200, assuming a mean strength of the magnetic field in the magnetised region, $\bar{B}$ in the range $6 - 316$ nG. Here $L_{\rm cr,iso} = 10^{46.5}$erg s^{-1} has been assumed. *Fermi*-LAT data points for this source here and throughout have been adapted from Vovk et al. (2012) and TeV data are from Aharonian et al. (2007); Aliu et al. (2014). The model spectra shown account for the attenuation by the EBL, for which the model of Kneiske & Dole (2008) has been considered.

between the model predictions and the data, is an over prediction of the energy flux beyond 0.1 TeV. The TeV spectrum of this source is significantly softer than those of the other sources considered here. Considering a lower value of $\bar{B}$ and/or a softer injection spectrum, would improve the fit to the tail of the spectrum and possibly provide a fit consistent with the data. However, the required UHECR luminosity is $L_{\rm cr,iso} = 3 \times 10^{49}$erg s^{-1}; therefore, even if a better fit can be obtained, the extreme luminosity requirements make the model implausible for this source.

5.3.3 UHE photons

If UHECRs are accelerated in AGN, $p\gamma$ interactions *inside* the source should also lead to the production of UHE photons and UHE neutrons (Murase et al. 2009). Such UHE neutral particles can leave the acceleration zone, if the target photon spectrum is thermal or suppressed by synchrotron self-absorption. In particular, if the radio emission from bubbles and lobes is not too strong, the mean free path to $\gamma\gamma$ pair production is ~ 2 Mpc, which is comparable to the size of the magnetised region considered here. So about one

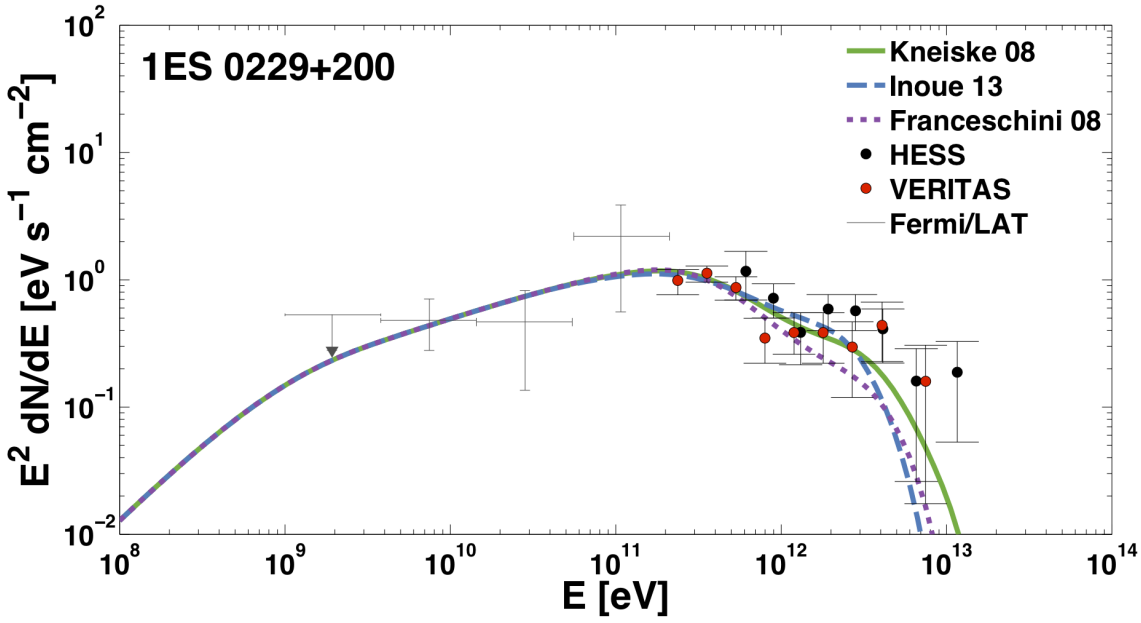

Figure 5.8. Robustness of the UHECR secondary electron synchrotron model to the EBL model considered for 1ES 0229+200. Here we show results with the EBL model of Franceschini et al. (2008)(purple dotted), Kneiske & Dole (2008) (green solid), Inoue et al. (2013) (blue long dashed). Model parameters assumed are $\bar{B} = 316$ nG and $L_{\rm cr,iso} = 10^{46.5}$erg s^{-1}.

half of the UHE photons can escape, while the other half would promptly produce electron-positron pairs in the magnetised intergalactic medium surrounding a source such as we have been discussing in this work. The secondary high energy electrons would in turn radiate synchrotron photons as in the case of runaway UHECRs that we have considered so far. This type of emission has recently been proposed and studied by Murase (2012).

One expects the signature of the secondary synchrotron emission of runaway UHE photons to differ from the emission that has been studied thus far, of runaway UHECR protons, in a number of ways. Firstly, the injection spectra in the two channels are different; in the case of runaway UHECRs the only relevant photon fields are the cosmic photon backgrounds, whereas the production spectrum of UHE photons must happen on a target photon field inside the source. Murase (2012) analytically calculated the expected UHE photon spectrum considering target photon spectra created by the synchrotron emission of electrons in the source environment. Further, and more importantly the main observable difference should be related to the different deflection properties and as a result the different timing properties of the signal in the two channels. In the UHE photon channel

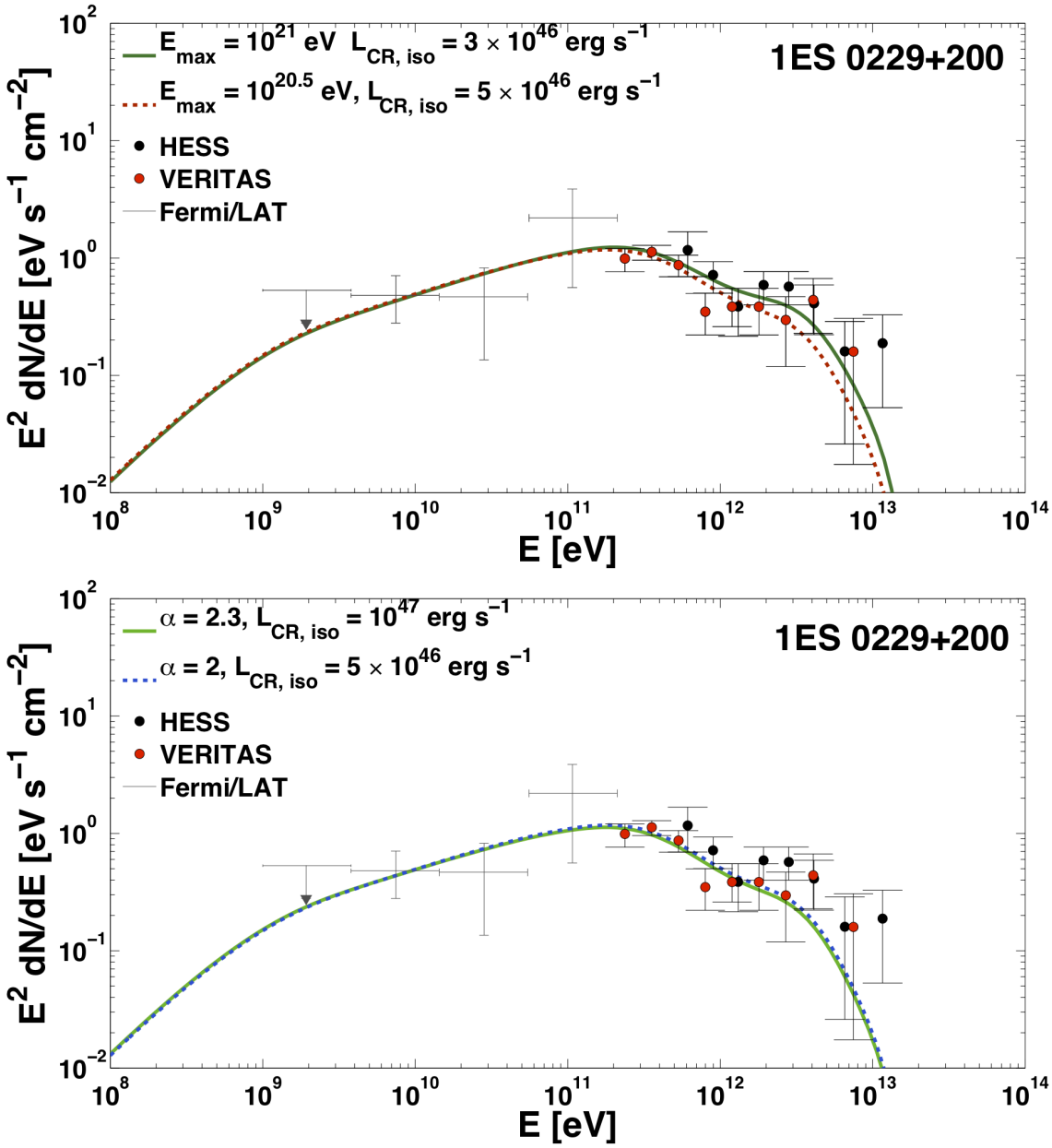

Figure 5.9. Robustness of the UHECR secondary electron synchrotron model fit to the spectrum of 1ES 0229+200, for different UHECR injection spectrum parameters. Here $\bar{B} = 316$ nG has been assumed.
Top panel: Model prediction for $E_{\max} = 10^{20.5}$ eV (red dotted line) and $E_{\max} = 10^{21}$ eV (green solid line).
Bottom panel: Model prediction for injection spectral index $\alpha = 2$ (blue dotted line) and $\alpha = 2.3$ (green solid line).

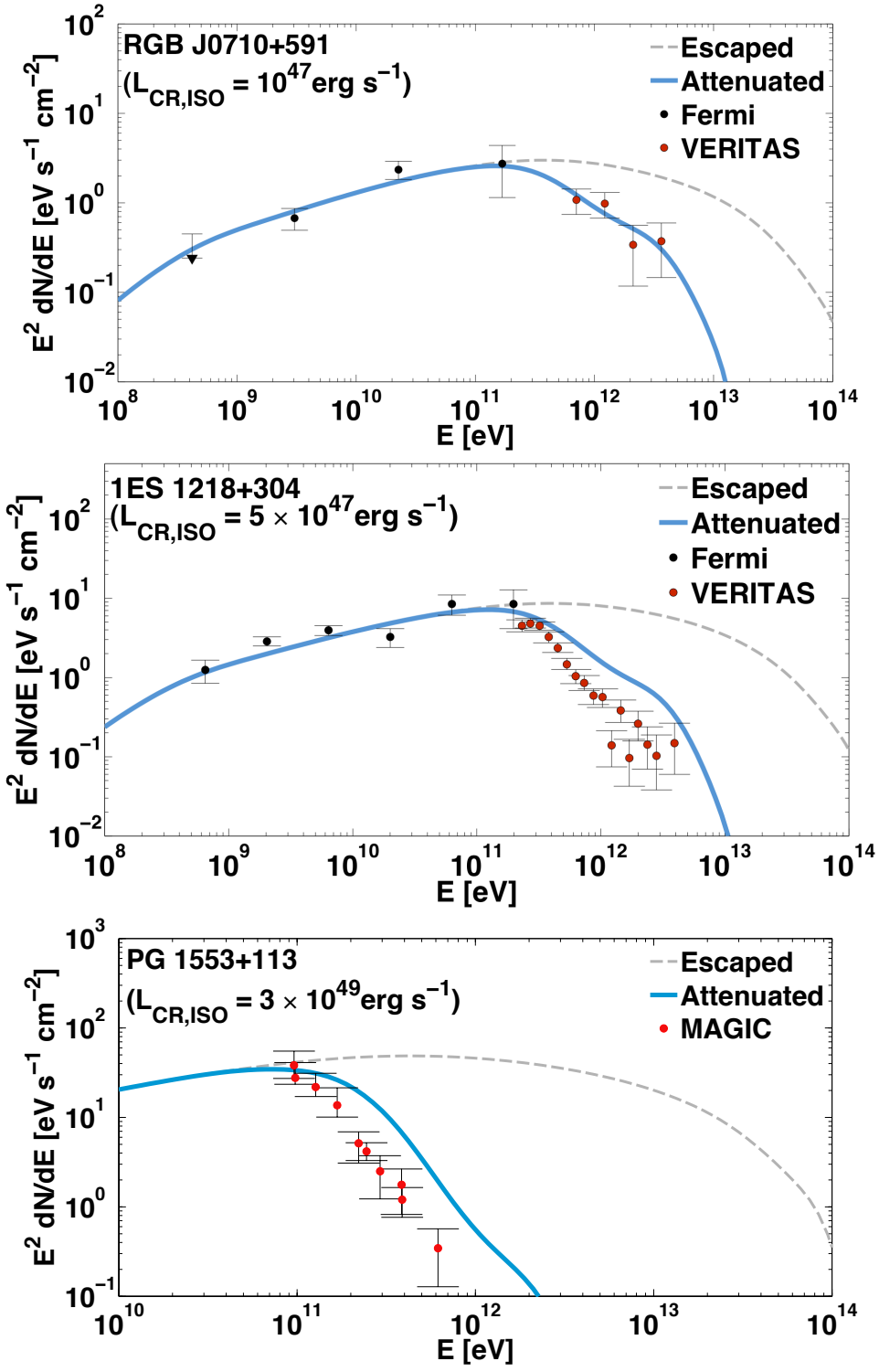

Figure 5.10. The expected photon energy flux, resulting from the UHECR secondary electron synchrotron model a magnetised region with average magnetic field strength $\bar{B} = 100$ nG for RGB J0710+591 (top), 1ES 1218+304 (middle) and PG 1553+113 (bottom). Long-dashed lines show the spectrum that escapes from the magnetised region. Blue solid lines show the spectra with account of the attenuation by the EBL, for which the model of Kneiske & Dole (2008) has been considered. Datapoints for RGB J0710+591 are from Acciari et al. (2010a), for 1ES 1218+304 from Acciari et al. (2010b) and for PG 1553+113 from Aleksic et al. (2012a).

any deflections will come from the secondary electrons and should be approximately

$$\theta_e \sim D_{\rm syn}/r_{\rm Lar} \sim 3 \times 10^{-4} (E_e/10^{19}\ {\rm eV})^{-2} (B/10\ {\rm nG})^{-1} \tag{5.4}$$

(note the difference to equation 5.1 as the relevant cooling process for electrons in this case is synchrotron emission). Typically this is a very small angle, smaller than typical values of $\theta_{\rm jet}$, hence the emission from this channel is expected to be beamed. If UHE photons are able to escape the source vicinity and enter the intergalactic medium, the mean free path to $\gamma\gamma$ pair production is $\lambda_{\gamma\gamma} \sim 2$ Mpc, which is smaller than the UHECR mean free path to photo-pion production in the intergalactic medium. Therefore, the secondary synchrotron signal from UHE photons is dominant when photo-pion production inside the source is efficient. As a result of the small deflections, the time spread δt of the signal should also be small. For a magnetised region of characteristic scale, d, Murase (2012) obtained $\delta t \sim \theta_e^2 d/2c \sim 0.3$ yr $(E_{\rm syn}/10^{2.5}\ {\rm GeV})({\rm min}[d, \lambda_{\gamma\gamma}]/{\rm Mpc})$ (c.f. equation 3.6).

In comparison the deflections suffered by UHECR protons in the magnetised region are larger, of order $\theta_p \sim \sqrt{d\ \lambda_{\rm coh}}/r_{\rm Lar} \sim 0.044\ (d/{\rm Mpc})(E/10^{20}\ {\rm eV})(\lambda_{\rm coh}/d)^{1/2}(B/10\ {\rm nG})$. The resulting time spread is also expected to be considerably larger for the UHECR proton channel, $\delta t \sim \theta_p^2 d/2c \sim 1.6 \times 10^3$ yr $(B/10\ {\rm nG})(\lambda_{\rm coh}/d)(d/{\rm Mpc})^3(E/10^{20}\ {\rm eV})^{-2}$.

In the case of blazars a characteristic signature of the UHE photon channel could be a transient event, such as a flare with a duration $\sim 0.1 - 1$ year, whereas the small time spread in the UHE photon channel implies that we may observe the echo of flaring activities. The two channels may be hard to distinguish between for a given steady gamma ray source, but if the UHE photon channel is dominant, the resulting emission will almost certainly be more variable.

Figures 5.11, 5.12 show the expected gamma ray spectra from the UHE photon channel for 1ES 0229+200 and 1ES 1218+304, motivated by their observed variability (or hints of such a variability in the case of 1ES 0229+200). Following Murase (2012), an injection spectrum of the form $L_\gamma = L_0 \times (E/E_\gamma^{\rm max})^{0.5} e^{-E_\gamma^{\rm min}/E} e^{E/E_\gamma^{\rm max}}$ has been considered. Here, the generation spectrum of UHE photons depends on the slope of the primary proton spectrum α, as well as the slope of the target photon spectrum ζ as $E_\gamma^2 {\rm d}\gamma/{\rm d}E_\gamma \propto E_p^{1+\zeta-\alpha}$. An index $\zeta \sim 1.5$ is assumed, which is typically expected for a photon field generated via synchrotron emission in AGN and $\alpha \simeq 2.0$ as throughout most of this work. The values of $E_\gamma^{\rm min} = 10^{18.5}$ eV and $E_\gamma^{\rm max} = 10^{19.5}$ eV are chosen to capture the typical energies of the

ultra high energy photons that are created through the $p\gamma$ interaction, corresponding to $E_{\rm p}^{\rm max} = 10^{20.5}$ eV. The normalisation $L_0 \simeq f_{p\gamma} L_{\rm cr,iso}$, where $f_{p\gamma}$ is the efficiency with which UHE photons are produced in $p\gamma$ interactions. For the setup considered here $f_{p\gamma} \sim 1/200$ at $E_p^{\rm max}$ is assumed. For a detailed derivation of the ultra-high energy photon generation spectrum see Murase (2012). Further, $\bar{B} = 316$ nG has been assumed in the magnetised region in the case of 1ES 0229+200 and $\bar{B} = 100$ nG in the case of 1ES 1218+304.

The model prediction is consistent with the GeV data of 1ES 0229+200 while slightly under-predicting the TeV flux. As discussed above, a slightly higher value of the magnetic field strength at the source would shift the peak of the synchrotron emission further into the TeV, providing consistency with the TeV observations for this source. The required luminosity is $L_0 = 10^{45}$erg s^{-1}, i.e. $L_{\rm cr,iso} = 2 \times 10^{47}$erg s^{-1}, similar to the required UHECR luminosity in the UHECR proton channel. In the case of UHE neutral beams the recent hints of variability of the TeV spectrum of this source in ~ 1 year timescales can be accommodated.

For 1ES 1218+304 the model prediction is consistent with the combined GeV-TeV observations of this source. The observed ∼day scale variability of this source cannot be explained by our current setup, where the UHE photons cascade over an ∼Mpc scale structured IGMF region. However, UHE neutral beams could possibly explain the variability of 1ES 1218+304, if the size of the region over which $\gamma\gamma/n\gamma$ interactions occur is significantly smaller (of order kpc), as in the model of Dermer et al. (2012) for FSRQs. Detailed work on the variability of these sources will be presented elsewhere.

Comparison of figures 5.9, 5.10 and 5.12 illustrates the differences between the two channels studied. A harder spectrum is observed in the UHECR channel for a given magnetic field strength. The injection of a spectrum with an exponential cut-off in the UHE photon channel partly explains why the resulting synchrotron spectrum in this model has a sharper cut-off than the synchrotron spectrum in the UHECR channel. A further difference comes from the contribution of the Bethe-Heitler process in the UHECR channel. The secondary pairs, that are created via Bethe-Heitler pair production, contribute to the spectrum that escapes the magnetised region, through the addition of photons with energy beyond $\sim 10^{14}$ eV via inverse-Compton scattering. This is because the Bethe-Heitler component, which peaks at $\sim 10^{15}$ eV, is below the critical energy for cooling via synchrotron emission, which is otherwise the dominant cooling mechanism in the magnetised regions we've been considering. This contribution from Bethe-Heitler pairs, results in a

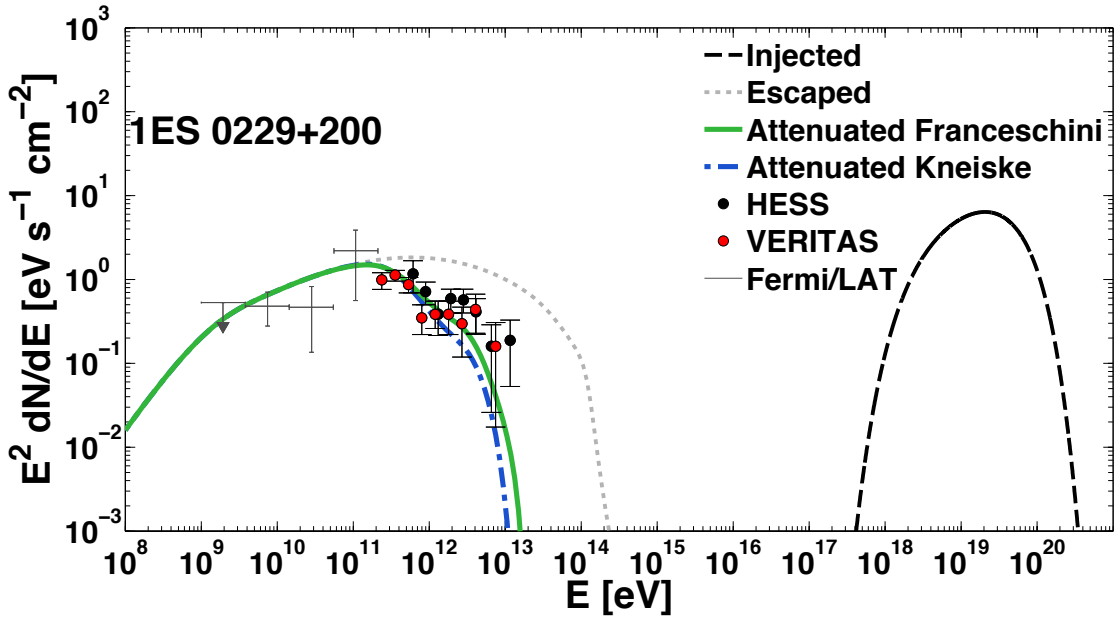

Figure 5.11. The arriving energy flux expected from the UHE photon emission escaping from a magnetised region with average magnetic field strength $\bar{B} = 316$ nG for 1ES 0229+200. The injected luminosity normalisation in ultra high energy photons is $L_0 = 10^{45}$erg s^{-1} (see text for details). The dashed black line gives the injected UHE photon spectrum, the grey dotted line shows the spectrum that escapes from the magnetised region. The green solid line and blue dot-dashed line show the expected attenuated spectra using the EBL model of Kneiske & Dole (2008) and Franceschini et al. (2008) respectively.

harder spectrum escaping the magnetised region in the UHECR channel. In this sense the observation of the UHE photon channel resulting in a softer TeV spectrum should not be considered a general result, the difference comes from the different initial conditions. To summarise, we observe that both channels are a very good fit to the observed gamma-ray spectra although discrimination between the ultra high energy photon and UHECR channels is challenging on the basis of the spectral fit alone for steady gamma-ray sources. The timing properties and the angular extension of the signal contribute towards such a discrimination, in particular the observed variability of 1ES 0229+200 and 1ES 1218+304 favour neutral beams as the population responsible for this emission.

5.4 Discussion

In 50 years of direct searches for the sources of UHECRs, as discussed in earlier chapters, we have not made conclusive progress on the subject. The proposed CTA is envisaged

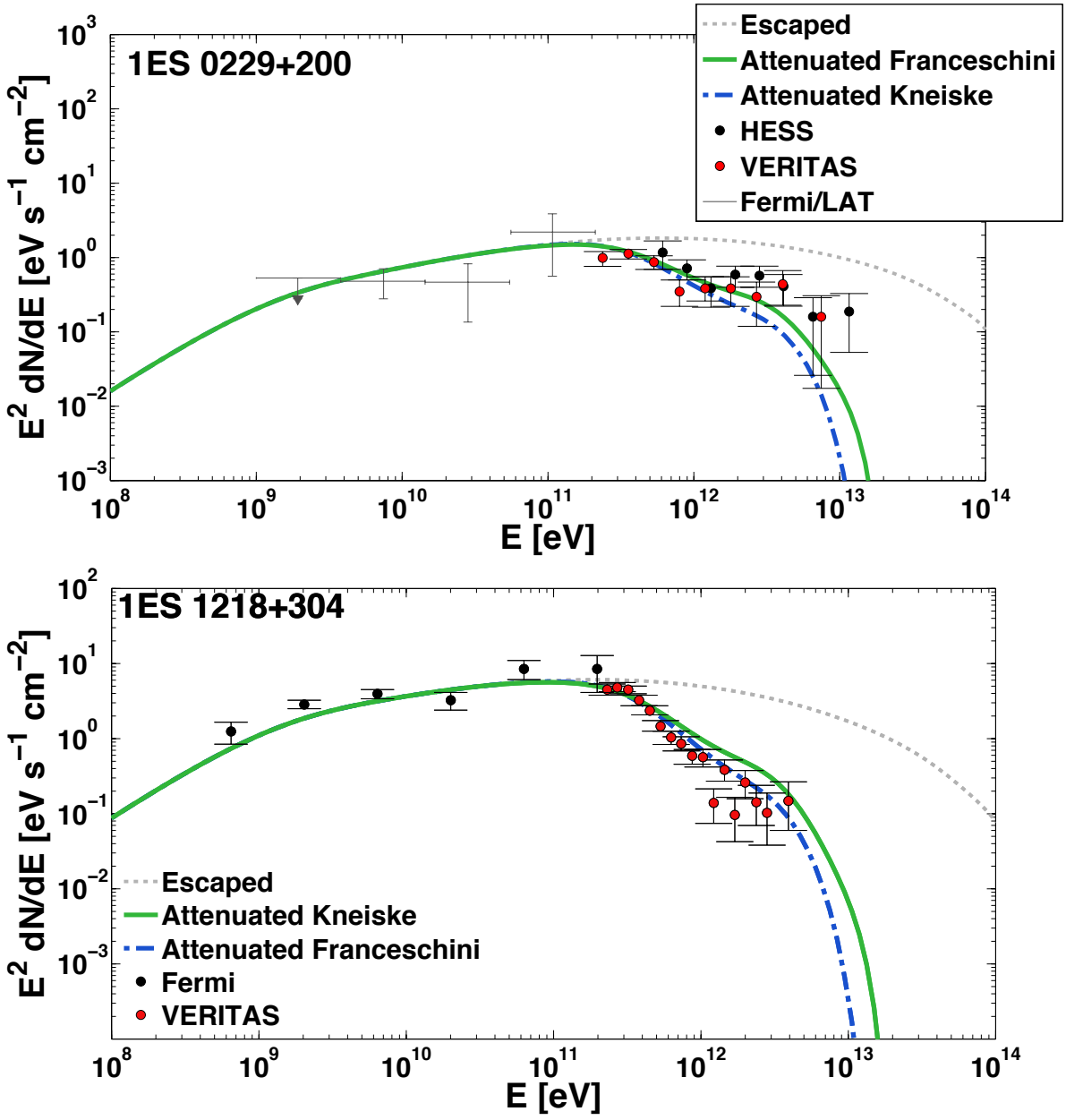

Figure 5.12. Middle: Same as figure 5.11 but zooming in at the arriving photon energy flux.
Bottom: Same as top panel but for 1ES 1218+304. The injected luminosity normalisation is $L_0 = 8 \times 10^{45}$erg s^{-1} and the volume averaged magnetic field strength inside the magnetised region is assumed to be $\bar{B} = 100$ nG.

to bring about an order of magnitude increase in VHE AGN detections and may thus allow us to make great progress in searches for the secondary emission of UHECRs. Its increased sensitivity by as much as a factor of ten compared to the current generation of IACTs, may make it possible to rule out or confirm the existence of the tail expected, if the observed VHE emission is due to a UHECR cascade. The absence of such a tail should imply that this emission is due to synchrotron radiation of secondary electrons from UHECRs or of leptonic origin. One can then examine the angular image of the source with the CTA to distinguish between these two possibilities. As shown analytically in Gabici & Aharonian (2005) and modelled numerically in Kotera et al. (2011), in the secondary electron synchrotron channel one expects a halo to form around the source as a result of the deflection of the primary protons and secondary electrons in the embedding magnetised region. Detailed modelling of the halo expected from this channel should make it possible to distinguish it from the halo expected from the leptonic channel (presented in e.g., Elyiv et al. 2009; Taylor et al. 2011).

As the loss length for protons via Bethe-Heitler pair production is of order 1 Gpc and through photo-meson production of order 100 Mpc in the absence of IGMFs one would expect the UHECR cascade signal to dominate over the secondary electron synchrotron signal. This is shown for example in figure 5.6 for a source at redshift $z = 0.14$, where we see that the secondary emissions of protons within the magnetised region are 1-2 orders of magnitude lower than the overall proton losses all the way to the observer. It was shown that, in both cases of UHECR-induced and UHE photon-induced synchrotron cascades, $L_{\rm iso,cr} \sim 10^{46} - 10^{47}$ erg s^{-1} is required. Due to the deflection of UHECRs in magnetised regions, similar UHECR luminosities are required in the case of inverse-Compton cascades propagating in the intergalactic medium, when UHECR sources are located in filaments but void IGMFs are negligible (Murase et al. 2012). The UHECR-induced inverse-Compton cascade signal however, will be further suppressed due to the deflection of the charged leptons in the cascade, if void IGMFs are non-negligible as is quantified below.

Following Kotera et al. (2011), the gamma-ray flux from a given UHECR source per

unit energy interval, can be approximated as

$$
\begin{aligned}
E_\gamma^2 \frac{\mathrm{d}N_\gamma}{\mathrm{d}E_\gamma} &\simeq f_{1d}(<B_\theta)\chi_e \frac{L_{\rm cr}}{8\pi d^2}\left(\frac{E_\gamma}{E_{\gamma,\rm max}}\right)^{1/2} \\
&\simeq 2.5\times10^{-10}\ \mathrm{GeV\ cm^{-2}\ s^{-1}} f_{1d}(<B_\theta)\chi_e \\
&\times \left(\frac{L_{E,19}}{10^{42}\ \mathrm{erg\ s^{-1}}}\right)\left(\frac{d}{100\ \mathrm{Mpc}}\right)^{-2}\left(\frac{E_\gamma}{E_{\gamma,\rm max}}\right)^{1/2},
\end{aligned}
\tag{5.5}
$$

where $\chi_e L_{\rm cr}(>E)$ is the luminosity injected in secondary photons and pairs over a distance d above cosmic ray energy E and $f_{1d}(<B_\theta)$ is the fraction of the distance in the line of sight, where the magnetic field strength is greater than B_θ. Redshift energy losses have been neglected in the above expression. For E, one may consider 10^{19} eV as below this energy the proton energy loss length via Bethe-Heitler, pair production becomes significantly larger and the contribution of lower energy particles to the observed flux can be neglected for an order of magnitude estimate. The fraction of energy transferred to pairs and pions at distances 100 Mpc $\leq d \leq$ 1 Gpc ranges from ~ 0.5 at $d = 100$ Mpc to ~ 1 at $d = 1$ Gpc (see proton energy loss lengths to dominant energy loss processes discussed in sections 2.2.1 and 2.2.2). The magnetic field strength. B_θ, is defined such that the deflection suffered by the low energy electrons at the final stage of the cascade is θ. For $\theta = 1°$, $B_\theta \sim 2\times10^{-14}$ G from equation 5.1, for the low energy electrons in the cascade. The one dimensional filling factor f_{1d} is the most uncertain quantity in the expression as we've discussed throughout this thesis. It is expected that it is related to the three-dimensional filling factor f_{1d} by $f_{1d} \sim f_{3d}$ by a constant of order ~ 1, which depends on the geometry of the magnetised structures. Several of the most sophisticated large scale magnetic field models find that a large fraction of the universe is filled with magnetic fields, where $B \gg 10^{-14}$ G (see e.g., figure 3.2). It is clear that if this is the case, the UHECR cascade signal will be isotropised and hence drop below experimental sensitivity (see e.g., figure 5 of Ahlers & Salvado (2011) where this effect of homogeneous magnetic fields of strength $B = 10^{-14}$ G is illustrated for the case of 1ES 0229+200). If the average magnetic field strength in voids is below 10^{-14} G as concluded e.g., in the work of Donnert et al. (2009), the expected flux level will depend on the number of magnetised structures crossed. Passing a galaxy or cluster of galaxies would isotropise the cascade but is unlikely, as these occupy a small fraction of the volume in the universe. Passing a filament is much more likely, but with a less dramatic effect on the cascade emission. Assuming that a

fraction $f \sim 0.1$ of the volume is filled with filaments of diameter $L \sim 1$ Mpc, passing through the latter would lower the cascade signal level by an order of magnitude. As the UHECR luminosity requirements are already very high, it remains largely dependent on the magnetisation properties of the IGMF whether this channel is ultimately detectable.

Throughout, sources that emit an isotropic cosmic ray luminosity $L_{\rm cr,iso} \sim 10^{47}$ erg s^{-1} above 10^{18} eV have been considered. Beamed emission eases the requirements on the accelerator by $(1 - \cos(\theta_{\rm j})) \cdot L_{\rm cr,iso}$. For a typical beaming factor of 100, this corresponds to a beaming-corrected luminosity of $L_{\rm j} \sim 10^{45}$ erg s^{-1}. This is smaller than the Eddington luminosity, the maximum possible luminosity due to accretion by the black hole which is given by $L_{\rm edd}(M_\bullet) \simeq 1.3 \times 10^{38}(M_\bullet/M_\odot)$erg s^{-1} (e.g., Dermer & Menon 2010), where $M_\bullet$ is the mass of the black hole and $M_\odot$ is one solar mass. For the blazars studied here, $M_\bullet \gtrsim 10^8 - 10^9 M_\odot$ have been derived (Wagner 2008; Woo et al. 2005). Therefore the required $L_{\rm j} \sim 10^{45}$ erg s^{-1} is high but not unreasonable (although the jet power is typically lower than the Eddington luminosity for BL Lacs, as discussed in Ghisellini 2010). Note that the required cosmic ray luminosity is at the same level as required by UHECR-induced inverse-Compton cascade models.

On the other hand the observed Auger UHECR spectrum suggests that in the Earth's GZK horizon the total power in UHECRs per unit volume per year at energy E is $E^2{\rm d}N/{\rm d}E \simeq 10^{44}$ erg Mpc^{-1} yr^{-1} assuming an isotropic distribution of sources (Murase & Takami 2009; Berezinsky et al. 2006; Waxman 1995b). Given that from observations the number density of sources locally is consistent with $n_0 \sim 10^{-5} - 10^{-4}$ Mpc^{-3}, typical local UHECR sources must have $L_{\rm j} \sim 10^{42}$ erg s^{-1}, therefore the sources discussed here must be rare and powerful and cannot be typical sources of UHECRs. Due to their distance and the energy losses (the Greisen-Zatsepin-Kuzmin or GZK effect, Greisen 1966; Zatsepin & Kuzmin 1966) their contribution to the observed UHECR spectrum should thus be limited to $\lesssim 10\%$. In fact, had any such sources been located within the Earth's GZK horizon one would expect a strong excess in the direction of the source in the arrival direction distribution of UHECRs.

In this work it is assumed that the maximum acceleration energy in the blazars studied is $E_p^{\rm max} \sim 10^{20.5} - 10^{21}$ eV. Such energies cannot be achieved by BL Lacs within the SSC model, where generally protons can reach up to $\sim 10^{19}$ eV (Murase et al. 2012; Tavecchio 2014). This is a drawback of the secondary synchrotron scenario for extreme TeV blazars. However as noted in Tavecchio (2014), the blazar jet parameters obtained in the SSC

model for classical BL Lacs can hardly be applicable to the extreme TeV blazars that have been studied here. In addition to the conventional shock acceleration mechanism, a number of acceleration mechanisms have been proposed that would allow protons in blazar jets to achieve energies $\sim 10^{20}$ eV. These include the shear acceleration mechanism (Rieger & Duffy 2004) and magnetic reconnection (e.g., Giannios 2010). As mentioned in section 5.1.3, other models exist in which one abandons the SSC interpretation altogether and considers a highly magnetised blazar jet $B \sim 10 - 100$ G (Aharonian 2000; Mücke et al. 2003). In such, purely hadronic models, proton energies of 10^{20} eV can be obtained, but in general in these conditions pion photo-production is inefficient compared to proton synchrotron, which is the dominant process responsible for the observed gamma-ray emission.

Despite the caveat stated above regarding the maximum proton energy, the synchrotron signal studied in this work is an interesting channel and it can coexist with other emission components. Proton acceleration in blazar jets remains highly uncertain, and our assumption for the maximum proton acceleration energy may be accommodated in some non-typical blazars such as the extreme TeV blazars studied here. Such high maximum proton acceleration energies in jets have also been discussed in relation to a possible excess of UHECRs in the direction of Cen A (see e.g., Rieger & Aharonian 2009). In the near future, detailed multi-wavelength observations of blazar jets will help to clarify the picture.

In conclusion, the synchrotron emission induced by UHECRs and UHE photons, in the context of blazars embedded in magnetised regions, was studied. It was demonstrated that the synchrotron emission of UHECR secondaries provides a possible alternative explanation to the more conventional leptonic SSC or UHECR-induced inverse-Compton cascade scenarios, for the GeV-TeV spectra of some extreme TeV blazars. In this channel, the flux at the peak energy is insensitive to variations in the overall IGMF strength, which is appealing in view of the large uncertainties on void IGMFs. it was also shown that the variability of blazar gamma-ray emission in ∼month-year timescales can be accommodated by the synchrotron emission of secondary products of UHE photons, if these are produced inside the source in accelerators of UHECRs and that the GeV-TeV spectrum of 1ES 0229+200 is consistent with this possible interpretation. The signal, and the model fit to the blazar data in this model depend only on the magnetic field strength in the vicinity of the source and can dominate over other emission components, unless the strength of

IGMFs in voids is negligibly small. A large fraction of observed galaxies reside in filaments and clusters of large scale structure and hence this is an almost guaranteed signature as long as the required energy output in hadrons can be met by the accelerator. Finally, one may remark that the UHECR-induced synchrotron signal from magnetised regions studied here and the UHECR-induced inverse-Compton cascade signal that primarily develops in the voids of large-scale structure are not mutually exclusive.

This page was intentionally left blank

Chapter 6

Simulations for a next-generation UHECR observatory

Only those who will risk going too far can possibly find out how far one can go.
-T. S. Eliot, *Transit of Venus*

In this chapter, the potential of a future, next-generation UHECR experiment to probe the sources of UHECRs is explored, focusing on the expected sensitivity to UHECR anisotropies at the highest energies. In chapter 4 it was concluded that although there are significant hints for a departure from isotropy at energies beyond the GZK cutoff, it remains difficult to draw firm conclusions as to the sources of UHECRs with available data. Given the lack of obvious progress in the quest of UHECR sources in almost 50 years, it is natural to wonder what the capabilities of a future instrument, that is able to overcome the problem of low statistics, will be. Here, an order of magnitude larger detector than current-generation UHECR observatories is considered as an example. Such a detector could be the next step in UHECR astronomy, if the proposed, space-based JEM-EUSO mission is realised.

6.1 Introduction

The current generation of UHECR detectors collect super-GZK events at a rate $\lesssim 2$ month. To make progress in the quest for UHECR sources, a natural strategy is to aim for an

increase in experimental detection area, although the prospects for source identification with a next-generation detector are debated as a result of the absence of a clear correlation signal with luminous sources so far. Further doubts as to the detectability of UHECR sources are raised by the recent experimental evidence for an increasingly heavy UHECR composition at the highest energies.

The next UHECR experiment could be a space-based telescope such as the proposed JEM-EUSO. Advantages of a space-based observatory over a future ground array include a full sky exposure and significantly larger detection area than can be achieved by ground based detectors. In contrast, a future ground based extensive air shower array could achieve a better energy resolution and better sensitivity to UHECR composition. JEM-EUSO is proposed to be mounted on the International Space Station in $\sim$ 2020. If launched, it will survey the night sky for the ultra-violet fluorescence and Cherenkov radiation produced when a UHECR hits the Earth's atmosphere (Adams et al. 2012). It is expected that JEM-EUSO would reach an annual exposure of 6×10^4 km^2 sr yr, which is 9 times the annual Auger exposure at 100 EeV, in *nadir* mode (that is when the instrument is pointing to the point on the Earth directly below its location). In *tilt* mode, where the instrument is tilted thus increasing its effective observation area at the cost of decreasing the energy resolution, it will have about 20 times the annual exposure of Auger. JEM-EUSO will be sensitive to UHECRs with energy $E \geq 40$ EeV and fully efficient beyond $60 - 70$ EeV. It will have a near uniform exposure over the full sky.

A number of simulation studies have been performed with the aim of assessing the anisotropy discovery potential of a next-generation full sky observatory. Blaksley et al. (2013) studied the fraction of observed UHECRs contributed by individual sources at the highest energies. It was shown that for a UHECR source number density, $\bar{n} = 10^{-5}$ Mpc^{-3} at energy above $E = 100$ EeV the brightest two to five sources in the sky can be expected to contribute more than half the total UHECR flux. In the work of d'Orfeuil et al. (2014) a study of the expected sensitivity of a future JEM-EUSO type detector to anisotropies for a large range of composition scenarios was performed. It was concluded that even for the most unfavourable composition scenarios, such as for example in a model where no protons are accelerated to the highest energies, an anisotropy should be observable, if UHECR sources follow the spatial and luminosity distribution of 2MRS galaxies. Denton et al. (2014) studied the sensitivity of JEM-EUSO to anisotropies in the UHECR arrival distribution that can be revealed through a spherical harmonic analysis. They found that

large scale anisotropies, which could arise if a bright nearby source or the Galaxy, or the Supergalactic plane contribute asymmetrically to the observed UHECR flux should be detectable with high statistical significance. In particular they showed that a dipole anisotropy, defined via a standard min/max asymmetry $\alpha = (I_{\max} - I_{\min})/(I_{\max} + I_{\min})$ with I the normalised cosmic ray intensity in a specified celestial direction (see e.g. Sommers 2001), should be detectable at the 5σ level with three years of JEM-EUSO as long as $\alpha \gtrsim 0.28$. In comparison a 5σ discovery can only be achieved with 10 years of Auger for dipole amplitudes $\alpha \gtrsim 0.80$. Decerprit et al. (2012) developed the formalism to constrain the responsible astrophysical model for a given UHECR dataset, in a 2D parameter space consisting of the source number density and angular deflection of the UHECRs. They showed that a significant anisotropy signal is expected to be detected for a large fraction of this 2D parameter space even for a moderate number of detected events, or, failing that, a large range of astrophysical models can be constrained.

As discussed in chapter 4, detecting a correlation of UHECRs with some astrophysical population does not in itself reveal the UHECR sources, but simply their astrophysical nature due to the clustering of matter. The relative bias of the distribution of UHECR sources with respect to that of galaxies has therefore long been an important question. Some authors (Waxman et al. 1997; Kashti & Waxman 2008) have studied whether through a statistical analysis of UHECR arrival directions one can constrain such a bias, which could reveal important hints about the sources of UHECRs. In the case of transient UHECR sources and a proton dominated composition, a different, degenerate with the former, bias is expected to occur. This would be the result of the spread in the arrival times of UHECRs, induced by intervening magnetic fields, which will occur preferentially in the denser regions of large scale structure, enhancing the UHECR flux expected from these regions (Kotera & Lemoine 2008b; Kalli et al. 2011). The conclusions of these studies, that such a bias should indeed be detectable, provide the motivation for taking a closer look here, at the potential of a future UHECR experiment to detect such an effect.

A study of the sensitivity of a next-generation UHECR detector to the expected UHECR anisotropy is presented, with focus on the prospect of a statistical discrimination between different astrophysical scenarios for the origin of UHECRs. A scan over the allowed parameter space is performed. The allowed parameter space includes the unknown UHECR source density, the unknown fraction of protons at the highest cosmic ray energies and the possible bias of the UHECR source distribution with respect to the galaxy distri-

bution, for which, a wider range of physically motivated models than have been studied in previous works, are considered. The probability of ruling out individual models for the sources of UHECRs, for the number of events expected to be detected within a few years of operation of a detector with an annual exposure comparable to that expected for JEM-EUSO, is presented. Such a study is timely, not least because the relative merit of a next-generation experiment, that focuses on high exposure over a ground based experiment, that can perform more precise measurements at the cost of more modest statistics, is at present a topic of debate.

Previously conducted simulation studies, referenced above, have focused on the low source density regime and the highest cosmic-ray energies, emphasising the expectation that in this limit, due to the drastically smaller GZK horizon, an anisotropic arrival direction distribution is expected to be observed as a result of multiplets from individual "bright" UHECR sources each of which produces a significant fraction of the observed UHECRs above some energy cutoff (generally $E \gtrsim 80$ EeV). In this study instead, the focus is on the "faint" source regime, where the probability of multiplets from an individual source is low. In this latter regime, any anisotropy detected should be intrinsic to the clustering in the distribution of the sources. Even for a relatively low source density, $\bar{n} \sim 10^{-4}$ Mpc^{-3}, one should be able to probe the intrinsic anisotropy of the source distribution by considering lower energy events (as long as $E \gtrsim 40$ EeV, below which energy deflections are expected to be too severe, see e.g. Kashti & Waxman 2008). Although the UHECR source density remains unknown, the faint source regime is favoured by the observed clustering of UHECRs as we've discussed in chapter 4 whereas models with $\bar{n} < 10^{-5}$ Mpc^{-3} are strongly disfavoured (Abreu et al. 2013).

The results presented are general and apply to any future UHECR detector with an order of magnitude higher exposure than current experiments. Given the prospect of JEM-EUSO being the next experiment dedicated to UHECR detection, some of its expected characteristics, namely its expected annual exposure, detection sensitivity, nearly uniform full sky exposure, pointing and energy resolution have been assumed. Throughout, the energy losses of UHECRs as they propagate through the background photon fields and their deflections in intervening magnetic fields are taken into account.

6.2 Model building

The work presented in this chapter although in the same theme as the work presented in chapter 4 is an independent analysis with numerous different characteristics. One of the main differences lies in the expected cosmic ray intensity maps which are presented in the rest of this section. In chapter 4 we discussed the correlation of UHECRs with PSCz and 6dF galaxies, that should accurately represent the overall matter distribution, possibly with some bias. In this chapter instead, Monte Carlo modelling of the unknown UHECR sources is performed and the expected UHECR arrival distributions are forecast, for a range of astrophysical models, which are presented next.

6.2.1 Bias prescription of UHECR source clustering

It is well established observationally that different galaxies are biased tracers of the underlying mass distribution in the universe and that different galaxy types cluster to the mass distribution with varying strengths. Clusters of galaxies cluster more strongly than galaxies themselves, whereas some subtypes of galaxies, in particular luminous red galaxies and AGN, are observed to cluster more strongly than the average galaxy field overall.

A number of different theories exist that aim to explain this observed bias. For example, the observed strong clustering of galaxy clusters, has been interpreted as a result of these, very massive structures sampling the high peaks of the underlying mass distribution (Kaiser 1984; Sheth & Tormen 1999). In this work, the focus is on the clustering of the unknown UHECR sources. Observationally, a way to constrain the latter sources is to consider their bias relative to that of galaxies overall. From this point on, in this work, the term bias refers to the bias of UHECR sources relative to catalogued galaxies, and not the bias relative to the underlying mass distribution.

A number of models for the bias of UHECR sources are considered, with the aim of capturing different astrophysical scenarios for the origin of UHECRs. If UHECRs are accelerated in common sources, then the overall UHECR distribution should follow that of galaxies. If for example UHECRs are accelerated primarily in young pulsars, then the distribution of UHECR sources should roughly follow the distribution of young starburst galaxies, which roughly follows that of ordinary galaxies (e.g., Owers et al. 2007). If on the other hand UHECRs are accelerated in uncommon, extreme sources such as AGN, and radio galaxies which tend to be found in over-dense regions, then the distribution of

UHECR sources should be more strongly clustered than that of galaxies.

Denoting the galaxy density field $\rho_{\rm g}$ and its mean value $\bar{\rho_{\rm g}}$ the local galaxy fractional overdensity can be expressed as

$$\delta_{\rm g} = \frac{\rho_{\rm g} - \bar{\rho_{\rm g}}}{\bar{\rho_{\rm g}}}. \tag{6.1}$$

Similarly, the local fractional overdensity of UHECR sources can be expressed as $\delta_{\rm s} = \rho_{\rm s}/\bar{\rho_{\rm s}} - 1$. The simplest (and often assumed) relationship between two overdensity fields, here denoted $\delta_{\rm s}$ and δ_g, is a linear bias of the form:

$$\delta_{\rm s} = b \cdot \delta_{\rm g}. \tag{6.2}$$

This, widely used model cannot hold in all cases. For example, it can result in negative densities if $b > 1$. It is however generally a good approximation on cosmological scales, where the density fluctuations $\delta \ll 1$. Here, to model the bias, b, of the unknown UHECR sources with respect to that of galaxies, the following models are considered:

- An *isotropic* model (I), where $\delta_{\rm s} = 0$ everywhere.
- An *unbiased* model (UB), where $\delta_{\rm s} = b \cdot \delta_{\rm g}$, with $b = 1$. The unbiased model describes a situation in which all galaxies (or sources in these galaxies) are equally likely to accelerate UHECRs to the highest energies. Such a model is consistent with the observed UHECR small scale clustering and derived bounds on the source density.
- A *linear* bias model (L), where $\delta_{\rm s} = b \cdot \delta_{\rm g}$, where $b = 3$. This model better describes a scenario in which observed UHECRs originate in sources that tend to preferentially populate overdense regions, such as AGN or radio galaxies (e.g., Shaver & Pierre 1989).
- A *threshold* bias model (TH), where $\delta_{\rm s} = \delta_{\rm g}$ if $\delta_{\rm g} > \delta_{\rm min}$ else $\delta_{\rm s} = -1$. This is a more extreme, ad hoc version of the linear bias model, in which only the densest regions (i.e. primarily galaxy clusters) contain sources responsible for the production of observed UHECRs (as we saw in section 1.3 galaxy clusters are some of the few viable candidates for UHECR acceleration).

In the next section these models are applied to the PSCz catalogue, in order to make predictions of the expected UHECR intensity maps.

6.2.2 UHECR intensity maps and simulations

Source distribution

The IRAS PSCz catalogue is used as the basis of the model of the expected UHECR source distribution; its (almost) full sky coverage is an important advantage over e.g., the 6dF which, in the volume it covers, provides a much more detailed survey of the nearby universe. For simplicity, identical UHECR sources are considered. The UHECR sources are assumed to produce a power-law spectrum, with maximum acceleration energy, $E_{\rm max} = 10^{21}$ eV, and injection spectral index, $\alpha = -2.0$. As discussed in chapter 4, $E_{\rm max}$ cannot be much lower than $\sim 10^{21}$ eV, given that UHECRs have been **observed** with energy $\sim 10^{20.5}$ eV. Further, the results presented here, are very weakly sensitive to varying $E_{\rm max}$ within its anticipated range of values, as UHECRs in this energy range promptly interact with background photons. The sensitivity of the results to the redshift evolution in the UHECR source model has not been investigated in this work, as it is almost negligible within the proton GZK horizon at the highest cosmic ray energies. As in chapter 4 the PSCz galaxies are weighted by the inverse of the selection function, given by equation 4.10, to correct for the incompleteness of the magnitude limited survey. Galaxy recession velocities are converted to the Local Group frame, for the reasons discussed in section 4.4.

To construct models of the UHECR source distribution, the galaxy distribution is split into radial shells of equal thickness; from this stage on, the source distribution models diverge from what has been presented in chapter 4. A thickness of 11 Mpc was chosen, as a compromise between degrading the resolution of the analysis and having large enough shells to capture large structures (as a reminder the typical radius of a galaxy cluster is a few Mpc). The bias is applied to individual radial shells, which are pixelised into equal area bins of angular size 0.93° (HealPix nside = 64). The bin size was chosen after testing, as a compromise between degrading the resolution of the maps, and having bins large enough to capture known galaxy clusters.

In the *linear* bias model, in some underpopulated bins, the model ends up with negative densities for the reason explained in section 6.2.1. Given that $\delta_{\rm s} < -1$ is unphysical one needs to set some underdense regions to have $\delta_{\rm s} = -1$, or equivalently, a number density equal to zero. For this analysis, the number density of under dense ($\delta_{\rm s} < -1$) bins was set to zero, after smoothing (see next section). This unavoidable procedure does not make a big difference to the expected correlation signal in practice, as the cross-correlation mainly

picks out the high density regions.

To construct the *threshold* bias model the procedure outlined below is used. A regular hard thresholding procedure would usually involve setting all the pixels below a fixed δ_{min} to $\delta_s = -1$. However given that the galaxy field changes as a function of distance (number density of galaxies in the sample increases and then decreases as shown in the top panel of figure 4.4) it would not be possible to maintain a fixed threshold for this situation. Instead the threshold is defined via a proportion of pixels. The cooler pixels are set to $\delta_s = -1$. The proportion of pixels to be set to $\delta_s = -1$ however, is dependent upon the pixel size. Through empirical tests it was determined that setting 99% of the coolest pixels with an angular size of 0.93° to $\delta_s = -1$ is sufficient to retain, on average, 10% of all galaxies which reside in the densest regions (hottest pixels). Choosing the threshold so as to retain this galaxy fraction, is motivated by the fact that approximately 10% of all galaxies are found in galaxy clusters. Figure 6.1 demonstrates that, for the chosen pixel size and threshold, the mean fraction of all galaxies per comoving shell in the model stays approximately at 10% for all distances.

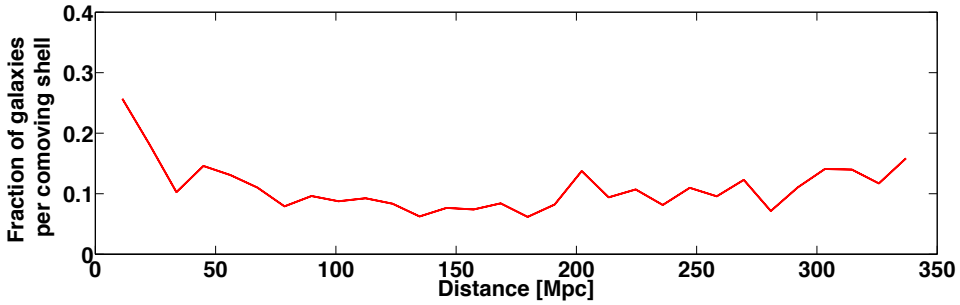

Figure 6.1. The fraction of PSCz galaxies that are included in the *threshold* bias model as a function of comoving distance. The threshold has been chosen such that the hottest 1% of all pixels contribute to the model.

Each radial shell is weighted for its expected contribution to the arriving UHECR flux, following equation 4.4. For all UHECR energy loss calculations, the results obtained by Monte Carlo in the work of Fodor & Katz (2001) have been used. An isotropic contribution to the expected UHECR flux by sources beyond 337 Mpc is considered. It is defined as follows: the GZK horizon for 99% of all cosmic rays, above a given energy, $r_{99\%}$, and subsequently the fraction of flux contributed by sources between 337 Mpc and $r_{99\%}$ are calculated. The fraction of cosmic rays contributed by sources beyond 337 Mpc is appreciable below 50 EeV ($\geq 30\%$) but smaller than 1% beyond 60 EeV after the onset of

the GZK process. This treatment of the homogeneous contribution from sources at high redshifts, is completely separate from the isotropic fraction in relation to the unknown composition of UHECRs, which will be introduced below.

The galaxy distribution is smoothed with a Gaussian filter of variable dispersion, following the prescription of Fisher et al. (1995). The smoothing length corresponds to different physical lengths at different distances and roughly reflects the mean galaxy-galaxy separation in the PSCz at different redshifts. Roughly, in comoving units, the smoothing length corresponds to $\lesssim 5$ Mpc out to 50 Mpc, $\lesssim 10$ Mpc out to 100 Mpc, $\lesssim 15$ Mpc out to 200 Mpc and $\lesssim 25$ Mpc out to 300 Mpc. Variable smoothing is important for maintaining high-resolution nearby, while suppressing shot noise at larger distances. The overall resolution of the maps after smoothing is of order $\sim 7^\circ$. The galaxy survey is masked with the PSCz mask (Saunders et al. 2000) which is dilated by 7°, to remove the areas around the masked region, that will have unavoidably been depleted by the smoothing procedure.

In figure 6.2 the integrated source density in the different bias models out to 337 Mpc are shown. As expected, the contrast is significantly enhanced in the linear and threshold bias models with respect to the unbiased model. In figures 6.3-6.5 the fluctuations in the mean of the expected UHECR intensity averaged over realisations, for UHECRs with energy above 40, 60, 80, 100 EeV in the various bias models are shown. Increasing the energy threshold drastically reduces the GZK horizon and it is clearly visible in the maps that as a result the number of sources contributing to the arriving UHECR flux reduces drastically. In the maps that correspond to 100 EeV UHECRs for example the contrast is significantly enhanced compared to the 40 EeV maps, as fewer, nearby sources contribute significantly to the expected flux.

Source density

A specific realisation of UHECRs is generated by drawing the expected number of sources, contributing one or more observed cosmic rays, from the smoothed underlying UHECR source distribution in the various models. The total number of sources depends on the number density of UHECR sources and is determined as follows: defining the effective volume to be contained within the radius $r_{\rm GZK}$ at which the surviving fraction of UHECRs drops to e^{-1}, N sources are drawn from the smooth maps, such that the source number density, $\bar{n} = N/V$, takes the value chosen for a specific realisation, with $V = (4/3)\pi r^3_{\rm GZK}$. The effective GZK radius, $r_{\rm GZK}$, depends on the UHECR energy. Here, for the source

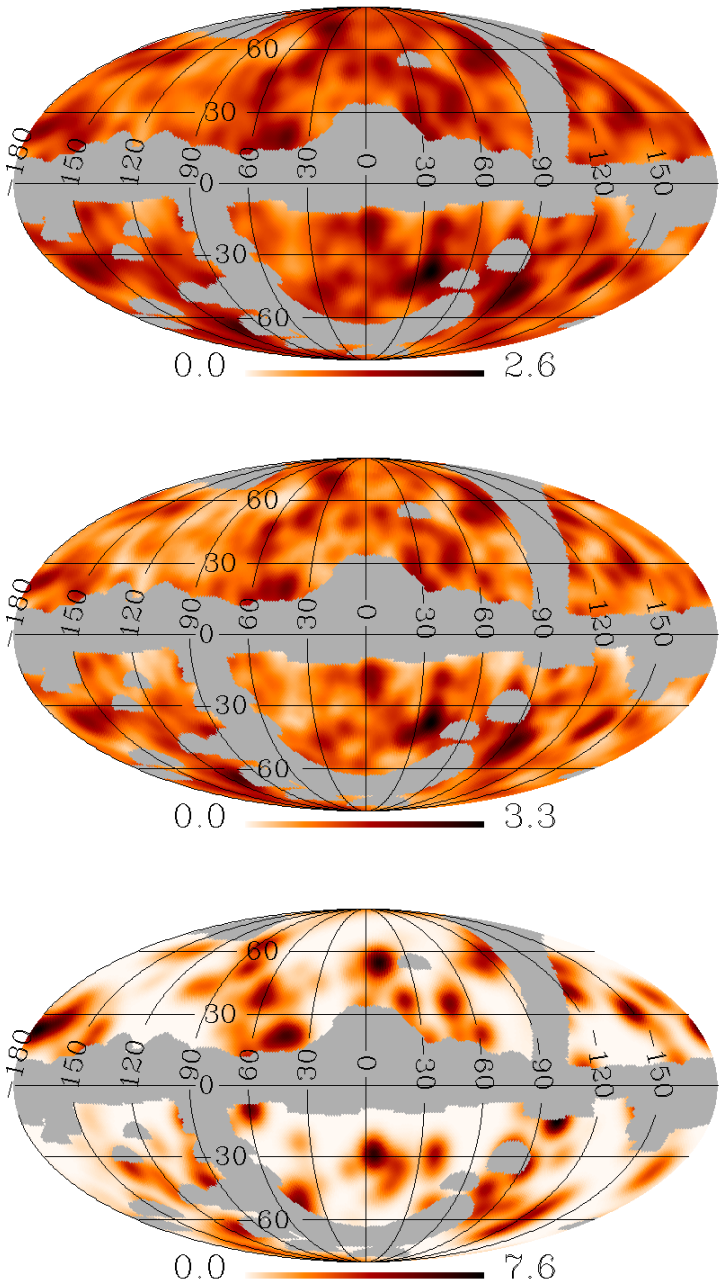

Figure 6.2. Maps of the integrated UHECR source distribution out to 337 Mpc in the unbiased (top), linear bias (middle) and threshold bias (bottom) models, in Galactic coordinates, with $l = 0°$ at the centre of the map and l increasing to the left. All maps have been normalised to their mean intensity.

number density, values in the range $\bar{n} = 10^{-4}$ Mpc^{-3} – 10^{-2} Mpc^{-3} are considered; the former being close to the lower limit of the source density derived from UHECR clustering (Abreu et al. 2013) and the latter the number density of bright galaxies.

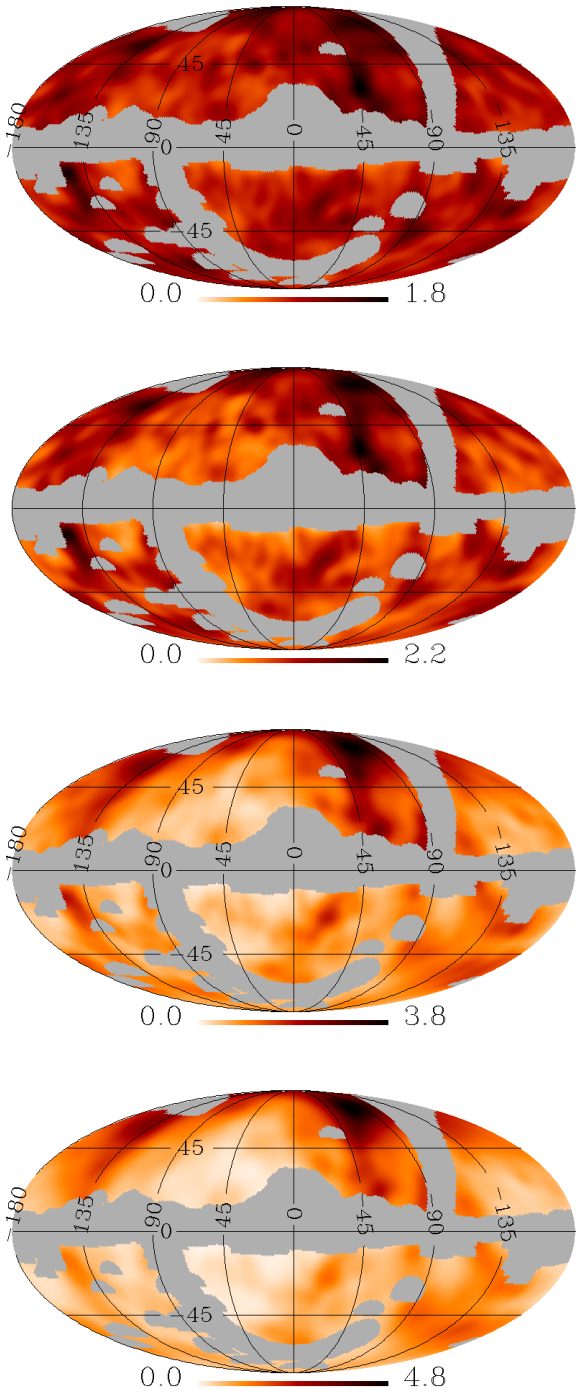

Figure 6.3. The expected UHECR intensity averaged over realisations for UHECRs with energy above 40, 60, 80, 100 EeV in the *unbiased* source model, in Galactic coordinates, with $l = 0°$ at the centre of the map and l increasing to the left.

Treatment of UHECR deflections

Tthe deflections expected to be suffered by UHECR protons at different energies are taken into account using an adhoc analytic scaling with energy, $\sigma = 3° + 1.5°(100 \text{ EeV}/E)$,

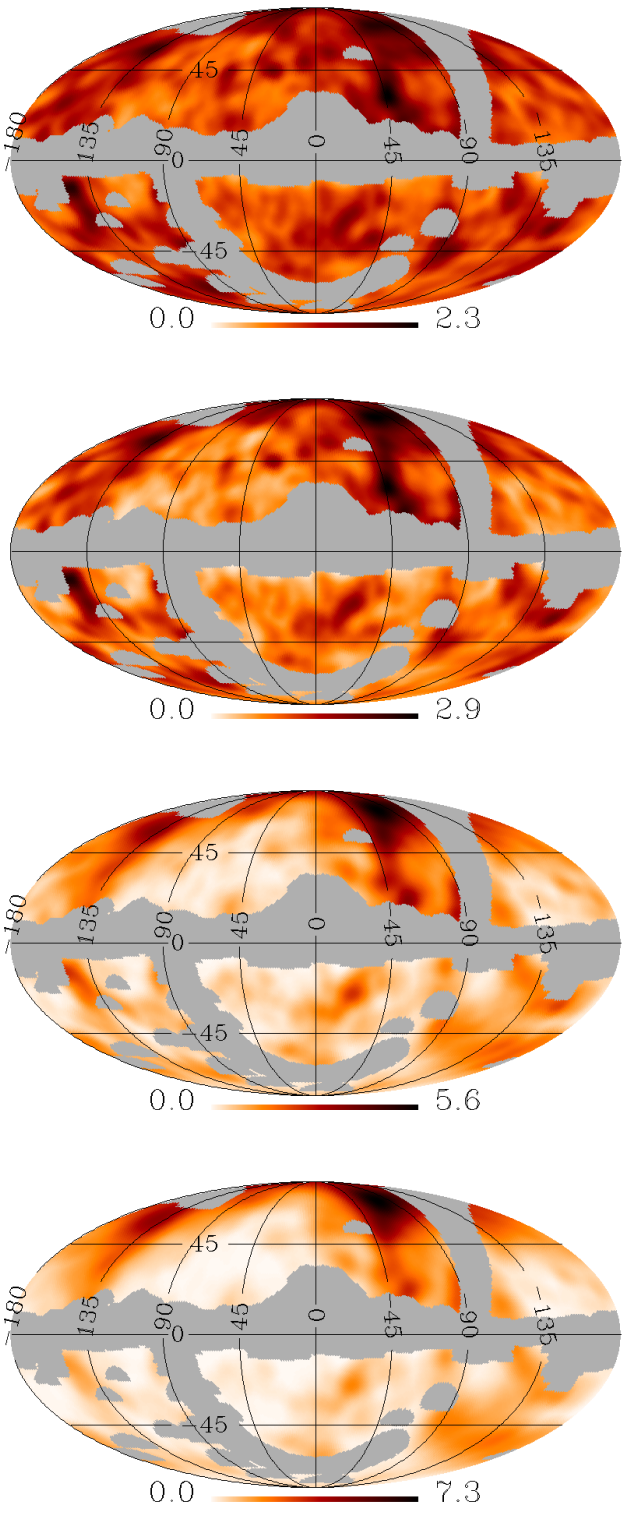

Figure 6.4. The expected UHECR intensity averaged over realisations for UHECRs with energy above 40, 60, 80, 100 EeV in the *linear bias* model, in Galactic coordinates, with $l = 0°$ at the centre of the map and l increasing to the left.

aimed to reflect the expected angular resolution of JEM-EUSO of $\leq 3^\circ$ and the energy dependent rigidity of proton UHECRs as they propagate through the extragalactic and Galactic magnetic fields (c.f. equation 3.5).

Expected number of events

The absolute energy scale of the observed UHECR spectrum is not precisely known due to the large systematic errors associated with the energy reconstruction of the primary UHECRs ($\sim$ 14% in Auger, $\sim$ 21% in the TA). The UHECR spectra that have been presented by the TA and Auger appear to have a systematic disagreement, but can be brought into agreement by a $\sim$ 20% rescaling of the energy (see Dawson et al. 2013), well within the published systematic uncertainties. This introduces an uncertainty to the expected number of UHECRs above a certain energy for a future detector like JEM-EUSO. To estimate the number of UHECR events detectable with JEM-EUSO in d'Orfeuil et al. (2014) two UHECR reference spectra were constructed: one with the Auger absolute energy scale and one with the TA absolute energy scale. Taking into account the JEM-EUSO detection efficiency presented in Adams et al. (2013) the expected number of events for an integrated exposure equal to 3×10^5 km^2 sr yr was found to be 1100, 250 and 100 events above 50, 80, 100 EeV respectively for the Auger energy scale. For the TA absolute energy scale 2100, 580, and 260 events are expected for the same energy thresholds. Here, these estimates are assumed for the number of expected UHECRs. Since the masked region is excluded from the statistical analysis but the total number of expected events is fixed, the number of expected UHECRs in a given trial is also determined by Monte Carlo and varies between realisations. An example sky map of the expected UHECR arrival direction distribution in the unbiased model, for the statistics that JEM-EUSO would collect in $\sim$ 5 years of operation, assuming the TA energy scale, is shown in figure 6.6, for a (reconstructed) energy threshold $E \geq 50$ EeV (see subsection 6.2.2 for details).

Energy resolution

To account for the energy resolution of the detector ($\sim$ 15% for Auger, $\sim$ 30% expected for JEM-EUSO) a Gaussian detector response is implemented for the reconstructed UHECR energy. The analysis is performed with the reconstructed energies, instead of the actual energies injected in the simulations. The degradation of the anisotropy signal with respect to expectations due to lower energy events being mis-reconstructed with a higher than

their true energy was not explicitly modelled in chapter 4, although the effect of a possible, systematic over(under) estimation of the energy of the Auger UHECRs on the results was investigated.

Statistical approach

To quantify the expected sensitivity of JEM-EUSO to any anisotropy signal in the UHECR arrival directions the statistic $X_{\rm M}$, introduced in chapter 4 is used

$$X_{\rm M} = \sum_i \frac{(N_{{\rm CR},i} - N_{{\rm iso},i}) \cdot (N_{{\rm M},i} - N_{{\rm iso},i})}{N_{{\rm iso},i}}. \tag{6.3}$$

Note the slight redefinition of the various terms in equation 6.3: $N_{{\rm CR},i}$ is the number of UHECRs detected in bin i. $N_{{\rm iso},i}$ is the number of UHECRs expected to be detected in bin i in the isotropic model and $N_{{\rm M},i}$ is the number of UHECRs expected to be detected in bin i in model M (i.e. either of the unbiased, linear and threshold models). Here, $X_{\rm M}$ is calculated over $7^\circ \times 7^\circ$ angular bins, to average over possible UHECR deflections. In practice, here $X_{\rm M}$ is evaluated assuming the UHECR source distribution follows the unbiased model so from here on it is denoted $X_{\rm UB}$. Note that unlike in chapter 4, where fluctuations in value of $X_{\rm UB}$ as a function of bin size were investigated, in the present analysis the value of $X_{\rm UB}$ does not vary significantly for bin sizes smaller than $\sim 7^\circ \times 7^\circ$, as a result of having previously smoothed the expected source distribution with a filter of a comparable smoothing length.

6.3 Results

In this section, the anisotropy signal expected to be detected with five years of data with JEM-EUSO, is calculated with the setup presented above.

6.3.1 Isotropic fraction

In this thesis so far it has been assumed that the highest energy cosmic-rays are protons, which is a firm prediction of most models for the origin of UHECRs. This standard, and well motivated interpretation is challenged by the composition sensitive measurements of Auger (see section 1.4 and references therein) and the absence of a clear anisotropy in the data collected so far by the Auger experiment, as we saw in chapters 3-4. In this section,

the sensitivity of JEM-EUSO to the expected anisotropy signal in the presence of a fraction of UHECRs, that have been deflected by large angles, is investigated. It is assumed that a fraction of UHECRs arrive without having retained a correlation with their sources i.e. isotropically. This fraction is treated as a free parameter in the simulations.

Figure 6.7 shows the distribution of values of $X_{\rm UB}$ obtained in 10000 Monte Carlo realisations of an isotropic model (black histograms), an unbiased model where 100% of UHECRs are protons (red histograms), an unbiased model where 30% of UHECRs arrive isotropically (blue histograms) and finally an unbiased model where 70% of UHECRs arrive isotropically (green histograms).

Concentrating on the solid thick histograms, we observe that choosing different isotropic fractions produces a smooth transition between the predicted mean value $X_{\rm UB}$ in the isotropic case and the fully anisotropic case. Further, it is clear that the expected anisotropy signal strongly depends on the number of events collected, and that it is significantly stronger if we consider all events collected with reconstructed energy $E \geq 50$ EeV than if we concentrate only on the smaller subset of the highest energy events.

6.3.2 Sensitivity to the UHECR source density

The different linestyles in figure 6.7 show the distribution of values of $X_{\rm UB}$ obtained for different values of the UHECR number density. We observe, as expected (see discussion in chapter 4) that the source number density does not affect the mean value of $X_{\rm UB}$ obtained for a specific model, but rather the width of the distribution of values of $X_{\rm UB}$ and therefore it does affect the significance with which a specific model for the UHECR source distribution can be ruled out. Further, we observe that a source number density similar to that of bright galaxies results in the strongest possible anisotropy signal and is thus the most favourable for the present study. Note that for an energy threshold of 80 EeV or higher it is not possible to constrain source number densities lower than 10^{-3} Mpc^{-3} with the present setup, as the number of sources contributing to the expected UHECRs drops radically (the horizon over which the survival probability of 80 EeV UHECRs drops to e^{-1} is ~ 60 Mpc, making the number contributing UHECR sources $(4/3)\pi(60^3)\bar{n} \sim 200$ for $\bar{n} = 10^{-4}$ Mpc^{-3}). As a result the distribution of $X_{\rm UB}$ becomes highly non-Gaussian, not allowing to derive unambiguous confidence intervals. For a study of this low source number density regime see the work of Blaksley et al. (2013).

6.3.3 Sensitivity to the bias of the source distribution

We now look at the sensitivity of a future UHECR detector to the anisotropy signal expected in the different clustering models that have been assumed for the cosmic ray sources. With the same setup as previously the distribution of values of $X_{\rm UB}$ is calculated in the different possible models of the source distribution and plotted in figures 6.8-6.10. As with the results of the previous section, we observe that the much larger number of lower energy events is crucial for distinguishing between the different bias models. In the bottom row of figure 6.8 we see that already at 1100 events there is significant distinction between the isotropic, unbiased and linear models and in particular the threshold model could be ruled in or out with a very high significance. The situation only improves, if the TA energy scale is assumed.

Further, inspection of figures 6.9 and 6.10 reveals that the trend for the mean of the distribution of $X_{\rm UB}$ changes in a similar way as the bias models change and as the isotropic fraction in the data changes. In other words, with future data it will be possible to constrain the 2D parameter space defined by the combination of the composition and the bias model with the statistic $X_{\rm UB}$ alone. Inspection of the histograms in figures 6.8-6.10 leads to a further, slightly disappointing, conclusion that has not been discussed before; namely that the mean value of the cross-correlation will have degeneracies as a result of the effect of the unknown composition/deflections of UHECRs and that of the unknown bias of the UHECR sources with respect to the galaxy distribution. Only knowledge of the composition of the UHECR sample studied will allow such a degeneracy to be broken.

Despite this drawback, the main concern here is whether a significant anisotropy should be expected or not. Tables 6.1 and 6.2 quantify the results that have thus far been discussed qualitatively in this section. Following the formalism developed in Waxman (1995b) the probability $P(\overline{M}_1|M_2)$ of ruling out a particular model of the source distribution M_1 at a specified confidence level (95%, 99%, 99.9%) assuming model M_2 is true is quoted. This is calculated, by counting the fraction of realisations of M_1 in which $X_{\rm UB}$ took more extreme values than in 95%, 99%, 99.9% of realisations of M_2 respectively. Note that confidence intervals in the two tables have been obtained assuming the baseline model M_1 (i.e. model M_1 with 0% events arriving isotropically). This is different to what is shown in figures 6.9 and 6.10 where all models have been plotted assuming an isotropic fraction of events.

Inspection of tables 6.1 and 6.2 confirms that the larger number of lower energy events

will be crucial for differentiating between the various models of the UHECR source distribution. Further, inspection of table 6.2 reveals that once the number of observed events beyond 50 EeV increases to above 1000, an anisotropy at the 99% level should be detectable if the number density of sources is comparable to that of galaxies, as long as the composition is proton dominated. Once the number of events increases to 2000 the anisotropy should be detectable at the 99% level, as long as the number density of UHECR sources is equal to or larger than $\bar{n} = 10^{-3}$ Mpc^{-3} and the fraction of protons is not lower than 70%. Further, if the UHECR sources cluster in a way similar to that of extreme, uncommon objects such as massive galaxy clusters, an anisotropy at the 99.9% level should be detectable once the number of events exceeds 2000, even if the fraction of protons above 50 EeV is as low as 30%. Finally, it is shown that a clear discrimination between a linear bias model and an unbiased model will not be possible even if 100% of UHECRs are protons. The confidence intervals quoted here, can be considered a firm lower limit to the expected anisotropy signal for the models considered; the assumption that heavier nuclei than protons arrive isotropically, certainly results in a very conservative estimate of the expected anisotropy. It should be noted that the conclusions drawn here for the full proton composition, are more conservative than those of Kashti & Waxman (2008) for a specified number of events, as a result of having taken more conservative values for the energy and pointing resolution of the experiment, given the possibility that the next generation UHECR detector might be in space.

6.4 Discussion

In this chapter, the UHECR anisotropy signal in arrival directions, expected to be detected with a detector with an order of magnitude larger annual exposure at energy 100 EeV than Auger, were forecast, under different astrophysical scenarios. The present study, focused on the anisotropy expected as a result of the intrinsic anisotropy of the UHECR sources, if these trace the distribution of extragalactic matter, as opposed to anisotropies which might arise if individual UHECR sources are "bright" and produce high multiplicity clusters of UHECRs (as presented in e.g. Blaksley et al. 2013; d'Orfeuil et al. 2014). The results presented here are general and apply to any future UHECR detector, although some of the characteristics of the proposed JEM-EUSO space telescope, which might be the next UHECR observatory to be realised, were assumed. In particular, the expected uniform

	95% CL					
iso [%]	P($\bar{\text{I}}$|UB)	P($\bar{\text{I}}$|L)	P($\bar{\text{I}}$|TH)	P($\overline{\text{UB}}$|L)	P($\overline{\text{UB}}$|TH)	P($\bar{\text{L}}$|TH)
0	90(> 99.9)	90(> 99.9)	99.9 (> 99.9)	57(64)	99(> 99.9)	68(98)
30	69(98)	93(> 99.9)	99.9 (> 99.9)	7(9)	69(91)	8(28)
50	48(49)	82(86)	99(> 99.9)	2(< 1)	28(26)	< 1(< 1)
70	23(53)	42(80)	79(99)	< 1(< 1)	2(< 1)	< 1(< 1)
90	10(14)	8(22)	17(40)	< 1(< 1)	< 1(< 1)	< 1(< 1)
0	59(89)	84(99)	99(> 99.9)	19(34)	67(89)	40(56)
30	34(68)	60(92)	88(99)	5(6)	29(53)	8(15)
50	26(50)	42(74)	73(96)	2(< 1)	12(16)	3(1)
70	13(25)	22(41)	38(72)	< 1(< 1)	1(< 1)	< 1(< 1)
90	7(9)	8(12)	9(18)	< 1(< 1)	< 1(< 1)	< 1(< 1)
	99% CL					
0	71(99)	99(99.9)	> 99.9 (> 99.9)	33(36)	95(> 99.9)	43(92)
30	41(92)	77(99)	99(> 99.9)	2(2)	45(74)	2(11)
50	22(70)	58(95)	94(> 99.9)	< 1(< 1)	12(9)	< 1(< 1)
70	7(27)	18(57)	56(96)	< 1(< 1)	< 1(< 1)	< 1(< 1)
90	2(3)	2(7)	5(18)	< 1(< 1)	< 1(< 1)	< 1(< 1)
0	33(74)	63(97)	94(> 99.9)	6(14)	43(74)	20(35)
30	16(68)	36(92)	74(99)	< 1(1)	10(30)	2(6)
50	11(23)	22(50)	53(89)	< 1(< 1)	3(4)	< 1(< 1)
70	13(9)	8(18)	18(49)	< 1(< 1)	< 1(< 1)	< 1(< 1)
90	2(2)	2(3)	3(5)	< 1(< 1)	< 1(< 1)	< 1(< 1)
	99.9% CL					
0	36(99)	92(> 99.9)	> 99.9 (> 99.9)	14(13)	85(99)	13(72)
30	14(80)	43(99)	96(> 99.9)	< 1(< 1)	22(47)	< 1(2)
50	5(49)	25(86)	75(> 99.9)	< 1(< 1)	3(2)	< 1(< 1)
70	< 1(12)	3(34)	23(89)	< 1(< 1)	< 1(< 1)	< 1(< 1)
90	< 1(< 1)	< 1(2)	< 1(7)	< 1(< 1)	< 1(< 1)	< 1(< 1)
0	14(53)	37(90)	83(99)	1(2)	19(45)	6(15)
30	4(22)	14(59)	48(95)	< 1(< 1)	2(9)	< 1(< 1)
50	2(9)	7(26)	26(76)	< 1(< 1)	< 1(< 1)	< 1(< 1)
70	< 1(2)	2(6)	5(27)	< 1(< 1)	< 1(< 1)	< 1(< 1)
90	< 1(< 1)	< 1(< 1)	< 1(< 1)	< 1(< 1)	< 1(< 1)	< 1(< 1)

Table 6.1. Probability of ruling out model M_1 assuming model M_2 is true P($\overline{M}_1|M_2$), for the I-*isotropic*, UB-*unbiased*, L-*linear* and TH-*threshold* models, at the specified confidence level (95%, 99%, 99.9%) with five years of a JEM-EUSO like exposure, considering only events expected to be detected with $E \geq 100$ EeV. Values outside (inside) brackets assume that the number of detected events will be 100 (260). In each of the three subtables (95%, 99% and 99.9% CL) the top five rows assume a UHECR source number density $\bar{n} = 10^{-2}$ Mpc^{-3} and the bottom five rows assume $\bar{n} = 10^{-3}$ Mpc^{-3}. Different rows assume a different fraction of the observed UHECRs arrives isotropically (denoted "iso"). From top to bottom iso= 0%, 30%, 50%, 70%, 90%.

full-sky exposure, as well as the modest pointing and energy resolution of a space based UHECR telescope and the proposed detection efficiency of JEM-EUSO (Adams et al. 2013) were assumed.

Sky maps of the expected UHECR intensity, in a range of models for the bias of

	95% CL					
iso[%]	P($\bar{\text{I}}$|UB)	P($\bar{\text{I}}$|L)	P($\bar{\text{I}}$|TH)	P($\overline{\text{UB}}$|L)	P($\overline{\text{UB}}$|TH)	P($\bar{\text{L}}$|TH)
0	99.9 (> 99.9)	> 99.9 (> 99.9)	> 99.9 (> 99.9)	72(90)	> 99.9 (> 99.9)	> 99.9 (> 99.9)
30	99(> 99.9)	> 99.9 (> 99.9)	> 99.9 (> 99.9)	5(5)	> 99.9 (> 99.9)	99.9 (> 99.9)
50	86(98)	99(> 99.9)	> 99.9 (> 99.9)	< 1(< 1)	99(> 99.9)	53(76)
70	52(72)	78(93)	> 99.9 (> 99.9)	< 1(< 1)	9(12)	< 1(< 1)
90	15(18)	21(29)	61(84)	< 1(< 1)	< 1(< 1)	< 1(< 1)
0	99.9 (> 99.9)	> 99.9 (> 99.9)	> 99.9 (> 99.9)	65(86)	> 99.9 (> 99.9)	> 99.9 (> 99.9)
30	97 (99.9)	99.9(> 99.9)	> 99.9 (> 99.9)	6(5)	> 99.9 (> 99.9)	99(> 99.9)
50	80(97)	97(> 99.9)	> 99.9 (> 99.9)	< 1(< 1)	97(> 99.9)	48(75)
70	45(69)	70(90)	> 99.9 (> 99.9)	< 1(< 1)	9(10)	< 1(< 1)
90	13(17)	19(26)	56(80)	< 1(< 1)	< 1(< 1)	< 1(< 1)
0	95(99)	99.9(> 99.9)	> 99.9 (> 99.9)	37(56)	> 99.9 (> 99.9)	99.9 (> 99.9)
30	76(94)	95(99)	> 99.9 (> 99.9)	4(5)	99(> 99.9)	71(96)
50	53(75)	78(95)	> 99.9 (> 99.9)	< 1(< 1)	73(91)	27(40)
70	27(40)	43(64)	97(99)	< 1(< 1)	9(9)	< 1(< 1)
90	10(12)	13(17)	34(52)	< 1(< 1)	< 1(< 1)	< 1(< 1)
	99% CL					
0	99.9(> 99.9)	> 99.9 (> 99.9)	> 99.9 (> 99.9)	46(73)	> 99.9 (> 99.9)	> 99.9 (> 99.9)
30	93(99)	99(> 99.9)	> 99.9 (> 99.9)	1(1)	> 99.9 (> 99.9)	> 99.9 (> 99.9)
50	65(92)	93(99)	> 99.9 (> 99.9)	< 1(< 1)	95(99)	25(52)
70	25(47)	51(80)	> 99.9 (> 99.9)	< 1(< 1)	2(3)	< 1(< 1)
90	4(6)	6(11)	32(64)	< 1(< 1)	< 1(< 1)	< 1(< 1)
0	99(> 99.9)	> 99.9 (> 99.9)	> 99.9 (> 99.9)	37(66)	> 99.9 (> 99.9)	> 99.9 (> 99.9)
30	87(99)	99(> 99.9)	> 99.9 (> 99.9)	< 1(6)	> 99.9 (> 99.9)	99(> 99.9)
50	55(87)	88(99)	> 99.9 (> 99.9)	< 1(< 1)	90(99)	23(54)
70	19(43)	43(74)	99(> 99.9)	< 1(< 1)	3(3)	< 1(< 1)
90	3(5)	5(10)	31(57)	< 1(< 1)	< 1(< 1)	< 1(< 1)
0	84(99)	99(> 99.9)	> 99.9 (> 99.9)	16(30)	99.9 (> 99.9)	99(> 99.9)
30	51(82)	84(98)	99.9(> 99.9)	< 1(< 1)	96(99)	71(87)
50	27(75)	54(95)	99.9(> 99.9)	< 1(< 1)	50(77)	< 1(< 1)
70	10(18)	19(38)	89(99)	< 1(< 1)	2(2)	< 1(< 1)
90	2(3)	4(5)	14(28)	< 1(< 1)	< 1(< 1)	< 1(< 1)
	99.9% CL					
0	98(> 99.9)	> 99.9 (> 99.9)	> 99.9 (> 99.9)	19(43)	> 99.9 (> 99.9)	> 99.9 (> 99.9)
30	76(98)	98(> 99.9)	> 99.9 (> 99.9)	< 1(2)	99.9 (> 99.9)	96(> 99.9)
50	36(75)	77(99)	> 99.9 (> 99.9)	< 1(< 1)	80(98)	10(22)
70	7(22)	24(55)	99(> 99.9)	< 1(< 1)	< 1(< 1)	< 1(< 1)
90	< 1(< 1)	< 1(3)	13(36)	< 1(< 1)	< 1(< 1)	< 1(< 1)
0	98(> 99.9)	> 99.9 (> 99.9)	> 99.9 (> 99.9)	16(39)	> 99.9 (> 99.9)	> 99.9 (> 99.9)
30	72(96)	98(> 99.9)	> 99.9 (> 99.9)	< 1(< 1)	> 99.9 (> 99.9)	92(99)
50	33(65)	73(98)	> 99.9 (> 99.9)	< 1(< 1)	72(98)	6(23)
70	7(17)	22(47)	99(> 99.9)	< 1(< 1)	< 1(< 1)	< 1(< 1)
90	< 1(1)	1(2)	11(29)	< 1(< 1)	< 1(< 1)	< 1(< 1)
0	60(92)	94(> 99.9)	> 99.9 (> 99.9)	4(10)	> 99.9 (> 99.9)	98(99)
30	24(60)	60(93)	> 99.9 (> 99.9)	< 1(< 1)	86(98)	47(71)
50	9(24)	26(61)	99(> 99.9)	< 1(< 1)	24(52)	3(6)
70	2(5)	5(15)	70(95)	< 1(< 1)	< 1(< 1)	< 1(< 1)
90	< 1(< 1)	< 1(< 1)	3(10)	< 1(< 1)	< 1(< 1)	< 1(< 1)

Table 6.2. Same as table 6.1 but considering all the events expected to be detected in five years of JEM-EUSO with energy $E \geq 50$ EeV. Values outside (inside) brackets assume that the number of detected events will be 1100 (2100). In each of the three subtables (95%, 99% and 99.9% CL) the top five rows assume a UHECR source number density $\bar{n} = 10^{-2}$ Mpc^{-3}, the five middle rows assume $\bar{n} = 10^{-3}$ Mpc^{-3} and the five bottom rows assume $\bar{n} = 10^{-4}$ Mpc^{-3}.

UHECR sources relative to the galaxy distribution, were constructed, motivated by the observed clustering of different astrophysical populations relative to the overall galaxy distribution. Motivated by recent measurements of UHECR composition, that suggest an increasingly heavy, mixed composition with energy above ∼20 EeV, the analysis was conducted assuming a fraction of the observed UHECRs are deflected by large angles. The effect of such heavily deflected UHECRs was simulated by assuming they arrive isotropically, smearing the expected anisotropy signal. For a given assumed fraction of protons in the data, this is almost certainly a conservative estimate of the expected anisotropy signal, as more than likely at least some of the observed nuclei will retain some correlation with their sources as shown for example by d'Orfeuil et al. (2014).

It was shown that if UHECR sources cluster to the matter distribution in a similar manner to that of galaxy clusters, a significant anisotropy should be detectable in the arrival directions when the number of events with energy $E \geq 50$ EeV exceeds 1000 even for the modest, energy and pointing resolution of a space based instrument and even if the fraction of protons at the highest energies is as low as 30%. Further, it was demonstrated that if the UHECR source distribution follows the distribution of galaxies, perhaps with some linear bias comparable to the observed bias of low redshift AGN, then the expected anisotropy signal will be lower but detectable with high statistical significance, as long as the fraction of light nuclei at the highest energies is $\geq 70\%$ and the UHECR source number density is comparable to that of bright galaxies, assuming the energy scale of the Auger experiment. Assuming the energy scale of the TA experiment means that double the number of events should be detectable annually. In that case, a statistically significant anisotropy should be expected, even if the number density of sources is an order of magnitude lower. The dependence of the results to the unknown UHECR source number density has been pointed out throughout and it was demonstrated that the larger the number of UHECR sources, the higher the expected anisotropy. In practice, the UHECR source number density should be possible to constrain with real data from the clustering in the dataset (number of "repeaters") as shown in chapter 4.

Throughout this chapter the expected UHECR flux sky maps were masked by the PSCz mask leading, unfortunately, to an incomplete sky coverage. In some of the studies that have been discussed in this chapter (e.g., Kashti & Waxman 2008; d'Orfeuil et al. 2014), the obscured region of the galactic plane and unobserved regions have been populated by drawing the number of galaxies in the obscured part of the sky from a Gaussian, or Poisson

distribution with a mean equal to the mean number of galaxies in adjacent observed regions. This technique was avoided here, as it can bias the results of the analysis.

In conclusion, it was shown that an order of magnitude larger detector than current UHECR experiments should push forward the study of UHECRs. Further, a significant anisotropy should be expected in most astrophysical scenarios in the parameter space explored, consistent with the complementary findings of d'Orfeuil et al. (2014). An absence of anisotropy with such an increase in experimental exposure, could only mean a completely heavy dominated composition and unexpectedly large UHECR deflections, which could be translated to bounds on the Galactic and local extragalactic magnetic fields or new physics.

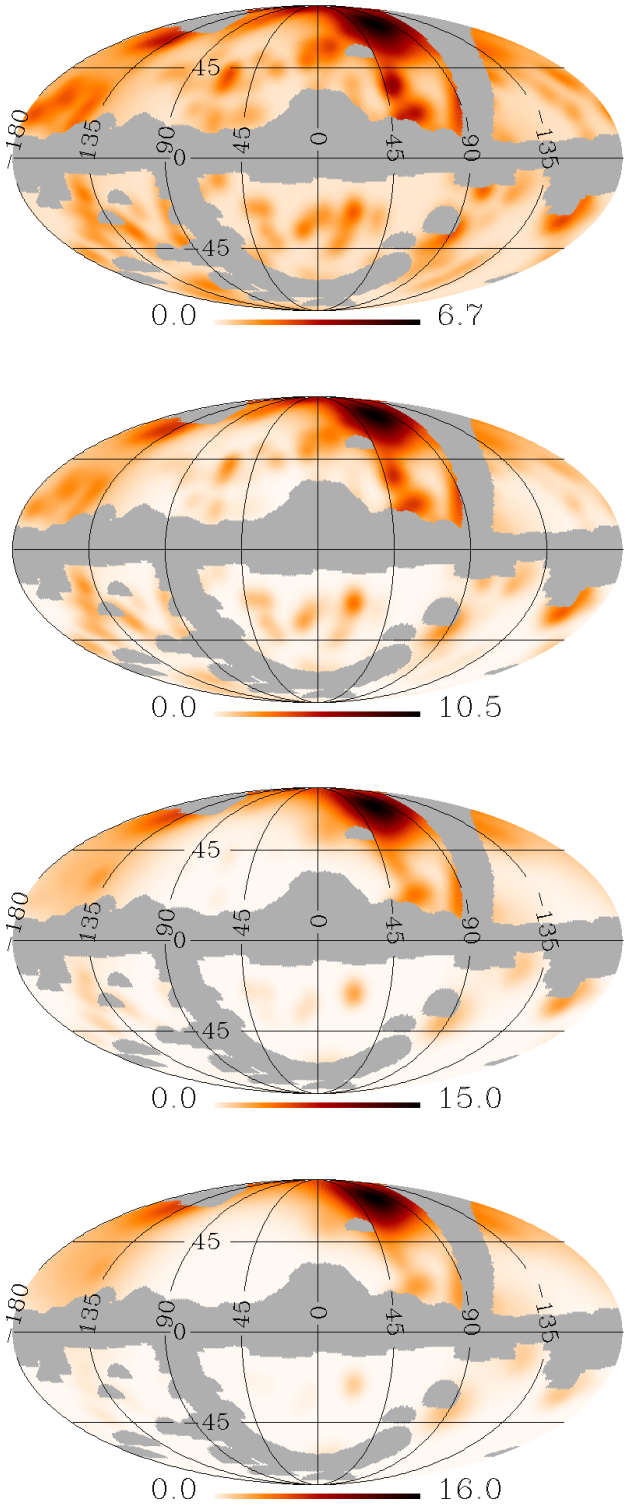

Figure 6.5. The expected UHECR intensity, averaged over realisations, for UHECRs with energy above 40, 60, 80, 100 EeV in the *threshold bias* model, in Galactic coordinates, with $l = 0°$ at the centre of the map and l increasing to the left.

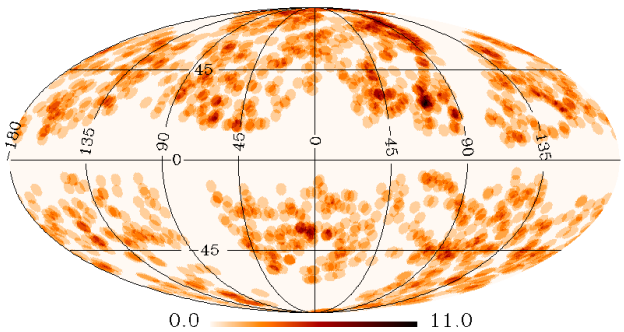

Figure 6.6. Example of the expected UHECR arrival direction distribution, for the statistics that JEM-EUSO would gather with a total exposure of 300000 km^2 sr yr ($\approx$ 5 years of operation), with a reconstructed energy $E \geq 50$ EeV, in the unbiased model. The expected flux has been calculated, assuming the flux normalisation given by the TA energy scale (see text). The map is in Galactic coordinates, with $l = 0°$ at the centre of the map and l increasing to the left.

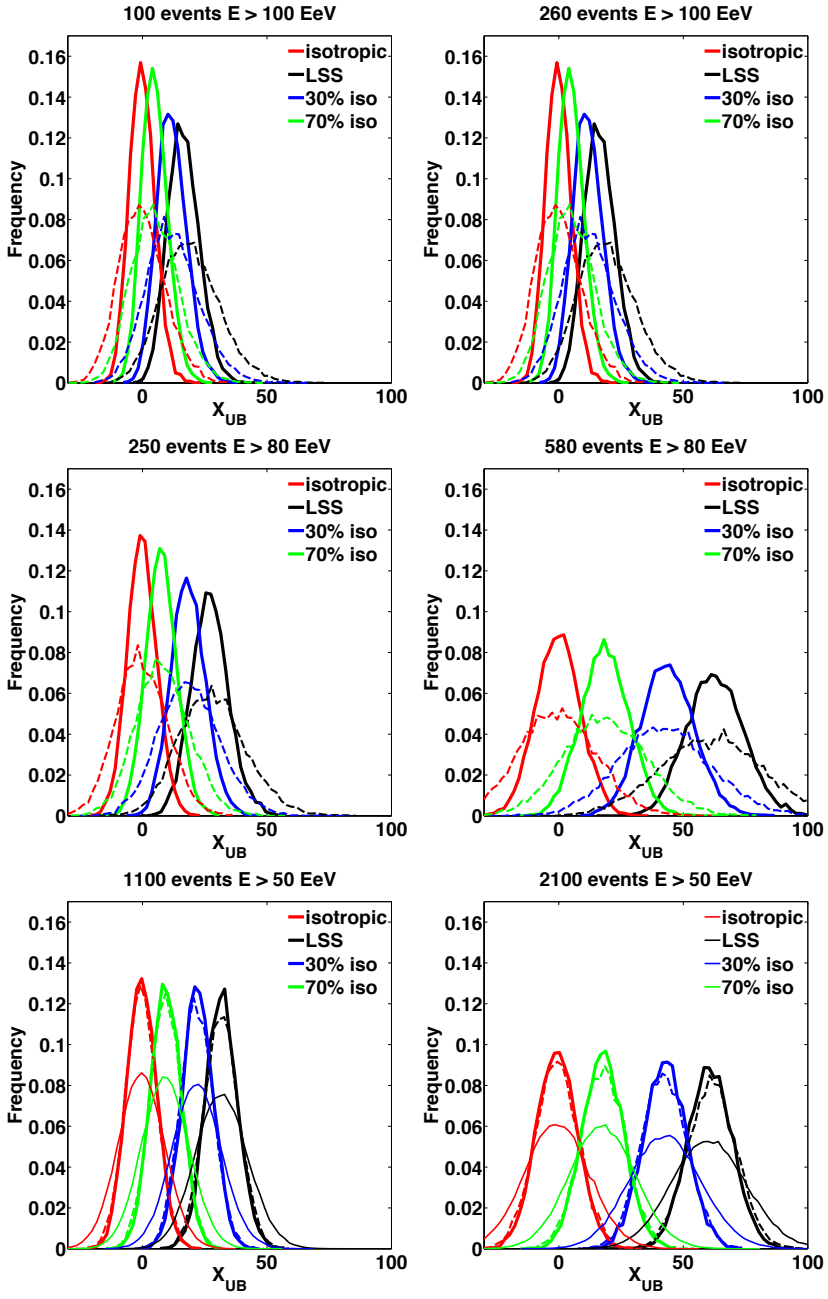

Figure 6.7. The distribution of values of $X_{\rm UB}$ in 10000 realisations of UHECRs with energy $E \geq 100, 80, 50$ EeV from top to bottom. Red lines give the isotropic expectation, black lines the expectation from the unbiased model, blue lines the expectation from the unbiased model assuming a 30% of the sample is isotropic and green lines the expectation for a sample that is 70% isotropic. Thick solid lines correspond to a UHECR source number density $\bar{n} = 10^{-2}$ Mpc^{-3}, dashed lines correspond to $\bar{n} = 10^{-3}$ Mpc^{-3} and thin solid lines to $\bar{n} = 10^{-4}$ Mpc^{-3} (the latter are only shown in the bottom row; see text for explanation). The left (right) column corresponds to the expected number of events in five years of JEM-EUSO following the Auger (TA/HiRes) energy scale.

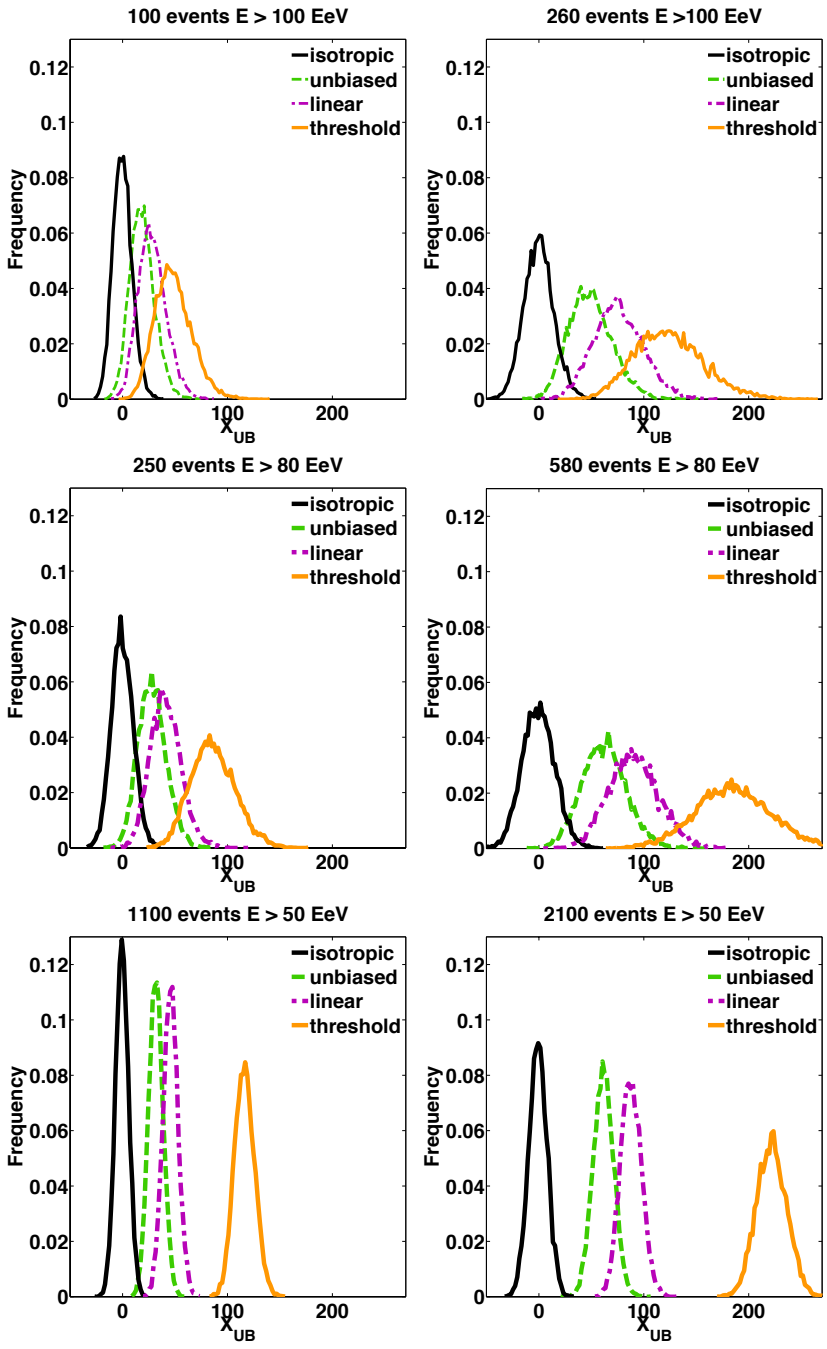

Figure 6.8. The distribution of values of $X_{\rm UB}$ in 10000 realisations of UHECRs with energy $E \geq 100, 80, 50$ EeV from top to bottom in the different bias models. Black histograms give the isotropic expectation, green histograms the expectation from the unbiased model, purple histograms the expectation from the linear bias model and orange histograms the expectation from the threshold bias model. The expected number of events shown in the left (right) column corresponds to the expected number of detected events with 5 years of JEM-EUSO following the Auger (TA) energy scale. The UHECR source number density has been assumed to be $\bar{n} = 10^{-3}$ Mpc^{-3}.

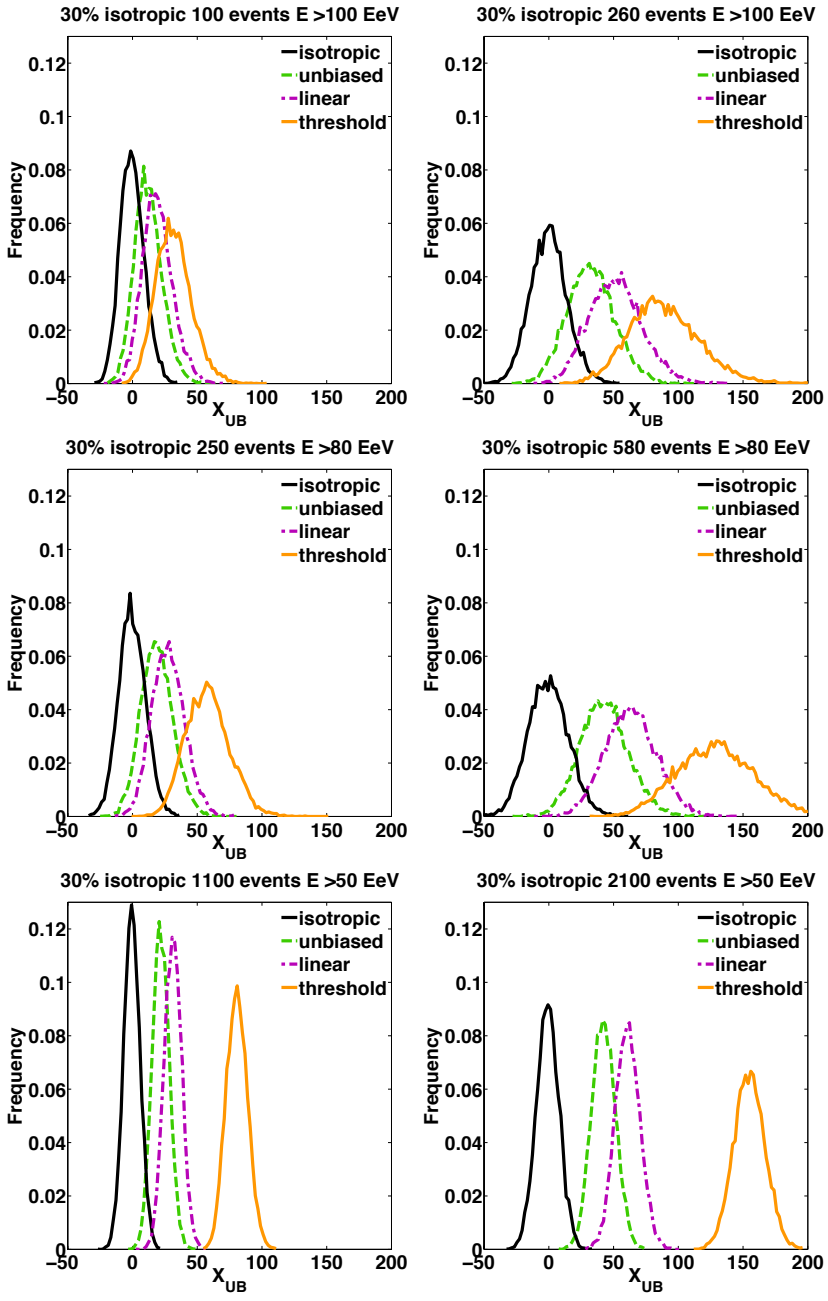

Figure 6.9. Same as figure 6.8 but assuming 30% of detected UHECRs arrive isotropically.

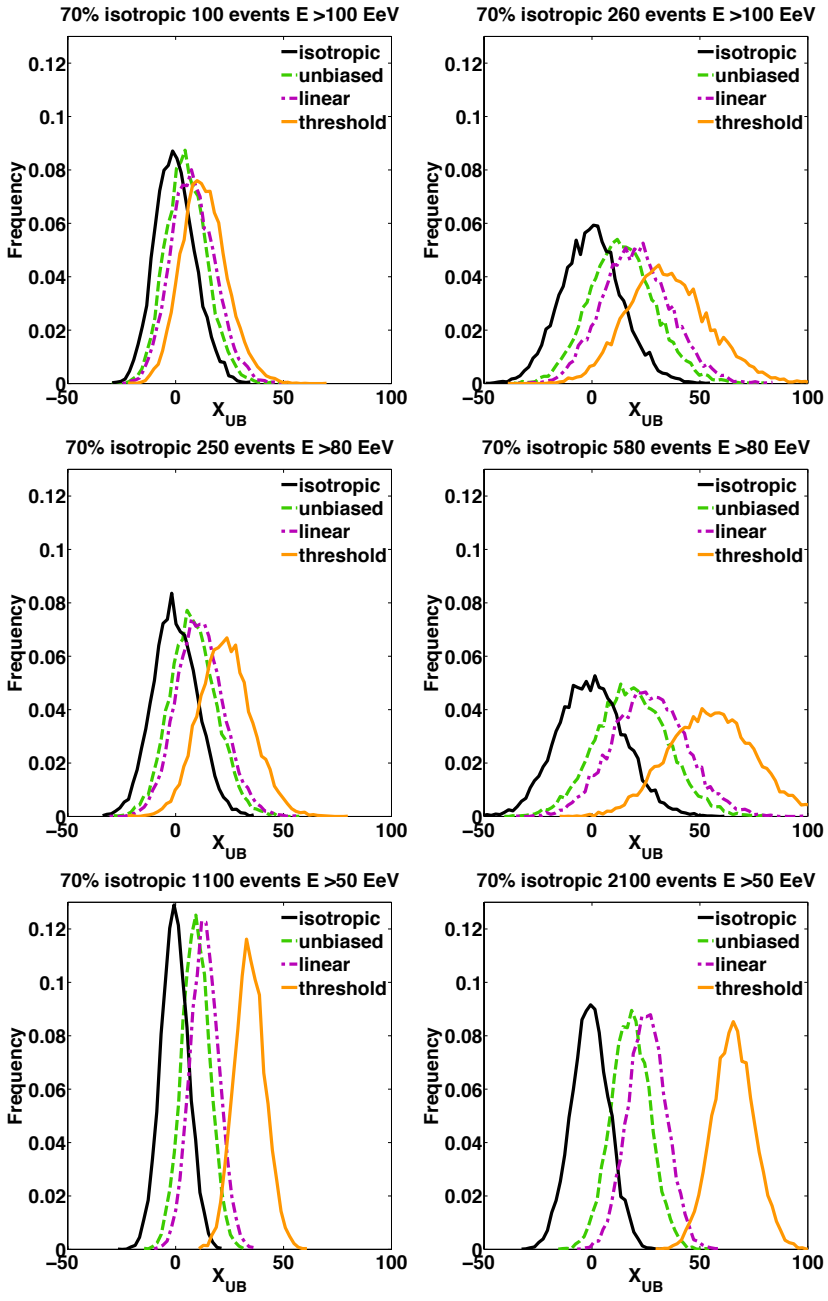

Figure 6.10. Same as figure 6.9 but assuming 70% of detected UHECRs arrive isotropically.

This page was intentionally left blank

Chapter 7

Conclusions and future work

We shall not cease from exploration, and the end of all our exploring will be to arrive where we started and know the place for the first time.

-T. S. Eliot, *Little Gidding*

In this thesis we set out to constrain the sources of ultra-high energy cosmic rays. What have we achieved in this endeavour?

In chapter 4, the expectation that the highest energy cosmic rays may reveal their sources, if they are protons, due to their short propagation horizon and small magnetic deflections. was examined. By studying the clustering in the arrival directions of the UHECRs detected by the Auger experiment and assuming that they are protons, the number density of UHECR sources was constrained to be larger than $\sim 10^{-4}$ Mpc^{-3}. By cross-correlating the Auger UHECR arrival directions with the local galaxy distribution, further constraints were placed on the unknown UHECR sources. It was shown that the Auger UHECRs exhibit a departure from isotropy at the 95% level and are consistent with the distribution of galaxies in the PSCz and 6dF surveys, if effective random deflections with amplitude $3^\circ - 5^\circ$ have been suffered. It was demonstrated that these conclusions are robust to the choice of galaxy catalogue, to the systematic uncertainty in the energy of the UHECRs and the unknown details of the UHECR spectrum produced by individual accelerators. Further, the possibility that UHECRs may correlate with a fraction of the

galaxy distribution was explored, by cross-correlating the Auger UHECRs with contiguous radial shells of galaxies. It was found, that there is no correlation with the galaxy distribution in the nearest $\sim$50 Mpc whereas the Auger UHECRs are consistent with the less anisotropic (by construction due to the larger volume covered) galaxy distribution in the more distant shells beyond $\sim$50 Mpc.

In chapter 5 we saw that gamma-ray emission is also a powerful tracer of hadronic acceleration in extragalactic sources and it should be possible to detect sources of UHECRs through their secondary gamma-ray signatures as long as hadronic and leptonic contributions can be disentangled. The gamma-ray spectra of a number of TeV BL Lacs, that are extreme in the sense that that their spectra are particularly hard and peak beyond 1 TeV, were studied. It was argued that standard leptonic scenarios strain to account for these observations. It was shown that inverse Compton cascades seeded by UHECRs in the intergalactic medium have also been invoked and can account for these spectra, only if very weak intergalactic magnetic fields are assumed. The synchrotron emission of UHECR secondaries produced in blazars located in magnetised environments, was studied, and hit was shown that it can provide an alternative explanation for the spectra of some of the sources studied. It was demonstrated that this, secondary synchrotron signal, is more robust to variations of the intergalactic magnetic field strength than the inverse Compton cascade signal, which is appealing in view of the large uncertainties on the intergalactic magnetic field strength. Finally, the possibility that the gamma-ray spectra of these sources originate in the synchrotron emission of secondary products of UHE photons, if these are emitted by UHECR accelerators inside magnetised regions, was considered. These could also naturally account for the observed blazar spectra, and in some cases they can also account for the observed variability, such as for example in the case of the blazar 1ES 0229+200, for which hints of a variability in $\sim$year long timescales have been observed.

In chapter 6, the potential of a future UHECR experiment, that is able to overcome the limitation of very low statistics to detect an anisotropy in the arrival directions of UHECRs, was explored. A future detector with an order of magnitude increased sensitivity to $\sim 10^{20}$ eV UHECRs compared to the current generation of experiments, such as the proposed space-based JEM-EUSO, was considered. The potential for a statistical discrimination between different astrophysical models, which was parametrised by the number density of UHECR sources, the possible bias of the UHECR accelerators with respect to the

galaxy distribution, and the unknown fraction of UHECRs that have been deflected by large angles was explored. It was shown that an anisotropy at the 99% level should be detectable, when the number of detected events exceeds 1000 beyond 50 EeV, as long as the composition is proton dominated and the number density of UHECR sources is high-comparable to that of bright galaxies. Once the number of detected events increases beyond 2000, the anisotropy should be detectable at the 99% level, even if the number density of UHECR sources is one order of magnitude lower, as long as the fraction of protons in the dataset is 70% or higher. Finally, it was shown that if the UHECR sources follow the distribution of galaxy clusters, an anisotropy at the 99.9% should be detectable once the number of detected events exceeds 2000, even if the fraction of protons at the highest energies is as low as 30%.

7.1 Future work

Much remains to do in future since not a single source of UHECRs is yet confirmed. For direct UHECR studies, such as the cross-correlation analysis presented in chapter 4 the main difficulty of course is the very small number of detected UHECR events. With Auger and and TA in full operation the available UHECR dataset has already doubled (although not yet been published) and is continuing to increase slowly. In light of this upcoming data it is important to use the best available galaxy survey to cross-correlate the arrival directions of the UHECRs. After the work in chapter 4 was completed the 2MASS selected 2MRS survey was completed and it would be important to check how the conclusions drawn evolve in light of the expanded UHECR datasets, when cross-correlated with the 2MRS, which is the densest sampled all-sky redshift survey to date and which improves over the sampling of the PSCz.

The uncertainty introduced in the cross-correlation results by the uncertainty in the measured redshift of the nearest galaxies, due to their peculiar velocities, was discussed. A possible refinement to the model of the expected UHECR source distribution, would be to consider a model of the reconstructed velocity field (see e.g., the work of Erdoğdu et al. 2006), which takes into account bulk flows due to known mass concentrations and would to some extent correct for this effect. The uncertainty introduced in the results by the magnitude limit of the survey was also discussed. To some extent, this was corrected for, by using the selection function of the surveys used. This method, which is unavoidable

if one wants to properly account for the relative contribution to the UHECR flux from sources as a function of distance, could bias the results by weighting observed structures over unobserved ones. A more sophisticated way to account for the magnitude limit of the survey without relying on the selection function would be to construct a volume (and magnitude) limited sample from the parent galaxy catalogue. Such a procedure is a natural extension of the models constructed in this work.

On the other hand, all the available surveys considered so far, are near or far infrared selected. It is natural to wonder how the conclusions of this analysis compare to an analysis of the cross-correlation of observed UHECRs with sources in different wavelength bands. Given the rapidly increasing number of extra-galactic gamma-ray detections a natural extension of the cross-correlation analysis presented here, would be to examine the cross-correlation of UHECRs with known extragalactic gamma-ray sources. By concentrating on gamma-ray emitters, which are known to be responsible for the production of photons with energy $\sim 10^{12}$ eV, one filters out the bulk of less extreme extragalactic emitters.

Similarly it would be beneficial to compare the conclusions of chapter 6 with those that one obtains when considering the 2MRS survey. The added benefit here is that a significant gain in exposure can be achieved with the improved coverage of the 2MRS compared to that of the PSCz near the galactic plane. It would also be important to compare the results obtained in the ad hoc threshold bias model constructed with the results that one obtains when considering instead a proper group and cluster catalogue such as the one presented by Crook et al. (2007). Another possible refinement of this analysis would be to consider a range of statistical tests in order to determine the ones most sensitive to the expected anisotropy signal with the number of events expected to be detected with a next generation experiment.

Much also remains to be done in the phenomenology of extragalactic gamma-ray sources, in the light of the upcoming high quality data by current and upcoming gamma-ray instruments. A natural extension to the study of the secondary gamma-ray synchrotron model presented in chapter 5 would be to study whether it provides a viable alternative explanation of the gamma-ray spectra of misaligned VHE AGN or FSRQs; the latter are expected to fulfil the high energetic requirements more comfortably than BL Lacs. The secondary UHE electron synchrotron emission should be observable independent of the jet orientation, as long as UHECRs are accelerated in AGN regions other than the jet, as the synchrotron gamma-rays are produced in the magnetised intergalactic medium that

surrounds the source.

In this thesis, the focus was on the study of the UHECR signatures of blazars, in the limit where intergalactic magnetic fields are strong enough to isotropise the inverse Compton cascade, which would otherwise be expected to develop in parallel. It would be important to study numerically with a robust self-contained setup, the relative contribution to the gamma-ray flux of the secondary synchrotron and inverse Compton cascade components, scanning the allowed parameter space; such a study has never been performed.

Another natural extension of the study presented in chapter 5, is to perform detailed modelling of the gamma-ray halo expected to form around the source in this channel and to compare it to the halo expected in other models of the blazar gamma-ray emission (see Kotera et al. 2011 for a discussion of the different channels). Gamma-ray halos around AGN are expected to form in a number of different ways and attract significant attention not least because of the possibility of constraining the strength of the intergalactic magnetic field, hence a detailed study would prepare the ground for interpreting the detection or absence of such a halo consistently. Finally, as mentioned in chapter 5, further work on the variability of the extreme TeV blazars that were studied is envisaged. It would be interesting to determine whether UHE neutral emission can account for the observed variability of extreme TeV blazars that are variable in $\sim$day timescales for reasonable injection parameters.

Based on the studies conducted in this thesis, it is concluded that the discovery of the sources of UHECRs that have for so long eluded us are within reach of upcoming UHECR and gamma-ray experiments. At the same time neutrino experiments are also closing in on the expected neutrino counterpart of a number of suspected extragalactic hadronic accelerators (e.g., Aartsen et al. 2013), making this an exciting moment for the field and highlighting the importance of a multi-messenger approach to particle astronomy.

This page was intentionally left blank

Appendix A

Appendix A: Distances in cosmology

The hubble parameter H_0 relates the recession speed v and the distance d in the expanding Universe:

$$v = H_0 d \tag{A.1}$$

at the present epoch $H_0 = 100\ h$ km^{-1} s^{-1}Mpc^{-1} where h is a dimensionless number that absorbs the uncertainty on H_0. The most recent measurement of H_0 comes from the Planck experiment that find $H_0 = 67.80 \pm 0.77$ km^{-1} s^{-1}Mpc^{-1} (Ade et al. 2013). The hubble parameter at redshift z can be expressed in terms of H_0 as

$$H = H_0 \cdot E(z) \tag{A.2}$$

where $E(z)$ is given by

$$E(z) = \sqrt{(\Omega_{\rm M}(1+z)^3 + \Omega_{\rm k}(1+z)^2 + \Omega_\Lambda}. \tag{A.3}$$

Here $\Omega_{\rm M}$, $\Omega_{\rm k}$, Ω_Λ are dimensionless density parameters given by:

$$\Omega_{\rm M} = \frac{8\pi G\rho_0}{3H_0^2}, \tag{A.4}$$

$$\Omega_{\mathrm{Lambda}} = \frac{\Lambda c^2}{3H_0^2}, \tag{A.5}$$

where ρ_0 is the matter density of the Universe today, and Λ the cosmological constant. The Ω_{k} parameter gives the curvature of space and is defined by the relation

$$\Omega_{\mathrm{M}} + \Omega_{\mathrm{k}} + \Omega_{\Lambda} = 1. \tag{A.6}$$

In a flat universe $\Omega_{\mathrm{k}} = 0$.

The *line-of-sight comoving distance*, d_{c}, between two objects is the distance that remains constant with epoch while the objects are moving with the Hubble flow. The total line of sight comoving distance to an object at redshift z is given by

$$d_{\mathrm{c}} = \frac{c}{H_0} \int_0^z \frac{\mathrm{d}z'}{E(z')}. \tag{A.7}$$

The *light travel distance* d_{T} is the product of ct_{L}, where t_{L} is the *look-back time*, that is, the difference between the age of the Universe at the time of observation t_0 and the age of the Universe when the photons were emitted t_e (according to the object). It is given by

$$t_{\mathrm{L}} = \frac{1}{H_0} \int_0^z \frac{\mathrm{d}z'}{(1+z')E(z')}. \tag{A.8}$$

The *luminosity distance* relates an object's observed integrated flux F to it's *intrinsic* luminosity integrated over all wavelengths, L:

$$d_{\mathrm{L}} = \sqrt{\frac{4\pi F}{L}}, \tag{A.9}$$

where the definition assumes a flat, non-expanding Universe. In a flat Universe d_{L} and d_{c} are related by:

$$d_{\mathrm{L}} = (1+z)d_{\mathrm{c}}. \tag{A.10}$$

The different distance measures are illustrated in figure A.1 for the currently favoured cosmological model, ΛCDM, with $\Omega_{\mathrm{M}} = 0.3$ and $\Omega_{\Lambda} = 0.7$. For a detailed discussion of

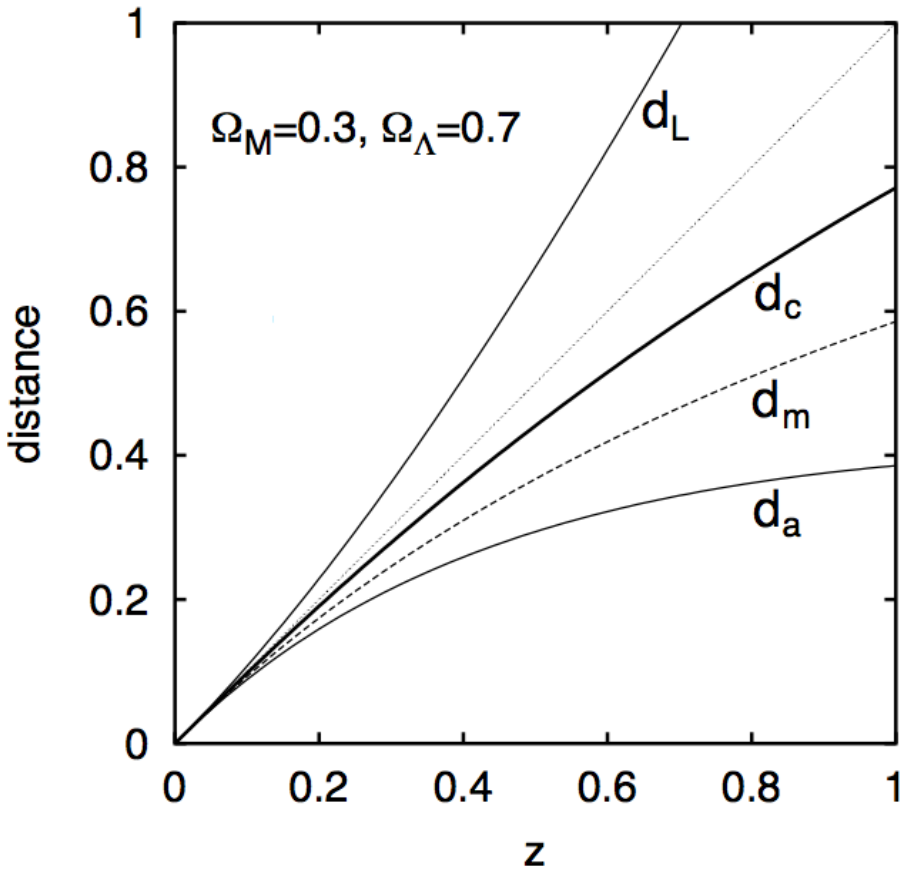

Figure A.1. Comparison of the different distance measures as a function of redshift, for a ΛCDM Universe with $\Omega_{\rm M} = 0.3$ and $\Omega_\Lambda = 0.7$. Here $d_{\rm L}$ is the luminosity distance, $d_{\rm c}$ is the comoving distance, $d_{\rm m}$ and $d_{\rm a}$ are the Mattig and angular diameter distance that we have not discussed in this work (see e.g. Martinez & Saar 2002). All distances are given in the units of the Hubble length c/H_0. Image from Martinez & Saar (2002).

distance measures in cosmology see Hogg (1999).

This page was intentionally left blank

Appendix B

Appendix B: Details of the Monte Carlo setup in chapter 5

The number of particles injected in a simulation with a power law spectrum $dN/dE \propto E^{-\alpha}$ between $E_{\mathrm{min,s}}$ and $E_{\mathrm{max,s}}$ is N_{s} and is given by:

$$\begin{aligned} N_{\mathrm{s}} = \int_{E_{\mathrm{min,s}}}^{E_{\mathrm{max,s}}} \frac{dN}{dE}\, dE &= \int_{E_{\mathrm{min,s}}}^{E_{\mathrm{max,s}}} k_{\mathrm{s}} \cdot \left(\frac{E}{E_{\mathrm{min}}}\right)^{-\alpha} dE \\ &= \frac{k_{\mathrm{s}}}{1-\alpha}\left[\frac{E^{1-\alpha}}{E_{\mathrm{min}}^{-\alpha}}\right]_{E_{\mathrm{min,s}}}^{E_{\mathrm{max,s}}} \\ &= \frac{k_{\mathrm{s}}}{1-\alpha} \cdot \frac{E_{\mathrm{max,s}}^{1-\alpha} - E_{\mathrm{min,s}}^{1-\alpha}}{E_{\mathrm{min}}^{-\alpha}} \end{aligned} \tag{B.1}$$

from which we get the weight of an individual particle in the simulation, k_{s}:

$$k_{\mathrm{s}} = N_{\mathrm{s}} \cdot (1-\alpha) \cdot \frac{E_{\mathrm{min}}^{-\alpha}}{E_{\mathrm{max,s}}^{1-\alpha} - E_{\mathrm{min,s}}^{1-\alpha}} \tag{B.2}$$

The luminosity of a source which emits a power law spectrum above energy $E_{\mathrm{min,L}}$ is:

$$\begin{aligned} L_{\mathrm{source}} = \int_{E_{\mathrm{min,L}}}^{E_{\mathrm{max,L}}} \frac{dN}{dE} \cdot E \; dE &= \int_{E_{\mathrm{min,L}}}^{E_{\mathrm{max,L}}} k_{\mathrm{L}} \cdot \frac{E^{1-\alpha}}{E_{\mathrm{min}}^{-\alpha}} dE \\ &= \frac{k_{\mathrm{L}}}{2-\alpha} \left[\frac{E^{2-\alpha}}{E_{\mathrm{min,L}}^{-\alpha}} \right]_{E_{\mathrm{min}}}^{E_{\mathrm{max,L}}} \\ &= \frac{k_{\mathrm{L}}}{2-\alpha} \cdot \frac{E_{\mathrm{max,L}}^{1-\alpha} - E_{\mathrm{min,L}}^{2-\alpha}}{E_{\mathrm{min}}^{-\alpha}}, \end{aligned} \tag{B.3}$$

hence:

$$k_{\mathrm{L}} = L_{\mathrm{source}} \cdot (2-\alpha) \cdot \frac{E_{\mathrm{min}}^{-\alpha}}{E_{\mathrm{max,L}}^{2-\alpha} - E_{\mathrm{min,L}}^{2-\alpha}} \tag{B.4}$$

To normalise the luminosity injected in a simulation to L_{source} we multiply the injected spectrum by $k_{\mathrm{L}}/k_{\mathrm{s}}$ which from equations B.2 and B.4:

$$\frac{k_{\mathrm{L}}}{k_{\mathrm{s}}} = \frac{L_{\mathrm{source}}}{N_{\mathrm{s}}} \cdot \frac{(2-\alpha)}{(1-\alpha)} \cdot \frac{E_{\mathrm{max,s}}^{1-\alpha} - E_{\mathrm{min,s}}^{1-\alpha}}{E_{\mathrm{max,L}}^{2-\alpha} - E_{\mathrm{min,L}}^{2-\alpha}} \tag{B.5}$$

To reweight a simulated spectrum with an injection spectrum $dN/dE \propto E^{-\alpha}$ (e.g. $\alpha = 1.1$) to a different injection index γ (e.g. $\gamma = -2$) the following expression can be used:

$$N_{\mathrm{s,w}} = N_{\mathrm{s}} \cdot \frac{1-\alpha}{1-\gamma} \cdot \frac{E_{\mathrm{max}}^{(1-\gamma)} - E_{\mathrm{min}}^{(1-\gamma)}}{E_{\mathrm{max}}^{(1-\alpha)} - E_{\mathrm{min}}^{(1-\alpha)}}, \tag{B.6}$$

where N_{s} is the number of simulated primaries, $N_{\mathrm{s,w}}$ is the number of simulated primaries if we account for the conversion from α to γ and $N_{\mathrm{tot,real}} = k'$ is the number of injected particles at the source given a luminosity L. The spectrum output from the simulation is finally normalised, multiplying by $N_{\mathrm{tot,real}}/N_{\mathrm{s,w}}$. Typically this reweighting procedure is employed when we are interested in simulating a soft intrinsic spectrum but inject instead a harder spectrum to improve computation time.

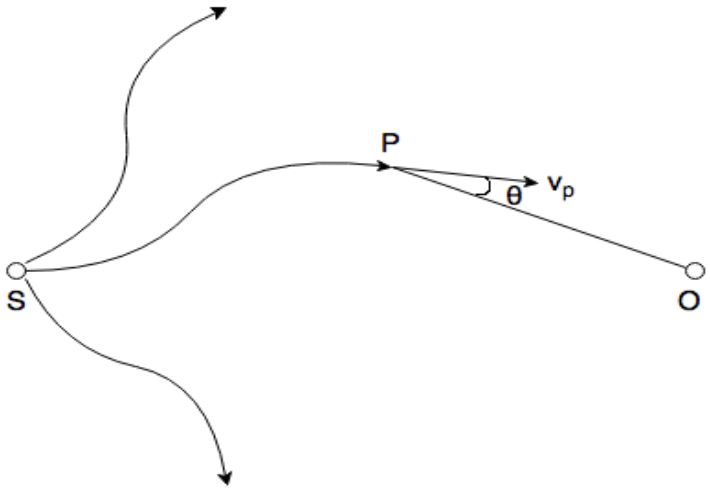

Figure B.1. Diagram depicting the source-observer setup and the condition for registering a newly created lepton during the UHECR propagation in our simulation volume. Here S is the source position and the curved lines depict the trajectories of UHECRs. At point P a lepton is created and O the position of the observer. The momentum vector of the newly created lepton is denoted v_p. Any lepton created with $\theta(OP, v_\mathrm{p}) \leq 11^\circ$ is recorded and propagated to the observer.

This page was intentionally left blank

Bibliography

Aab, A., Abreu, P., Aglietta, M. et al. (Pierre Auger Collaboration) 2013, The Pierre Auger Observatory: Contributions to the 33rd International Cosmic Ray Conference (ICRC 2013), 1307.5059

Aartsen, M. et al. (IceCube Collaboration) 2013, Evidence for High-Energy Extraterrestrial Neutrinos at the IceCube Detector, Science 342, 6161, 947, 1311.5238

Aartsen, M. G., Abbasi, R., Abdou, Y. et al. (IceCube Collaboration) 2013, Search for time-independent neutrino emission from astrophysical sources with 3 years of IceCube data, ArXiv e-prints 1307.6669

Abbasi, R., Abdou, Y., Abu-Zayyad, T. et al. (IceCube Collaboration) 2012, An absence of neutrinos associated with cosmic-ray acceleration in γ-ray bursts, Nature484, 351, 1204.4219

Abbasi, R., Abu-Zayyad, T., Archbold, G. et al. (HiRes Collaboration) 2002, Geometry and optics calibration for air fluorescence detectors using star light, Astroparticle Physics 18, 237

Abbasi, R. U., Abu-Zayyad, T., Allen, M. et al. (HiRes Collaboration) 2008, First Observation of the Greisen-Zatsepin-Kuzmin Suppression, Physical Review Letters 100, 10, 101101, astro-ph/0703099

Abbasi, R. U., Abu-Zayyad, T., Allen, M. et al. (HiRes Collaboration) 2010, Analysis of Large-scale Anisotropy of Ultra-high Energy Cosmic Rays in HiRes Data, The Astrophysical Journal Letters713, L64, 1002.1444

Abdo, A. et al. 2011, The Second Catalog of Active Galactic Nuclei Detected by the Fermi Large Area Telescope, The Astrophysical Journal743, 171, 1108.1420

Abdo, A. A., Ackermann, M., Ajello, M. et al. (Fermi LAT Collaboration) 2010, Spectrum of the Isotropic Diffuse Gamma-Ray Emission Derived from First-Year Fermi Large Area Telescope Data, Physical Review Letters 104, 10, 101101, 1002.3603

Abeysekara, A. U., Alfaro, R., Alvarez, C. et al. 2013, Sensitivity of the high altitude water Cherenkov detector to sources of multi-TeV gamma rays, Astroparticle Physics 50, 26, 1306.5800

Abraham, J., Abreu, P., Aglietta, M. et al. (Pierre Auger Collaboration) 2007, Correlation of the Highest-Energy Cosmic Rays with Nearby Extragalactic Objects, Science 318, 938, 0711.2256

Abraham, J., Abreu, P., Aglietta, M. et al. (Pierre Auger Collaboration) 2008, Correlation of the highest-energy cosmic rays with the positions of nearby active galactic nuclei, Astroparticle Physics 29, 188, 0712.2843

Abraham, J., Abreu, P., Aglietta, M. et al. (Pierre Auger Collaboration) 2009, Astrophysical Sources of Cosmic Rays and Related Measurements with the Pierre Auger Observatory, ArXiv e-prints 0906.2347

Abraham, J., Abreu, P., Aglietta, M. et al. (Pierre Auger Collaboration) 2010a, Measurement of the Depth of Maximum of Extensive Air Showers above 10^{18} eV, Physical Review Letters 104, 9, 091101, 1002.0699

Abraham, J., Abreu, P., Aglietta, M. et al. (Pierre Auger Collaboration) 2010b, Measurement of the energy spectrum of cosmic rays above 10^{18} eV using the Pierre Auger Observatory, Physics Letters B 685, 239, 1002.1975

Abraham, J., Aglietta, M., Aguirre, I. C. et al. (Pierre Auger Collaboration) 2004, Properties and performance of the prototype instrument for the Pierre Auger Observatory, Nuclear Instruments and Methods in Physics Research A 523, 50

Abramowski, A., Aharonian, F., Benkhali, F. A. et al. (H. E. S. S. Collaboration) 2014, Search for Extended Gamma-ray Emission around AGN with H.E.S.S. and Fermi-LAT, ArXiv e-prints 1401.2915

Abreu, P., Aglietta, M., Ahlers, M. et al. (Pierre Auger Collaboration) 2012a, Large-scale Distribution of Arrival Directions of Cosmic Rays Detected Above 10^{18} eV at the Pierre Auger Observatory, The Astrophysical Journal Supplement Series203, 34, 1210.3736

Abreu, P., Aglietta, M., Ahlers, M. et al. (Pierre Auger Collaboration) 2012b, Search for ultrahigh energy neutrinos in highly inclined events at the Pierre Auger Observatory [Phys. Rev. D 84, 122005 (2011)], Physical Review D85, 2, 029902, 1202.1493

Abreu, P., Aglietta, M., Ahn, E. J. et al. (Pierre Auger Collaboration) 2011a, Anisotropy and chemical composition of ultra-high energy cosmic rays using arrival directions measured by the Pierre Auger Observatory, JCAP 1106, 022, 1106.3048

Abreu, P. et al. (Pierre Auger Collaboration) 2010, Update on the correlation of the highest energy cosmic rays with nearby extragalactic matter, Astroparticle Physics 34, 314, 1009.1855

Abreu, P. et al. (Pierre Auger Collaboration) 2011b, The pierre auger observatory ii: Studies of cosmic ray composition and hadronic interaction models, International Cosmic Ray Conference 2011 1107.4804

Abreu, P. et al. 2011, The exposure of the hybrid detector of the Pierre Auger Observatory, Astropart.Phys. 34, 368, 1010.6162

Abreu, P. et al. (Pierre Auger Collaboration) 2012a, A Search for Point Sources of EeV Neutrons, Astrophys.J. 760, 148, 1211.4901

Abreu, P. et al. (Pierre Auger Collaboration) 2012b, The Pierre Auger Observatory V: Enhancements, J.Phys.Conf.Ser. 375, 052006, 1107.4807

Abreu, P. et al. (Pierre Auger Collaboration) 2013, Bounds on the density of sources of ultra-high energy cosmic rays from the Pierre Auger Observatory, JCAP 1305, 009, 1305.1576

Abu-Zayyad, T., Aida, R., Allen, M. et al. (Telescope Array Collaboration) 2013a, The Cosmic-Ray Energy Spectrum Observed with the Surface Detector of the Telescope Array Experiment, The Astrophysical Journal Letters768, L1, 1205.5067

Abu-Zayyad, T., Allen, M., Anderson, R. et al. (Telescope Array Collaboration, Pierre Auger Collaboration) 2013b, Pierre Auger Observatory and Telescope Array: Joint Contributions to the 33rd International Cosmic Ray Conference 1310.0647

Acciari, V. A., Aliu, E., Arlen, T. et al. (VERITAS Collaboration) 2010a, The Discovery of γ-Ray Emission from the Blazar RGB J0710+591, The Astrophysical Journal Letters715, L49, 1005.0041

Acciari, V. A., Aliu, E., Beilicke, M. et al. (VERITAS Collaboration) 2010b, Discovery of Variability in the Very High Energy γ-Ray Emission of 1ES 1218+304 with VERITAS, The Astrophysical Journal Letters709, L163, 1001.2590

Ackermann, M., Ajello, M., Allafort, A. et al. 2013, Detection of the characteristic pion-decay signature in supernova remnants, Science 339, 6121, 807, http://www.sciencemag.org/content/339/6121/807.full.pdf, URL `http://www.sciencemag.org/content/339/6121/807.abstract`

Actis, M. et al. (CTA Consortium) 2011, Design concepts for the Cherenkov Telescope Array CTA: An advanced facility for ground-based high-energy gamma-ray astronomy, Exper.Astron. 32, 193, 1008.3703

Adams, J. et al. (JEM-EUSO Collaboration) 2012, The JEM-EUSO Mission: Status and Prospects in 2011 1204.5065

Adams, J. H., Ahmad, S., Albert, J.-N. et al. (JEM-EUSO Collaboration) 2013, An evaluation of the exposure in nadir observation of the JEM-EUSO mission, Astroparticle Physics 44, 76, 1305.2478

Ade, P. A. R., Aghanim, N., Armitage-Caplan, C. et al. (Planck Collaboration) 2013, Planck 2013 results. I. Overview of products and scientific results 1303.5062

Aharonian, F., Akhperjanian, A. G., Anton, G. et al. 2009, Constraints on the multi-TeV particle population in the Coma galaxy cluster with HESS observations, Astronomy and Astrophysics502, 437, 0907.0727

Aharonian, F., Akhperjanian, A. G., Barres de Almeida, U. et al. 2007, New constraints on the mid-IR EBL from the HESS discovery of VHE γ-rays from 1ES 0229+200, Astronomy and Astrophysics475, L9, 0709.4584

Aharonian, F., Akhperjanian, A. G., Bazer-Bachi, A. R. et al. 2006, Evidence for VHE γ-ray emission from the distant BL Lac PG 1553+113, Astronomy and Astrophysics448, L19, astro-ph/0601545

Aharonian, F., Essey, W., Kusenko, A. et al. 2013, TeV gamma rays from blazars beyond z=1?, Physical Review D87, 6, 063002, 1206.6715

Aharonian, F. et al. (H.E.S.S. Collaboration) 2006, A Low level of extragalactic background light as revealed by gamma-rays from blazars, Nature 440, 1018, astro-ph/0508073

Aharonian, F. A. 2000, TeV gamma rays from BL Lac objects due to synchrotron radiation of extremely high energy protons, New Astronomy5, 377, 0003159

Aharonian, F. A., Coppi, P. S. & Voelk, H. J. 1994, Very high energy gamma rays from active galactic nuclei: Cascading on the cosmic background radiation fields and the formation of pair halos, ApJl 423, L5, astro-ph/9312045

Ahlers, M. & Salvado, J. 2011, Cosmogenic gamma rays and the composition of cosmic rays, Physical Review D84, 8, 085019, 1105.5113

Albert, J., Aliu, E., Anderhub, H. et al. 2006, Discovery of Very High Energy Gamma Rays from 1ES 1218+30.4, The Astrophysical Journal Letters642, L119, astro-ph/0603529

Alcock, C. & Hatchett, S. 1978, The effects of small-angle scattering on a pulse of radiation with an application of X-ray bursts and interstellar dust, Astrophys. J. 222, 456

Aleksic, J. et al. (MAGIC Collaboration) 2012a, Constraining Cosmic Rays and Magnetic Fields in the Perseus Galaxy Cluster with TeV observations by the MAGIC telescopes, Astron.Astrophys. 541, A99, 1111.5544

Aleksic, J. et al. (MAGIC Collaboration) 2012b, PG 1553+113: five years of observations with MAGIC, Astrophys.J. 748, 46, 1101.2764

Aliu, E., Archambault, S., Arlen, T. et al. 2014, A Three-year Multi-wavelength Study of the Very-high-energy gamma-Ray Blazar 1ES 0229+200, The Astrophysical Journal782, 13, 1312.6592

Aliu, E. et al. (MAGIC Collaboration) 2008, Very-High-Energy Gamma Rays from a Distant Quasar: How Transparent Is the Universe?, Science 320, 1752, 0807.2822

Allard, D. 2012, Extragalactic propagation of ultrahigh energy cosmic-rays, Astroparticle Physics 39, 33, 1111.3290

Allard, D., Busca, N., Decerprit, G. et al. 2008, Implications of the cosmic ray spectrum for the mass composition at the highest energies, JCAP 0810, 033, 0805.4779

Allison, P., Auffenberg, J., Bard, R. et al. (ARA Collaboration) 2012, Design and initial performance of the Askaryan Radio Array prototype EeV neutrino detector at the South Pole, Astroparticle Physics 35, 457, 1105.2854

Aloisio, R., Berezinsky, V. & Gazizov, A. 2009, Ultra High Energy Cosmic Rays: The disappointing model, ArXiv e-prints 0907.5194

Aloisio, R., Berezinsky, V. & Gazizov, A. 2011, Ultra High Energy Cosmic Rays: The disappointing model, Astropart.Phys. 34, 620, 0907.5194

Alvarez-Muñiz, J., Engel, R. & Stanev, T. 2002, Ultrahigh-Energy Cosmic-Ray Propagation in the Galaxy: Clustering versus Isotropy, Astrophys. J. 572, 185, astro-ph/0112227

Anchordoqui, L. A., Goldberg, H. & Weiler, T. J. 2001, Auger Test of the Cen A Model of Highest Energy Cosmic Rays, Physical Review Letters 87, 8, 081101, astro-ph/0103043

Apel, W. et al. 2011, Kneelike structure in the spectrum of the heavy component of cosmic rays observed with KASCADE-Grande, Phys.Rev.Lett. 107, 171104, 1107.5885

Arlen, T. C., Vassiliev, V. V., Weisgarber, T. et al. 2012, Intergalactic Magnetic Fields and Gamma Ray Observations of Extreme TeV Blazars, ArXiv e-prints 1210.2802

Atwood, W. B., Abdo, A. A., Ackermann, M. et al. 2009, The Large Area Telescope on the Fermi Gamma-Ray Space Telescope Mission, The Astrophysical Journal697, 1071, 0902.1089

Axford, W. I., Leer, E. & Skadron, G. 1977, The acceleration of cosmic rays by shock waves, 132–137

Bahcall, J. N. & Waxman, E. 2000, Ultra-High-Energy Cosmic Rays May Come from Clustered Sources, The Astrophysical Journal542, 542, hep-ph/9912326

Bahcall, J. N. & Waxman, E. 2003, Has the GZK cutoff been discovered?, Phys.Lett. B556, 1, hep-ph/0206217

Bahcall, J. N. & Waxman, E. 2003, Has the GZK suppression been discovered?, Physics Letters B 556, 1, hep-ph/0206217

Barcikowski, E. et al. (Pierre Auger, TA, Yakutsk Collaborations) 2013, Mass Composition Working Group Report at UHECR-2012, EPJ Web Conf. 53, 01006, 1306.4430

Beck, R. & Krause, M. 2005, Revised equipartition and minimum energy formula for magnetic field strength estimates from radio synchrotron observations, Astronomische Nachrichten 326, 414, astro-ph/0507367

Beck, R. & Wielebinski, R. 2013, Magnetic Fields in Galaxies, 641

Bell, A. R. 1978, The acceleration of cosmic rays in shock fronts. I, MNRAS 182, 147

Berezinsky, V., Gazizov, A. & Grigorieva, S. 2006, On astrophysical solution to ultrahigh energy cosmic rays, Phys. Rev. D 74, 4, 043005, hep-ph/0204357

Berezinsky, V. S. & Zatsepin, G. T. 1969, Cosmic rays at ultrahigh energies (neutrino?)., Physics Letters B 28, 423

Bergeson, H. E., Cassiday, G. L., Chiu, T.-W. et al. 1977, Measurement of light emission from remote cosmic-ray air showers, Physical Review Letters 39, 847

Beringer, J., Arguin, J. F., Barnett, R. M. et al. (Particle Data Group) 2012, Review of particle physics, Phys. Rev. D 86, 010001, URL `http://link.aps.org/doi/10.1103/PhysRevD.86.010001`

Berlind, A. A., Farrar, G. R. & Zaw, I. 2010, Correlations Between Ultrahigh Energy Cosmic Rays and Infrared-luminous Galaxies, The Astrophysical Journal716, 914, 0904.4276

Bertone, G., Isola, C., Lemoine, M. et al. 2002, Ultrahigh energy heavy nuclei propagation in extragalactic magnetic fields, Phys. Rev. D 66, 10, 103003, astro-ph/0209192

Bhattacharjee, A. & Sigl, G. 2000, Origin and propagation of extremely high energy cosmic rays, Phys. Rep. 327 327, 109

Blaksley, C., Parizot, E., Decerprit, G. et al. 2013, Ultra-high-energy cosmic ray source statistics in the GZK energy range, Astronomy and Astrophysics552, A125

Blandford, R. D. & Ostriker, J. P. 1978, Particle acceleration by astrophysical shocks, ApJ Letters 221, L29

Blasi, P., Burles, S. & Olinto, A. V. 1999, Cosmological Magnetic Field Limits in an Inhomogeneous Universe, ApJl 514, L79, astro-ph/9812487

Blasi, P., Epstein, R. I. & Olinto, A. V. 2000, Ultra-High-Energy Cosmic Rays from Young Neutron Star Winds, ApJ Letters 533, L123

Blumenthal, G. R. & Gould, R. J. 1970, Bremsstrahlung, Synchrotron Radiation, and Compton Scattering of High-Energy Electrons Traversing Dilute Gases, Reviews of Modern Physics 42, 237

Broderick, A. E., Chang, P. & Pfrommer, C. 2012, The Cosmological Impact of Luminous TeV Blazars. I. Implications of Plasma Instabilities for the Intergalactic Magnetic Field and Extragalactic Gamma-Ray Background, The Astrophysical Journal752, 22, 1106.5494

Casse, F., Lemoine, M. & Pelletier, G. 2002, Transport of cosmic rays in chaotic magnetic fields, Phys. Rev. D 65, 2, 023002, astro-ph/0109223

Cavallo, G. 1978, On the sources of ultra-high energy cosmic rays, Astronomy and Astrophysics65, 415

Chiba, N., Hashimoto, K., Hayashida, N. et al. 1991, Akeno Giant Air Shower Array (AGASA) Covering 100km^2 Area, 700

Clark, T. A., Brown, L. W. & Alexander, J. K. 1970, Spectrum of the Extra-galactic Background Radiation at Low Radio Frequencies, Nature228, 847

Coppi, P. S. & Blandford, R. D. 1990, Reaction rates and energy distributions for elementary processes in relativistic pair plasmas, Monthly Notices of the RAS245, 453

Courteau, S. & van den Bergh, S. 1999, The Solar Motion Relative to the Local Group, Astronomical Journal118, 337, astro-ph/9903298

Crook, A. C., Huchra, J. P., Martimbeau, N. et al. 2007, Groups of Galaxies in the Two Micron All Sky Redshift Survey, The Astrophysical Journal655, 790, astro-ph/0610732

Cuoco, A., D'Abrusco, R., Longo, G. et al. 2006, The footprint of large scale cosmic structure on the ultrahigh energy cosmic ray distribution, Journal of Cosmology and Astro-Particle Physics 1, 9, astro-ph/0510765

Cuoco, A., Hannestad, S., Haugbølle, T. et al. 2009, A Global Autocorrelation Study After the First Auger Data: Impact on the Number Density of UHECR Sources, The Astrophysical Journal702, 825, 0809.4003

Danforth, C. W., Keeney, B. A., Stocke, J. T. et al. 2010, HST/COS Observations of the Ly alpha Forest toward the BL Lac Object 1ES1553+113, ArXiv e-prints 1005.2191

Dar, A. 2012, Neutrinos And Cosmic Rays From Gamma Ray Bursts, ArXiv e-prints 1205.3479

Das, S., Kang, H., Ryu, D. et al. 2008, Propagation of Ultra-High-Energy Protons through the Magnetized Cosmic Web, ApJ 682, 29, 0801.0371

Dawson, B. R., Mariş, I. C., Roth, M. et al. 2013, The energy spectrum of cosmic rays at the highest energies, in European Physical Journal Web of Conferences, European Physical Journal Web of Conferences, volume 53, 1005, 1306.6138

Decerprit, G., Busca, N. G. & Parizot, E. 2012, Extended clustering analyses to constrain the deflection angular scale and source density of the ultra-high-energy cosmic rays, Astronomy and Astrophysics538, A16, 1111.4867

Deligny, O., Letessier-Selvon, A. & Parizot, E. 2004, Magnetic horizons of UHECR sources and the GZK feature, Astroparticle Physics 21, 609, astro-ph/0303624

Denton, P. B., Anchordoqui, L. A., Berlind, A. A. et al. (JEM-EUSO Collaboration) 2014, Sensitivity of orbiting JEM-EUSO to large-scale cosmic-ray anisotropies 1401.5757

Dermer, C. D., Cavadini, M., Razzaque, S. et al. 2011, Time Delay of Cascade Radiation for TeV Blazars and the Measurement of the Intergalactic Magnetic Field, The Astrophysical Journal Letters733, L21, 1011.6660

Dermer, C. D. & Menon, G. 2010, High Energy Radiation from Black Holes: A Summary, ArXiv e-prints 1001.1760

Dermer, C. D., Murase, K. & Takami, H. 2012, Variable Gamma-Ray Emission Induced by Ultra-high Energy Neutral Beams: Application to 4C +21.35, The Astrophysical Journal755, 147, 1203.6544

Dermer, C. D. & Schlickeiser, R. 1993, On the location of the acceleration and emission sites in gamma-ray blazars astro-ph/9312052

Dolag, K., Kachelriess, M., Ostapchenko, S. et al. 2011, Lower Limit on the Strength and Filling Factor of Extragalactic Magnetic Fields, The Astrophysical Journal Letters727, L4, 1009.1782

Dolag, K. et al. 2005, Constrained simulations of the magnetic field in the local Universe and the propagation of ultrahigh energy cosmic rays, JCAP 1, 9, astro-ph/0410419

Dole, H., Lagache, G., Puget, J.-L. et al. 2006, The cosmic infrared background resolved by Spitzer. Contributions of mid-infrared galaxies to the far-infrared background, Astronomy and Astrophysics451, 417, astro-ph/0603208

Dominguez, A., Primack, J., Rosario, D. et al. 2011, Extragalactic Background Light Inferred from AEGIS Galaxy SED-type Fractions, Monthly Notices of the Royal Astronomical Society 410, 4, 2556

Donato, D., Ghisellini, G., Tagliaferri, G. et al. 2001, Hard x-ray properties of blazars, aa 375, 739

Donnert, J., Dolag, K., Lesch, H. et al. 2009, Cluster magnetic fields from galactic outflows, MNRAS 392, 1008, 0808.0919

d'Orfeuil, B. R., Allard, D., Lachaud, C. et al. 2014, Anisotropy expectations for ultra-high-energy cosmic rays with future high statistics experiments 1401.1119

Dubovsky, S. L. & Tinyakov, P. G. 1998, Galactic anisotropy as signature of "top-down" mechanisms of ultrahigh-energy cosmic rays, Soviet Journal of Experimental and Theoretical Physics Letters 68, 107, hep-ph/9802382

Dubovsky, S. L., Tinyakov, P. G. & Tkachev, I. I. 2000, Statistics of Clustering of Ultrahigh Energy Cosmic Rays and the Number of Their Sources, Physical Review Letters 85, 1154, astro-ph/0001317

Dumm, J. (VERITAS Collaboration) 2013, Highlights from the VERITAS Blazar Program, International Cosmic Ray Conference 2013

Durrer, R. & Neronov, A. 2013, Cosmological magnetic fields: their generation, evolution and observation, Astronomy and Astrophysics Reviews21, 62, 1303.7121

Dwek, E. & Krennrich, F. 2013, The Extragalactic Background Light and the Gamma-ray Opacity of the Universe, Astropart.Phys. 43, 112, 1209.4661

Elyiv, A., Neronov, A. & Semikoz, D. V. 2009, Gamma-ray induced cascades and magnetic fields in the intergalactic medium, Physical Review D80, 2, 023010, 0903.3649

Erdoğdu, P., Lahav, O., Huchra, J. P. et al. 2006, Reconstructed density and velocity fields from the 2MASS Redshift Survey, Monthly Notices of the RAS373, 45, astro-ph/0610005

Essey, W., Ando, S. & Kusenko, A. 2011, Determination of intergalactic magnetic fields from gamma ray data, Astroparticle Physics 35, 135, 1012.5313

Essey, W., Kalashev, O. E., Kusenko, A. et al. 2010, Secondary Photons and Neutrinos from Cosmic Rays Produced by Distant Blazars, Physical Review Letters 104, 14, 141102, astro-ph/0912.3976

Essey, W. & Kusenko, A. 2010, A new interpretation of the gamma-ray observations of distant active galactic nuclei, Astroparticle Physics 33, 81, 0905.1162

Essey, W. & Kusenko, A. 2013, Understanding the spectrum of a distant blazar PKS 1424+240 and its implications, ArXiv e-prints 1310.3440

F. Aharonian, A. G. Akhperjanian, A. R. Bazer-Bachi et al. 2006, Observations of the crab nebula with hess, AA 457, 3, 899, URL `http://dx.doi.org/10.1051/0004-6361:20065351`

Fabian, A. C. & Barcons, X. 1992, The origin of the X-ray background, Annual Review of Astronomy and Astrophysics30, 429

Fanaroff, B. L. & Riley, J. M. 1974, The morphology of extragalactic radio sources of high and low luminosity, Monthly Notices of the RAS167, 31P

Fang, K., Kotera, K., Murase, K. et al. 2013a, A decisive test for the young pulsar origin of ultrahigh energy cosmic rays with IceCube, ArXiv e-prints 1311.2044

Fang, K., Kotera, K. & Olinto, A. V. 2012, Newly Born Pulsars as Sources of Ultrahigh Energy Cosmic Rays, The Astrophysical Journal 750, 118, 1201.5197

Fang, K., Kotera, K. & Olinto, A. V. 2013b, Ultrahigh energy cosmic ray nuclei from extragalactic pulsars and the effect of their Galactic counterparts, JCAP 3, 010, 1302.4482

Farrar, G. R. & Gruzinov, A. 2009, Giant AGN Flares and Cosmic Ray Bursts, ApJ 693, 329, 0802.1074

Fazio, G. G., Ashby, M. L. N., Barmby, P. et al. 2004, Number Counts at $3 < \lambda < 10$ μm from the Spitzer Space Telescope, The Astrophysical Journal Supplement Series154, 39, astro-ph/0405595

Feretti, L., Dallacasa, D., Giovannini, G. et al. 1995, The magnetic field in the Coma cluster., Astronomy and Astrophysics302, 680, astro-ph/9504058

Fermi, E. 1949, On the Origin of the Cosmic Radiation, Physical Review 75, 1169

Ferrari, C., Govoni, F., Schindler, S. et al. 2008, Observations of Extended Radio Emission in Clusters, Space Science Reviews134, 93, 0801.0985

Ferrigno, C., Blasi, P. & De Marco, D. 2005, High energy gamma ray counterparts of astrophysical sources of ultrahigh energy cosmic rays, Astropart.Phys. 23, 211, astro-ph/0404352

Finke, J. D., Razzaque, S. & Dermer, C. D. 2010, Modeling the Extragalactic Background Light from Stars and Dust, The Astrophysical Journal712, 238, 0905.1115

Fisher, K. B., Huchra, J. P., Strauss, M. A. et al. 1995, The IRAS 1.2 Jy Survey: Redshift Data, The Astrophysical Journal Supplement Series100, 69, astro-ph/9502101

Fodor, Z. & Katz, S. D. 2001, Ultrahigh energy cosmic rays from compact sources, Physical Review D63, 2, 023002, hep-ph/0007158

Fodor, Z., Katz, S. D., Ringwald, A. et al. 2003, Bounds on the cosmogenic neutrino flux, Journal of Cosmology and Astro-Particle Physics 11, 15, hep-ph/0309171

Fortin, P. 2008, VERITAS Observations of the BL Lac Object 1ES 1218+304, in American Institute of Physics Conference Series, American Institute of Physics Conference Series, volume 1085 (edited by Aharonian, F. A., Hofmann, W. & Rieger, F.), 565–568, 0810.0301

Fossati, G. 1998, Unifying all blazars, Proceedings of the "BL Lac Phenomenon" Meeting, Turku, Finland, 1998 June astro-ph/9812158

Franceschini, A., Rodighiero, G. & Vaccari, M. 2008, The extragalactic optical-infrared background radiations, their time evolution and the cosmic photon-photon opacity, Astron.Astrophys. 487, 837, 0805.1841

Fukushima, M., Ivanov, D., Kawata, K. et al. (Telescope Array Collaboration) 2013, TA anisotropy Summary: Contributions to the 33rd International Cosmic Ray Conference

Fukushima, M. et al. 2013, Search for large-scale anisotropy of ultra-high energy cosmic rays with the Telescope Array

Funk, S., Hinton, J. A. & for the CTA Consortium 2013, Comparison of Fermi-LAT and CTA in the region between 10-100 GeV, Astroparticle Physics 43, 348, 1205.0832

Gabici, S. & Aharonian, F. A. 2005, Point-like gamma ray sources as signatures of distant accelerators of ultrahigh energy cosmic rays, Phys.Rev.Lett. 95, 251102, astro-ph/0505462

Gabici, S. & Aharonian, F. A. 2007, Gamma ray signatures of ultrahigh energy cosmic ray accelerators: electromagnetic cascade versus synchrotron radiation of secondary electrons, Astrophys.Space Sci. 309, 465, astro-ph/0610372

George, M. R., Fabian, A. C., Baumgartner, W. H. et al. 2008, On active galactic nuclei as sources of ultra-high energy cosmic rays, Monthly Notices of the RAS388, L59, 0805.2053

Ghisellini, G. 2010, The jet/disk connection in blazars, in American Institute of Physics Conference Series, American Institute of Physics Conference Series, volume 1242 (edited by Bertin, G., de Luca, F., Lodato, G. et al.), 43–54, 1002.4619

Ghisellini, G., Tavecchio, F. & Chiaberge, M. 2005, Structured jets in TeV BL Lac objects and radiogalaxies. Implications for the observed properties, Astronomy and Astrophysics432, 401, 0406093

Giacinti, G., Kachelriess, M., Semikoz, D. et al. 2012, Cosmic Ray Anisotropy as Signature for the Transition from Galactic to Extragalactic Cosmic Rays, JCAP 1207, 031, 1112.5599

Giannios, D. 2010, UHECRs from magnetic reconnection in relativistic jets, Monthly Notices of the RAS408, L46, 1007.1522

Gilmore, R. C., Madau, P., Primack, J. R. et al. 2009, GeV Gamma-Ray Attenuation and the High-Redshift UV Background, Monthly Notices of the Royal Astronomical Society 399, 4, 1694, URL `http://dx.doi.org/10.1111/j.1365-2966.2009.15392.x`

Ginzburg, V. L. & Syrovatskii, S. I. 1964, The Origin of Cosmic Rays

Giommi, P., Polenta, G., Lähteenmäki, A. et al. 2012, Simultaneous Planck, Swift, and Fermi observations of X-ray and γ-ray selected blazars, Astronomy and Astrophysics541, A160, 1108.1114

Giuliani, A., Cardillo, M., Tavani, M. et al. 2011, Neutral pion emission from accelerated protons in the supernova remnant w44, The Astrophysical Journal Letters 742, 2, L30, URL `http://stacks.iop.org/2041-8205/742/i=2/a=L30`

Gorbunov, D. S., Tinyakov, P. G., Tkachev, I. I. et al. 2004, Testing the correlations between ultrahigh-energy cosmic rays and BL Lac-type objects with HiRes stereoscopic data, Soviet Journal of Experimental and Theoretical Physics Letters 80, 145

Gorham, P. W., Allison, P., Baughman, B. M. et al. (ANITA Collaboration) 2010, Observational Constraints on the Ultra-high Energy Cosmic Neutrino Flux from the Second Flight of the ANITA Experiment, ArXiv e-prints 1003.2961

Górski, K. M., Hivon, E., Banday, A. J. et al. 2005, HEALPix: A Framework for High-Resolution Discretization and Fast Analysis of Data Distributed on the Sphere, The Astrophysical Journal622, 759, astro-ph/0409513

Greisen, K. 1966, End to the cosmic-ray spectrum?, Phys. Rev. Lett. 16, 748

Gunn, J. E. & Ostriker, J. P. 1969, Acceleration of High-Energy Cosmic Rays by Pulsars, Physical Review Letters 22, 728

Harari, D., Mollerach, S. & Roulet, E. 1999, The toes of the ultra high energy cosmic ray spectrum., Journal of High Energy Physics 8, 22, astro-ph/9906309

Harari, D., Mollerach, S. & Roulet, E. 2002a, Astrophysical magnetic field reconstruction and spectroscopy with ultra high energy cosmic rays, Journal of High Energy Physics 7, 6, astro-ph/0205484

Harari, D., Mollerach, S., Roulet, E. et al. 2002b, Lensing of ultra-high energy cosmic rays in turbulent magnetic fields, Journal of High Energy Physics 3, 45, astro-ph/0202362

Hartman, R. C., Bertsch, D. L., Bloom, S. D. et al. 1999, Third EGRET catalog (3EG) (Hartman+, 1999), VizieR Online Data Catalog 212, 30079

Hauser, M. G. & Dwek, E. 2001, The cosmic infrared background: measurements and implications, Ann.Rev.Astron.Astrophys. 39, 249, astro-ph/0105539

He, H.-N., Liu, R.-Y., Wang, X.-Y. et al. 2012, Icecube Nondetection of Gamma-Ray Bursts: Constraints on the Fireball Properties, The Astrophysical Journal752, 29, 1204.0857

Heitler, W. 1954, Quantum theory of radiation

Hess, V. 1912, Uber Beobacktunden der durchdringenden Strahlung bei sieben Freiballonfahrten, Physik. Zeitschr. 13, 1084

Hillas, A. M. 1984, The Origin of Ultra-High-Energy Cosmic Rays, Annual Review of Astronomy and Astrophysics22, 425

Hillas, A. M. 2005, TOPICAL REVIEW: Can diffusive shock acceleration in supernova remnants account for high-energy galactic cosmic rays?, Journal of Physics G Nuclear Physics 31, 95

Hinton, J. A. & Hofmann, W. 2009, Teraelectronvolt Astronomy, ARAA 47, 523, 1006.5210

Hogg, D. W. 1999, Distance measures in cosmology, ArXiv Astrophysics e-prints 9905116

Hooper, D. & Taylor, A. M. 2010, On The Heavy Chemical Composition of the Ultra-High Energy Cosmic Rays, Astropart.Phys. 33, 151, 0910.1842

Horns, D. & Meyer, M. 2012, Indications for a pair-production anomaly from the propagation of VHE gamma-rays, Journal of Cosmology and Astroparticle Physics2, 033, 1201.4711

Huan, H., Weisgarber, T., Arlen, T. et al. 2011, A New Model for Gamma-Ray Cascades in Extragalactic Magnetic Fields, The Astrophysical Journal Letters735, L28, 1106.1218

Inoue, Y., Inoue, S., Kobayashi, M. A. R. et al. 2013, Extragalactic Background Light from Hierarchical Galaxy Formation: Gamma-Ray Attenuation up to the Epoch of Cosmic Reionization and the First Stars, The Astrophysical Journal768, 197, 1212.1683

Ivanov, A. A., Knurenko, S. P. & Sleptsov, I. Y. 2009, Measuring extensive air showers with Cherenkov light detectors of the Yakutsk array: the energy spectrum of cosmic rays, New Journal of Physics 11, 6, 065008, 0902.1016

Jansson, R. & Farrar, G. R. 2012, A New Model of the Galactic Magnetic Field, The Astrophysical Journal757, 14, 1204.3662

Jiang, Y.-Y., Hou, L. G., Han, J. L. et al. 2010, Do Ultrahigh Energy Cosmic Rays Come from Active Galactic Nuclei and Fermi γ-ray Sources?, The Astrophysical Journal719, 459, 1004.1877

Jones, D. H., Read, M. A., Saunders, W. et al. 2009, The 6dF Galaxy Survey: final redshift release (DR3) and southern large-scale structures, MNRAS 399, 683, 0903.5451

Jui, C. C. (Telescope Array Collaboration) 2012, Cosmic Ray in the Northern Hemisphere: Results from the Telescope Array Experiment, J.Phys.Conf.Ser. 404, 012037, 1110.0133

Kachelrieß, M. & Semikoz, D. V. 2006, Clustering of ultra-high energy cosmic ray arrival directions on medium scales, Astroparticle Physics 26, 10, astro-ph/0512498

Kaiser, N. 1984, On the spatial correlations of Abell clusters, The Astrophysical Journal Letters284, L9

Kajino, F. 2010, The jem-euso mission to explore the extreme universe, Nuclear Instruments and Methods in Physics Research Section A: Accelerators, Spectrometers, Detectors and Associated Equipment 623, 1, 422 , ¡ce:title¿1st International Conference on Technology and Instrumentation in Particle Physics¡/ce:title¿, URL `http://www.sciencedirect.com/science/article/pii/S0168900210005875`

Kalli, S., Lemoine, M. & Kotera, K. 2011, Distortion of the ultrahigh energy cosmic ray flux from rare transient sources in inhomogeneous extragalactic magnetic fields, Astronomy and Astrophysics528, A109+, 1101.3801

Kampert, K.-H., Kulbartz, J., Maccione, L. et al. 2013, CRPropa 2.0 – a Public Framework for Propagating High Energy Nuclei, Secondary Gamma Rays and Neutrinos, Astropart.Phys. 42, 41, 1206.3132

Kashti, T. & Waxman, E. 2008, Searching for a correlation between cosmic-ray sources above 10^{19} eV and large scale structure, Journal of Cosmology and Astro-Particle Physics 5, 006, 0801.4516

Katz, B., Budnik, R. & Waxman, E. 2009, The energy production rate the generation spectrum of UHECRs, Journal of Cosmology and Astro-Particle Physics 3, 20, 0811.3759

Kelner, S. R. & Aharonian, F. A. 2008, Energy spectra of gamma rays, electrons, and neutrinos produced at interactions of relativistic protons with low energy radiation, Physical Review D78, 3, 034013, 0803.0688

Khan, E., Goriely, S., Allard, D. et al. 2005, Photodisintegration of ultra-high-energy cosmic rays revisited, Astroparticle Physics 23, 191, astro-ph/0412109

Kim, K.-T., Kronberg, P. P., Dewdney, P. E. et al. 1990, The halo and magnetic field of the Coma cluster of galaxies, The Astrophysical Journal355, 29

Kim, K.-T., Kronberg, P. P., Giovannini, G. et al. 1989, Discovery of intergalactic radio emission in the Coma-A1367 supercluster, Nature341, 720

King, E. J. & Coles, P. 2006, Amplification of primordial magnetic fields by anisotropic gravitational collapse, MNRAS 365, 1288, astro-ph/0508370

Kneiske, T. M., Bretz, T., Mannheim, K. et al. 2004, Implications of cosmological gamma-ray absorption. II. Modification of gamma-ray spectra, A&A 413, 807, astro-ph/0309141

Kneiske, T. M. & Dole, H. 2008, A strict lower-limit EBL Applications on gamma-ray absorption, in American Institute of Physics Conference Series, American Institute of Physics Conference Series, volume 1085 (edited by Aharonian, F. A., Hofmann, W. & Rieger, F.), 620–623, 0810.1612

Kneiske, T. M. & Dole, H. 2010, A lower-limit flux for the extragalactic background light, Astronomy and Astrophysics515, A19, 1001.2132

Koers, H. B. J. & Tinyakov, P. 2009, Testing large-scale (an)isotropy of ultra-high energy cosmic rays, Journal of Cosmology and Astroparticle Physics4, 3, 0812.0860

Kotera, K., Allard, D. & Lemoine, M. 2011, Detectability of ultrahigh energy cosmic-ray signatures in gamma-rays, A&A 527, A54+, 1011.0575

Kotera, K., Allard, D. & Olinto, A. V. 2010, Cosmogenic neutrinos: parameter space and detectabilty from PeV to ZeV, Journal of Cosmology and Astroparticle Physics10, 013, 1009.1382

Kotera, K. & Lemoine, M. 2008a, Inhomogeneous extragalactic magnetic fields and the second knee in the cosmic ray spectrum, Phys. Rev. D 77, 2, 023005, 0706.1891

Kotera, K. & Lemoine, M. 2008b, Optical depth of the Universe to ultrahigh energy cosmic ray scattering in the magnetized large scale structure, Phys. Rev. D 77, 12, 123003, 0801.1450

Kotera, K. & Olinto, A. V. 2011, The Astrophysics of Ultrahigh Energy Cosmic Rays, ARAA 49, 119, 1101.4256

Krawczynski, H., Carter-Lewis, D., Duke, C. et al. 2006, Gammahadron separation methods for the {VERITAS} array of four imaging atmospheric cherenkov telescopes, Astroparticle Physics 25, 6, 380 , URL `http://www.sciencedirect.com/science/article/pii/S0927650506000466`

Kronberg, P. P. 1994, Extragalactic magnetic fields, Reports on Progress in Physics 57, 325

Kronberg, P. P. & Perry, J. J. 1982, Absorption lines, Faraday rotation, and magnetic field estimates for QSO absorption-line clouds, ApJ 263, 518

Kronberg, P. P. & Simard-Normandin, M. 1976, New evidence on the origin of rotation measures in extragalactic radio sources, Nature263, 653

Kuempel, D. (Pierre Auger Collaboration) 2013, Directional search for ultra-high energy photons with the Pierre Auger Obser- vatory

Kulsrud, R. M. & Zweibel, E. G. 2008, On the origin of cosmic magnetic fields, Reports on Progress in Physics 71, 4, 046901, 0707.2783

Lawrence, M. A., Reid, R. J. O. & Watson, A. A. 1991, The cosmic ray energy spectrum above $4*10^{17}$ eV as measured by the Haverah Park array, Journal of Physics G Nuclear Physics 17, 733

Lee, S. 1998, On the propagation of extragalactic high-energy cosmic and gamma-rays, Phys.Rev. D58, 043004, astro-ph/9604098

Lefa, E., Rieger, F. M. & Aharonian, F. 2011, Formation of Very Hard Gamma-Ray Spectra of Blazars in Leptonic Models, The Astrophysical Journal740, 64, 1106.4201

Lemoine, M. & Waxman, E. 2009, Anisotropy vs chemical composition at ultra-high energies, JCAP 0911, 009, 0907.1354

Linsley, J. 1963, Evidence for a primary cosmic-ray particle with energy 10^{20} ev, Phys. Rev. Lett. 10, 146, URL `http://link.aps.org/doi/10.1103/PhysRevLett.10.146`

Madau, P. & Pozzetti, L. 2000, Deep galaxy counts, extragalactic background light and the stellar baryon budget, Monthly Notices of the RAS312, L9, astro-ph/9907315

Mannheim, K. 1993, The proton blazar, A&A 269, 67, astro-ph/9302006

Martinez, V. & Saar, E. 2002, Clustering statistics in cosmology, in Astronomical Data Analysis II, Society of Photo-Optical Instrumentation Engineers (SPIE) Conference Series, volume 4847 (edited by Starck, J.-L. & Murtagh, F. D.), 86–100, astro-ph/0209208

Mastichiadis, A. & Kirk, J. G. 1997, Variability in the synchrotron self-Compton model of blazar emission., Astronomy and Astrophysics320, 19, 9610058

Matthews, J. 2005, A Heitler model of extensive air showers, Astroparticle Physics 22, 387

Mazin, D. & Raue, M. 2007, New limits on the density of the extragalactic background light in the optical to the far-infrared from the spectra of all known TeV blazars, Astron.Astrophys. 471, 439, astro-ph/0701694

Medina-Tanco, G., Asano, K., Cline, D. et al. 2009, JEM-EUSO Science Objectives, 0909.3766 0909.3766

Meyer, M., Raue, M., Mazin, D. et al. 2012, Limits on the extragalactic background light in the Fermi era, Astronomy and Astrophysics542, A59, 1202.2867

Miniati, F. & Elyiv, A. 2013, Relaxation of Blazar-induced Pair Beams in Cosmic Voids, The Astrophysical Journal770, 54, 1208.1761

Mirabal, N. & Oya, I. 2010, Correlating Fermi gamma-ray sources with ultra-high-energy cosmic rays, Monthly Notices of the RAS405, L99, 1002.2638

Mostafa, M. (HAWC) 2013, The High Altitude Water Cherenkov Observatory, ArXiv e-prints 1310.7237

Mücke, A., Protheroe, R. J., Engel, R. et al. 2003, BL Lac objects in the synchrotron proton blazar model, Astroparticle Physics 18, 593, astro-ph/0206164

Mücke, A. et al. 1999, Photohadronic processes in astrophysical environments, Publications of the Astronomical Society of Australia 16, 160, astro-ph/9808279

Murase, K. 2012, High-energy Emission Induced by Ultra-high-energy Photons as a Probe of Ultra-high-energy Cosmic-Ray Accelerators Embedded in the Cosmic Web, The Astrophysical Journal Letters745, L16, 1111.0936

Murase, K., Dermer, C. D., Takami, H. et al. 2012, Blazars as Ultra-High-Energy Cosmic-Ray Sources: Implications for TeV Gamma-Ray Observations, Astrophys.J. 749, 63, 1107.5576

Murase, K., Inoue, S. & Nagataki, S. 2008a, Cosmic Rays above the Second Knee from Clusters of Galaxies and Associated High-Energy Neutrino Emission, ApJl 689, L105, 0805.0104

Murase, K., Mészáros, P. & Zhang, B. 2009, Probing the birth of fast rotating magnetars through high-energy neutrinos, Phys. Rev. D 79, 10, 103001, 0904.2509

Murase, K., Takahashi, K., Inoue, S. et al. 2008b, Probing Intergalactic Magnetic Fields in the GLAST Era through Pair Echo Emission from TeV Blazars, The Astrophysical Journal Letters686, L67, 0806.2829

Murase, K. & Takami, H. 2009, Implications of Ultra-High-Energy Cosmic Rays for Transient Sources in the Auger Era, Ap. J. 690, L14, 0810.1813

Neronov, A. & Vovk, I. 2010, Evidence for Strong Extragalactic Magnetic Fields from Fermi Observations of TeV Blazars, Science 328, 73, 1006.3504

Nolan, P. L., Abdo, A. A., Ackermann, M. et al. 2012, Fermi Large Area Telescope Second Source Catalog, The Astrophysical Journal Supplement Series199, 31, 1108.1435

Norman, C. A., Melrose, D. B. & Achterberg, A. 1995, The Origin of Cosmic Rays above 10 18.5 eV, The Astrophysical Journal454, 60

Oikonomou, F., Connolly, A., Abdalla, F. B. et al. 2013, A search for correlation of ultra-high energy cosmic rays with IRAS-PSCz and 2MASS-6dF galaxies, Journal of Cosmology and Astroparticle Physics5, 015, 1207.4043

Oikonomou, F., Kotera, K. & Abdalla, F. 2014a, Simulations for a next-generation UHECR observatory, In preparation for submission to JCAP

Oikonomou, F., Murase, K. & Kotera, K. 2014b, Synchrotron pair halo and echo emission from blazars in the cosmic web: application to extreme TeV blazars, A&A submitted

Olinto, A. V. 2005, The Highest Energy Cosmic Rays, in High Energy Gamma-Ray Astronomy, American Institute of Physics Conference Series, volume 745 (edited by Aharonian, F. A., Völk, H. J. & Horns, D.), 48–59, astro-ph/0410685

Owers, M. S., Blake, C., Couch, W. J. et al. 2007, The environments and clustering properties of 2df galaxy redshift survey selected starburst galaxies, Monthly Notices of the Royal Astronomical Society 381, 2, 494, http://mnras.oxfordjournals.org/content/381/2/494.full.pdf+html

Pe'Er, A., Murase, K. & Mészáros, P. 2009, Radio-quiet active galactic nuclei as possible sources of ultrahigh-energy cosmic rays, Physical Review D80, 12, 123018, 0911.1776

Penzias, A. A. & Wilson, R. W. 1965, A Measurement of Excess Antenna Temperature at 4080 Mc/s., The Astrophysical Journal142, 419

Prosekin, A., Essey, W., Kusenko, A. et al. 2012, Time Structure of Gamma-Ray Signals Generated in Line-of-sight Interactions of Cosmic Rays from Distant Blazars, The Astrophysical Journal757, 183, 1203.3787

Prosekin, A. Y., Kelner, S. & Aharonian, F. 2011, Non-variable cosmologically distant gamma-ray emitters as an imprint of propagation of ultra-high-energy protons, Astron.Astrophys. 536, A30, 1105.1947

Protheroe, R. & Biermann, P. 1996a, A New estimate of the extragalactic radio background and implications for ultrahigh-energy gamma-ray propagation, Astropart.Phys. 6, 45, astro-ph/9605119

Protheroe, R. & Biermann, P. 1996b, A New estimate of the extragalactic radio background and implications for ultrahigh-energy gamma-ray propagation, Astropart.Phys. 6, 45, astro-ph/9605119

Ptitsyna, K. V. & Troitsky, S. V. 2010, Physical conditions in potential accelerators of ultra-high-energy cosmic rays: updated Hillas plot and radiation-loss constraints, Physics Uspekhi 53, 691, 0808.0367

Puget, J. L., Stecker, F. W. & Bredekamp, J. H. 1976, Photonuclear interactions of ultrahigh energy cosmic rays and their astrophysical consequences, The Astrophysical Journal205, 638

Rachen, J. 1996, Ph.D. thesis, Universitat zu Bonn

Rachen, J. P. & Biermann, P. L. 1993, Extragalactic Ultra-High Energy Cosmic-Rays - Part One - Contribution from Hot Spots in Fr-II Radio Galaxies, A&A 272, 161, astro-ph/9301010

Rieger, F. M. & Aharonian, F. A. 2009, Centaurus A as TeV γ-ray and possible UHE cosmic-ray source, Astronomy and Astrophysics506, L41, 0910.2327

Rieger, F. M., de Oña-Wilhelmi, E. & Aharonian, F. A. 2013, TeV astronomy, Frontiers of Physics 1302.5603

Rieger, F. M. & Duffy, P. 2004, Shear Acceleration in Relativistic Astrophysical Jets, The Astrophysical Journal617, 155, astro-ph/0410269

Roberts, J. & Farrar, G. 2013, UHECR correlations taking account of composition and Galactic magnetic deflections 1308.4115

Romero, G. E., Combi, J. A., Perez Bergliaffa, S. E. et al. 1996, Centaurus A as a source of extragalactic cosmic rays with arrival energies well beyond the GZK cutoff, Astroparticle Physics 5, 279, gr-qc/9511031

Rouille d'Orfeuil, B. (Pierre Auger Collaboration) 2011, Search for Galactic point-sources of EeV neutrons

Ryu, D., Kang, H. & Biermann, P. L. 1998, Cosmic magnetic fields in large scale filaments and sheets, A&A 335, 19, astro-ph/9803275

Salesa Greus, F. (Pierre Auger Collaboration) 2013, Searches for Galactic neutron sources with the Pierre Auger Observatory

Saunders, W., Sutherland, W. J., Maddox, S. J. et al. 2000, The PSCz catalogue, MNRAS 317, 55, astro-ph/0001117

Seiffert, M., Fixsen, D., Kogut, A. et al. 2009, Interpretation of the Extragalactic Radio Background 0901.0559

Settimo, M. (Pierre Auger Collaboration) 2011, An update on a search for ultra-high energy photons using the Pierre Auger Observatory

Shaver, P. A. & Pierre, M. 1989, Large-scale anisotropy in the sky distribution of extragalactic radio sources, Astronomy and Astrophysics220, 35

Sheth, R. K. & Tormen, G. 1999, Large-scale bias and the peak background split, Monthly Notices of the RAS308, 119, astro-ph/9901122

Sigl, G., Miniati, F. & Enßlin, T. A. 2004a, Cosmic Magnetic Fields and Their Influence on Ultra-High Energy Cosmic Ray Propagation, Nuclear Physics B Proceedings Supplements 136, 224, astro-ph/0409098

Sigl, G., Miniati, F. & Enßlin, T. A. 2004b, Ultrahigh energy cosmic ray probes of large scale structure and magnetic fields, Phys. Rev. D 70, 4, 043007, astro-ph/0401084

Simard-Normandin, M. & Kronberg, P. P. 1980, Rotation measures and the galactic magnetic field, ApJ 242, 74

Simpson, J. A. 1983, Elemental and Isotopic Composition of the Galactic Cosmic Rays, Annual Review of Nuclear and Particle Science 33, 323

Singal, J., Stawarz, L., Lawrence, A. et al. 2010, Sources of the Radio Background Considered, Mon.Not.Roy.Astron.Soc. 409, 1172, 0909.1997

Sironi, L. & Giannios, D. 2014, Relativistic pair beams from tev blazars: A source of reprocessed gev emission rather than intergalactic heating, The Astrophysical Journal 787, 1, 49, URL `http://stacks.iop.org/0004-637X/787/i=1/a=49`

Soiaporn, K., Chernoff, D., Loredo, T. et al. 2012, Multilevel Bayesian framework for modeling the production, propagation and detection of ultra-high energy cosmic rays, ArXiv e-prints 1206.4569

Sokolsky, P. et al. (HiRes Collaboration) 2010, Final Results from the High Resolution Fly's Eye (HiRes) Experiment, PoS ICHEP2010, 444, 1010.2690

Sommers, P. 2001, Cosmic ray anisotropy analysis with a full-sky observatory, Astroparticle Physics 14, 271, astro-ph/0004016

Sreekumar, P. et al. (EGRET Collaboration) 1998, EGRET observations of the extragalactic gamma-ray emission, Astrophys.J. 494, 523, astro-ph/9709257

Stanev, T. 1997, Ultra–High-Energy Cosmic Rays and the Large-Scale Structure of the Galactic Magnetic Field, The Astrophysical Journal479, 290, astro-ph/9607086

Stanev, T. 2005, High energy astrophysical processes, ArXiv Astrophysics e-prints astro-ph/0504401

Stanev, T. et al. 1995, Arrival Directions of the Most Energetic Cosmic Rays, Physical Review Letters 75, 3056, astro-ph/9505093

Stecker, F. W. 1968, Ph.D. thesis, AA (Harvard University)

Stecker, F. W., Malkan, M. A. & Scully, S. T. 2006, Intergalactic Photon Spectra from the Far-IR to the UV Lyman Limit for 0 ¡ z ¡ 6 and the Optical Depth of the Universe to High-Energy Gamma Rays, ApJ 648, 774, astro-ph/0510449

Stecker, F. W. & Salamon, M. H. 1999, Photodisintegration of Ultra-High-Energy Cosmic Rays: A New Determination, ApJ 512, 521, astro-ph/9808110

Steele, I., Mundell, C., Barres de Almeida, U. et al. 2012, RINGO2 Optical Polarimetric Observations of PG 1553+113 during a MAGIC Gamma-ray Flare, The Astronomer's Telegram 4078, 1

Sun, X. H., Reich, W., Waelkens, A. et al. 2008, Radio observational constraints on Galactic 3D-emission models, Astronomy and Astrophysics477, 573, 0711.1572

Takami, H., Murase, K. & Dermer, C. D. 2013, Disentangling Hadronic and Leptonic Cascade Scenarios from the Very-High-Energy Gamma-Ray Emission of Distant Hard-Spectrum Blazars, Astrophys.J. 771, L32, 1305.2138

Takami, H., Nishimichi, T. & Sato, K. 2009a, Systematic Survey of the Correlation between Northern HECR Events and SDSS Galaxies, ArXiv e-prints 0910.2765

Takami, H., Nishimichi, T., Yahata, K. et al. 2009b, Cross-correlation between UHECR arrival distribution and large-scale structure, Journal of Cosmology and Astroparticle Physics6, 031, 0812.0424

Takami, H., Yoshiguchi, H. & Sato, K. 2006, Propagation of Ultra-High-Energy Cosmic Rays above 10^{19} eV in a Structured Extragalactic Magnetic Field and Galactic Magnetic Field, ApJ 639, 803, astro-ph/0506203

Takeda, M., Sakaki, N., Honda, K. et al. 2003, Energy determination in the Akeno Giant Air Shower Array experiment, Astroparticle Physics 19, 447, astro-ph/0209422

Tavani, M., Giuliani, A., Chen, A. W. et al. 2010, Direct evidence for hadronic cosmic-ray acceleration in the supernova remnant ic 443, The Astrophysical Journal Letters 710, 2, L151, URL `http://stacks.iop.org/2041-8205/710/i=2/a=L151`

Tavani, M. et al. (AGILE Collaboration) 2009, The AGILE Mission, Astron.Astrophys. 502, 995, 0807.4254

Tavecchio, F. 2014, On the hadronic cascade scenario for extreme BL Lacs, Monthly Notices of the RAS438, 3255, 1312.4281

Tavecchio, F., Ghisellini, G., Bonnoli, G. et al. 2011, Extreme TeV blazars and the intergalactic magnetic field, MNRAS 414, 3566, 1009.1048

Tavecchio, F., Maraschi, L. & Ghisellini, G. 1998, Constraints on the Physical Parameters of TeV Blazars, The Astrophysical Journal509, 608, 9809051

Taylor, A., Hinton, J., Blasi, P. et al. 2009, Identifying Nearby UHECR Accelerators using UHE (and VHE) Photons, Phys.Rev.Lett. 103, 051102, 0904.3903

Taylor, A. M., Vovk, I. & Neronov, A. 2011, Extragalactic magnetic fields constraints from simultaneous GeV-TeV observations of blazars, Astronomy and Astrophysics529, A144, 1101.0932

Tegmark, M., Hartmann, D. H., Briggs, M. S. et al. 1996, The Angular power spectrum of BATSE 3B gamma-ray burst, Astrophys.J. 468, 214, astro-ph/9510129

Teyssier, R. 2002, Cosmological hydrodynamics with adaptive mesh refinement. A new high resolution code called RAMSES, Astronomy and Astrophysics385, 337, 0111367

Tinyakov, P. G. & Tkachev, I. I. 2001, BL Lacertae are Probable Sources of the Observed Ultrahigh Energy Cosmic Rays, Soviet Journal of Experimental and Theoretical Physics Letters 74, 445, astro-ph/0102476

Tinyakov, P. G. & Tkachev, I. I. 2005, Deflections of cosmic rays in a random component of the Galactic magnetic field, Astroparticle Physics 24, 32, arXiv:astro-ph/0411669

Tueller, J., Baumgartner, W. H., Markwardt, C. B. et al. 2010, The 22 Month Swift-BAT All-Sky Hard X-ray Survey, The Astrophysical Journal Supplement Series186, 378, 0903.3037

Urry, C. M. & Padovani, P. 1995, Unified schemes for radio-loud active galactic nuclei, Publ.Astron.Soc.Pac. 107, 803, astro-ph/9506063

Vallee, J. P. 1997, Observations of the Magnetic Fields Inside and Outside the Milky Way, Starting with Globules (˜ 1 parsec), Filaments, Clouds, Superbubbles, Spiral Arms, Galaxies, Superclusters, and Ending with the Cosmological Universe's Background Surface (at ˜ 8 Teraparsecs), Fundamental Cosmic Physics19, 1

Véron-Cetty, M.-P. & Véron, P. 2006, A catalogue of quasars and active nuclei: 12th edition, A&A 455, 773

Vietri, M. 1995, The Acceleration of Ultra–High-Energy Cosmic Rays in Gamma-Ray Bursts, ApJ 453, 883, astro-ph/9506081

Vovk, I., Taylor, A. M., Semikoz, D. et al. 2012, Fermi/LAT Observations of 1ES 0229+200: Implications for Extragalactic Magnetic Fields and Background Light, The Astrophysical Journal Letters747, L14, 1112.2534

Wagner, R. M. 2008, Synoptic studies of 17 blazars detected in very high-energy γ-rays, Monthly Notices of the RAS385, 119, 0711.3025

Watson, L. J., Mortlock, D. J. & Jaffe, A. H. 2011, A Bayesian analysis of the 27 highest energy cosmic rays detected by the Pierre Auger Observatory, Monthly Notices of the RAS418, 206, 1010.0911

Waxman, E. 1995a, Cosmological Gamma-Ray Bursts and the Highest Energy Cosmic Rays, Physical Review Letters 75, 386, astro-ph/9505082

Waxman, E. 1995b, Cosmological Origin for Cosmic Rays above 10 19 eV, ApJl 452, L1+, astro-ph/9508037

Waxman, E. 2011, High energy cosmic ray and neutrino astronomy, ArXiv e-prints 1101.1155

Waxman, E., Fisher, K. B. & Piran, T. 1997, The Signature of a Correlation between Cosmic-Ray Sources above 10 19 eV and Large-Scale Structure, Astrophys. J. 483, 1, 9604005

Waxman, E. & Miralda-Escude, J. 1996, Images of Bursting Sources of High-Energy Cosmic Rays: Effects of Magnetic Fields, The Astrophysical Journal Letters472, L89, astro-ph/9607059

Weekes, T. C., Cawley, M. F., Fegan, D. J. et al. 1989, Observation of TeV gamma rays from the Crab nebula using the atmospheric Cerenkov imaging technique, The Astrophysical Journal342, 379

Widrow, L. M. 2002, Origin of galactic and extragalactic magnetic fields, Reviews of Modern Physics 74, 775, astro-ph/0207240

Woo, J.-H., Urry, C. M., van der Marel, R. P. et al. 2005, Black Hole Masses and Host Galaxy Evolution of Radio-Loud Active Galactic Nuclei, The Astrophysical Journal631, 762, astro-ph/0506316

Zacharopoulou, O., Khangulyan, D., Aharonian, F. A. et al. 2011, Modeling the Hard TeV Spectra of Blazars 1ES 0229+200 and 3C 66A with an Internal Absorption Scenario, The Astrophysical Journal738, 157, 1106.3129

Zatsepin, G. & Kuzmin, V. 1966, Upper limit of the spectrum of cosmic rays, J. Exp. Theor. Phys. Lett. 4, 78

Zatsepin, G. T. & Kuz'min, V. A. 1966, Upper Limit of the Spectrum of Cosmic Rays, Soviet Journal of Experimental and Theoretical Physics Letters 4, 78

Zech, A. & Cerruti, M. (CTA Consortium) 2013, Signatures of relativistic protons in CTA blazar spectra, International Cosmic Ray Conference 2013, 1307.3038